University of Granada

Department of Electromagnetism and Matter Physics

PhD Thesis

Numerical simulation and experimental study of the natural electromagnetic waves in the ELF and VLF bands

by

Sergio Toledo Redondo

Advisors:

Alfonso Salinas Extremera

Jesús Fornieles Callejón

Jorge Portí Durán

Granada, April 2012

Editor: Editorial de la Universidad de Granada
Autor: Sergio Toledo Redondo
D.L.: GR 2883-2012
ISBN: 978-84-9028-200-7

UNIVERSIDAD DE GRANADA

Numerical simulation and experimental study of the natural electromagnetic waves in the ELF and VLF bands

por

Sergio Toledo Redondo

Directores

Alfonso Salinas Extremera

Jesús Fornieles Callejón

Jorge Portí Durán

Memoria presentada por Sergio Toledo Redondo para optar al grado de Doctor por la Universidad de Granada.

Fdo. Sergio Toledo Redondo

Declaración de Autoría

El **Dr. Alfonso Salinas Extremera**, Profesor Titular del Departamento de Electromagnetismo y Física de la Materia de la Universidad de Granada,

El **Dr. Jesús Fornieles Callejón**, Profesor Titular del Departamento de Electromagnetismo y Física de la Materia de la Universidad de Granada, y

El **Dr. Jorge Portí Durán**, Profesor Titular del Departamento de Física Aplicada de la Universidad de Granada.

CERTIFICAN

Que el presente trabajo titulado **"Numerical simulation and experimental study of the natural electromagnetic waves in the ELF and VLF bands"** ha sido realizado bajo su dirección y constituye la Tesis Doctoral de **Sergio Toledo Redondo**.

Con esta fecha autorizamos su presentación ante la Comisión de Doctorado de la Universidad de Granada.

En Granada, a 11 de Abril de 2012

Fdo: Alfonso Salinas Fdo: Jesús Fornieles Fdo: Jorge Portí

La realidad existe de manera independiente de la mente humana.
La naturaleza es regular, al menos en alguna medida.
El ser humano es capaz de comprender la naturaleza.

Al parecer, ante la turbación que nos crea el cuestionar estas afirmaciones, los científicos de hoy en día hemos decidido obviar su discusión, junto con la trascendencia que ésta conlleva.

Agradecimientos

Cuando me embarqué en el proyecto de comenzar la tesis doctoral, me parecía más bien un proyecto o estilo de vida que algo que tendría un inicio y un final. Al inicio de esta andadura, se podría decir que era otra persona viviendo en otro universo. Para nada tengo la sensación de que cuatro años han pasado volando, más bien al contrario. Infinidad de cosas me han ocurrido a mí y a mi alrededor, y este eje o hilo conductor que ha sido la ciencia, la universidad, el grupo de investigación, ha sido un pilar en este largo camino plagado de buenas sensaciones.

La primera persona a la que le debo gran parte de esta tesis es a María, mi madre. Puede sonar a tópico, pero fueron muchos los momentos de duda y de flaqueza sobre el camino hacia el punto en el que me encuentro. Mi madre siempre estuvo al pie del cañón, siempre dispuesta a escuchar mis planteamientos y hablarme desde la voz de alguien que lleva muchos años más de andadura. Y ahora estoy seguro de que sus consejos y opiniones me han llevado por una de las mejores sendas que se me han abierto durante mi camino por el mundo. Por fin ha llegado el día tantas veces referenciado, "*algún día me entenderás*". Tengo claro que sin tu amor y tu apoyo incondicional no estaría hoy donde estoy. Gracias.

Las siguientes palabras son sin duda alguna para Alfonso, mi principal director de tesis. Has sido un punto de referencia para mi, y no me refiero sólo al ámbito científico, que también. Trabajar a tu lado (porque desde el primer día te desmarcaste de estar por encima) ha sido una fuente de inspiración, de serenidad, de confianza. No te imaginas la tranquilidad que da saber que estás ahí siempre que hay que sacar las castañas del fuego. Además, la línea de investigación que has iniciado y a la que yo me he unido, me parece tan interesante en sus contenidos como noble en sus objetivos. Para mi este punto ha sido muy importante, ya que creo firmemente en la trascendencia de mis actos, y para embarcarme en un proyecto de cuatro años necesitaba una temática con unas líneas leales a mi forma de pensar. Tú la tenías. Gracias.

Las gentes que conforman el grupo de investigación en el que estado inmerso son grandes. Juan Antonio, tu experiencia y sabiduría están todavía conmigo. En el plano científico, has sido la persona con más bagaje con la que he podido compartir mis experiencias. Y tu capacidad para dejar de lado nuestras pequeñas diferencias siempre me asombró, me hizo aprender a ser una persona más íntegra.

Respecto a la última de tus enseñanzas, aún no he podido asimilarla. Jesús, la alegría y la frescura del grupo. Por supuesto añadidos a tu ya larga y consistente trayectoria. Cada vez que abordabas un nuevo tema y te veía desgranarlo más allá de sus partículas elementales, quedaba simplemente fascinado. Espero algún día ser capaz de ahondar de esa manera en los enigmas que se me presenten. Además he tenido la suerte de estar cerca tuyo viendo como tu familia crecía, y he podido contagiarme de esos momentos de gozo y alborozo. Jorge, quizá nuestra interacción no haya sido tan intensa como con otros componentes del grupo, con la notable excepción de la recta final de esta tesis, en la que has jugado un papel clave y fundamental. Desde el primer día en que tuvimos una charla sobre TLM quedé maravillado por la profundidad de tus conocimientos sobre él. Esto unido a tu capacidad de relacionar conceptos, te dota de una capacidad pedagógica fuera de serie. Y Antonio, compañero de fatigas, de alegrías, de disgustos, y de tantas cosas en estos 4 años. Un cálculo rápido me dice que hemos pasado más de 7,000 horas juntos en estos últimos años!!! Tu capacidad matemática, junto con tu rigurosidad en el trabajo y tu vocación por la excelencia me han sacado del atolladero tantas veces... En esas más de 7,000 horas siempre estuviste dispuesto a escuchar mis dudas y dedicarles el tiempo que necesitaran, fuera el que fuera. En fin, soy consciente de que he tenido un equipo con una calidad científica y, más importante aún, humana, formidables. A todos, Gracias.

Michel, tu m'as accueilli avec les bras ouverts sans même me connaître. Pendant ces trois mois à travailler près de toi, j'ai beaucoup appris, tu es un scientifique prestigieux et tu m'as transmis cette grandeur en me permettant de travailler à ton côté. Tu as investi ton temps et tu as mis tous tes moyens à ma disposition. Ainsi grâce à toi, j'ai pu découvrir le fascinant monde de l'espace. Merci.

Y cuantas otras mentes inquietas han sido compañeras de andanzas! Sebastiano, el músico filosofísico, cuántos momentos buenos, los mejores en la Sierra, no? Carlos, hemos transitado montañas, ecuaciones y fiestas por doquier juntos, vaya mezcla eh?, Jordi, tú que solo necesitas papel y lápiz para trabajar, a ti se te veía más en las fiestas que por las montañas... Jose, el omnipresente informático que todo lo sabe, para los PhD vulgares eres la solución de todo lo no solucionable, Jesús y Pamela, cuando empezó esta andadura erais dos individuos y ahora sois una familia! enhorabuena. Margarita, del equipo papel y boli, que pérdida cuando te fuiste para Cádiz, Manolo, nuestra andadura no se ha cruzado mucho, pero soy

consciente de que llevamos 4 años remando en paralelo, codo con codo. A todos, Gracias.

Rai, tu me abriste las puertas al llegar a Granada, y me enseñaste las muchas maravillas que alberga. Con tu alegría, tu sonrisa y tu amistad has hecho que me sienta como en casa. Gracias.

Y todos esos amigos, mi familia de Granada, que me habéis dado tantas alegrías y buenos momentos: Antoine, María, Miki, Beltram, Aitor, Lore, Kike, Nico, Ana, Ainhoa, Dani, Trini, David, Paula, Alex, Reme, Pablo, María (no hay más que una), Guío, Jose...pff y podría no parar y la tesis entera sería una infinidad de nombres que de solo pensar en ellos una sonrisa se me dibuja en el rostro. A todos, Gracias.

Y a mis gentes de Menorca, que os llevo en el corazón, no hace falta ni poner nombres ni decir nada, porque nuestra comunicación y conexión está por encima del lenguaje racional. Aun así dos claves: Alaior y GOB. Os quiero, y habría que inventar un nuevo tiempo verbal para conjugar este verbo, uno que no fuera ni pasado, ni presente, ni futuro, sino los tres a la vez.

Contents

A Juan Antonio Morente,

porque tu obra perdura más allá de la vida o la muerte.

Overview

The main motivation of this study is to characterize the natural electromagnetic phenomena occurring in the Earth-ionosphere cavity, with the aim of extracting information from the natural processes which are involved in its generation and propagation.

This story starts at the end of the XIX century, with various scientists starting to think on the Earth as a global electromagnetic circuit. A great historical review of the beginnings of this topic was made by Besser [4]. The study of the electromagnetic natural noise recovered its interest with the work by Williams [5], who related the Schumann resonance parameters with the global temperature, setting the basis to study the global climate by means of the electromagnetic natural emissions. Recently, several studies prove that these phenomena can be employed for prediction of natural disasters like earthquakes or volcano eruptions, e.g. [6].

We perform two independent experimental studies based on the measurement of these signals on a large time scale (in the order of years). Time series recorded at ground level are employed for the first study, and records from DEMETER satellite are analyzed in the second. Signals in the Extremely Low Frequency band, 3 Hz - 3 kHz, and in the VLF band, 3 kHz - 30 kHz, are discussed in this dissertation.

Then, a way to model the full 3D Earth-ionosphere cavity by means of TLM method is presented. The model employes parallelization techniques, due to the memory and computation requirements to model the problem. The model is validated through comparison with analytical solutions to simplifications of the real cavity, as well as results from experimental measurements of the modeled phenomena. Finally, the first results obtained with this tool are presented, like for instance the effect of an atmospheric disturbance on the SR, or the implications of the day-night asymmetry of the cavity.

Chapter 1

Introduction

Up to the moment, Environmental and Geophysical Sciences have not considered natural electromagnetic phenomena as a means to test the Earth's state, mainly due to the fact that (1) many of these phenomena are not known in depth yet, that is to say, there are experimental measurements but not models generating results coherent with these measurements; and (2) variations generated by anomalies or changes in the environment are small and, therefore, difficult to measure and model.

Is it possible to get a reliable short term prediction of an earthquake? Is it possible to measure the global warming of the Earth through a *natural thermometer*? An affirmative answer to these questions would be a significant advance to environmental sciences and to disaster prevention.

Regarding the first question, the debate on what must be understood as a seismic prediction arises [7]. We can define the following prediction levels: (1) Time-independent risk with a fully probabilistic prediction in terms of the area under study; (2) time-dependent and cyclic risk in the sense that the longer the time elapsed since the last earthquake event, the longer the expected time for a new earthquake to occur; (3) Prediction based on facts which anticipate the seismic event, with a probabilistic calculation, with the aim of alerting authorities but with an uncertainty of weeks or months; (4) Deterministic prediction of the location, magnitude and moment at which the earthquake will occur.

Naturally, this last option is the more desirable for the scientists involved and for the society in general. Present predictions are vague up to the point that, by

using historical studies together with satellite determination of movements of the Earth's crust and voltage measurements at its interior, scientists can predict with high probability of success a seismic event in a time span of 30 years [8]. Short term prediction will not arise from the study of Earth's crust movement, but from electromagnetic phenomena, instead, and not only from phenomena happening at the Earth's surface but also at the ionosphere: DEMETER (Detection of Electro-Magnetic Emissions Transmitted from Earthquake Regions) satellite was launched into orbit in June 2004 to measure different ionosphere variables, especially at regions with high seismic activity [9].

Regarding the second question, in 1992, a paper was published in Science magazine, in which a mechanism for detecting the global temperature in the tropic regions was proposed [5]. This method was based on the study of an electromagnetic phenomenon of natural origin, the Schumann resonance frequencies [10], which occurs inside the natural cavity formed by the Earth's surface and the lower ionosphere, both defining two enormous concentric conducting surfaces separated by a lossy dielectric, the atmosphere. The size of this cavity is peculiar: together with a perimeter of around 40,000 km, the height of the ionosphere is only 50 - 60 km during daytime and around 80 - 90 km during nighttime.

Schumann resonances consist of ELF oscillations generated by lightning events, which propagate through the whole cavity as Transverse Magnetic (TM) modes, thus providing a tool for the study the parameters of the lower ionosphere and the intensity of lightning activity. Studies carried out by Williams during a six-years span proved the existence of a correlation between annual variations in the amplitude of the first Schumann resonances and the temperature at the Tropics, calculated through the time average of the number of lightning strokes in the Earth. Constant discharges simultaneously produced in the Earth are electromagnetic field sources which propagate in the atmosphere, continuously reflecting at the Earth's surface and the ionosphere. In the ELF band, and due to the atmosphere conductivity, waves can propagate several turns around the Earth's perimeter generating the mentioned resonances.

Natural electromagnetic phenomena occurring around us can be classified into three categories: (1) those associated with lightning strokes in the atmosphere, (2) those happening in the plasma of the ionosphere and the magnetosphere, and (3) those generated at the lithosphere [11]. Multiple different phenomena are being observed in the two first categories, such as optic emissions at the mesosphere,

as a consequence of lightning discharges and which lead to think of an electrodynamic coupling between mesosphere and ionosphere. The third category is completely new and gathers evidences indicating that seismic-electromagnetic phenomena could be a means to obtain short-term earthquake predictions [6]. Emissions in the frequency range from Ultra Low Frequency (ULF) to Very High Frequency (VHF) (including DC) originate at the lithosphere, and also perturbations caused by earthquakes have been detected on the atmosphere and the ionosphere. Nevertheless, the mechanisms generating these emissions and the coupling between lithosphere-atmosphere-ionosphere are nowadays hardly understood. It becomes evident that analytical models are unable to describe the complexity of the system, and numerical methods are necessary to corroborate hypotheses by studying the concordance between obtained results and experimental measurements. In this sense, we consider very interesting the proposal of the technical committee of Electromagnetic Theory of the Institute of Electric Engineers of Japan, leaded by professor Masahi Hayakawa, from the University of Electro Communications of Tokyo (Japan), to create a research topic termed "Natural Electromagnetic Phenomena and Electromagnetic Analysis". This research joins experiences in the field of natural electromagnetic phenomena and computational Electromagnetics.

As concerns experimental observations of signals produced by seismic events, together with DEMETER satellite launched into orbit with French Government majority stake, Japanese government has started two research projects based on a network of terrestrial observatories: Frontier/RIKEN to study the seismic-electromagnetic effects inside the Earth, and Frontier/NASDA to study the effects at the atmosphere and/or ionosphere. The American company QuakeFinder (located in Palo Alto, California) is investing millions of dollars in ULF sensors located on ground and in launching into orbit a satellite intended for seismic prevention (*http://www.quakefinder.com*). At present, there exists research groups concerned with this field in Japan, Russia (with active collaboration between them), China, Taiwan, France, Italy, Greece, USA, Ukraine, Mexico, Israel, India, and Germany, at least.

Besides these observatories, which can be regarded as recent ones, a network of observatories for ELF signals is working in multiple countries. These observatories emerged in the 60s and, by means of electric and/or magnetic sensors, a record of the electromagnetic field in the frequency band ranging from a few to 40 - 50

Hertz is made (although some stations are able to record up to several hundreds of Hertz) [12].

1.1 Resonances inside the Earth-ionosphere cavity

Our planet is a solid conducting sphere covered with a thin layer of dielectric atmosphere. The width of this layer is around 30 km. This means that 99% of the atmospheric mass is located below that height and that only 1% is above this point. Nevertheless, this part plays a fundamental role in the electromagnetic behavior of the whole atmosphere, since conductivity gradually increases 6 magnitude orders, generating the ionosphere, a layer located above 60 km during daytime and above 90 km during nighttime.

The ionosphere plays an essential role in radio propagation and its effect on electromagnetic waves strongly depends on frequency. In the GHz band, its role reduces to a small perturbation in the signals (above a few tens of MHz it is practically transparent), in the HF and LF bands, signals reflect, and in the ELF and VLF bands, propagation is seriously affected, even for small distances. Radio waves of a few Hertz may travel around the Earth and go back to the starting point. If the phase difference generated in this journey is 2π, a global resonance phenomenon is produced. W.O. Schumann predicted the existence of these resonances in 1952. Sixty years later, natural electromagnetic phenomena are a powerful tool in the study of global lightning activity and the properties of the lower ionosphere at planetary scale [1, 2, 12].

The Radio Engineering History begun around one hundred years ago, during the end of the 19th century. Several scientists started to conceive the Earth as one element of a radio system. Although some controversies remain when it comes to establish the first author on the field, there is an excellent review by Besser [4], which extensively documents these origins. At those times, electromagnetic radiation was observed either from lightning activity or from discharges generated at the laboratory. Later, radio waves with harmonic variation were used for signal transmission. Once the ionosphere was discovered, a great expansion in shortwave radio was produced (HF band, between 3 and 30 MHz). During and after the II World War, radar was developed for military applications, and it was employed later for remote-sensing the environment. W.O. Schumann predicted in 1952 [10]

the existence of resonances in the whole Earth-ionosphere cavity. Experimental evidence of this fact was achieved in 1960 by Balser and Wagner [13]. The frequency values calculated by Schumann and the measurements are in disagreement by a few Hertz for all the resonances. This fact is well known and it is attributed to the conductivity profile with height of the real cavity [14], not accounted for in the calculations made by Schumann.

During the second half of the XX Century, a strong research on the VLF and ELF bands emerged with goals (mainly of military kind) in global radio communications and submarine communications. With the decay of the Cold War, research in the ELF band was drastically reduced. However, the interest in Schumann resonances emerged in the 90s to use them as a tool to study the global warming through monitoring of global lightning activity in storms generated by atmospheric convection, which depends on the Earth's surface temperature [5]. This interest has also grown due to the possibility of locating high-intensity lightning strokes which generate transient ELF signals (Q-bursts), causing variations in the mesosphere (sprites, elves, etc.).

Three research problems emerge in a natural way from the resonances at the Earth-ionosphere cavity: i) the Physics of radio propagation, ii) the characterization of lightning through their electromagnetic radiation, and iii) the derivation of the properties of the lower ionosphere, since it is the outer limit of the electromagnetic cavity and, in addition, there exist electromagnetic couplings with the atmosphere [12].

The Earth-ionosphere system can be regarded as a waveguide, a cavity, or a capacitor, depending on the wavelength under consideration. We will consider a waveguide if the Earth's radius, a, is much longer than the wavelength, λ, i.e., $a >> \lambda$. Natural oscillations become quasi-electrostatic in the opposite case, $a << \lambda$ and the field description can be reduced to the charge and discharge process of a spherical capacitor. The term resonator is appropriated when the wavelength is comparable to the Earth's perimeter, $\lambda \simeq 2\pi a$. Due to its three-dimensional character, three types of resonances are produced in the Earth-ionosphere cavity. In addition to Schumann resonances, associated to the Earth's perimeter, those produced when an integer number of half wavelengths match the ionosphere height must exist, and they are known as transverse resonances. The third type is concerned with azimuthal propagation and appears, very slightly, as a splitting of the Schumann resonances in a non-uniform and anisotropic model of the cavity.

Resonance frequencies can be derived in an approximated way for Schumann resonances as well as for transverse resonances. In the first case, the condition to be met is that the phase shift due to the journey around the Earth, with a perimeter around ($2\pi a \simeq 40$ Mm), is an integer multiple of the wavelength:

$$f_n = \frac{c}{2\pi a} n = 7.5n \tag{1.1}$$

As for the transverse resonances, the condition to be met is that the effective height, $h \simeq 75$ km, of the cavity is an integer multiple of a half-wavelength.

$$F_p = \frac{c}{2h} p = 2\ 10^3 p \text{ Hz} \tag{1.2}$$

For frequencies of tens of Hertz, attenuation in the atmosphere is only of a few tenths of dB per 1,000 km, which allows the signal to travel several turns around the Earth before significant damping. On the other side, transverse resonances are local phenomena due to the high level of atmospheric attenuation at these frequencies, around 20 dB/1,000 km, which causes that the wave cannot travel far from the source (lightning strokes) and, therefore, the resonance has local nature. Transverse resonances are better observed at night since hiss noise from the ionospheric plasma is much lower under nighttime conditions.

In the VLF band, the signal wavelength is of the order on 100 km and it could be said that the Earth-ionosphere system behaves as a cavity. However, resonance frequencies at this band are usually referred to as cut-off frequencies for the Earth-ionosphere waveguide in the specialized literature [15–17]. Due to the high losses occurring at these frequencies, signals from lightning travel only a small portion of the Earth-ionosphere cavity. Under this situation, the problem can be approximated as a parallel conducting plates waveguide.

As it will be discussed in Section 1.3, for the ideal case of a spherical shell cavity without losses defined by perfectly conducting spheres, frequencies allowed to propagate, for TE and for TM modes, correspond to resonance frequencies obtained by imposing boundary conditions on the limiting surfaces, defining the region where the solution is valid (boundary value problem). Although this model shows a very limited practical validity, it allows us to provide new theoretical background to the actual problem. However, it is also worth noting that analytical solutions (semi-analytical, approximated and/or semi-empirical) are formulated in

the frequency domain, where each harmonic must be defined from $t = -\infty$ to $t = -\infty$, while the actual problem consists of a superposition of the transients excited by successive lightning strokes generated on Earth at a rate of several tens per second. Translation of concepts in the frequency domain to the time domain may cause a partial loss of its original meaning. This is the reason why talking about resonance frequency or cut-off frequency may have similar meaning in the system under study.

Let us now present a review of the different parameters and different approaches for the propagation of electromagnetic signals in the Earth-ionosphere cavity.

Cummer [18], approaches the study as follows. The Earth's crust is usually considered as an homogeneous medium with the vacuum permeability, μ_0, conductivity σ_g=10^2 S/m, and relative permittivity ε=15. Due to the difference between this conductivity and that corresponding to the lower atmosphere, it is usual to consider a perfect conducting behavior to model the Earth's crust. If conductivity is finite, instead, several times the depth of penetration must be considered and the homogeneous Earth's crust may be substituted by an equivalent reflection coefficient. This supposed homogeneity works well for the sea and most of the materials in the Earth's crust, but fails in the modeling of the lower conductivity of the polar icecaps.

Ionosphere is usually considered as a cold plasma, inhomogeneous and anisotropic, this model being valid as long as the field associated to the wave does not modify it, condition which is not met near high intensity lightning strokes [19]. The study of electromagnetic wave propagation in a cold plasma is carried out through Maxwell equations and Lorentz Force law, which provide an equation for the current [20]:

$$\frac{\partial \vec{J}_n}{\partial t} + \nu_n \vec{J}_n = \frac{q_n}{|q_n|}\omega_{\mathrm{Bn}} \left(\vec{J}_n \times \vec{b}_E \right) + \epsilon_0 \omega_{\mathrm{pn}}^2 \vec{E} \tag{1.3}$$

where ω_{pn} $\left(\sqrt{Nq^2/\left(m\epsilon_0\right)}\right)$ is the plasma frequency of each particle species, ω_{Bn} (qB/m) is the gyrotropic frequency, and ν_n is the collision frequency. Vector $\vec{b}_E$ is the unitary vector along the terrestrial magnetic field, $\vec{B}_E$, direction. The total current is obtained by adding the contribution from all species, $\vec{J}_T = \sum \vec{J}_n$. The concentration (or distribution) of electrons and positive ions are strongly dependent on height and the night-day condition. The collision frequency also varies with height but it does not depend on local time. Negative ions also appear

and the number of them is determined from the neutrality charge of the system. Solar radiation is the main source of ionization, while nighttime main sources are energetic electron precipitation, ionization by meteorites, and cosmic rays [21]. The contribution to the current by ions is not usually considered for the study of the Earth-ionosphere cavity, but its effect is very significant in the ELF band due to its high density for low heights.

The study of radio wave propagation in the Earth-ionosphere cavity requires different approximations to be made. Some of them simplify the ionosphere model as inhomogeneous and anisotropic cold plasma and others approximate the conductivity profile (density of electrons), the terrestrial magnetic field orientation and the frequency range in which the obtained solution remains valid.

A first approximation for anisotropic conductor is met if $\nu >> \omega$ for all frequencies of interest and all heights at which the wave is expected to reach. In this case, the term $\partial\vec{J} \Big/ \partial t$ can be neglected when compared to $\nu\vec{J}$. This causes $\vec{J}$ vector to be a linear function of $\vec{E}$ vector and the system behaves as an anisotropic conductor whose conductivity is frequency independent (anisotropic but non dispersive medium).

A second approximation, termed isotropic plasma condition, is met when $\nu >> \omega_B$ for all heights. In this case, the cross product term in Lorentz equation can be neglected and the medium turns to be isotropic (but dispersive).

If both approximations are valid, the medium turns into an isotropic conductor with $\sigma_i = \epsilon_0 \, {\omega_p}^2 / \nu$. This approximation is usually adopted in the day-time propagation due to the electron concentration [18].

We can highlight other simplifications that have been considered in the analytical solution through modes, such as: Greifinger and Greifinger [22] approximate the conductivity profile to an exponential model and neglect the magnetic field; these same authors [23] improve the model by adding a vertical terrestrial magnetic field; Wait [24] considers an Earth's crust with finite conductivity and solves by decomposing the solution in terms of propagation modes.

Morente et al. [14] embraces the study of the cavity as explained below. In the Earth's atmosphere, there are about 2,000 permanently active thunderstorm cells which produce approximately 50 lightning events every second [25]. These lightning discharges are the strongest source of natural electromagnetic noise and are

radiated mainly at ELF and VLF bands. The observed signals can be divided into two groups: atmospherics and whistlers [26]. Atmospherics are, broadly speaking, all the electromagnetic signals produced by lightning discharges that remain trapped in the cavity between the Earth's surface and the ionosphere. Their frequency range varies from a few Hertz to tens of kiloHertz. Besides atmospherics, whistlers are the other group of electromagnetic pulses generated by lightning strokes. When a lightning flash occurs in the Southern Hemisphere, radio noise is generated at all frequencies. Part of the electromagnetic energy is produced as a right-hand circular-polarized wave with a propagation vector parallel to the Earth's magnetic field. These electromagnetic waves, following the geomagnetic field lines, travel from the Southern Hemisphere to the Northern Hemisphere, where they can be detected by radio receivers. A whistler frequency spectrum ranges from about 100 Hz to over 10 kHz, since this kind of signal is an electromagnetic wave propagating in the Earth's magnetic plasma and has a resonance frequency at the electron gyrofrequency. It must therefore have frequencies lower than the lowest gyrofrequency along the propagation path. While atmospherics are confined between the ground and lower layers of the ionosphere in a cavity approximately 90 km wide, the whistler modes separate from the Earth's surface between two or three terrestrial radii, traversing from the ionosphere into the magnetosphere, then propagating along the geomagnetic field to the opposite hemisphere, and, finally, traversing the ionosphere again in the downward direction towards the ground. The dispersion characteristics of a typical whistler in the magnetospheric plasma are such that the group velocity increases with frequency. Thus, the lower frequencies arrive later than the higher ones, and the received signal is typically a series of descending glide tones, which can be heard on a loudspeaker like a whistle [27].

1.2 Electromagnetic phenomena associated to earthquakes and volcanic eruptions

We call Seismo - Electromagnetics to the discipline recently emerged to study electromagnetic phenomena originated by seismic events. Nowadays, many experimental observations have been carried out, but there is still a lack of theoretical models able to generate data in good agreement with these measurements [6]. The frequency range for these phenomena covers from DC to VHF bands, but we will concentrate on those which are more relevant (or which seem to be more relevant

according to recent research) for short-term earthquake prediction. This interest in non-seismic observations appears as a consequence of the doubts about if merely seismic observations can predict seismic activity [8].

1.2.1 Electric seismic signals

Laboratory experiments show that igneous rocks under high torsion turn into a battery able to supply a current flux and produce charge densities [28, 29]. This would explain the electric signal generation, but not their propagation, since some observatories near the epicenter have detected the signal while others, also near, have not been able to measure it, which suggests the presence of a certain selection, apparently caused by inhomogeneities or heterogeneities in the lithosphere [29].

1.2.2 Seismic emissions at ULF band

First, we should clarify the meaning of ELF and ULF for the Seismo-Electromagnetics discipline. In the following table, the frequency ranges for each band are shown for three different areas of knowledge. Column termed "ITU" corresponds to International Telecommunication Union, (*http://en.wikipedia.org/wiki/ITU:Radio:Bands#ITU*), column termed Seismo-Electromagnetics corresponds to the term used in this field, which can be found in Bleier and Freund [8], and column termed Geo-Electromagnetics corresponds to the geophysical area defined in Nickolaenko and Hayakawa [12].

In this section, we will adopt the Seismic-Electromagnetics criterion in order to be coherent with the literature.

	"ITU"	**"Seismo-Electromagnetics"**	**"Geo-Electromagnetics"**
"3-30 Hz"	**"ELF"**	**"ULF"**	**"ELF"**
"30-300 Hz"	**"SLF"**	**"ELF"**	**"ELF"**
"300 Hz- 3kHz"	**"ULF"**	**"VF (voice frequency)"**	**"ELF"**
"3-30kHz"	**"VLF"**	**"VLF"**	**"VLF"**

Although the history of seismic originated emissions is very recent, the most extended belief in the scientific community is that it will become a very important tool for seismic prevention. Clear evidences have been observed in large

earthquakes indicating that, one or two weeks before, a wide peak followed by a calm period is produced, with a sudden increase days before the earthquake [30–32]. The most relevant emission frequency is 0.1 Hz. The separation between charges due to micro fractures has been proposed as the generating mechanism [28], although there is not much agreement between expected and measured data, mainly due to the fact that the model employed does not take into account the lithosphere structure [33]. Nevertheless, fractal characteristics analogous in ULF emission associated to earthquakes and magnetic storms have been observed [34].

In the ELF band, many evidences of emissions previous to large earthquakes with ground epicenter have been also reported [35, 36], but the generation and propagation mechanisms are not clear enough. Tsarev and Sasaki [37] explain the propagation by modeling the Earth's crust as a waveguide for ELF waves generated by seismic mechanisms. Other researchers propose models which include alterations of the ionosphere due to the seismic/volcanic phenomena, or even artificial phenomena (input and output spacecraft, for instance), this variation generating changes in the Schumann resonances measured from terrestrial stations [38]. In specific cases, these anomalies in Schumann resonances can be explained by interference between the direct wave from the storm area in South America and the wave dispersed by anomalies produced by an earthquake in Taiwan, with the measurement station located in Japan [39]. In other situations, anomalies are partially explained by generation of gyrotropic waves in the conductivity changes with origin in the ionosphere zone, close to the earthquake region [40].

1.2.3 Lithosphere-atmosphere-ionosphere coupling

The detection of perturbations in the atmosphere as well as in the ionosphere has been a great surprise. The perturbation of the atmosphere affects the propagation of VHF waves, which reach a much higher range at days previous to the earthquake [41] and, at the moment, there is still no explanation of how pre-seismic phenomena modify the refraction index at these frequencies.

In other frequency ranges, sub-ionospheric propagation of VLF waves shows daily phase variations, with minimum values at sunrise and sunset. However, variations in the hour at which these minima occur have been observed during earthquake events [28]. Experimental evidences of this phenomenon have already been observed by the National Space Development Agency of Japan (NASDA),

under the Earthquake Remote Sensing Frontier Project, where a network of seven VLF and ELF measurement stations have been settled. The explanation for this phenomenon seems to rely on a displacement of the lower ionosphere frontier, of a few kilometers, which could be produced by superficial earthquakes with intensity above 6. Coupling channels could have three main explanations: (a) chemical channel, based on variations in the atmospheric conductivity caused by gas emissions which would disturb the electric field at ground level and would induce a redistribution of the ionosphere plasma; (2) acoustic channel, due to gravity waves that would affect the ionosphere; (3) electromagnetic channel: the ULF waves would propagate up to the inner part of the magnetosphere, interacting with energetic protons and producing precipitation at the lower ionosphere.

1.3 Resonances in a spherical shell cavity

In order to find the resonance frequencies for a spherical cavity formed by the Earth and the ionosphere, Maxwell equations have to be solved, with the use of the constitutive equations for the electric and magnetic field. Due to the dispersive character of the medium, it is usual to describe the situation in the frequency domain. In the ELF band (from 3 Hz to 3 kHz), the magnetic field effect can be neglected and the medium permittivity can be considered as an scalar function which depends on position and frequency $\epsilon\left(\vec{r},\omega\right)$. In this frequency range, the Earth can also be regarded as a perfect conductor.

The model that Schumann employed in his first work [10] considered a permittivity profile for the atmosphere given by

$$\epsilon\left(\vec{r},\omega\right) = \begin{cases} 1 & a \leq r < b \\ \epsilon & r \geq b \end{cases}$$

where a is the inner radius and b the outer radius of the concentric spheres. To model the ionosphere as a perfect conductor, the limit $\varepsilon \to \infty$ was taken.

The solution of Maxwell equations without sources in the frequency domain is easier to obtain by using Debye potentials [15, 16] (U and V are associated to the electric and magnetic part of the electromagnetic field, respectively). In the

case that the ionosphere is not considered as a perfect conductor, although homogeneous, an additional condition on Debye potentials must be imposed, condition known as Sommerfeld radiation condition [42].

The modal analysis is realized by alternatively imposing zero value for the Debye potentials. TM modes (or electric wave) are obtained by making $V = 0$, $U \neq 0$, while TE modes (or magnetic wave) are obtained imposing $U = 0$, $V \neq 0$.

For TM modes, the boundary condition is obtained by derivation of the U potential with respect to r. The resonance frequencies are obtained through the dispersion relation, but, in order to get an analytical expression, a series expansion must be performed, based on the small difference between the Earth's radius (a=6,370 km) and the ionosphere's height (between 60 and 100 km for daytime and nighttime). Bearing this in mind, the following expression for the resonance frequencies can be found

$$f_n = \frac{c}{2\pi a}\sqrt{n(n+1)} \tag{1.4}$$

This expression was published by Schumann in 1952 and referred to as Schumann resonance or Schumann resonances (both terms are included in the paper). The first resonances occur at 10.6, 18.3, 25.9, and 33.5 Hz. The fields for this propagation mode have mainly radial electric field component and azimuthal magnetic field component. They are TM modes, which are usually referred to as TEM modes due to the orthogonal character of the fields and the direction of propagation. This fact explains the low height-dependence of the field [12]. For this propagation mode we can talk of zero frequency, for $n = 0$. This is the case of static solution generated by the Earth-ionosphere capacitor charged with a potential of some hundreds of kilovolts, with zero magnetic field and electric field oriented from the ionosphere towards the Earth, and values of 120 V/m at points near the surface (fair weather field) [12].

Bliokh et al. [43] derives a more approximated formula

$$\beta_n a = \sqrt{n(n+1)\left(1 - \frac{b-a}{a}\right)} \tag{1.5}$$

where $\beta = 2\pi/\lambda$ and b stands for the ionosphere radius (not its height).

Schumann resonances correspond to waves that can travel several turns around the Earth and, therefore, they can be observed at any point of the planet, thus

carrying global information of the ionosphere properties. This fact is the reason why Schumann resonances have generated a great interest in using them as a tool for the study of the properties and state of the ionosphere and the global distribution of radiation sources at the ELF band [12].

In an analogous manner as regards TE modes, the boundary condition is imposed directly from V potential, and the dispersion relation obtained by approximating $\beta a, \beta b >> 1$ is:

$$\beta_{pn} \approx \sqrt{\frac{n(n+1)}{a^2} + \left(\frac{p\pi}{b-a}\right)^2} \tag{1.6}$$

where two indexes are present, related with the transversal and longitudinal propagation. The first one, p, specifies the number of half wavelengths matching the cavity height, while the second index, n states the number of wavelengths matching the terrestrial perimeter. The fundamental transverse resonance ($p = 1$), referred to as cut-off frequency, is around 1-2 kHz, and, since these resonances are better detected at night [44], the ionosphere height could be roughly 100 km and $f_{10} \approx 1.5$kHz.

In this section, we are going to derive longitudinal and transverse resonance frequencies, but now using vector potentials and starting form Maxwell symmetrical equations [45]. We will numerically solve the dispersion relation without the need of imposing any approximation concerning the cavity dimensions.

Maxwell symmetrical equations in the frequency domain and for linear, homogeneous and isotropic media can be written in the form:

$$\vec{\nabla} \times \vec{E} = -\vec{M} - j\omega\mu\vec{H} \tag{1.7a}$$

$$\vec{\nabla} \times \vec{H} = \vec{J} + j\omega\epsilon\vec{E} \tag{1.7b}$$

$$\vec{\nabla} \cdot \vec{E} = q_{\mathrm{ve}}/\,\epsilon \tag{1.7c}$$

$$\vec{\nabla} \cdot \vec{H} = q_{\mathrm{vm}}/\,\mu \tag{1.7d}$$

Let us introduce the vector potentials for the electric and the magnetic field, together with the scalar potentials related with the vector potentials through Lorenz contrast. If

$$\vec{\nabla} \cdot \vec{B} = 0, \qquad \vec{M} = 0, \tag{1.8}$$

then

$$\vec{H}_A = \frac{1}{\mu}\vec{\nabla} \times \vec{A} \tag{1.9a}$$

$$\vec{E}_A = -\vec{\nabla}\phi_e - j\omega\vec{A} \tag{1.9b}$$

$$\phi_e = \frac{-1}{j\omega\mu\epsilon}\vec{\nabla} \cdot \vec{A} \tag{1.9c}$$

If

$$\vec{\nabla} \cdot \vec{D} = 0, \qquad \vec{J} = 0, \tag{1.10}$$

then

$$\vec{E}_F = -\frac{1}{\epsilon}\vec{\nabla} \times \vec{F} \tag{1.11a}$$

$$\vec{H}_F = -\vec{\nabla}\phi_m - j\omega\vec{F} \tag{1.11b}$$

$$\phi_m = \frac{-1}{j\omega\mu\epsilon}\vec{\nabla} \cdot \vec{F} \tag{1.11c}$$

Combining both sets of equations, a wave equation for the potentials can be obtained:

$$\nabla^2\vec{A} + \beta^2\vec{A} = -\mu\vec{J} \tag{1.12a}$$

$$\nabla^2\vec{F} + \beta^2\vec{F} = -\epsilon\vec{M} \tag{1.12b}$$

where $\beta^2 \equiv \omega^2\mu\epsilon$. The following vector identity is used to calculate the ∇^2 operator:

$$\nabla^2\vec{G} = \vec{\nabla}\left(\vec{\nabla} \cdot \vec{G}\right) - \vec{\nabla} \times \left(\vec{\nabla} \times \vec{G}\right) \tag{1.13}$$

where $\vec{G}$ stands for $\vec{A}$ or $\vec{F}$, and ϕ stands for ϕ_e or ϕ_m. Considering $\vec{G} = \hat{r}G_r$, the solution can be decomposed into TM^r and TE^r modes:

$$\phi = \frac{-1}{j\omega\mu\epsilon}\frac{\partial G_r}{\partial r} \tag{1.14a}$$

$$\left(\nabla^2 + \beta^2\right)\frac{G_r}{r} = 0 \tag{1.14b}$$

If we consider points far away from the sources, we can obtain one field in terms of the rotational of the other field and express the fields as shown in Table 1.1.

TABLE 1.1: Expression for electric and magnetic field components.

	$\mathrm{TE}^r\left(\vec{F}=\hat{r}F_r, \vec{A}=0\right)$	$\mathrm{TM}^r\left(\vec{A}=\hat{r}A_r, \vec{M}=0\right)$
$\vec{E}$	$\frac{-1}{\epsilon}\vec{\nabla}\times\vec{F}$	$\frac{1}{j\omega\mu\epsilon}\vec{\nabla}\times\vec{\nabla}\times\vec{A}$
E_r	0	$\frac{1}{j\omega\mu\epsilon}\left(\frac{\partial^2}{\partial r^2}+\beta^2\right)A_r$
E_θ	$\frac{-1}{\epsilon}\frac{1}{r\mathrm{Sin}[\theta]}\frac{\partial F_r}{\partial\phi}$	$\frac{1}{j\omega\mu\epsilon}\frac{1}{r}\frac{\partial^2 A_r}{\partial r\partial\theta}$
E_ϕ	$\frac{1}{\epsilon}\frac{1}{r}\frac{\partial F_r}{\partial\theta}$	$\frac{1}{j\omega\mu\epsilon}\frac{1}{r\mathrm{Sin}[\theta]}\frac{\partial^2 A_r}{\partial r\partial\phi}$
$\vec{H}$	$\frac{1}{j\omega\mu\epsilon}\vec{\nabla}\times\vec{\nabla}\times\vec{F}$	$\frac{1}{\mu}\vec{\nabla}\times\vec{A}$
H_r	$\frac{1}{j\omega\mu\epsilon}\left(\frac{\partial^2}{\partial r^2}+\beta^2\right)F_r$	0
H_θ	$\frac{1}{j\omega\mu\epsilon}\frac{1}{r}\frac{\partial^2 F_r}{\partial r\partial\theta}$	$\frac{1}{\mu}\frac{1}{r\mathrm{Sin}[\theta]}\frac{\partial A_r}{\partial\phi}$
H_ϕ	$\frac{1}{j\omega\mu\epsilon}\frac{1}{r\mathrm{Sin}[\theta]}\frac{\partial^2 F_r}{\partial r\partial\phi}$	$\frac{-1}{\mu}\frac{1}{r}\frac{\partial F_r}{\partial\theta}$

The equation that is still to be solved is the Helmholtz scalar wave equation:

$$\left(\nabla^2+\beta^2\right)\frac{G_r}{r}=0, \tag{1.15}$$

where G_r stands for F_r in TE^r modes and for A_r in TM^r modes. The solution of this equation is obtained by the variable separation method:

$$G_r(r,\theta,\phi)=f(r)g(\theta)h(\phi), \tag{1.16}$$

where function $g(\theta)$ can be represented by the Associated Legendre polynomials of the first and the second kind ($P_n^m[\mathrm{Cos}(\theta)]$, $Q_n^m[\mathrm{Cos}(\theta)]$), while azimuthal dependence is solved using complex exponential functions or sine and cosine functions.

For the distance dependence, it is required the use of functions based on the spherical Bessel functions ($j_n(\beta r), y_n(\beta r)$) and Hankel ($h_n^{(1)}(\beta r), h_n^{(2)}(\beta r)$) functions, introduced by Schelkunoff [46] through relation

$$\hat{B}_n(\beta r)=\beta r b_n(\beta r)=\beta r\sqrt{\frac{\pi}{2\beta r}}B_{n+1/2}(\beta r), \tag{1.17}$$

where $\hat{B}_n$ stands for the new functions, b_n are the spherical functions and $B_{n+1/2}$ the cylindrical functions.

For the spherical cavity, the solution is composed of functions in the form:

$$\begin{aligned} G_r(r,\theta,\phi) = &\left(A_1\hat{J}_n(\beta r) + B_1\hat{Y}_n(\beta r)\right)\cdot \\ &\cdot\left(C_2 P_n^m[\mathrm{Cos}(\theta)] + D_2 Q_n^m[\mathrm{Cos}(\theta)]\right)\cdot \\ &\cdot\left(C_3\mathrm{Cos}(m\phi) + D_3\mathrm{Sin}(m\phi)\right), \end{aligned} \tag{1.18}$$

with m, n integer values. The coefficient D_2 must equal zero since Q_n^m represents singularities at $\theta = 0, \pi$. The solution for $n = 0$ vanishes, as well as for the case $|m| > n$. For spherical cavities, B_1 must vanish to avoid singularities at the origin. Since this point is outside of the space defined by the Earth-ionosphere cavity (it would be better to talk of a spherical shell), both Bessel functions have to be considered in the solution

$$G_r(r,\theta,\phi) = \left(A\hat{J}(\beta r) + B\hat{Y}(\beta r)\right) P_n^m[\mathrm{Cos}(\theta)]\left[C\mathrm{Cos}(m\phi) + D\mathrm{Sin}(m\phi)\right]. \tag{1.19}$$

It is interesting to notice a remark on the m value in the associated Legendre polynomials: the relationship between associated and ordinary polynomials is described through expression [47]

$$P_n^m(x) = \left(1 - x^2\right)^{m/2} \frac{d^m}{dx^m} P_n(x), \tag{1.20}$$

from which it can be deduced that negative values of m are not defined. However, if $P_n(x)$ is expressed through Rodrigues formula, m values can be negative as long as they are confined in the interval $-n \leq m \leq n$ and the relation between $P_n^m(x)$ and $P_n^{-m}(x)$ turns to be [47]:

$$P_n^{-m}(x) = (-1)^m \frac{(n-m)!}{(n+m)} P_n^m(x). \tag{1.21}$$

Boundary conditions impose the tangential components of the electric field to be zero at the conducting surfaces, $E_\theta(r = a) = E_\theta(r = b) = E_\phi(r = a) = E_\phi(r = b) = 0$. As regards the TE^r modes, the condition is directly imposed on the Bessel functions, while for the TM^r modes, the derivation of these functions has to be carried out. Therefore, for TE^r modes, it can be found that

$$A\hat{J}_n(\beta a) + B\hat{Y}_n(\beta a) = 0, \tag{1.22a}$$

$$A\hat{J}_n(\beta b) + B\hat{Y}_n(\beta b) = 0, \tag{1.22b}$$

and eliminating constants

$$\hat{J}_n(\beta a)\hat{Y}_n(\beta b) - \hat{Y}_n(\beta a)\hat{J}_n(\beta b) = 0. \tag{1.23}$$

Regarding the TM^r modes

$$A\frac{\partial}{\partial r}\hat{J}_n(\beta a) + B\frac{\partial}{\partial r}\hat{Y}_n(\beta a) = 0, \tag{1.24a}$$

$$A\frac{\partial}{\partial r}\hat{J}_n(\beta b) + B\frac{\partial}{\partial r}\hat{Y}_n(\beta b) = 0, \tag{1.24b}$$

and eliminating constants

$$\frac{\partial}{\partial r}\hat{J}_n(\beta a)\frac{\partial}{\partial r}\hat{Y}_n(\beta b) - \frac{\partial}{\partial r}\hat{Y}_n(\beta a)\frac{\partial}{\partial r}\hat{J}_n(\beta b) = 0. \tag{1.25}$$

We can plot the functions implied in the dispersion relationship. For example, we can consider a spherical cavity like Earth-ionosphere one but with radii 1 and 2 (arbitrary units) in order to better understand how resonant frequencies are distributed.

In Figure 1.1, $\hat{J}_n(\beta a)\hat{Y}_n(\beta b) - \hat{Y}_n(\beta a)\hat{J}_n(\beta b)$ is plotted as a function of β. Resonant frequencies correspond to zeros of the function. For each value of n, the curve cuts at zero and each one can be numbered by an index p. Then, β_{pn} represents the p zero of the n curve. For each p we have different values of β_{pn} and therefore different resonant frequencies.

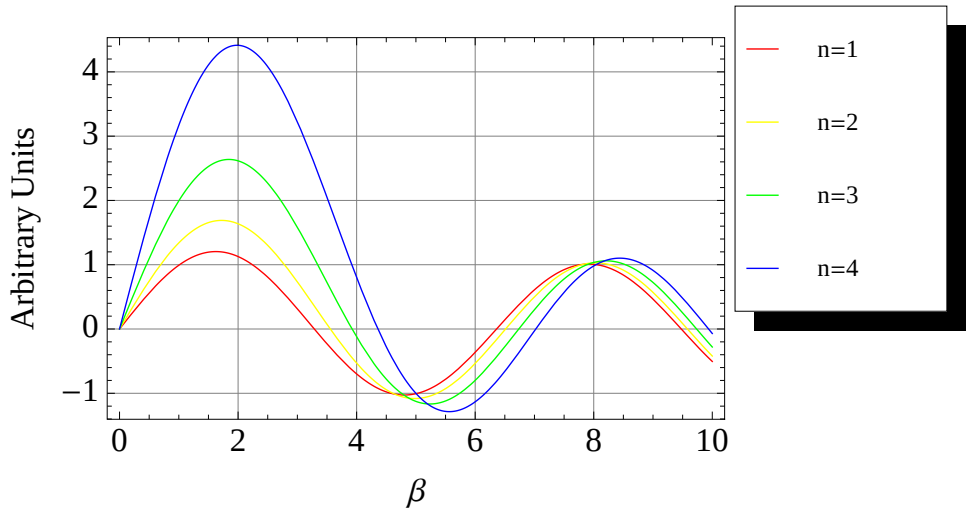

FIGURE 1.1: TE dispersion relationship.

A similar plot can be obtained from TM^r dispersion relationship. Following the same example, in Figure 1.2 we plot the corresponding function from Equation 1.25.

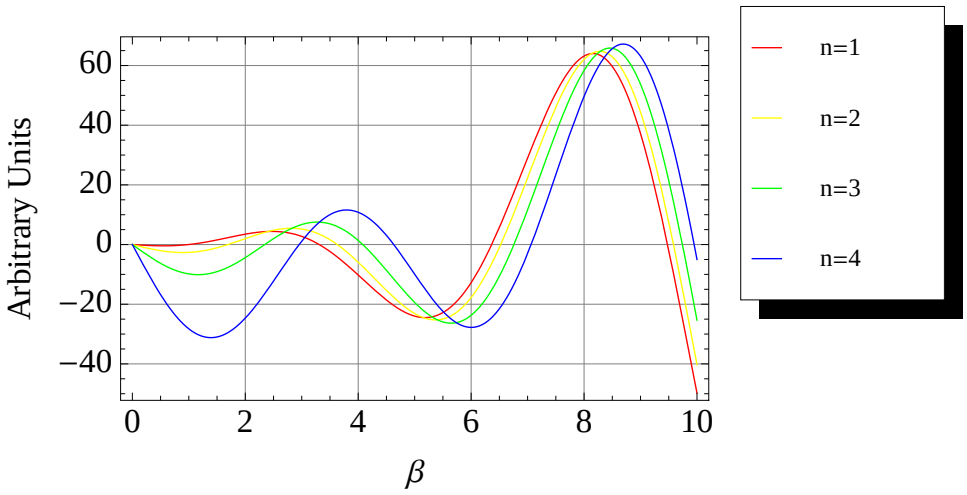

FIGURE 1.2: TM dispersion relationship.

Similar behavior can be observed except at the origin, where the curves have another zero for each value of n, beginning with different concavity. For example, near to β=4, 6, 10 both kinds of modes have similar resonances. In fact, we can amplify near to one value (see Figure 1.3) and it can be observed that resonances for each value of n are very close but TE^r resonances are slightly smaller than TM^r.

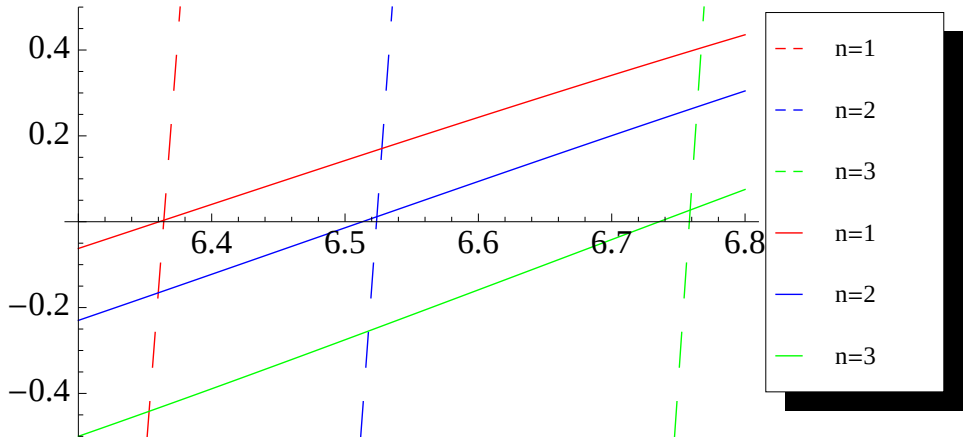

FIGURE 1.3: Detail of (dashed line) TM^r and (solid line) TE^r dispersion relationships.

For TM^r modes, we can consider the first zero as p=0, in such way that for $p \geq 1$ the resonant frequencies for both kinds of modes are similar. This is consistent

with the approximate resonant frequencies obtained by Bliokh et al. [43], and expressed by Equation 1.6. Regarding the last equation, it is only valid when $(b-a) << a, \beta a, \beta b >> 1$. Then, the next step is to consider the Earth-ionosphere cavity dimensions ($a = 6,370$ km, $b = 6,470$ km). Figure 1.4 shows both functions for n=1 to 4.

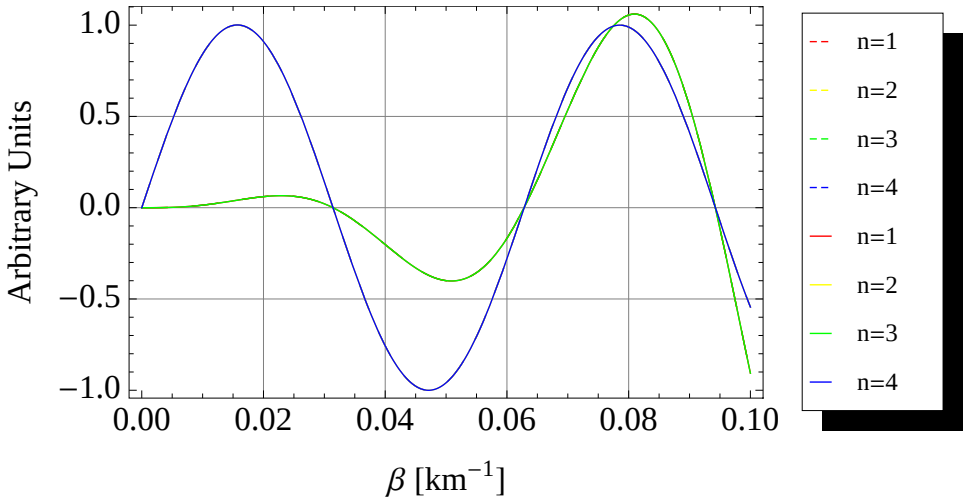

FIGURE 1.4: (dashed line) TM^r and (solid line) TE^r dispersion relationships for the Earth-ionosphere cavity.

From the plots, it can be observed that, due to Earth-ionosphere cavity dimensions, the resonant frequencies for TE^r and TM^r for $p \geq 1$ match at every value of n. For $p = 0$ and TM^r modes, we obtain the Figure 1.5. It can be observed that for $n = 1$ the dispersion relation is almost met for every value of β and this fact justifies the denomination of Quasi-TEM mode.

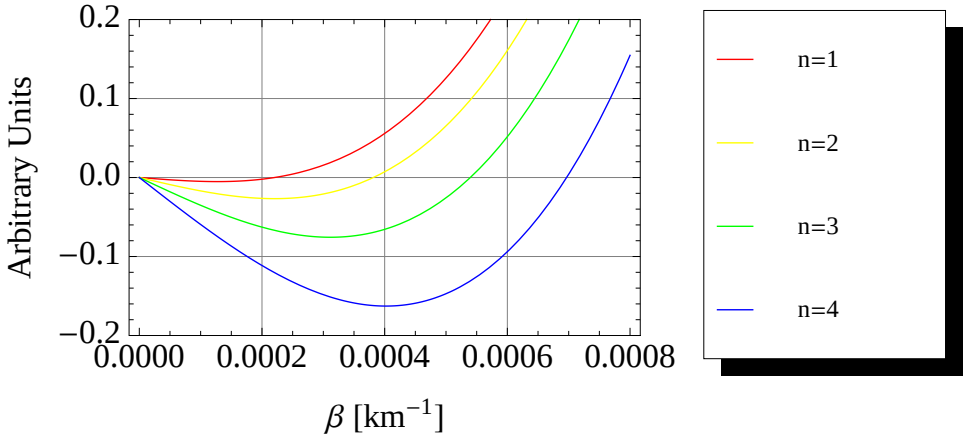

FIGURE 1.5: Detail of Figure 1.4, showing SR for TM^r modes.

TABLE 1.2: Comparison of the SR central frequencies obtained (1st column) numerically by us, (2nd column) anallytically by Schumann, and (3rd column) anallytically by Bliokh, for the lossless cavity.

	Numer.	Schumann	Bliokh
1	10.51	10.59	10.50
2	18.20	18.34	18.20
3	25.74	25.94	25.74
4	33.23	33.49	33.23
5	40.70	41.02	40.70
6	48.16	48.54	48.16
7	55.61	56.05	55.61
8	63.06	63.55	63.05
9	70.50	71.05	70.49
10	77.94	78.55	77.94

TABLE 1.3: Comparison of transverse resonance frequencies obtained by different approaches.

	p=1	p=2	p=3
WG	1498.96	2997.92	4496.89
Theor.(n=1)	1499.	2997.94	4496.9
Theor.(n=4)	1499.34	2998.11	4497.01
$TM^r_{p,1}$	1499.	2997.94	4496.9
$TM^r_{p,4}$	1499.33	2998.11	4497.01
$TE^r_{p,1}$	1499.	2997.94	4496.9
$TE^r_{p,4}$	1499.33	2998.11	4497.01

We summarize the results in the following Tables where resonant frequencies for n=1,...10, p=0 for TM^r modes, and n=1,...3 and p=1,...3 for TE^r are obtained by solving numerically the dispersion relationships. We have used Equation 1.6 as initial values in the iterative procedure.

From Tables 1.2, 1.3, we can observe that Schumann resonances are in the lower part of ELF band whereas transverse resonances belong to lower part of VLF.

Schumann resonance frequencies obtained from numerical solution of dispersion relationship agree very well with approximate formula obtained from Bliokh, specially for higher values of n.

As we commented before, due to dimensions of the Earth-ionosphere cavity, resonant frequencies for TM^r and TE^r almost coincide for every value of n (see Table 1.3). In the same way, these frequencies agree with approximate formulae from Nickolaenko [12], labeled as *Theor.* in Table 1.3. The first row corresponds to simple model of waveguide in which cut-off frequencies are defined by the relation of height of the waveguide, which must be multiple of half wavelength.

After resonant frequencies have been obtained, we can obtain fields from potential vector as is explained in Table 1.1. Using the dimensions of the real cavity, we can represent the spatial dependence of the fields for every mode, but we are going to concentrate about the ones which represent Schumann resonances (see Figure 1.6). For a lossless cavity, the dependence of the fields with height is weak. For E_r, variations about 0.1% are obtained by means of J_n and 5% by means Y_n in the whole height of the cavity (from 0 to 100 km). A similar behavior can be observed for the other components.

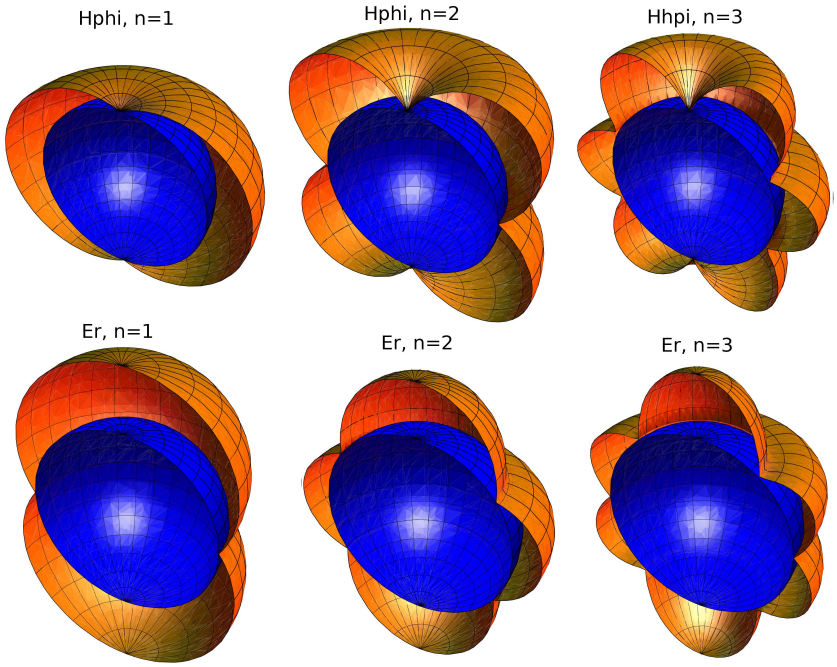

FIGURE 1.6: E_r and H_ϕ fields in the Earth-ionosphere cavity, for m=0 (i.e., symmetry in ϕ), near to the ground.

When the excitation source has symmetry along the ϕ coordinate, only fields for $m = 0$ can be excited. In that case, only E_r, H_ϕ, and E_θ are different from zero However, for the dimensions of Earth, the component E_θ is 3 orders of magnitude lower than E_r, and therefore the relevant fields can be reduced to E_r and H_ϕ.

1.4 Earth-ionosphere as a plane-parallel waveguide

In the VLF band, the wavelengths associated are in the order of hundreds of kilometers, and the Earth-ionosphere cavity can be considered as a waveguide. Due to the high losses presented in this band, the electromagnetic signals produced by lightning at these frequencies can only propagate few thousands of km before vanishing and, therefore, they cannot interfere with themselves by completing circles around the Earth's surface. In the literature, the resonant frequencies defined by $p \geq 1$ (sferics, transverse resonances) are known as cut-off frequencies. As we have shown before, due to the special dimensions of the cavity, for each value of p we have only one value in a way almost independent of n under TE^r or TM^r assumptions. Considering Maxwell equations without sources, assuming z as the propagation direction, and an orientation of plates normal to y axes (then the problem becomes x-independent) we can write:

$$E_x = \frac{1}{\gamma^2 + \epsilon\mu\omega^2}\left(-i\mu\omega\frac{\partial H_z}{\partial y}\right) \tag{1.26a}$$

$$E_y = \frac{1}{\gamma^2 + \epsilon\mu\omega^2}\left(-\gamma\frac{\partial E_z}{\partial y}\right) \tag{1.26b}$$

$$H_x = \frac{1}{\gamma^2 + \epsilon\mu\omega^2}\left(+i\epsilon\omega\frac{\partial E_z}{\partial y}\right) \tag{1.26c}$$

$$H_y = \frac{1}{\gamma^2 + \epsilon\mu\omega^2}\left(-\gamma\frac{\partial H_z}{\partial y}\right) \tag{1.26d}$$

$$\frac{\partial^2 E_z}{\partial y^2} + \left(\gamma^2 + \epsilon\mu\omega^2\right) E_z = 0 \tag{1.26e}$$

$$\frac{\partial^2 H_z}{\partial y^2} + \left(\gamma^2 + \epsilon\mu\omega^2\right) H_z = 0 \tag{1.26f}$$

where γ is the propagation constant. In this problem, we can separate the solution into components in TE^z and TM^z modes, if we consider $E_z = 0$ or $H_z = 0$. Then, the field structure is completely different than the one from a spherical cavity problem. For both kind of modes we obtain the same dispersion relationship that defines cut-off wave numbers:

$$\beta = \sqrt{\epsilon\mu\omega^2 - \left[\left(\frac{p\pi}{b}\right)^2\right]} \Longrightarrow \beta_c(p) \equiv \frac{p\pi}{b} \Longrightarrow \lambda_c(p) \equiv \frac{2\pi}{\beta_c(p)} = \frac{2}{\left(\frac{p}{b}\right)} = \frac{2b}{p}$$

$$\beta_c(p) = \frac{p\pi}{h}$$

where h is the height of the waveguide and p an integer different from zero. Propagation in a plane-parallel waveguide can be considered as two TEM waves propagating in the oblique directions to both plates, and with an incident angle with discrete values and defined by cut-off wave numbers [48].

1.5 Electricity in the atmosphere

On an regular day, over flat desert country, or over the sea, the electric potential increases with altitude by roughly 100 volts per meter. Thus, there is a vertical electric field of 100 V/m in the air, directed to the Earth, usually named as Fair Weather field. This field, due to the small conductivity of air, generates a current density of about 10 μA/m^2 from the ionosphere to the Earth. The total electric current reaching the Earth's surface at any time is nearly constant, roughly 1,800 A. The problem is: How is the positive charge maintained there? How is it pumped back? [49].

The batteries are the thunderstorms and their lightnings. Lightning storms carry negative charges to the Earth. It is the thunderstorms throughout the world who are charging the Earth with an average of 1,800 A, which is then being discharged through regions of fair weather [49].

Lightning discharges are associated with specific climatological and weather conditions, which are able to maintain the separation of electric charge and its accumulation to the levels exceeding the breakdown level, but the thunderstorms may occur in many possible locations. There are always approximately 2,000 active thunderstorm cells over the whole Earth [12]. Even nowadays, finding the global distribution of lightning strokes is not a simple task as it may seem. One way is, since there is an obvious coupling between weather conditions and lightning distribution, using the former to describe the general distribution of the lightning activity over the Earth. The World Meteorological Organization (WMO) long-term climatological data from 1956 present the global distribution in space of the *thunderstorm days*, averaged for different periods of time [50]. Direct climatological data and re-calculated distributions indicate a few distinct areas with an extremely high lightning activity. These territories were called global thunderstorm centers, and they are found in Central Africa and Madagascar, South and Central America, Caribbean Basin, South-East Asia and Indonesia. These results

are in extreme good agreement with those from the Optical Transient Detector (OTD), reported almost 50 years later by Christian et al. [25], see Figure 1.7.

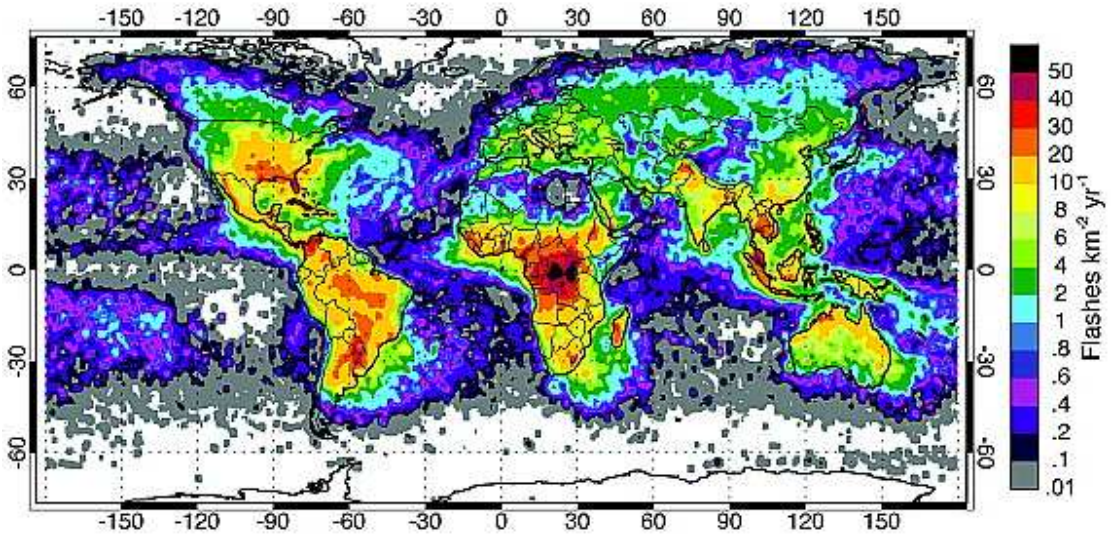

FIGURE 1.7: The annualized distribution of total lightning activity (in units of fl km^{-2} yr^{-1}. Extracted from [25].

Other method concerning spatial distribution of lightning is based on measuring electromagnetic radiation from the strokes. Such systems reliably work and worked over the land, like the National Lightning Detection Network (NLDN) works in the USA [51, 52] and in Japan [53], or some commercial networks over European countries [54]. Also, the VLF satellite measurements onboard Ariel 4 can give information about the global lightning map.

Spaceborne optical detectors [25] are another source of information about spatial lightning distribution. Many problems appear in this case linked with the limited data resolution and synchronization, with fine and unrepeatable coverage of the ground surface.

Finally, ELF radio waves and Schumann resonances have the substantial advantage of their global nature. The problem with ELF lies in signals overlapping making very difficult their separate processing except for super-powerful strokes (Q-bursts), which occur approximately once in a minute.

The thunderstorm activity is a function of local time. Its diurnal pattern is conditioned by heating of the ground soil by the Sun, which provides the atmospheric convection. Since thunderstorms become most active in the afternoon local time, the maximum of the global activity is found somewhere between the point of

local noon and the evening terminator (day-night interface). In Nickolaenko and Hayakawa [12], a relation between the main storm centers is shown, see Figure 1.8. During the year, the thunderstorms drift to the North and to the South following the Sun. As a result, the global lightning distribution undergoes modifications from month to month.

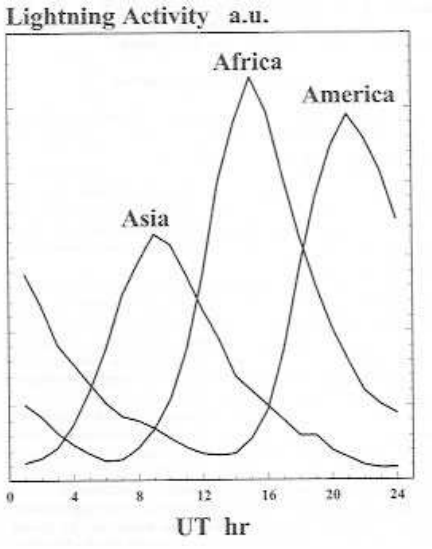

FIGURE 1.8: Diurnal variations of the lightning activity in the three principal regions. Extracted from [12].

1.6 Experimental Schumann resonance studies

In this section, we describe a Schumann resonance observatory and its most recent experimental results. Fist of all we show the typical Schumann resonance amplitude obtained from the first measure that we did in June, 2011 with a magnetometer designed and developed by our research team, Figure 1.9. The spectrum recorded in the mountains of Alfaguara (close to Granada) at noon time contains four Schumann resonances. Such successful measurements of Schumann resonance are rare in the cities because of the high level of man-made interference present here. An observatory must be placed in a rural region far away from power supply and communication lines. The figure corresponds to N-S magnetic field component. The waveform was recorded by the data acquisition system working with a sampling frequency of 128 Hz. The record had 483,136 points, was divided into samples 20 s long, and each sample was processed by using the Discrete Fourier transform algorithm. Then the total individual amplitude spectra were averaged, and the effective amplitude spectrum was thus obtained (see Chapter 2). The

presented spectrum in Figure 1.9 corresponds to a record of approximately 1 hour length. The data are un-calibrated and the fourth resonant is amplified by the response of the magnetometer. We can observe in the resonances a typical narrow band man-made interference at the frequency around 50 Hz. Amplitude of such a signal (and its lower harmonics) may sometimes become so powerful that the rest of the spectra become jammed, and the Schumann resonance peaks cannot be observed.

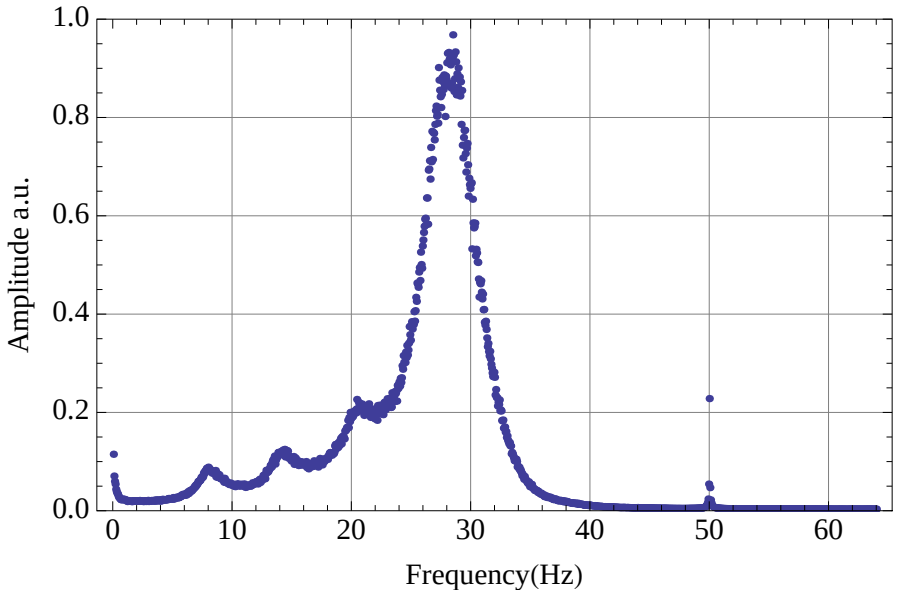

FIGURE 1.9: Uncalibrated Schumann resonance spectrum recorded in Granada, Spain, June 2011.

The observatory should be a lonely place without any industrial activity, away from the traffic and even from pedestrians that inevitably shake the ground. Magnetic antennae are buried into the ground to avoid the signals induced by vibrations and by the wind. For our station, both horizontal magnetic field components are detected with two magnetometers with *Nillomag77* alloy core covered with about 1,000,000 turns of copper wire. They must be placed at about 100 m away from recording instruments, to avoid interferences.

The long term Schumann resonance monitoring has shown that diurnal variations of resonance parameters may seriously deviate from day to day thus reflecting the random nature of the sources. Typically, the final results are revealed on a month (or even longer) time span, such as averaged diurnal variations.

Successful experimental investigations of Schumann resonance started in the 60's, when it was understood that relatively long time accumulation of the power

spectra of natural electromagnetic field reveals a modal peak around 8, 14, 20, and 26 Hz frequencies. It is impossible to mention all the measurements and all the results published in the literature, so we only highlight these and name some key authors. Detailed information may be obtained from the references containing the names listed below.

Balser and Wagner were the first who measured SR power spectra, established parameters of resonance and discovered diurnal variations. Sátori and Zieger record SR since May 1993 from Nagycenk (Hungary) observatory. Since 1994, Williams, Boldi, Heckman and Huang have monitored SR parameters and monthly mapped the global location of sources of Q-bursts from MIT (USA). Ondraskova, Kostecky, Sevckit and Rosenberg begin to record data from December 2001 in the Astronomical and Geophysical Observatory of Comenius University (Bratislava, Slovakia), and long-term analysis of Schumann resonance parameters are being studied. Since 1998 observations of the SR have been conducted in the Negev desert (Israel) at the Mitzpe Ramon field station by C. Price et al., and important correlations between the Terminator Effect and SR have been reported. Measurements in polar latitudes have been done by Fraser-Smith and Bannister in the 1975-1998 period, and by Bloglazov, Akhmetov, Vasilév and Kosolapenko in Observatory of Lvozero, in the Kola Peninsula (Russia). Belyaev, Schekotov, Nickolaenko and Shvets are monitoring power spectra and the Poynting vector of SR from Lekhta observatory, Kerelia, Russia, since 1998. Hayakawa and Hobara from the University of Electro-Communications in Tokyo, Japan, analyze coordinated measurements of ELF transients, VLF ratio signals and optical observations of red sprites.

As a result of the research project *"Study of Natural Electromagnetic Phenomena for Monitoring the Environment"* granted by Junta de Andalucía Government, in summer 2012 there will be an operative new SR observatory in Sierra Nevada (Granada, Spain), located at 2,500 m above the sea level, with two magnetometers to measure both components of the horizontal magnetic field.

1.7 Background of our research group in planetary atmospheres

The research on natural electromagnetic fields in planetary atmospheres, carried out by the research group in which this thesis has been developed, began in December 2000, when Dr. Konrad Schwingenschuh, from the Institute of Spatial Research (IWF) of the Academy of Sciences of Austria (OEAB), scientific coordinator of HASI instrument, requested to the group a study of the Schumann resonances in Titan's atmosphere, to indicate the Cassini/Huygens engineers which band was the most appropriated for tuning the mutual impedance sensor of the PWA experiment, with the final aim of detecting these resonances in Titan. This study was carried out and published in the Icarus Journal of the Astrophysics American Society [55]. The scientific interest in this topic is reflected by the fact that, soon afterwards, a special number of Radio Science magazine entitled *Recent Advances in Studies of Schumann Resonances on Earth and Other Planets of the Solar System* [56], in whose introductory section, V. P. Pasko references the work by Gregorio Molina-Cuberos with his research group on Schumann Resonances on Mars [57]. Similar studies were carried out for the Earth [14, 58–60]. Due to memory and time calculation requirements, the model used for the cavity considered the space between two meridians, with the source located at the z-axis of a spherical coordinate system with the sphere at its center. The symmetric shape of the system allowed considering it as 2D which turned into a remarkable reduction of memory and time calculation resources, allowing noticeably good results.

As regards analysis of the experimental results, J.A. Morente devised a filtering algorithm which separated source terms, associated to early-time, and system or resonance terms, associated to the late time response and with very low amplitude. The separation allowed Dr. Morente to study the low-amplitude information masked in the measurements by the much higher amplitude source terms. The filtering algorithm was applied in the ELF band [61], as well as in the VLF band [62].

Chapter 2

Time series analysis from Magnetotelluric records [1]

In this chapter we present the results of analyzing Time Series (TS), measured with the Magnetotelluric method (MT), which contain Schumann resonance (SR) data. Two different methods have been employed; Fourier analysis (FA) and Rescaled Range analysis (R/S). The first is a well-known technique employed in many fields of science, while the second was developed by E. Hurst in 1965 [63], who devoted his lifetime to the study of the Nile floods.

The Chapter is divided into two main sections: FA and R/S. The first part starts defining the Bartlett method, which derives from the work of J. Fourier, the technique of fitting SR by Lorentzian curves, and the MT method. Then the dataset employed is introduced, with its different campaigns. Finally, a study of daily and seasonal variations of SR is carried out. In the second section we start by defining the R/S method, and then we apply it to TS from the dataset taken in Antarctica. Finally, we present the results of a simulation which corroborate the main purpose of the method: estimating the lightning rate from electromagnetic records.

2.1 Spectral Analysis

2.1.1 Spectral estimation with Bartlett's method

The spectral analysis is a very widely spread method of signal processing. It is based on initial work by Joseph Fourier [64], which decomposes arbitrary functions into infinite sums of trigonometric functions. There is a lot of literature about this method ([65], and references therein), so we will not extend on it.

The core of Fourier analysis is based in decomposition on Fourier series, and states that any arbitrary periodic function $s(t)$, t being a real variable, (which can include finite discontinuities) can be approximated by a (probably infinite) sum of trigonometric functions, namely sines and cosines or complex exponentials:

$$s(t) \sim \frac{a_0}{2} + \sum_{n=1}^{\infty} \left[a_n \cos\left(\frac{2\pi n}{T} t\right) + b_n \sin\left(\frac{2\pi n}{T} t\right) \right] = \sum_{n=-\infty}^{\infty} c_n e^{2\pi j \frac{n}{T} t}, \tag{2.1}$$

where j is $\sqrt{-1}$, T is the period of $f(t)$ and a_n, b_n, and c_n are the so-called Fourier coefficients.

From the possibility of expressing arbitrary functions by a set of coefficients, the Fourier transform (FT) $S(f)$ arises. It is defined as:

$$S(f) = \int_{-\infty}^{\infty} s(t) e^{-2\pi j f t} dt, \tag{2.2}$$

where $s(t)$ is the signal in time domain, and $S(f)$ is the transformed signal, in the frequency domain.

From definition of the FT, the Discrete Fourier Transform (DFT) can be also defined. In this case, both the time domain signal $s[n]$ and the transformed domain signal $S[m]$ are of discrete nature. If the time domain signal is N samples length, then the DFT is defined as

$$S[m] = \sum_{n=0}^{N-1} s[n] e^{-2\pi j f n / N}. \tag{2.3}$$

The aim of using FA in our work is to estimate the amplitude spectra of both magnetic and electric field recorded by specific instruments. There are different

methods based on FA in order to do that. Our election was the Bartlett's Method [66]. We will briefly describe how we applied it, since the method can be slightly different depending on the references.

The phenomenon we want to study is regarded as noise for many applications such as radio broadcasting systems, cellular phones or other communication systems which use the atmosphere as their propagating channel. We inverse the situation, and part of the *noise* (natural electromagnetic emissions from lightning) becomes our signal, while the common signals (coming from radio stations, cellular phones, etc.) are our noise. We want to point out that the phenomenon under study is of very low intensity (few pT for the magnetic field and in the order of μV/m for the electric field) and therefore hard to detect. Because of that, some kind of external noise reduction must be performed. This is accomplished by time averaging several spectra, and it is known as the Bartlett's method of spectral estimation.

Given a time series $s[n]$ of N_T samples length, we must split it into L data blocks of equal length (N), where N_T=NL. Then, each data block is multiplied by a Hanning window H (see Figure 2.1), which is defined by the following expression:

$$H[n] = 2\left(1 - \cos^2\left[\frac{\pi n}{N}\right]\right). \tag{2.4}$$

The Hanning window is employed with the purpose of minimizing the effects of truncating the initial signal. The DFT of a digital signal is the result of effectively calculating the transform of the initial signal repeated over the whole time axis. Therefore there is an undesired effect at the edges of the time signal, where its last sample is attached to its initial sample, but the result of this junction does not contain information of interest. By weighting the time samples by the Hanning function we can reduce this effect.

The Discrete Fourier Transform (DFT) of each data block is then calculated:

$$\tilde{F}_l[f_k] = \sum_{n=0}^{N-1} s[Nl+n]H[n]e^{-j2\pi kn/N}, \qquad l = 0...L-1. \tag{2.5}$$

The Bartlett spectral estimator F for the time series s is:

$$F[f_k] = \frac{1}{L}\sum_{l=0}^{L-1} |\tilde{F}_l[f_k]|. \tag{2.6}$$

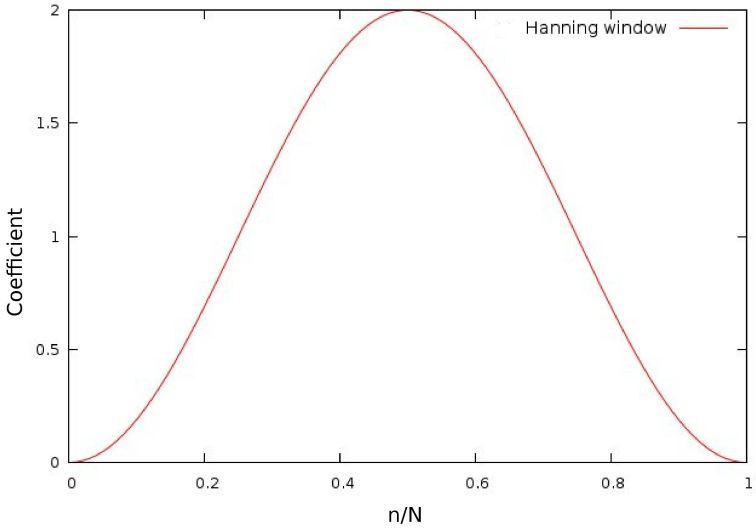

FIGURE 2.1: Function of Hanning window employed in this study.

The decision of L and N_T are related to the time and frequency resolution desired for the estimator. N_T is related to the time resolution, since we will obtain an independent spectral estimator for the period N_T/f_m, where f_m is the sampling frequency of the TS. On the other hand, the frequency resolution of the estimator will be

$$\Delta f = \frac{f_m L}{N_T} = \frac{f_m}{N} \tag{2.7}$$

In Figure 2.2, it can be seen the result of choosing different N_T and L parameters for the same time series. Four different durations (T_{total}= 5, 15, 30, and 60 minutes) of the TS are evaluated at each panel (N_T can be inferred by multiplying the total time length by f_m, i.e., $N_T = f_m T_{total}$). At each panel, a different time length (T_L) for the data blocks has been chosen (1, 5, 10, 15, 30, and 60 seconds), resulting in different L (quotient between total time and data block time, i.e., $L = T_{total}/T_L$) values. For higher values of L, the resulting estimators do not contain noise, but they have poor frequency resolution. On the other hand, for lower values of L, the spectrum obtained is very noisy. If we suppose a white Gaussian noise N(0,1), i.e., an stochastic process with Normal distribution with zero mean and standard deviation equal to one, superimposed to the signal of interest, the Bartlett method reduces its energy by a factor $1/\sqrt{L}$ [67].

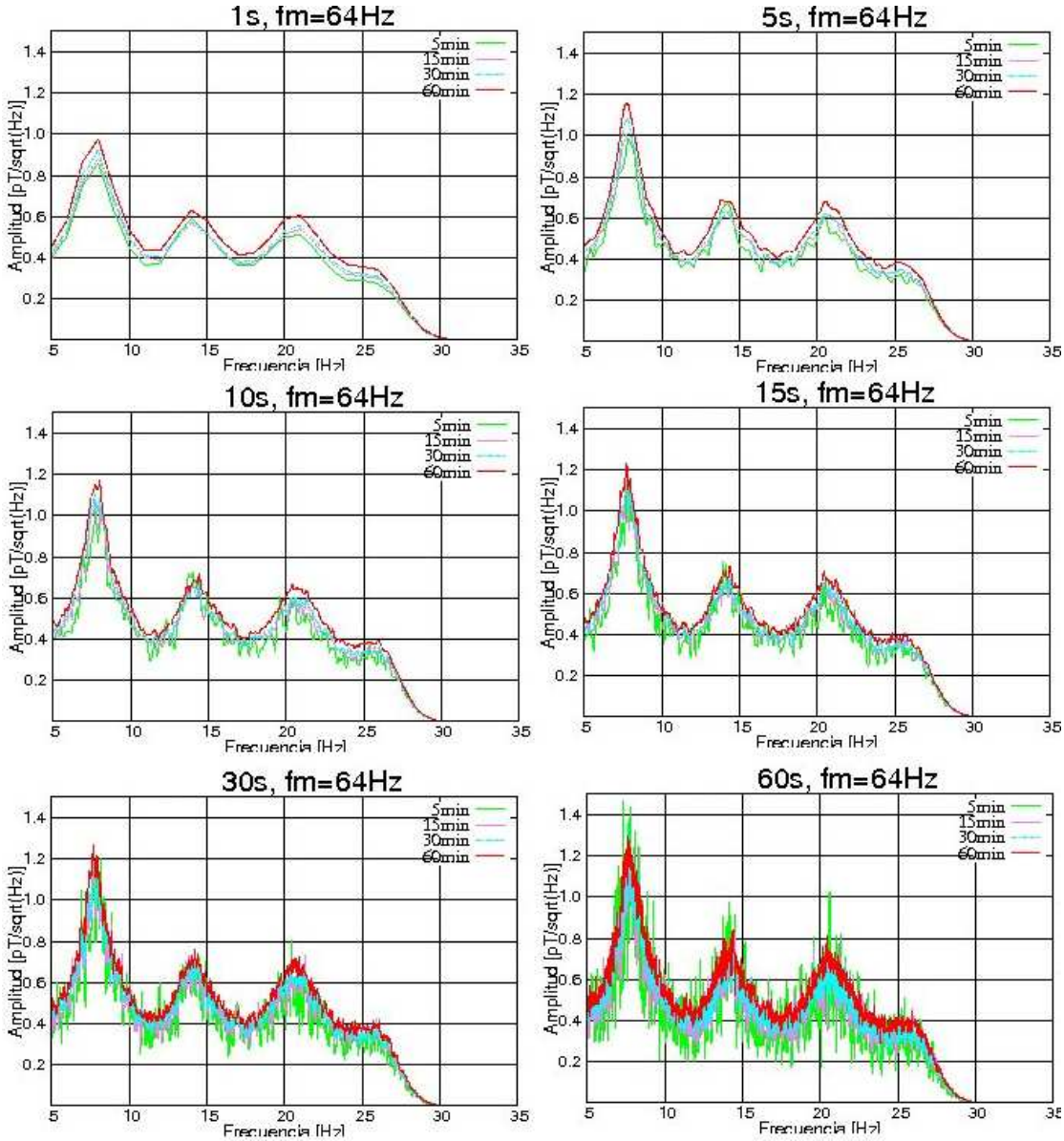

FIGURE 2.2: Different configurations for spectral estimation of a time series with Bartlett's method.

2.1.2 Lorentzian fit of Schumann Resonances

Once the spectrum has been estimated, it is necessary to extract and quantify the peak resonances which appear in it, in order to be able to compare and categorize them. For this purpose, we apply Lorentzian fit for each of the estimated spectra [68], obtained by the technique described in previous section. Lorentzian fit consists in finding the minima square fit between the spectrum and a sum of

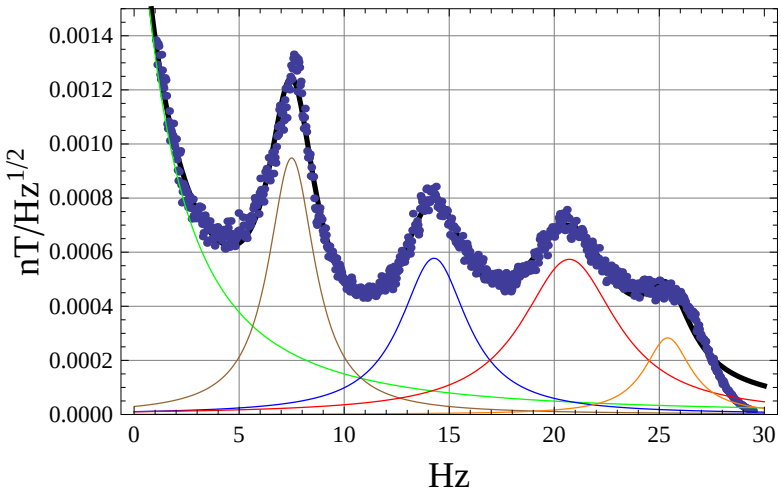

FIGURE 2.3: Lorentzian fit of Schumann resonance spectrum.

Lorentzians:

$$F_{Lfit}(f) = \sum_{n=0}^{N} \frac{B_n}{\left(\frac{f-f_{max,n}}{\Delta f_n}\right)^2 + 1}. \tag{2.8}$$

In this way, each resonance (n) is reduced to three coefficients; amplitude (given by B_n), central frequency ($f_{max,n}$), and its 3 dB bandwidth (Δf_n), which is related to the Quality factor (Q_n) by

$$Q_n = \frac{f_{max,n}}{\Delta f_n}. \tag{2.9}$$

The parameter B_n is a measure of the strength of the mode, since it stands for the maximum amplitude of the Lorentzian curve. Several facts, like the distance source - observer or the lightning intensity may affect this parameter. Central frequencies ($f_{max,n}$), are mainly dependent on the geometry of the cavity, and therefore their central values are well-known. The average values given in [12] were used as starting points for our fitting algorithm. The quality factor (Q_n) gives a measure of the cleanliness of the resonance.

One Lorentzian (n=0) must be employed as well for the DC level, or otherwise the fit of the first SR is slightly displaced to the left, in order to compensate the DC weight. Similarly, the last resonance fitted should not be accounted for, since the effects of the tail of the spectra modify its parameters. In other words, depending on at which frequency we cut the spectra, the value of the last resonance differs. An example of the Lorentzian fit can be seen in Figure 2.3.

2.1.3 The Magnetotelluric method, applied to Schumann resonance studies

The Magnetotelluric method is intended to measure and infer the structure and composition of the terrestrial subsoil in a passive way. However, since it is based in recording electric and magnetic fields, we will use MT campaigns data to extract the recorded Schumann resonances. The three components (NS, EW and vertical or radial) are measured for the magnetic field, and NS plus EW for the electric field. From them, the impedance tensor of the ground can be inferred, thus giving information of the composition [69, 70]. The measurements are repeated at different positions in order to cover broad areas, resulting in geographical maps of the subsoil in the area under study. The daily deployment of the equipments is an issue for SR studies, since local conditions, like the precise alignment of the sensors or sources of interferences, may vary for each measurement of a survey.

A very wide range of frequencies is employed in the measurement, ranging from less than 1 mHz to up to 20 kHz, with multiple hardware configurations in order to have good resolution at different scales. Measurements at different frequencies give information from different depths of the ground, so the method is able to draw 3D maps of the subsoil. It is important to note that only a small portion of the recorded spectra is useful for SR studies (roughly 1 - 50 Hz).

Since the equipments are very sensitive, SR are present in these measurements, both in magnetic and electric field time series. From the study shown in Chapter 1, we know that the main components containing SR are H_ϕ and E_r. MT method records the first one, but not the second. This is an important fact to keep in mind because we will not be able to reconstruct the Poynting vector from these measurements, and therefore many techniques like for instance direction finding of Q-bursts, are not available from these surveys. On the other hand, SR can be found in all horizontal $\vec{E}$ measurements, as well as in few B_r time series (less than 5% of them). Dedicated SR stations usually do not measure these fields, so they can give information which usually is not taken into account. In Figure 2.4, a typical deployment of the instruments during a MT campaign is shown. Following MT nomenclature, x direction stands for North - South, while y does so for East - West direction.

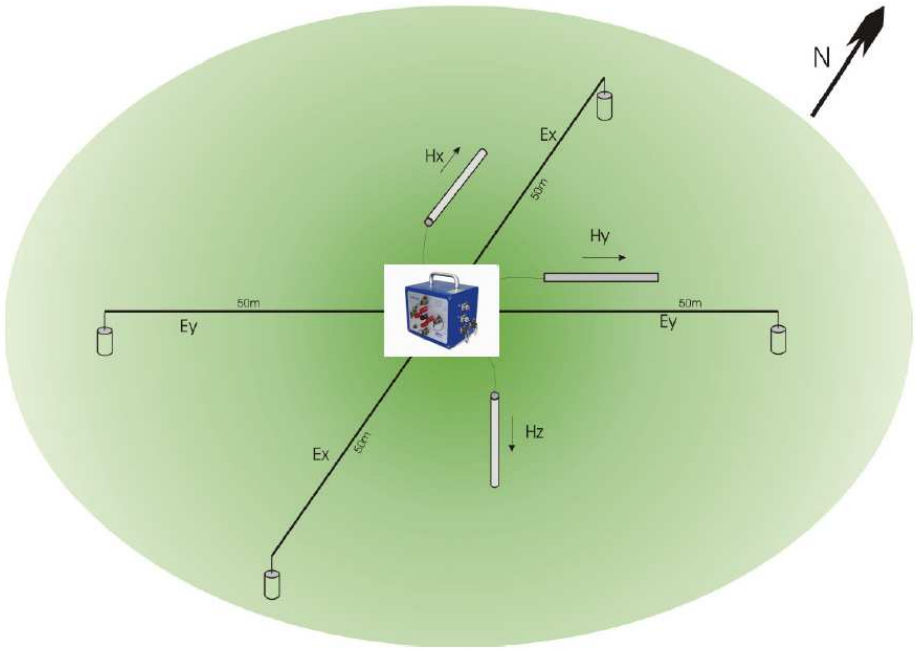

FIGURE 2.4: Deployment of the MT measurement equipment.

The equipment employed in the surveys of this study is from Metronix [71]. An ADU-06 data logger was employed, connected to EFP-06 electrodes and MFS-06 magnetometers. We briefly describe the instruments below.

2.1.3.1 Data logger ADU-06

ADU stands for Analog Digital Unit. It is in charge of digitizing the continuous measurements from the sensors and either storing or sending them. The five sensors (three magnetic, two electric) are connected to it. It has in-built GPS in order to obtain precise time and position for each recorded time series. Its most relevant characteristics are summarized in Table 2.1, and a picture of it is shown in Figure 2.5.

Technical characteristics of ADU-06	
Spectral range	DC to 20 kHz
Sampling frequencies	2-64-128-256-512-1,024-4,096-40,960 Hz
A/D conversion	24 bits, independent for each channel
Synchronization	GPS clock $\pm 130ns$.
Weight	Around 6.5 kg
Dimensions	230 x 200 x 180 mm^3
Power consumption	7-12 W (5 channels), depending on configuration

TABLE 2.1: Technical data of ADU-06.

FIGURE 2.5: ADU-06 data logger employed in this study.

2.1.3.2 Electric field measurements

EFP stands for Electric Field Probe. Each sensor is composed by a pair of electrodes like the ones shown in Figure 2.6 (left panel). The manufacturer recommends deploying them at a distance of roughly 100 m. Each pair of electrodes will be oriented in NS or EW directions. The voltage values obtained, when divided by the distance between them, give the amplitude of the electric field, usually expressed in [mV/km].

2.1.3.3 Magnetic field measurements

The acronym MFS stands for Magnetic Field Sensor. It is based on induction coils of several thousand turns around a high-permeability ferromagnetic core. It has an embedded low-noise pre-amplifier which permits to obtain sensibilities of around few cents of pT. It is covered by a cylindrical plastic shield. Its total dimensions are 1250 mm length and 75 mm diameter. It weights around 8.5 kg.

Induction coils do not measure the magnetic field itself but, instead, its first derivative with time, as it is expressed on the induction law:

$$V_{ind} = n\frac{d\Phi}{dt}, \tag{2.10}$$

FIGURE 2.6: Electrode EFP-06 employed for electric field measurement (left panel). Magnetometers MFS-06 (left) and MFS-07 (right) (right panel).

where V_{ind} is the inducted voltage at the wire, n is the number of turns and Φ is the magnetic flux which crosses its section. The flux can be calculated as

$$\Phi = BA = \mu_0 \mu_c HA,$$

where B is the flux density parallel to the sensor axis, μ_0 is the permeability constant in vacuum, μ_c is the permeability of the core, A is the cross section area, and H is the amplitude of the magnetic field. For a sinusoidal magnetic field, we can express H in terms of the phasor $\tilde{H} = \hat{H}e^{j\omega t}$. The induced voltage is therefore:

$$\tilde{V}_{ind} = \hat{V}_{ind}e^{j\omega t} = 2\pi j n \mu_0 \mu_c A f \hat{H} e^{j\omega t} = j f S_0 \tilde{H}.$$

The parameter S_0 is defined as the sensor's sensitivity constant which gives the relation between the magnetic field's amplitude and the induction voltage.

This is a theoretic equation and does not take into account several effects as for instance the resistivity of the wire or its parasitic capacities. The equivalent circuit of a MFS-06 is somewhat more complex. A better approach is depicted in Figure 2.7.

Referring to the source, the induced sensor voltage V_{ind}, the coil resistance R,

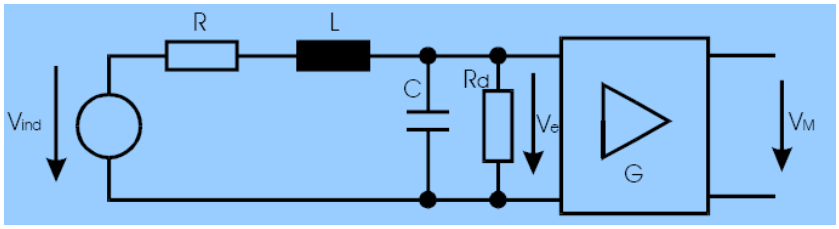

FIGURE 2.7: Equivalent circuit for MFS-06 magnetometer.

the input resistance of the amplifier R_d, the coil inductivity L, and the capacity C yield a damped serial resonance circuitry and the transfer function of the sensor will show a strong peak at its resonance frequency. For the sensor itself, without the preamplifier, we get the transfer function

$$\frac{V_e}{V_{ind}} = \frac{R_d/(R_d+R)}{1-(f/f_0)^2+j2D(f/f_0)}$$

with the amplifier's input resistance R_d, Gain G, resonance frequency f_0 and attenuation D defined as

$$f_0 = \frac{1}{2\pi\sqrt{ALC}} \qquad G = \frac{V_M}{V_e} \qquad 2D = \sqrt{\frac{R_d}{R_d+R}}\frac{\sqrt{L/C}}{R_d} + \frac{R}{\sqrt{L/C}}$$

Having this in mind the resulting transfer function between the magnetic field and the sensor output voltage becomes

$$F_{sensor} = \frac{V_e}{\tilde{H}} = \frac{jS_0R_d/(R_d+R)f}{1-(f/f_0)^2+j2D(f/f_0)}$$

The equivalent circuit diagram of the magnetometer leads to a frequency dependent sensitivity $E(f)$ referred to the preamplifier output of:

$$E(f) = E_0\frac{Ve}{V_{ind}}, \qquad E_0 = GS_0$$

In order to avoid the auto-resonance of the sensor (located at around 800 Hz), a feedback branch is attached, which acts as a filter for frequencies near f_r. The measured voltage at a MFS-06 sensor can be expressed as

$$V_M(f) = \frac{jfH(f)E(f)}{1+j\frac{f}{f_c}}, \tag{2.11}$$

and the cut-off frequency of the magnetometer is f_c= 4 Hz. The transfer function including the effects of the feedback is depicted in Figure 2.8.

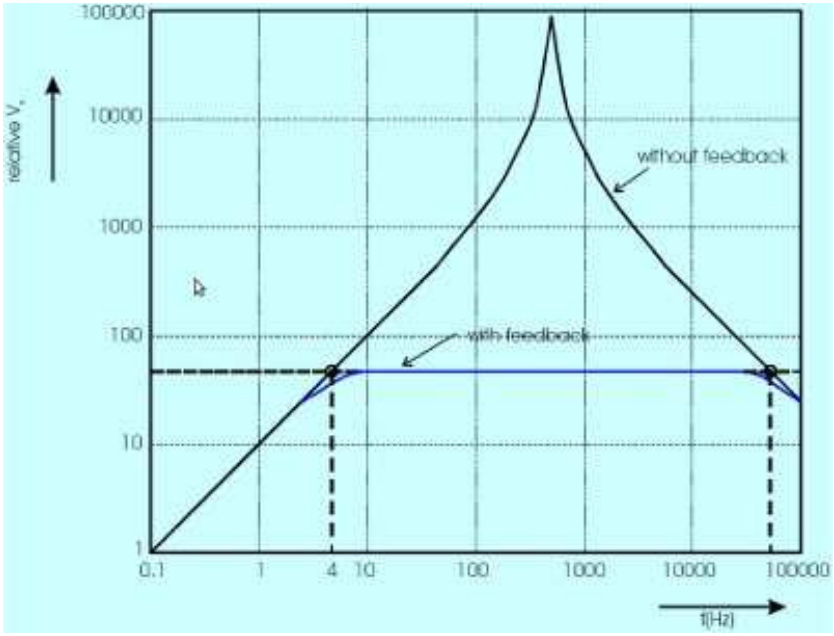

FIGURE 2.8: Transfer function of MFS-06 magnetometer.

2.1.4 Description of the MT Surveys

The department of Geodynamics of the University of Granada works with Magnetotelluric method since some years ago [72, 73]. They have built up a database with the resulting time series, which has been available for our study of Schumann Resonances. Up to eight independent surveys have been employed in this study. Each of them is taken over a time span of roughly 1 month, over an area whose radius is in the order of tens of km.

In Table 2.2, a summary of the principal parameters of each survey is shown. Seven of them pertain to the Western Mediterranean geographical area, while the other was performed in Antarctica.

The angular distances between the surveys and the main storm centers which dominate the lightning generation were calculated, and depicted in Figure 2.9. The areas with a density of flashes greater than 20 flashes/km^2/year on average [25] are gray-shadowed. The epicenters of the main storm centers move from month to month, and therefore the distances may slightly vary. From these distances, we inferred the degree of contribution of each storm center to each of the three first modes of SR, based on the theoretical results from Chapter 1 (see Figure 2.10). It is important to note that the amplitude of mode n=2 is nearly zero for sources located in the African epicenter.

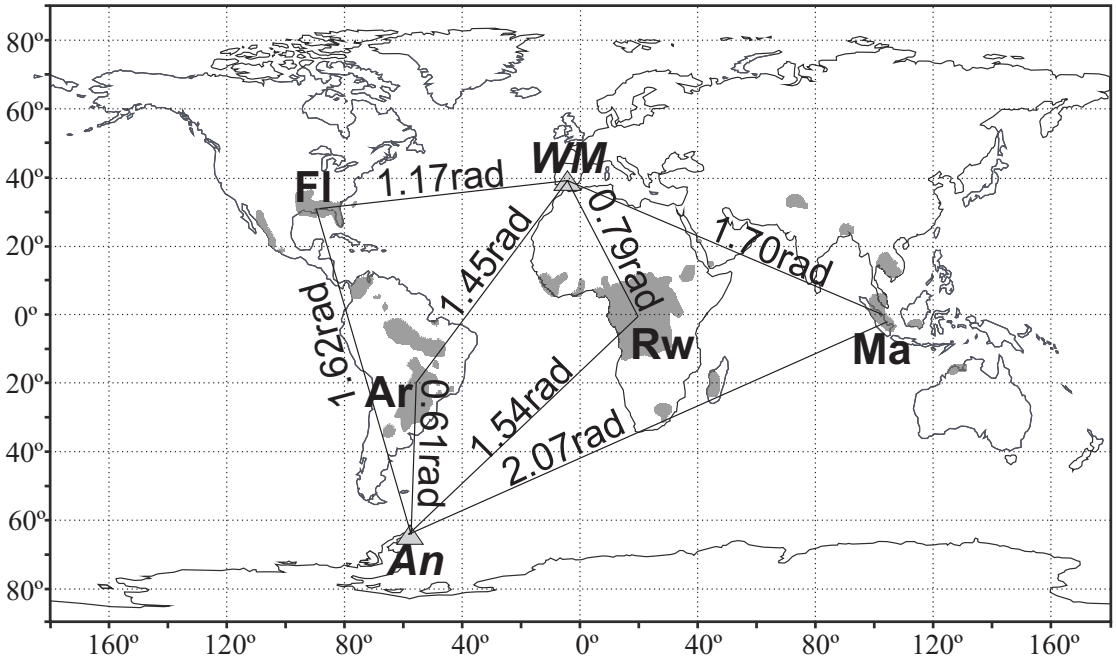

FIGURE 2.9: Global map with the angular distances between the MT campaigns and the main storm centers.

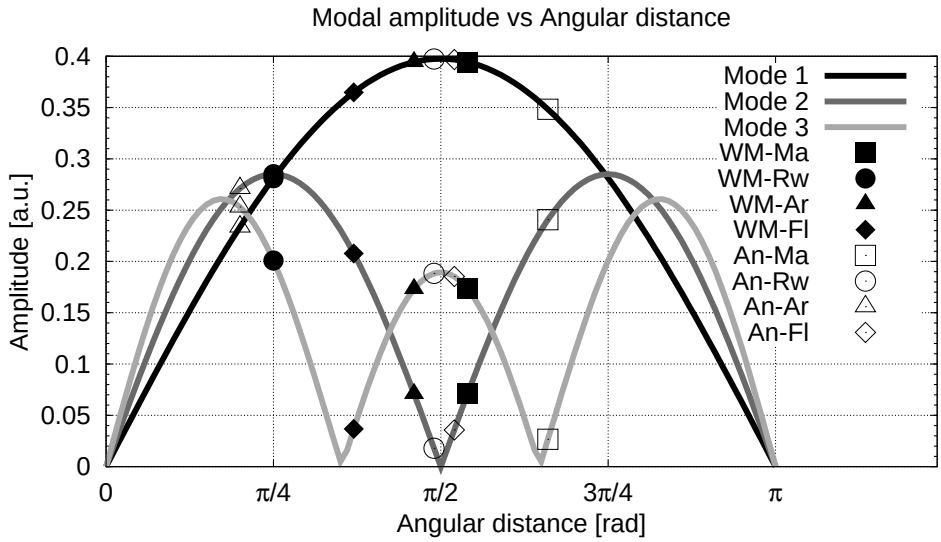

FIGURE 2.10: Dependence of the three first modes of SR with angular distance to the source, based on the spherical shell model.

TABLE 2.2: Location, key, date, and number of time series for each campaign used in the study.

Number	Location	Key	Date	Number of time series	Latitude	Longitude
1	Granada	Gra	May 2005	7	37 °10'N	3 °34'W
2	Almanzora	Alm1	Jul 2005	5	37 °20'N	2 °09'W
3	Rif	Rif	Feb 2006	19	35 °10'N	3 °50'W
4	Almanzora	Alm2	May 2006	3	37 °20'N	2 °09'W
5	Malaga	Mal	Nov 2006	4	36 °50'N	5 °09'W
6	Alcudia	Alc1	Jul 2007	22	38 °30'N	4 °30'W
7	Alcudia	Alc2	Sep 2007	4	38 °30'N	4 °30'W
8	Antarctica	Ant	Jan 2008	7	62 °50'S	60 °30'W

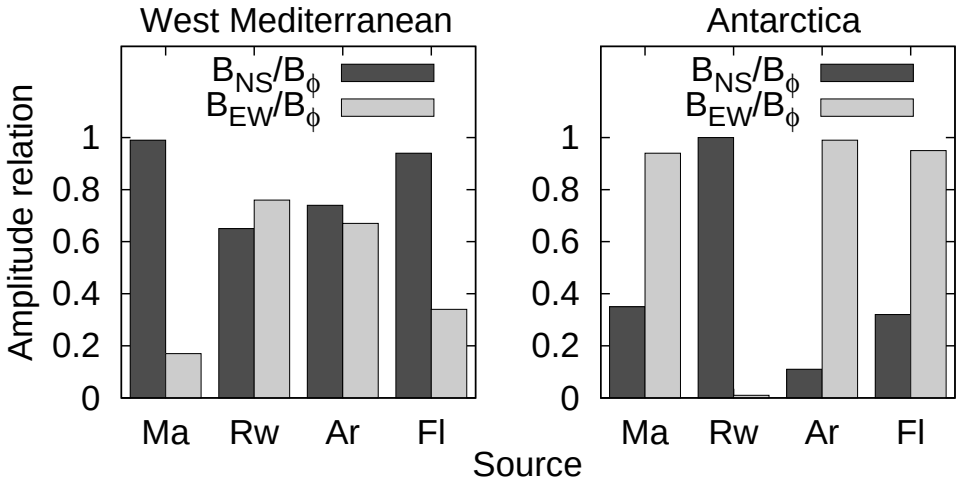

FIGURE 2.11: Projections of B_ϕ field over EW and NS axis, depending on the angular distance between the source and the survey point.

The MT magnetometers are always oriented with EW and NS axis. Since the main storm center relative position varies with daytime and depends on the observation point, we have calculated the inclination angles between the survey points and the main thunderstorm areas. Since the B field propagates in ϕ direction (for a source located at θ=0, see Section 1.3), we can calculate the amount of energy which will be projected on each direction (EW and NS). These results are shown in Figure 2.11. The square sum of both EW and NS components (because they are depicted in amplitude) is the unity. It is interesting to note the behavior of the projections in the Antarctic survey. Each storm center has its preferred axis (EW for Malaysia and America, NS for Rwanda).

As commented in Section 2.1.3, the MT method implies measuring at different geographical positions of the area under study. We have found that electric field

measurements heavily vary its amplitude (up to one order of magnitude) owing to the characteristics of the ground where the electrodes are deployed, as well as to local effects originated by the particular orography of each measurement point. On the other hand, magnetic field components are not affected by these local effects, and they have all similar amplitude regardless of the measuring point of the campaign.

2.1.5 Spectrograms from the time series

There are two large time series in the MT survey database from the Geodynamics department. They were taken in Morocco (survey 3) and Antarctica (survey 8), and their sample frequencies are 128 and 64 Hz. Their duration is 15 and 14 hours respectively and, therefore, the daily evolution of the SR can be observed on them. In Figures 2.12 and 2.13 their correspondent spectrograms have been plotted. Each vertical line is computed from 10 minutes of the series, previously splitted into data blocks of 3 seconds.

The spectrograms from Morocco time series (see Figure 2.12) correspond to the night of 5 - 6 February 2006, from 20:05 UT to 09:15 UT. The bandwidth of the signal is up to 32 Hz, but the filters of the measurement equipment distort the higher frequencies, so they have been depicted up to 27 Hz. In the first quarter of the series (up to 24:00 UT) there are many saturated spectra (white lines). This is due to electromagnetic interferences with the measurement equipment. The first four SR can be identified at their typical frequencies (roughly 8, 14, 20, and 26 Hz). It is interesting to note that there is an increase of SR energy at around 06:00 - 08:00 UT. This time corresponds to the time of activation of the Malaysian storms.

In Figure 2.13, the magnetic field component spectrograms from the Antarctica time series have been plotted. They correspond to the night of 29 - 30 January 2008, from 22:00 UT to 12:00 UT. Since the sampling frequency was 128 Hz, up to seven SR can be identified. Electric field measurements contain corrupted data and therefore could not be plotted. Most of the SR energy is measured in the EW component, as it is expected by the analytical model when the sources are located either in America (22:00 UT) or in Malaysia (08:00 UT). There is an increase on the SR energy between roughly 06:00 UT and 10:00 UT (which is noticeable

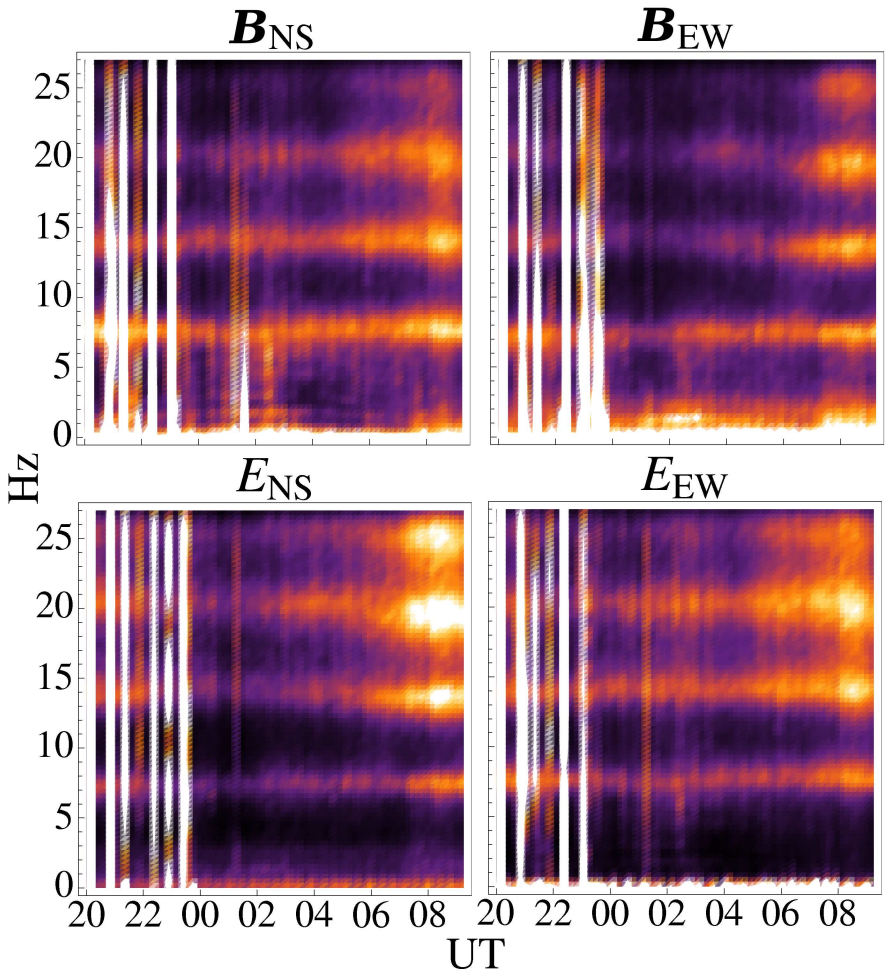

FIGURE 2.12: Spectrogram of magnetic and electric components from 5 - 6 February 2006, taken during Morocco survey.

for higher resonances), probably indicating the activation of the Malaysian storm center.

2.1.6 Daily variations of Schumann resonances

The volume of data contained in the database does not permit to perform an exhaustive study of the daily variations of SR, since there are not continuous records of them. Instead, we have small pieces at different daytimes and months. Therefore, we will limit this part of the study to evidence a behavior that can be observed in the second SR mode in Antarctica survey, which is related to the main thunderstorm centers time of activation.

The angular orthodromic distance between the Antarctic survey and Rwanda (epicenter for African storms) is roughly $\pi/2$, so the second SR mode is highly

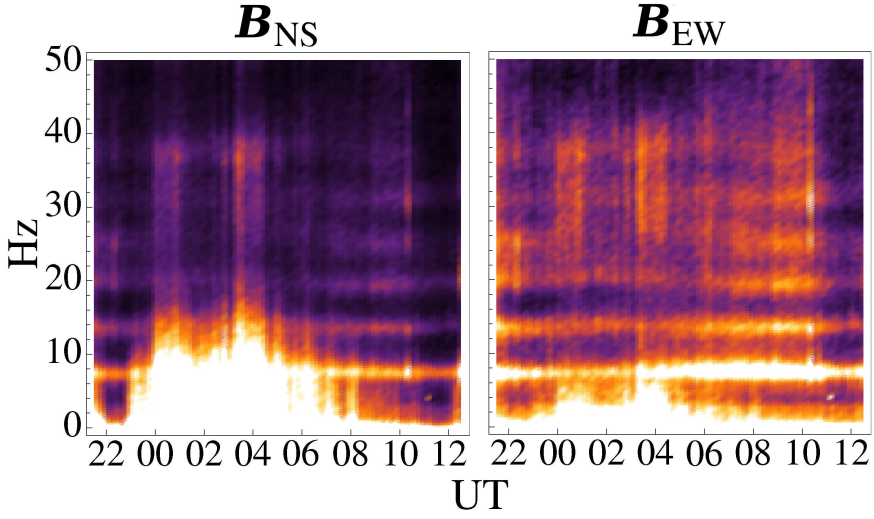

FIGURE 2.13: Spectrogram of magnetic components from 29 - 30 January 2008, taken in Antarctica survey.

attenuated (see Figure 2.10) for the lightning coming from there, according to the analytical model presented in chapter 1. The same situation stands for Florida storm center, but we cannot study the effect because its time of activation is roughly the same as in Argentina, where the second mode does contain energy. In addition, since the Antarctica survey was performed in January, the American influence should be coming mainly from the Argentina storm center.

We have averaged the four available spectra at African storms time window (roughly 14:30 - 17:30 UT), as well as the four available spectra at American time window (roughly 17:30 UT - 22:30 UT). The results are shown in Figure 2.14. By looking at the upper panel (magnetic field), it can be noted that effectively the 2nd mode of NS component has lower amplitude than the third for the African time window. This is the only spectra in the entire database where this situation occurs for the magnetic field. By looking at the EW component for the African time window, we observe that second and third mode have roughly the same amplitude. We believe this is due to a mixture of influence from African storms and storms from other areas, due to its orientation. If we look at American time window spectra, the second mode has higher amplitude than the third, as it occurs with the rest of the spectra of this study. As predicted by the analytical model (see Figure 2.11), the level of the EW component is stronger for the magnetic field.

It can be observed, in Figure 2.14, that B_{NS} is correlated with E_{EW} and vice versa, so the effect of the 2nd mode diminishing is well observed in both B_{NS} and E_{EW} (for the time 14:30 - 17:30 UT).

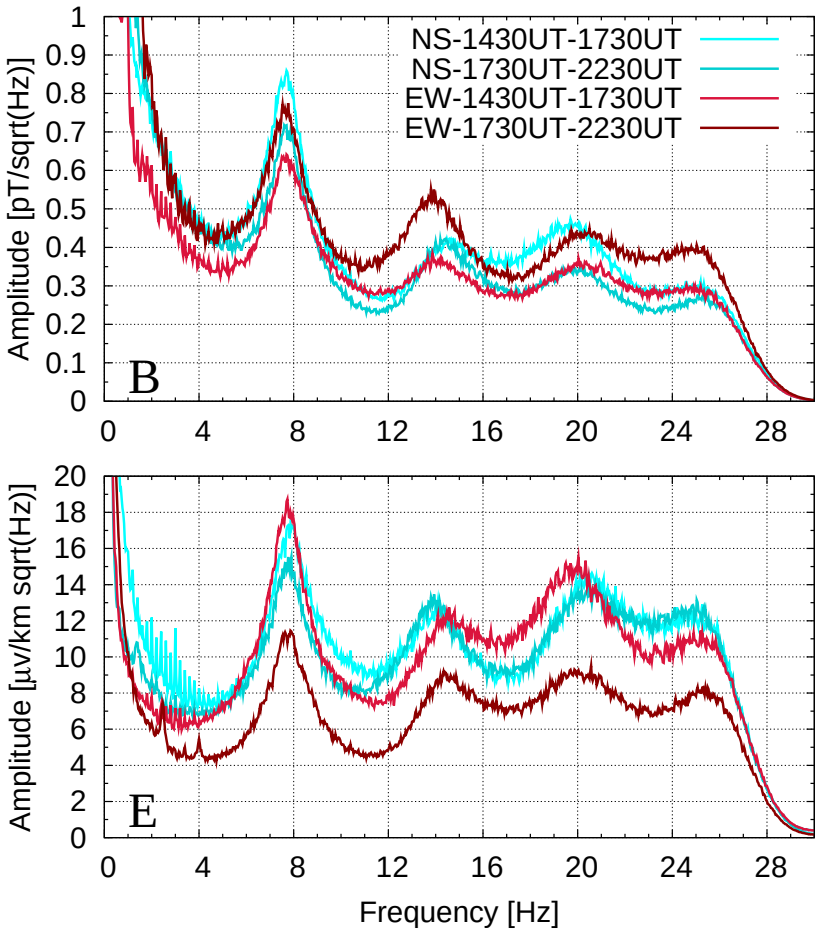

FIGURE 2.14: Averaged spectra of eight TS, from the Antarctic survey, at African (14:30 - 17:30 UT) and American (17:30 - 22:30 UT) storm time activation.

Another interesting effect is the frequency shift that occurs for the 2nd and 3rd SR modes. The central frequencies of the modes for the magnetic field are shown in table 2.3. Both EW components exhibit lower central frequency for the second mode (0.5 Hz less) and higher for the third (0.5 Hz more) when compared to the NS components. The first mode does not follow the tendency, and the maximum shift is 0.19 Hz. Each component registers storms from different locations at different degrees of contributions. Different nature of the sources, as well as different distances and path configurations may be the reason for these shifts [74].

2.1.7 Seasonal variations of the Schumann Resonances

The SR parameters of the whole TS from each campaign have been averaged, in order to observe the general tendencies of them along the year. A Lorentzian fit

TABLE 2.3: Central frequencies of NS and EW components (magnetic field) of time series taken in Antarctica at the activation time of African and American storm centers.

UT range	Component	Frequency (Hz)		
		1st mode	2nd mode	3rd mode
1430-1730 UT	NS	7.69	14.56	19.86
1430-1730 UT	EW	7.80	14.05	20.50
1730-2230 UT	NS	7.73	14.45	20.07
1730-2230 UT	EW	7.61	13.83	20.53

(see Section 2.1.2) has been applied to each spectrum, yielding amplitude, central frequency and Δf_{3dB} for each of the three first SR modes. Less than 10 % of the series were not well adjusted by the algorithm and had to be disregarded. This situation occurred mainly adjusting the first (mode 0) and fifth (mode 4) Lorentzian curves, when they were either too strong or too weak. It is important to note that the results are not really statistically significant, since there were only few hours of records for each month. Anyway we could corroborate some results and tendencies addressed in other works [74–76].

All the signals with at least 90 minutes of length were considered, leading to the number of series for each campaign shown in Table 2.2. Each TS was splitted into data blocks of 30s, so the frequency resolution of the Bartlett's spectral estimator is 0.033 Hz.

The magnetic field amplitude evolution of the SR modes can be observed in Figure 2.15. It is interesting to note the different behavior between the two components (NS and EW) [75]. For the WM surveys, there is more energy in the NS components, as it is expected by looking the results of Section 2.1.4. The EW component exhibits certain stability throughout the study, but the NS component clearly exhibits higher maxima for the northern warm season months. The months with less amplitude are February 2006 and January 2008, which is in agreement with the observations of other authors [77, 78].

Electric field measurements show high variability of amplitude between TS for the same survey. As commented before, this is due to the changing location of the measurement point. Up to one order of magnitude variations have been found for the same survey, and therefore we cannot extract conclusions of their seasonal behavior. The interesting fact is that there is no decay of amplitude as the mode number increases (see Figure 2.16). As opposed with magnetic field measurements,

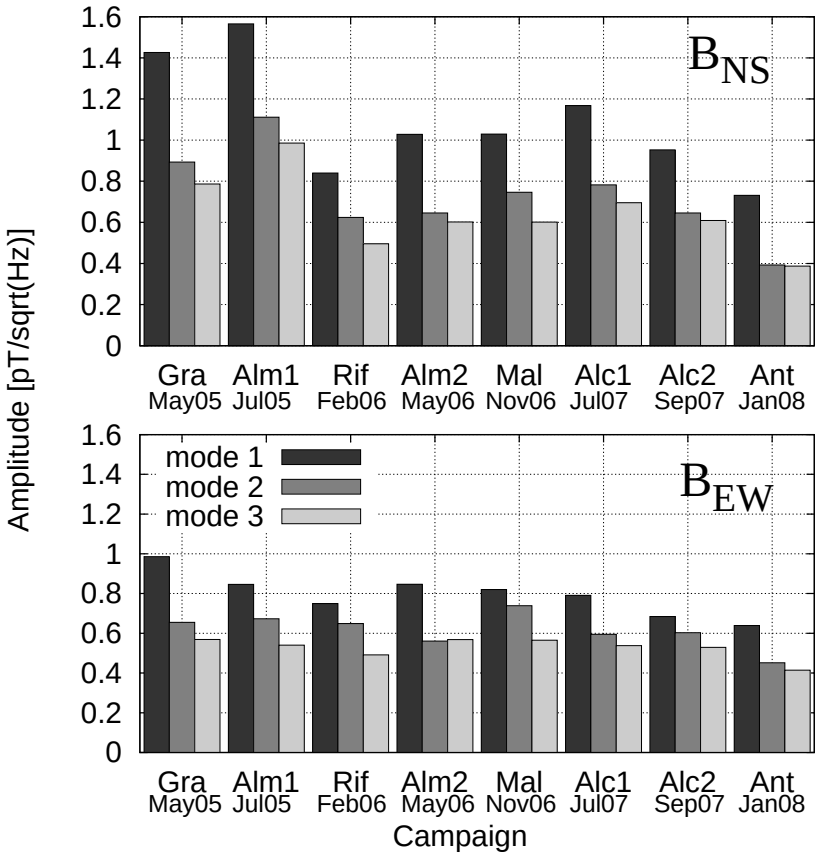

FIGURE 2.15: Magnetic field peak amplitudes for the three first SR modes. Both NS component (top panel) and EW component (bottom panel) are depicted.

the three modes of the electrical field exhibit similar peak amplitudes at each campaign. This may indicate the convenience of these kind of measurements for studying higher modes of the SR.

The central frequency values for the first three SR modes oscillate around 7.8, 14, and 20.5 Hz respectively (see Figure 2.17). It is interesting to note the correlation that exists between B_{NS} and E_{EW} and vice versa. In many of the campaigns there is a shift in central frequency between the two magnetic field components, and this shift is in agreement with a shift in the electric field components. The most prominent example is, as commented in previous section, the Antarctica survey, with shifts of 0.6 and 0.5 Hz for the second and third modes, respectively. According to [74], central frequency shifts of the SR modes may be related to the effective size of the main storms.

The last parameter which has been calculated and plotted is the quality factor Q (see Figures 2.18 and 2.19). It quantifies the spectral cleanliness of the resonance. High value of the Q factor implies a narrow band resonance. The principal

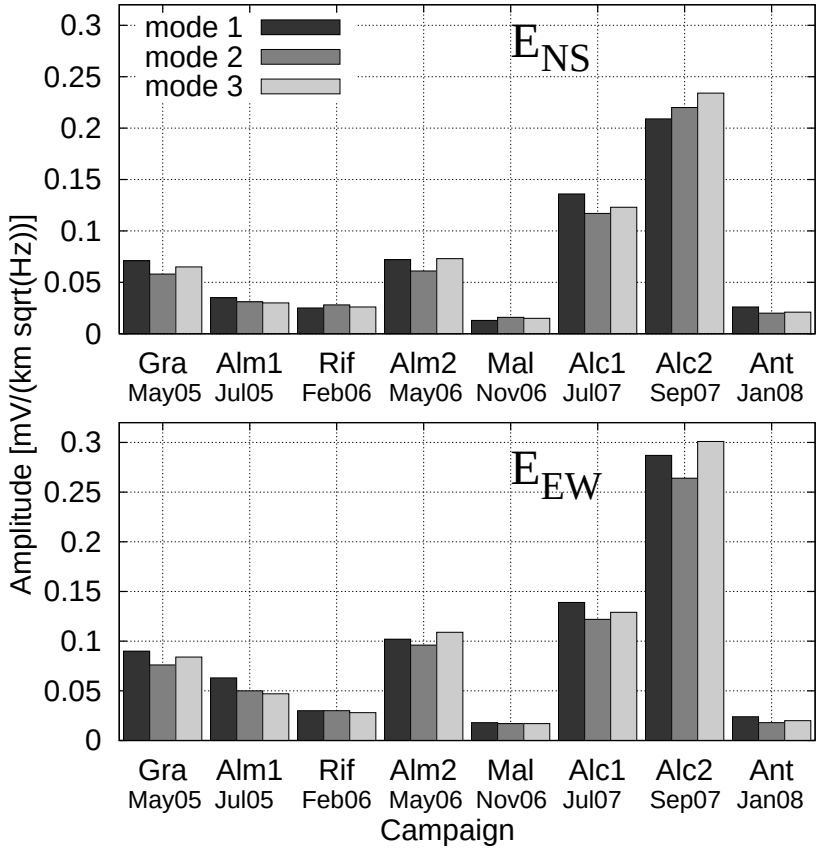

FIGURE 2.16: Electric field peak amplitudes for the three first SR modes. Both NS component (top panel) and EW component (bottom panel) are depicted.

reason (as we will see in Chapter 6) for lower Q is the conductivity profile with height of the cavity.

It can be seen from the Figures 2.18 and 2.19 that Q factors behave similarly for electric and magnetic field components, and they do not change too much over campaigns. Higher modes have higher Q, in general.

Lastly, it is important to note, as stated in [75], that Q factor measurements depend on the Lorentzian fit employed. Different studies utilize slightly different configurations, which can modify the final values of Q. Therefore caution is needed when comparing this value with results from other studies.

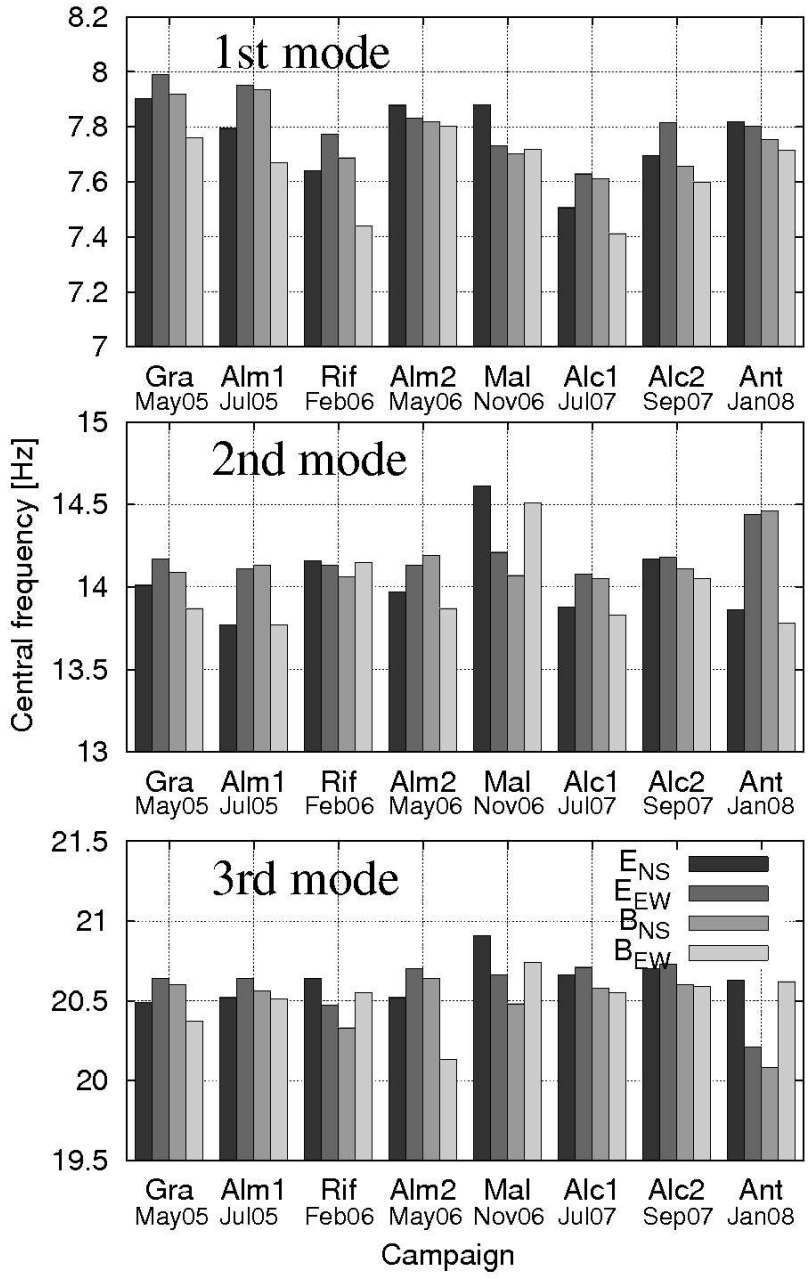

FIGURE 2.17: Averaged central frequencies of the three first SR modes for the different surveys and components.

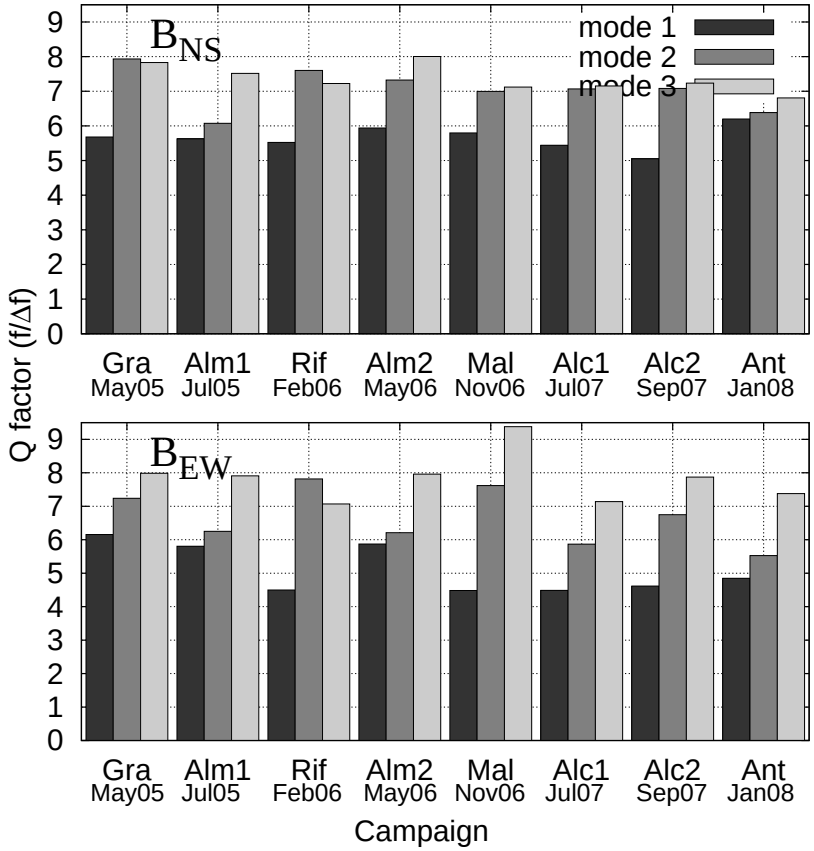

FIGURE 2.18: Q factors of the three first modes of SR at different surveys, for the magnetic field spectra.

2.2 Rescaled Range Analysis (R/S)

2.2.1 Description of the method

Time series can be regarded as the result of a sum of different components. One component is the trend component, or macroscopic behavior, accounting for the long term tendency of the TS. Another component would comprise the discontinuities that may appear in the TS due to different reasons. There is a periodic component, which is common in signals originated from natural processes (tides, rotation of planets, etc.). Finally, there is a stochastic component, which includes the fluctuations not included in the trend or periodic component. These fluctuations can be of diverse nature, such as noise or unpredictable events.

The Rescaled Range Analysis is based on studying the persistence of the TS stochastic component [63, 79]. Persistence is defined in terms of the relationship between adjacent and nearby samples, by looking for the correlation between them.

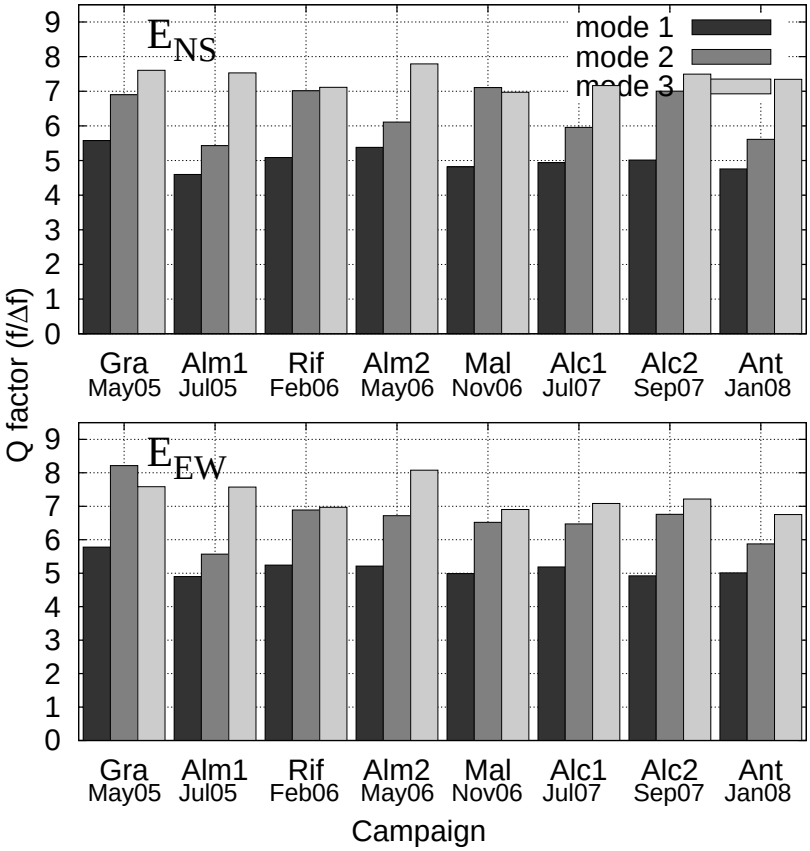

FIGURE 2.19: Q factors of the three first modes of SR at different surveys, for the electric field spectra.

If adjacent values of the TS are not correlated, then it exhibits random behavior. If the correlation is positive, then distance between adjacent samples is lower than for a random TS, this behavior being known as persistent. On the other side, if the correlation is negative, the distance in between nearby samples is greater than for a random TS, and this situation is called anti-persistent behavior.

A standard procedure for evaluating the persistence of a time series is described in [80], the so-called Rescaled Range Analysis (R/S), based on calculating the Hurst exponent (Hu). It is applied to TS of 2^N samples length, $x[t_n]$, where x is a TS with a sampling frequency of $f_s = 1/\Delta t$. For each value of the index $i = 1...N$, we define a partition of the TS in segments of length $M = 2^i$ samples. Then, the following is applied to each partition i:

1. We calculate the mean for each segment j of partition i

$$\langle x \rangle_{i,j} = \frac{1}{M} \sum_{l=1}^{M} x_j[l] = \frac{1}{M} \sum_{l=1}^{M} x\left[M(j-1)+l\right] \tag{2.12}$$

2. Then we obtain the sum (integral) of the time series

$$y_j[k] = \sum_{l=1}^{k} \left(x_j[l] - \langle x \rangle_{i,j}\right). \tag{2.13}$$

3. Now, we calculate the range and standard deviation for each segment j of the partition i

$$R_{i,j} = Max\left(y_j[k]\right) - Min\left(y_j[k]\right) \tag{2.14}$$

$$S_{i,j} = \sqrt{\frac{1}{M}\sum_{l=1}^{M}\left(x_j[l] - \langle x \rangle_{i,j}\right)^2}. \tag{2.15}$$

4. The average value of $R_{i,j}$ and $S_{i,j}$ is evaluated at each partition i, their quotient being defined as $Z[M]$:

$$Z[M] \equiv \frac{R_M}{S_M} = \frac{\langle R_{i,j} \rangle}{\langle S_{i,j} \rangle}. \tag{2.16}$$

5. The Hurst exponent Hu, sometimes referred as K or H, is defined by the following power relation between the Z coefficient and the number of samples M:

$$Z = \left(\frac{M}{2}\right)^{Hu}. \tag{2.17}$$

This last relation is of empirical nature, and presupposes scale invariance.

The Rescaled Range analysis finds a relation between the Z coefficient and the number of samples M. The best-fit constant-slope of the curve $\log_2(Z[M])$ against i=$\log_2[M]$ is the Hurst exponent (Hu). In general, $Hu \in [0.7, 0.8]$ for the majority of natural geophysical processes [81].

When R/S analysis is applied to a signal which contains only Gaussian white Noise, the Hurst exponent tends towards 0.5, being this value the boundary between persistent and anti-persistent phenomena. Signals whose $Hu \in (0.5, 1]$ are persistent, while the signals whose $Hu \in [0, 0.5)$ are anti-persistent. According to [80], most of the natural signals are persistent. Intuitively, a process is persistent if it tends to maintain its tendency. For instance, for a continuous, zero-mean stochastic process which has a positive value at $t = t_0$, a value of Hu near to 1 indicates that the probability of the process being positive for $t > t_0$ is high.

TABLE 2.4: Date and time of the records used in the R/S analysis plus an estimation of the storm intensity [12].

Site	Date	time	Estimated intensity (a.u.)			
			Asia	Africa	America	Total
22	25 Jan 2008	2030 UT	0.2	1.5	5.0	6.7
23	26 Jan 2008	1730 UT	0.5	5.0	2.5	8.0
27	04 Feb 2008	1430 UT	1.0	4.0	0.2	5.2

2.2.2 TS from Antarctica

The method described above has been applied to time series from the Antarctica survey, where the anthropogenic noise is almost inexistent. Signals with f_m=512 Hz have been employed, in order to ensure good resolution even with small number of samples. The duration of the TS is 2^{18} samples (roughly 9 minutes). The data pertains to three different days and times detailed in Table 2.4.

The Z coefficient as a function of the number of samples M has been calculated for the mentioned time series. The results are depicted in Figure 2.20 (top). The series belong to different days, times of the day and components of the magnetic field (NS and EW), but they exhibit common behavior when analyzed trough R/S. The estimations of the Hurst exponent Hu for the six time series of this study fall between 0.72 and 0.93, indicating that the phenomenon is persistent.

The Hu values of Figure 2.20 (bottom) have been calculated by linear adjustment of previous and following Z coefficients. We do not presuppose anymore that Hu is independent from the scale. From Figure 2.20, three regions can be differentiated in every curve. This indicates that a different value of Hu should be noted at each scale range. Calculating different Hurst exponents for different scales was suggested by [82], for the study of ocean waves.

Three different areas for Hu arise from Figure 2.20 (bottom). The first area stands for I=[2, 5], or time scale up to 1/16 seconds, where all the signals practically have the same value of Hu. The Hurst exponent (i.e., the Z slope) takes values between 0.75 and 0.85 depending on the series, which are the typical values for persistent natural phenomena. The next interval is for I=[6, 10], or time scale between 1/8 and 2 seconds. Here the slopes tend to 0.5, indicating random behavior at these time scales. For greater values of I, the slopes first increase up to values greater than one, and then decrease towards zero.

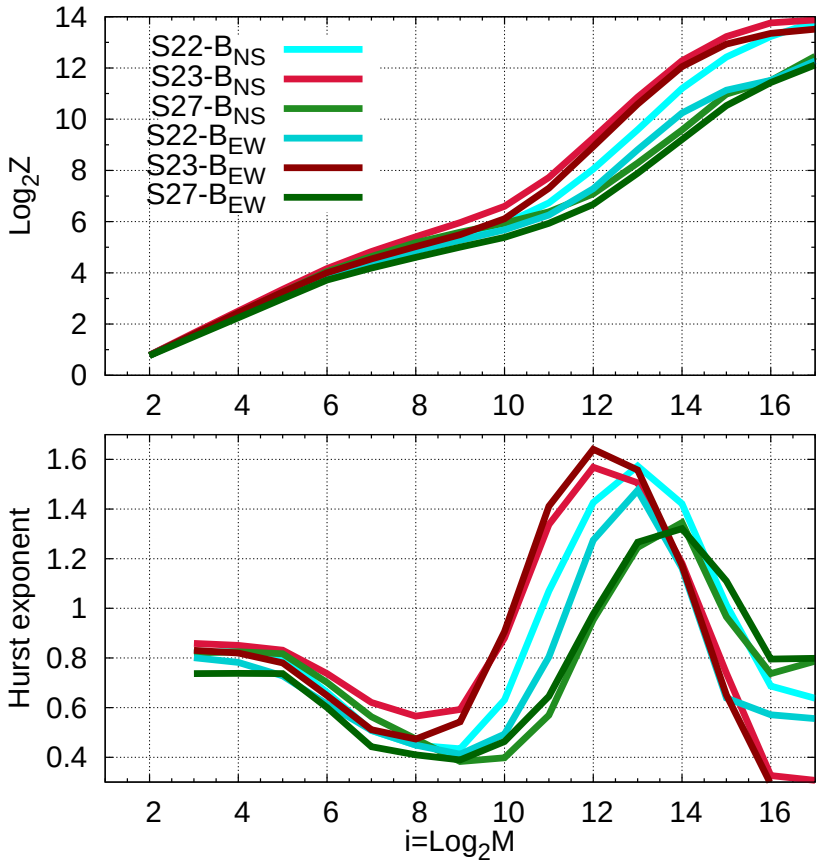

FIGURE 2.20: Results of the R/S analysis applied to time series from Antarctica.

Rescaled Range analysis, when applied to a noisy signal, is sensitive to its internals. As stated in [12, 81], variations on the pulse ratio drive the standard deviation and the range of a noise. Therefore, the average lightning rate directly affects the R/S analysis of a signal which measures the electromagnetic fields inside the Earth-ionosphere cavity. According to [81], these variations shift the knee area found at curves $\log_2 Z$ - I (see Figure 2.20). Following the equation

$$r = \frac{f_s}{M_k} \tag{2.18}$$

where r is the average lightning rate, f_s is the sampling frequency, and M_k is the sample number at which the knee transition is located, the lightning rate can be estimated from R/S analysis.

There is not a great difference between the three signals analyzed in Figure 2.20, probably meaning that a similar average rate of lightning was involved during the generation of all of them. That being said, the results suggest that S_{27} has a perceptible lower rate of discharges than the rest, being S_{23} the one with higher r.

Since the sampling frequency is f_s=512 Hz, the estimation for the lightning rate on these signals is roughly 16 - 32 flashes per second, obtained from taking $M_k \simeq 2^4$ - 2^5.

2.2.3 Synthetic simulation

In order to confirm that it is possible to determine the pulse rate of a signal from the inertia transition position of $Z(N)$ in R/S analysis, a numerical simulation has been performed. The radiated field of a thin wire antenna supplied by a Gaussian pulse has been employed as single input pulse (simulating the field radiated by lightning). The Method of Moments was employed to solve the integral equation obtained from Hallen's equation [83]. The load and current densities have been obtained for each frequency of the Gaussian pulse. The resulting fields were calculated directly in time domain, by Fourier transform of the sources. The field was calculated at a point in the equatorial plane of the antenna at a distance of 5 times its length. In Figure 2.21 (top), the time evolution of one pulse stroke can be observed.

Since the antenna is a resonant system, there are preferred frequencies which are more amplified than the rest. This can be regarded as an analogy in the spectrum to the resonant frequencies of the Earth-ionosphere cavity. In Figure 2.21 (bottom), the Fourier transform of the stroke pulse has been depicted. The antenna resonances can be observed, and the depicted spectrum reminds to Schumann resonance spectrum.

Starting from this pulse, a signal of 2^{16} samples is created by periodically repeating the discharge from Figure 2.21. Each discharge is composed by 774 samples, and we will suppose dt=1 (the inverse of the sampling frequency f_s), both in arbitrary units for simplicity. In order to avoid the initial transient of the signal we will not consider the first 500 samples, and take the next 2^{16}. Let r be the number of discharges per unit of time and dr= $1/r$, i.e., the time between two discharges. The quotient n_c=dr/dt defines the distance in samples between discharges. Three different values for dr have been considered: 16, 64, and 128.

When R/S analysis is applied to the synthetic signals described above, it leads to the results shown in Figure 2.22. The three signals have common behavior of their Z coefficient, until they reach the time scale where M=dr. From this point

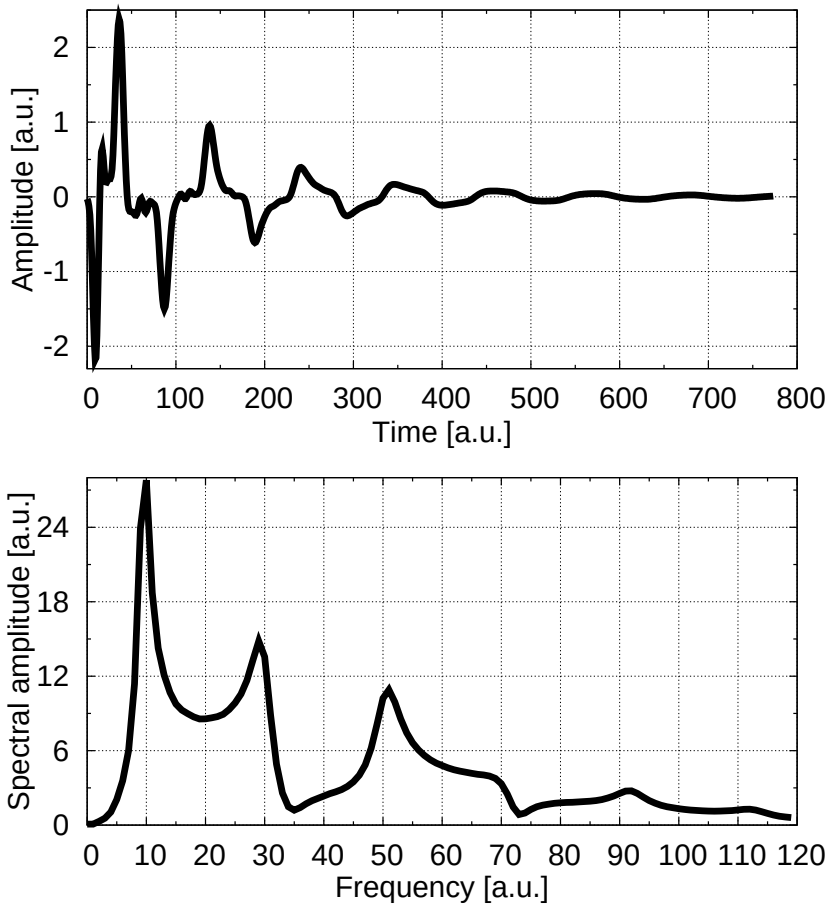

FIGURE 2.21: Field generated by thin wire antenna excited by a high bandwidth Gaussian pulse.

the Z coefficient remains constant. Since the signal comes from a unique source and all the discharges are equal, when the number of samples is large enough both the range and the standard deviation become constant, and the Hurst exponent tends to zero. In the simulation, it is easy to infer the rate of discharges from the value of I at which the inertia of Z changes.

2.3 Conclusion

This Chapter proves the presence of Schumann resonances in magnetotelluric records. The magnetotelluric dataset obtained by the Geophysics Group at the University of Granada in successive campaigns performed in Antarctica and the western Mediterranean area has been analyzed. Although not specifically designed for detecting SR, these measurements show advantages over those taken at a fixed

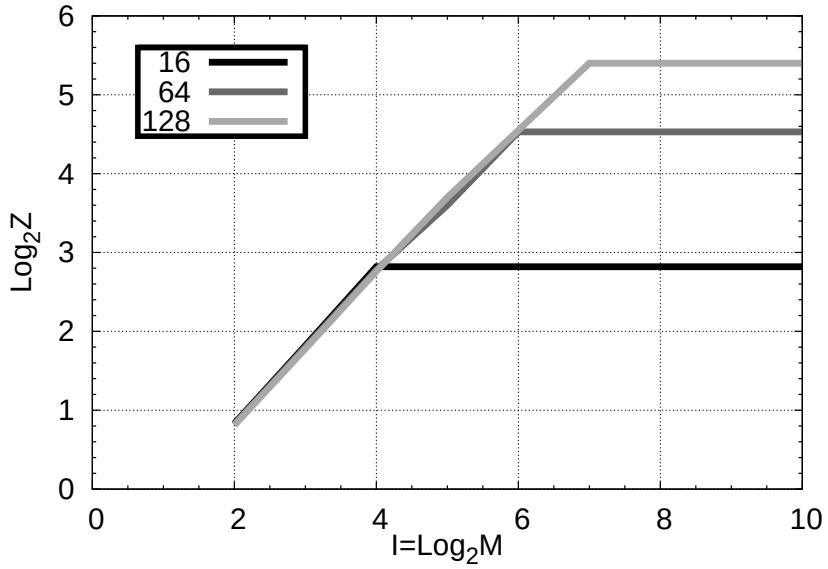

FIGURE 2.22: $\mathrm{Log}_2 Z$-I curve of a synthetic signal simulating natural ELF noise.

station. Since they were recorded at various places separated by a distance on the order of km, it was possible to study the influence of local effects. Furthermore, the MT method records electric horizontal components, not frequently measured for SR research. Finally, the broad sweep in frequency that the MT method requires has provided interesting time series with different sample frequencies between 64 and 512 Hz. In contrast, MT measurements are not taken continuously in time, which means that results are less statistically significant, but still suitable and can confirm behaviors and tendencies.

All the measured components (NS and EW for the electric field, NS, EW and vertical for the magnetic field) contain SR except the vertical magnetic field (even though 5% of these also showed the resonances).

For the signal processing of the time series, two different methods have been employed: spectral analysis through the Fast Fourier Transform and Rescaled Range Analysis calculating the Hurst exponents. For the first, signals with a sample frequency of 64 Hz and 90 minutes long have been used. At each signal, data blocks of 30s have been taken, applying FFT plus a Hanning window to each. The resulting spectra were then averaged in order to obtain a spectral estimator of the signal. Subsequently, the estimation of the spectrum was adjusted by a sum of Lorentzian in order to quantify the amplitude, central frequency and bandwidth of each resonant mode. In addition, the spectrograms of two exceptionally long

time series were obtained. From the spectral analysis, the following conclusions can be formed:

1. Evidence of three main storm centers located in Asia, Africa and America with their main activity in the local afternoon. The field amplitudes observed for each component are in agreement with the predictions for the TM^r modes. Therefore, the campaigns registered in January and February show less modal amplitude, while those taken during the northern hemisphere spring and summer are the most energetic. Moreover, a decay in amplitude with the modal order is observed in the magnetic components, while this is not present for the electric components. The magnetic field measurements have been shown to be robust regarding local effects, and small shifts of km of the observation point do not affect the measurement, while electric field measurements can vary their amplitude up to one order of magnitude within a few km of distance. However, the frequency contents do not vary with the shift of the point of observation either in magnetic or in electric field measurements.

2. According to the prediction of the analytical model, measurements have shown that a minimum of amplitude appears in the second mode of the magnetic NS (and electric EW) component in the Antarctic campaign, when the main center of storms is located in Africa (around 1600 UT).

3. The central frequencies for the first three SR modes averaged in the different campaigns are 7.8, 14, and 20.5 Hz. The measurements around these central values are subject to shifts, and seem to be correlated inversely with the size of the source where the resonances originated. These variations are stronger in the second and third modes than in the first.

4. In all the time series, the spectral correlation between magnetic NS and electric EW components has been proved. The same occurs between magnetic EW and electric NS. The modes show close frequency shifts and relative amplitudes between them.

The rescaled range analysis has been applied to series taken in Antarctica and with a sample frequency of 512 Hz, to guarantee enough resolution with a low number of samples in the analysis. This sample frequency is considerably higher

than that typically used in other fixed station SR measurements (usually around 100 - 200 Hz).

The curve $\log_2 Z$ - $\log_2 M$ has been depicted, and a value for the Hurst exponent has been obtained at each point of the curve, as the result of a linear adjustment of the previous and following points. The resulting curve, Hu - $\mathrm{Log}_2 M$, has three clearly distinguishable parts. The first part comprises $I = \{2, 5\}$, corresponding to time scales between 4 and 62 ms. On this range, Hu is approximately constant, maintaining its value between 0.75 and 0.85 for the different series analyzed, thus indicating persistence based on a power law. Therefore, there is a fractal behavior on this time scale. The second part ($I = \{6, 10\}$) corresponds to a time scale up to 2 seconds. In this range, the signal approximates random behavior, with Hu taking values around 0.5. The third part of the curve corresponds to higher values of I and the value of Hu increases beyond unity.

By following the analysis by Nickolaenko et al. [81], the transition from the first to the second part of the curve can be matched with the average rate of discharges from which the signal originated, as stated in Equation 2.18. In order to corroborate this statement, a numerical simulation has been performed, in which each discharge is modeled by the radiated field of a wire antenna excited by a Gaussian pulse. It is found that the Hurst exponent tends to zero for $I \geq 1/r$, where r is the rate of discharges per unit of time. According to this, the signals analyzed show an average rate of around 16 - 32 discharges per second.

Chapter 3

Ionospheric effective height determination from monitoring the 1st cut-off frequency [2]

A novel technique to draw global maps of the ionospheric effective height of the Earth-ionosphere waveguide is presented in this chapter. The aim is to characterize the dimensions and properties of the waveguide, with the purpose of better understanding the electrodynamics which occur inside it. The technique is based on electric field measurements taken from the satellite DEMETER. Lightning in the atmosphere generates signals in the VLF band known as atmospherics, which propagate in the waveguide several thousand of km before vanishing. Part of their energy leaks up to the satellite orbit (∼700 km), and therefore the first cut-off frequency of the waveguide can be tracked from the space. This frequency is directly related to the height of the waveguide. This study has revealed seasonal patterns for this effective height, as well as dependence with the kind of surface on Earth, which evidences coupling between the lithosphere and the ionosphere. In addition, the study indicates that there is correlation between the solar activity and the global value of the cut-off frequency. From these results, together with data from empirical models, it is possible to infer the electron density and other plasma parameters at a region which is hard to study because is too low for satellites to orbit inside it and to high for balloons to reach it.

The Chapter starts defining the DEMETER mission and specially its electrical

field measurements. Then we explain the methodology employed to track the cut-off frequency from the dataset, and the way to obtain the electron density from the measurements. After that, we analyze and discuss the results obtained, where certain seasonal patterns repeating over the years have been found. Finally, we attempt to compare the results from our method with empirical reference models for the ionosphere, putting into manifest that these seasonal patterns are not present in them, due to the lack of measurements at this height of the ionosphere.

3.1 The DEMETER mission

DEMETER [9, 84] is a French micro-satellite, the first of the Myriade series, developed by CNES (Centre National d'Études Spatiales) for low-cost science missions. DEMETER stands for Detection of Electro-Magnetic Emissions Transmitted from Earthquake Regions, and it is the name of the Greek goddess of Earth. Its dimensions are 60 x 85 x 110 cm, and its weight is around 130 kg. It was designed and launched with the purpose of studying ionospheric perturbations caused by natural phenomena and human activity. One of its main targets is to establish the connection between natural disasters (primarily earthquakes and volcano eruptions) and ionospheric perturbations, in order to provide knowledge for future prediction systems [85–87].

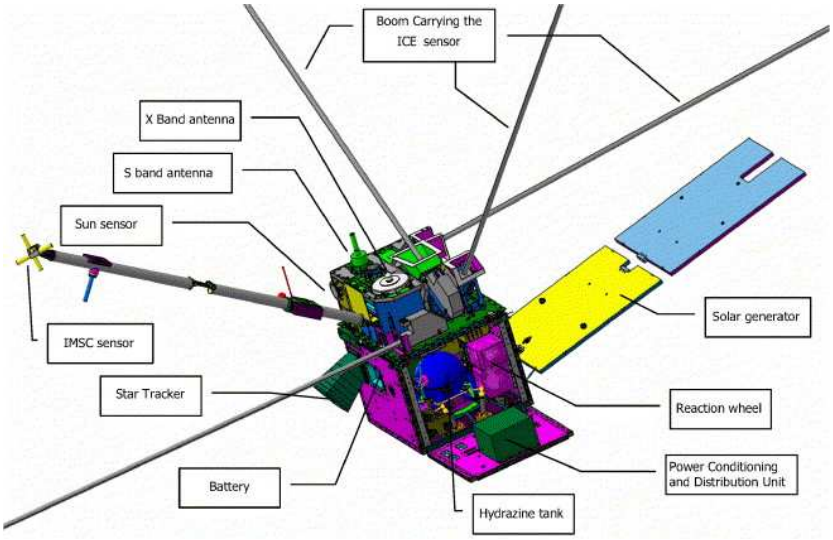

FIGURE 3.1: Layout of the DEMETER satellite, taken from [84].

DEMETER was launched on June 29th 2004 from Baikonour (Kazakhstan) by a Dnepr launcher. It was put on a polar Sun-synchronous circular orbit with

98° inclination. Its initial altitude was 710 km, but it was changed to 660 km in December 2005 by the mission center. Due to its synchronous orbit, DEMETER always records data either at roughly 10.30 LT (down-going half orbit) or at 22.30 LT (up-going half orbit). It performs 14 orbits in one day. It gathers data between the invariant geomagnetic latitudes ±65°, and the time over the auroral regions is used for maintenance of the satellite.

There are two operational modes of data recording: survey and burst. When DEMETER is not over sensible zones (seismic zones, VLF transmitters, special experiments, etc.) it operates on survey mode, and the amount of recorded data (number of components, sampling frequency, waveforms) is sensibly lower (25 Kbits/s). When DEMETER crosses certain areas, burst mode is activated and its full capabilities of recording are activated, generating 1.6 Mbits/s of data.

Its scientific payload is composed of five different measurement instruments: ICE (Instrument Champe Electrique), IMSC (Instrument Magnetic Search Coil), ISL (Instrument Sonde de Langmuir), IAP (Instrument d'Analyse du Plasma), and IDP (Instrument pour la Detection des Particles). In addition there is an electronic unit (BANT) which processes the data on board and is in charge for telemetering the data to the mission center.

The ICE measures the three components of the electric field by means of four electrodes, each one located at 4 m of the spacecraft with the aid of booms. Since it is the instrument employed for acquiring the data analyzed in this Chapter, it is extensively described in Section 3.1.1.

The IMSC [88] is intended for measuring the magnetic field and is composed of three orthogonal search coil antennae with pre-amplifiers. Each antenna has a permalloy core, and 12,000 turns of copper wire around it. Few additional turns are used as a feedback branch in order to avoid the resonant frequency of the RLC system (see Section 2.1.3.3). Its cross-section is 4 x 4 mm and its length 170 mm.

The ISL Langmuir probe [89] has been designed for in situ measurements of the bulk parameters of the ionospheric thermal plasma, basically the electron density and temperature. In addition, it is possible to infer the ion density and its variation, but with a higher error margin. The parameters are obtained with a resolution equal to 1 s. The instrument is comprised of two sensors: a cylindrical sensor and a spherical sensor subdivided in seven segments. The first sensor is

a typical scalar Langmuir probe [90], based on applying a bias voltage to a conductor immersed in the plasma under study. The second one permits to infer the direction of the electron flow, but it was under test during this mission and was not extensively employed.

The IAP [91] provides measurements of the main parameters of the thermal ion population. It can directly measure disturbances on the plasma caused by seismic events on the ground, and, in addition, it obtains the characteristics of the plasma which are necessary to interpret measurements from ICE and IMSC (e.g., plasma density and ion composition).

The IDP [92] is a electron spectrometer aimed to measure trapped electron fluxes in the energy range from 70 keV to roughly 0.8 MeV, and to provide information on the electron fluxes in the range 0.8 - 2.5 MeV. Its resolution is less than 10 keV. It is intended to study the radiation belts on Earth.

DEMETER mission defines three levels of data: 0, 1, and 2 [93]. The Level 0 data stands for raw data, and are directly the series telemetered by the spacecraft. Level 1 data corresponds to scientific calibrated data, while Level 2 data corresponds to high-resolution displays (i.e. plots of the Level 1 data).

3.1.1 The ICE sensor

The ICE instrument is in charge of measuring the electric field that surrounds the spacecraft. Electromagnetic changes in the ionosphere due to natural disasters have been reported several times (e.g., [6, 30, 31, 94, 95]), and therefore this instrument, together with IMSC, are the most important ones for DEMETER mission. The three components of electric field are recorded over sensible seismic zones (burst mode), in order to be able to reconstruct the $\vec{k}$ vector of the detected electromagnetic waves [96].

In order to measure the three components of the electric field, DEMETER has four electrodes on board. Each of them is disposed at 4 meters from the spacecraft core by means of stacer booms. They are deployed according to Figure 3.2. With this arrangement, it exists some redundancy for reconstructing the radial electric field component, E_r, in case an electrode fails.

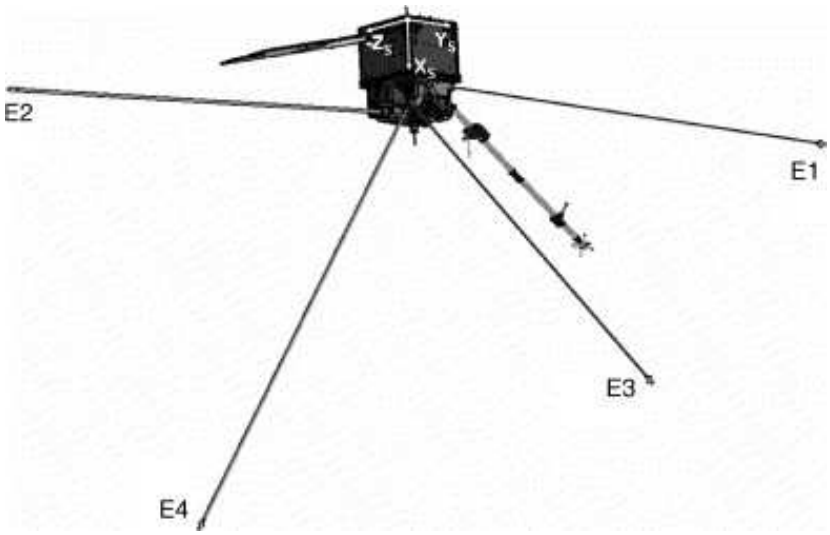

FIGURE 3.2: Electrodes configuration of ICE experiment, taken from [96].

DEMETER has on board attitude control, and therefore the direction X_s (see Figure 3.2) always points to the center of the Earth. -Z_s is the velocity direction of the satellite. In this dissertation, the measurements from E_1 to E_2 electrodes have been employed. They roughly correspond to the East - West direction in the Earth.

Four different channels (depending on the frequency range) are processed by the electronic unit on board. The signals coming from the electrodes are first filtered and then digitized. From the digitized signal, the power spectrum is computed by this unit. Depending on the frequency range, operation mode (survey or burst), and set up from mission center, different spectra and waveforms are stored and telemetered to the Earth. A schema of the general configuration can be observed in Figure 3.3.

DC/ULF (0 - 15 Hz): The waveform of all electrodes is digitized with sampling frequency f_s=39.0625 Hz and 16 bits resolution, corresponding to sensibility of ∼40 μV/m for electric field measurement. All the data are available for both survey and burst modes.

ELF (15 Hz - 1 kHz): Three channels (E_{12}, E_{34}, and E_r) are digitized with f_s=2.5 kHz and 16 bits. ELF is only available during burst mode.

VLF (15 Hz - 17.4 kHz): Only one channel of the three (E_{12}, E_{34}, or E_r) is computed by the electronic unit, and it is selected by telecommand. The filtered analog signal is sampled at 40 kHz and digitized with 16 bits. The power spectrum

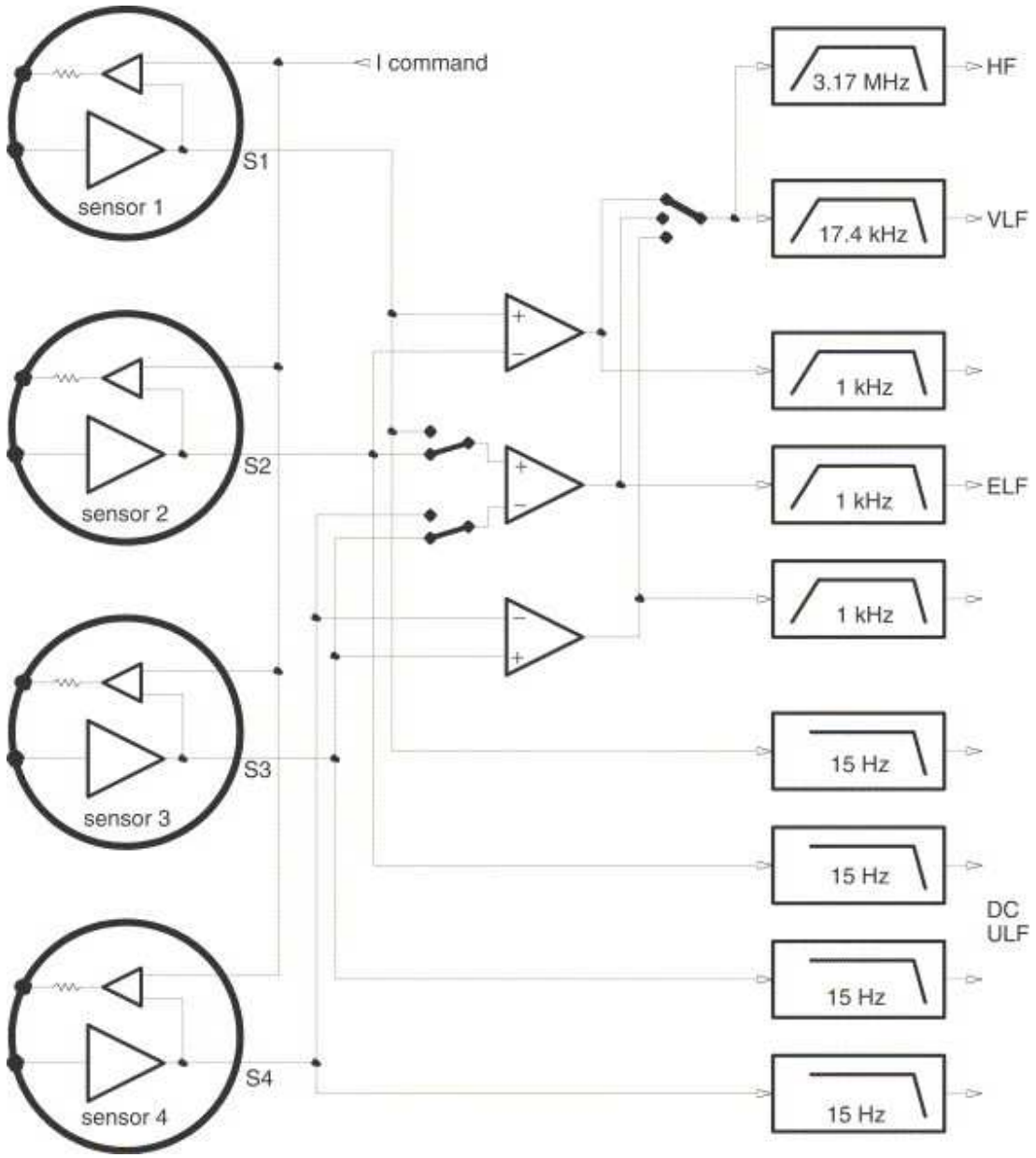

FIGURE 3.3: Schema of electronics involved in processing ICE measurements, taken from [96].

is computed on board with 19.53 Hz frequency resolution. Then, 40 spectra are averaged, providing a final time resolution of 2.048 s. Each averaged spectrum is normalized by its maximum value and telemetered to the Earth with 8 bits resolution. If burst mode is activated, the waveform of the signal is telemetered together with the computed spectra. In survey mode only spectra is telemetered, and there exist three possible configurations. The first is as described above, the second reduces time resolution to 0.512 s (only 10 spectra averaged), and the third reduces frequency resolution to 78.125 Hz by averaging over 4 consecutive frequencies. In

this work only data from the first configuration have been employed, because it was the default configuration for the major part of the mission. In Figure 3.4, a spectrogram constructed from VLF data can be observed.

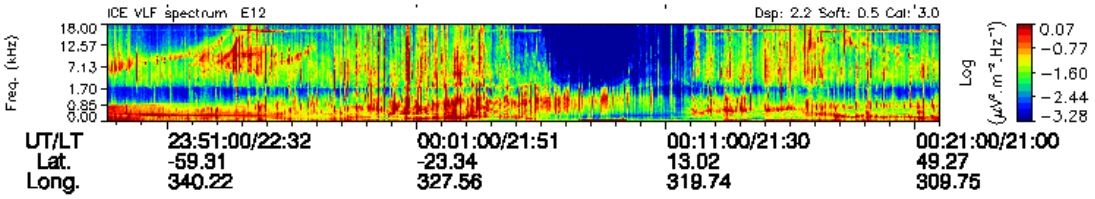

FIGURE 3.4: ICE - VLF spectrogram of October 1, 2010 (nighttime), recorded by DEMETER.

HF (10 kHz - 3.175 MHz): Only one channel is available, the same as selected for VLF channel. The signal is sampled with 6.66 MHz and digitized with 8 bits. Then, 40 data snapshots 0.6144 ms long each are used to compute 40 individual power spectra on board every 2.048 s (the elementary interval of VLF records). The spectra (frequency resolution of 3.25 kHz) are averaged, thus resulting in one averaged power spectrum every 2.048 seconds. In burst mode, in addition to the averaged spectrum, one waveform of the 40 is also telemetered. It is either the first or the one with the strongest power (selected by telecommand). In survey mode, only the spectra are telemetered and there are three possible configurations, according to VLF configuration: one spectrum every 2.048 s, one spectrum every 0.512 s, and 13 kHz frequency resolution spectrum (instead of 3.25 kHz) every 2.048 seconds.

3.2 Detection of the waveguide 1st cut-off frequency

The surface of the Earth and the lower ionosphere are both conductive in the ELF-VLF bands. The gap between the two conductive spheres contains air, the atmosphere. When considered as a whole, we talk about the Earth-ionosphere cavity or waveguide. While the lower boundary of the cavity is sharp and well defined, the conductivity increases with height at the upper boundary, which means that this interface is not clearly defined. It mainly depends on the electron and neutral density profiles, which are affected by several parameters such as local time, solar activity index, or geomagnetic field [21].

Due to the geometry of the cavity, i.e. large but thin, it behaves in different manner for different frequency ranges of waves, originated mainly due to thunderstorms. In the ELF band, where the wavelength, λ, is on the order of the Earth's circumference, it acts as a resonator, accommodating standing waves which are present in the whole cavity. These are the well known Schumann Resonances (SR) [10, 12], which correspond to TM modes of the cavity, introduced in Chapter 1 and studied in Chapter 2.

In addition, it also behaves as a waveguide in the VLF band, where λ is on the order of the separation, h, between the two conductive spheres. This waveguiding effect can be approximated, on a first approach, by conducting parallel plates. This effect is local and the generated signals travel a certain distance from the source before vanishing due to losses. These signals in the waveguide are known as atmospherics, or sferics [44, 97]. Sferics suffer multiple reflections between the two conductive spheres, and its n-th mode cut-off frequency can be related, according to Chapter 1, to the effective height of the ionosphere (h) by $f_n = \frac{nc}{2h}$, where c is the speed of light in vacuum, n is the cut-off frequency mode number, and f_n the associated cut-off frequency of the mode. The first cut-off frequency is around 1.7 kHz, corresponding to an effective height of $\sim$90 km.

Below the cut-off frequency, only the TEM mode can propagate. For frequencies above the cut-off, the TM and TE modes also propagate, their attenuation being maximum right at the cut-off frequency [98]. Therefore, there is a detectable minimum of energy in the atmospheric spectrum for this frequency. Cummer [18] employed the numerical method of Finite Differences in Time Domain, or FDTD [99], in order to simulate sferics propagation in the Earth-ionosphere waveguide, his results being consistent with this minimum of energy at the cut-off frequency.

The principal source of excitation of the cavity at these frequencies is lightning. This fact enables the interest of studying the resonances for global climate analysis [5], and, since they contain information of thunderstorm activity [1], they can be a tool to study thunderstorms and the dynamics related to them.

3.2.1 Methodology for cut-off frequency finding

In order to draw global maps of the cut-off frequency, a grid step must be chosen. We have worked with grid steps ranging from 1° to 5°. Then a time interval (e.g.,

one month or one season) is selected. Once these parameters are fixed, we take all the available nighttime spectra in DEMETER database which pertains to the cell and average them. Ionospheric conditions are highly dependent on local time, due to the influence of solar wind. Nighttime ionosphere is much more stable and predictable, and the measurements are less noisy. This is the motivation to use only night spectra.

Level 1 VLF-ICE spectra are expressed in $\log(\mu V^2 m^{-2} Hz^{-1})$. The first step realized was to linearize them, by applying to each spectrum:

$$S_{linear}[f] = 10^{S_{l1}[f]} \quad [\mu V^2 m^{-2} Hz^{-1}], \tag{3.1}$$

where S_{linear} is the linear spectrum, and S_{l1} is the Level 1 spectrum we want to linearize. The measurements exhibit high variable average power. For the purpose of location of the position of a minimum of energy in frequency domain, we want all the available spectra to contribute, so it is necessary to normalize them by its mean power:

$$S_{Norm}[f] = \frac{S_{linear}[f]}{\langle S_{linear} \rangle}, \tag{3.2}$$

where S_{Norm} stands for the normalized spectrum, and the angle brackets denote the mean value of the whole spectrum.

The next step is to average all the spectra which belong to the same grid cell:

$$S_{cell}[f] = \frac{1}{N} \sum_{n=1}^{N} S_{Norm,n}[f], \tag{3.3}$$

where S_{cell} is the final averaged spectrum for the cell, and $S_{Norm,n}$ are the corresponding independent normalized spectra which belong to the grid cell.

Each spectrum S_{cell} is then smoothed by a digital Low Pass Filter (LPF). The purpose of this step is to prepare the data for automatic detection of minima [100]. The filter employed is of constant ripple in its attenuated band. It has 47 degrees of freedom, and it reduces by 60 dB in its attenuated band. Its transition band goes from 0.075 to 0.175 (frequency normalized to 1). Both its waveform (top) and Bode diagram (bottom) can be observed in Figure 3.5.

An algorithm of minima detection, based on comparison with nearby samples, is then applied to the smoothed spectra. All the local minima should be found by the algorithm. An example of detection is shown in Figure 3.6. The found minima

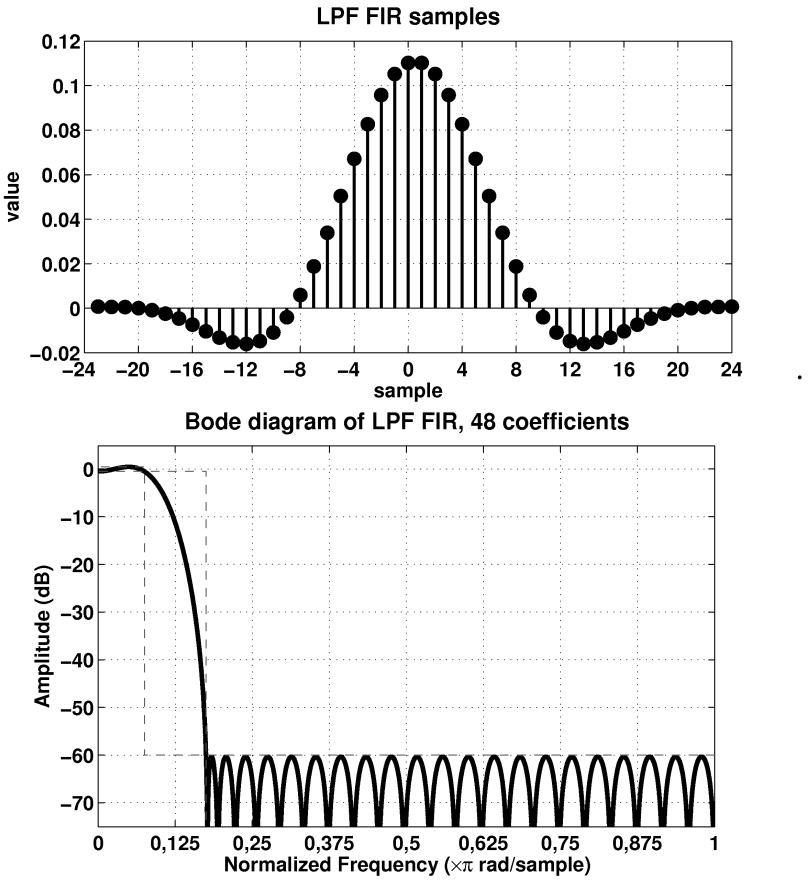

FIGURE 3.5: Waveform (top panel) and Bode diagram (bottom panel) of digital FIR LPF employed for smoothing the averaged spectra.

are classified in two groups: those under 1.4 kHz and those above. The first group is disregarded, since they do not correspond to the cut-off frequency. If there is more than one minimum in the range 1.4 - 2.0 kHz, or if the first minimum is above this range, the cut-off frequency is considered as non-detectable for that spectrum. Otherwise the minimum in the range 1.4 - 2.0 kHz is taken as the cut-off frequency for the corresponding grid cell.

3.2.2 Calculation of electron density at effective reflection height

The technique described above permits to obtain the value of the first cut-off frequency for an arbitrary area of the globe, and for an arbitrary time span. As it is shown in Equation 1.2, the effective reflection height can be obtained from the cut-off frequency. It is possible from these values to infer the electron density at the effective height. In order to do that, it is necessary to know the neutral

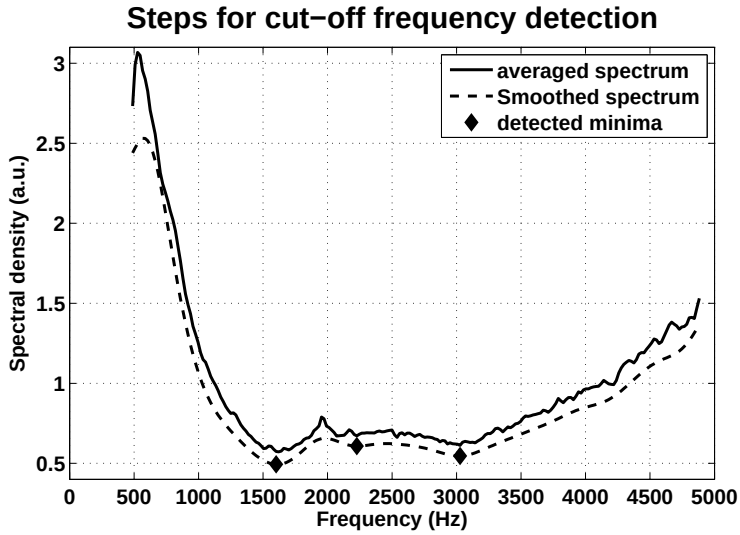

FIGURE 3.6: Results at the different steps of detecting the cut-off frequencies.

density (N_n) at the altitude of interest. This parameter has been extracted from the empirical model MSIS [101, 102], which will be introduced in Section 3.2.4.

Following Ratcliffe [103], the reflection of the wave in the ionosphere occurs when

$$\omega_p^2 = \omega\nu, \tag{3.4}$$

where ω_p is the angular plasma frequency, ω is the angular frequency of the wave, and ν is the collision frequency of the plasma. This last parameter depends only on the electron mobility μ_e

$$\nu = \frac{q_e}{m_e\mu_e}, \tag{3.5}$$

where q_e is the electron charge and m_e its mass. In Pasko et al. [104], the following expression relating the electron mobility to the density of neutrals is given:

$$\mu_e = \frac{1.36N_0}{N_n}, \tag{3.6}$$

where N_n is the neutral density and N_0 is $2.688{\cdot}10^{25}$ m^{-3}, i.e. the neutral density under standard conditions at the surface of Earth. This expression will be used to obtain the collision frequency from the neutral density given by the MSIS model. Then, the electron density (N_e) at the effective height can be inferred from

$$f_p = \frac{1}{2\pi}\sqrt{\frac{q_e^2 N_e}{m_e\varepsilon_0}} \approx 8.978\sqrt{N_e}, \tag{3.7}$$

where f_p is the plasma frequency in Hz and N_e the electron density in m^{-3}. This expression is valid for cold plasmas [103]. With this method, it is possible to interpret the effective height in terms of ionospheric electron density. Finally, the effective conductivity (σ_e) at the reflection height can also be obtained:

$$\sigma_e = \frac{N_e q_e^2}{m\nu} = q_e N_e \mu_e = N_e q_e 1.36 N_0/N_n. \tag{3.8}$$

3.2.3 Results

A data set from ICE (E_{12}, which corresponds to electric field measured in the East - West direction) which comprises since January 2006 till February 2010 (i.e. roughly 20,000 nighttime half-orbits) has been analyzed, by the techniques described above. The study reveals changes in the effective reflection height according both to seasons as well as to the kind of Earth's surface.

First, we examined the data in month time windows, and we found certain patterns which tended to last for several months every year, and repeating over the years. This motivated to perform a monthly grouping along years, as well as a seasonal grouping of the data, in order to have better spatial resolution of the observed variations.

In Figure 3.7, the data of same months is averaged along the four years referred before. This averaged year evolution reveals different behaviors of the effective reflection height for different geographical areas. In general terms, it can be noted that the effective reflection height is of lower value for the northern hemisphere cold season, i.e. roughly from November to March. This shift is more prominent at the ocean, but it can be observed in land areas as well. There is a great exception over eastern Asia and over western Pacific Ocean, where no shift can be appreciated with season. The shift observed is in the order of 5 - 10 km.

The most prominent seasonal effect over the effective reflection height occurs at the Pacific Ocean, only in the Southern Hemisphere (area roughly comprised between latitudes -60° to 0° and longitudes 180° to 280°, see Figure 3.9). In this area, the effective height takes values higher than 100 km between May and September, for the higher latitudes. It decreases to ∼90 km from November to March for the same latitudes. At the lower latitudes (roughly -30° to 0°) of the area defined above, the effect is similar but the threshold value of the effective

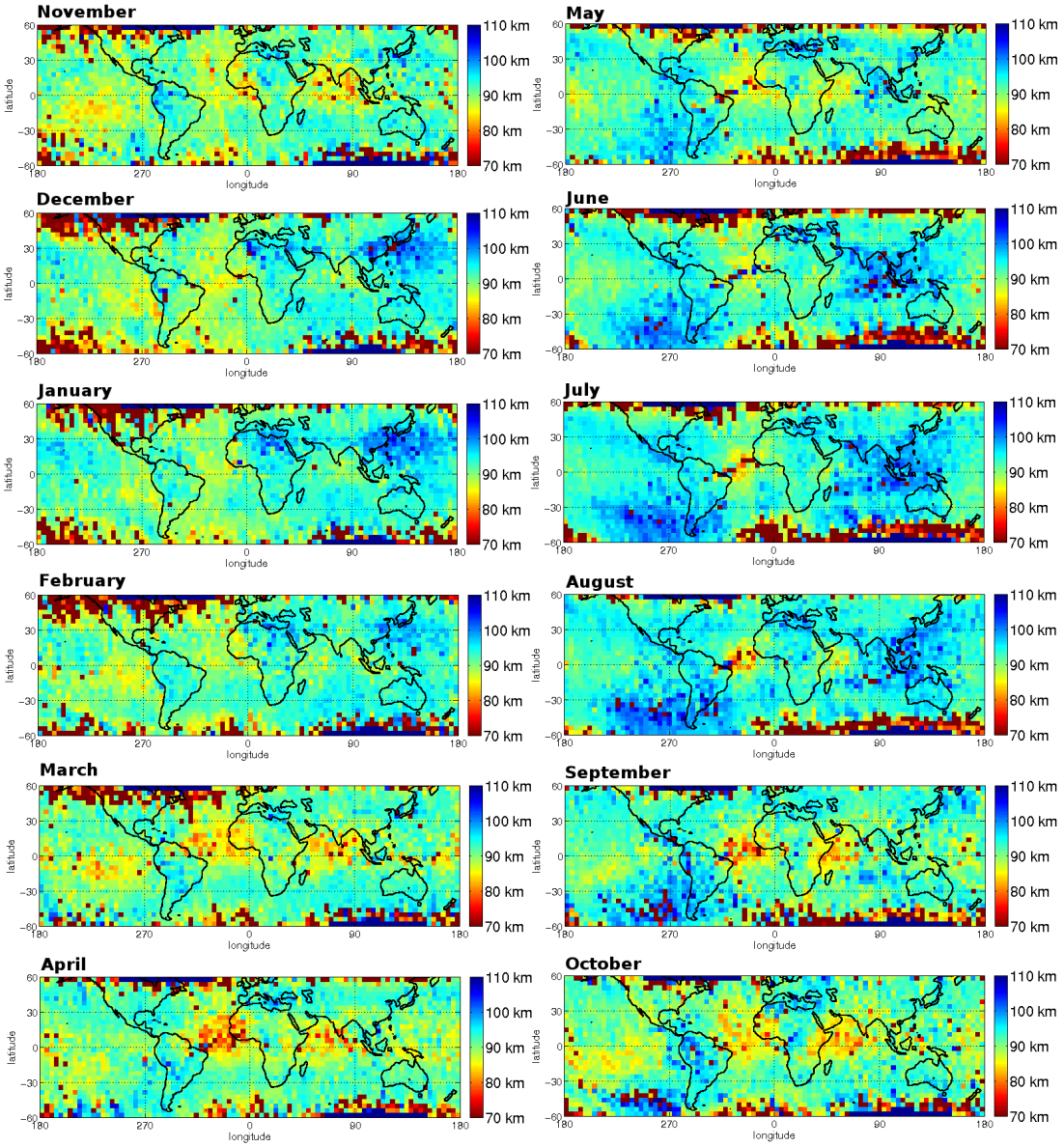

FIGURE 3.7: Map of the effective height for different months averaged among four years. Left column corresponds to northern cold season, and right column to northern warm season.

height is lower, shifting from ∼90 km in southern cold season to ∼85 km for the local warm season. It is interesting to note that this shift appears in the four years of the study (see Figure 3.8). Owing to its seasonal nature, we believe that this shift must be related to the change of solar irradiation between seasons, and/or changes in the thunderstorm pattern.

Another registered variation occurs at equatorial latitudes, for both the Atlantic and the Indian Oceans. Although these two oceans are separated by the African continent, they shift their effective height accordingly two times per year.

The epicenters of these disturbances are located at roughly (0°, 340°) for the Atlantic Ocean, and at (0°, 80°) for the Indian Ocean. At the epicenters of this disturbance, the effective height is of lower value (around 88 km) during all the months. The area where the effective height exhibits this lower value considerably increases during the months March - April and again during September - October, being the low effective height area 2 - 4 times bigger than for the rest of the months. The region where this variation is located for the Atlantic Ocean corresponds to the inter-tropical convergence zone, where the ionosphere presents a maximum of plasma bubbles and is highly variable [105, 106]. Therefore, these results must be taken with caution, since DEMETER ICE sensors may be registering other signals superimposed to the atmospherics. However, it is still intriguing the apparent connection between the measurements at the Atlantic and Indian Oceans.

Several red points (out of scale) can be noticed in Figures 3.7 - 3.10. As we explained before, there are situations where our algorithm fails to properly detect the minimum of energy associated to the cut-off frequency. The red points indicate either that more than one energy minimum was found on the frequency range 1.4 - 2 kHz, or that the first minimum is above this range. This automatic energy minimum detection on the VLF spectra mainly fails when the intensity of the natural waves coming from above the spacecraft exceeds the intensity of the atmospherics propagating in the Earth-ionosphere waveguide. It can be seen, from Figure 3.7, that it mainly occurs at high latitudes, where waves like VLF auroral hiss, chorus, or lower hybrid electrostatic noise are preponderant.

These red points appear also in the Atlantic Ocean region between Brazil and Cape Verde. The explanation here, as commented before, is that this area corresponds to the inter-tropical convergence zone, where the ionosphere is highly variable and presents a maximum of plasma bubbles. At this location, DEMETER records disturbed electric field.

We have grouped the months by seasons in order to better see the shift of the effective height over the Pacific Ocean. For each year of the study, we have averaged two periods: May - September and November - March. The results are depicted in Figure 3.8. It can be observed that the shift mentioned above over the Pacific Ocean occurs every year, being its nominal value and location very similar. It is also interesting to note, on this Figure, that the shift for the months November to March is abruptly disrupted at the western South American coast,

the effect appearing in the four years. On the other hand, this behavior is not observed for the months May to September.

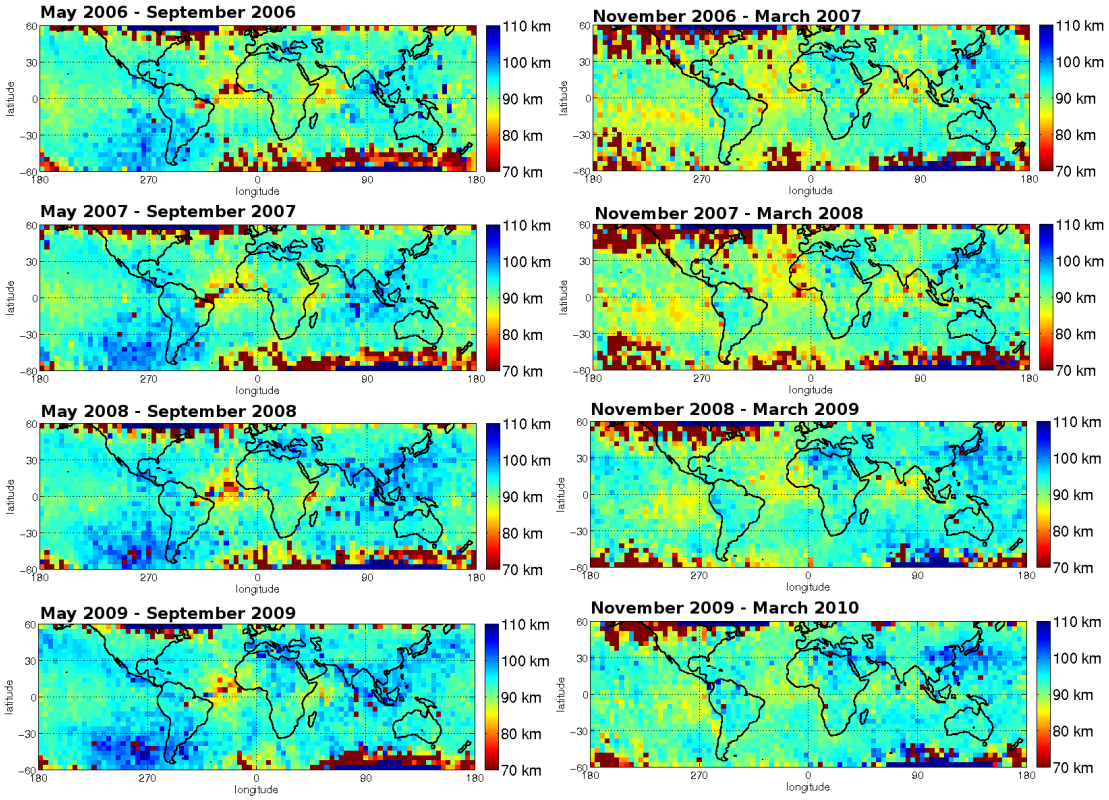

FIGURE 3.8: Map of the effective reflection height for different seasons and years. Left column corresponds to northern cold season (November - April), and right column to northern warm season (May - October). A seasonal effect which repeats every year can be observed.

Finally, we have averaged the seasons shown in Figure 3.8, grouping them in two blocks: the northern warm season and the northern cold season (see Figure 3.9). The shift over the Pacific Ocean can be observed again. In addition, the northern winter plot (bottom panel) reveals that the effective reflection height has lower value around the geomagnetic equator, predominantly over ocean areas.

The observed shifts occur predominantly, although not sharply limited to, over the ocean. Certainly we do not have a clear explanation for that, but we can mention several hypotheses to explain this difference:

1. It is known that aerosols have an effect on the global electric circuit (for the definition of the global electric circuit, see for example the review by Rycroft et al. [107], Williams [108]). The values of the electric field in the global circuit differ between ocean and land measurements and this discrepancy

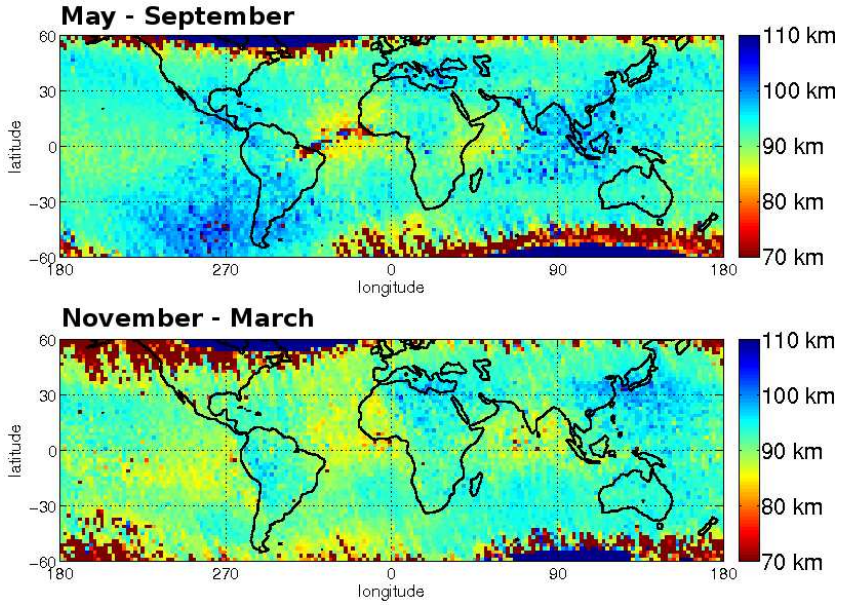

FIGURE 3.9: Map of the effective reflection height for the averaged seasons among four years (2006, 2007, 2008, and 2009).

is attributed to differences in aerosol and associated air conductivity [109]. This result is due to polluted conditions over land [110, 111]. This effect can change the current in the global electric circuit and may affect the cut-off frequency. Another possibility is the effect that sea salt aerosols can have over the atmosphere [112]. Large clouds of this kind of aerosol can induce modifications of the electrical properties of the Earth ionosphere waveguide. This possibility would also explain why the frontiers of the cut-off frequency shift are not sharply related to the coast line in general. There is one place where the border of the shift roughly coincides with the coast line (see Figure 3.9, bottom panel); the western coast of South-America. Along this coast line is the Andes Cordillera, which is a natural barrier for wind and, therefore, for aerosols [113].

2. The effect of the thunderstorm activity because it is known from the Optical Transient Detector experiment that the occurrence of thunderstorms is less important above oceans than above land [25]. This cannot be an artifact in our detection method because this method is independent of the number of whistlers. But the thunderstorm activity also modifies the global electric circuit. Using a model, Pasko et al. [104] claimed that Positive Cloud-to-Ground (+CG) discharges can lead to large electric fields and to the removal of large quantities of charge from ionospheric altitudes (see also Pasko et al. [114], Füllekrug [115], and the review paper by Inan et al. [116]). However,

Rycroft et al. [117] concluded that the contribution of +CG or Negative Cloud-to-Ground (-CG) strokes to the global electric circuit is not significant relative to conduction and convection currents associated with electrified thunderclouds to maintaining the ionospheric potential. It remains that the electron density at the bottom of the ionosphere can be globally different above oceans and above land because thunderstorms are not so numerous above oceans.

3. The effect of some Transient Luminous Events (TLE) (e.g., elves, red sprites, blue jets, etc.) due to powerful lightning strokes. A simulation of the effect of these strokes has been made by Rodger et al. [118] which shows increases in the electron density of the lower ionosphere, with the largest increases at ∼90 km altitude. The study carried out by Mende et al. [119] indicates that elves can ionize the upper atmosphere and that it could be a significant source of ionization in the low- to mid-latitude nighttime D region. Later on, Chen et al. [120] have shown that occurrence of elves is much more important above oceans than above land. They also determined that the total electron content at the lower ionosphere above elve hot zones can be increased by more than 5%. This can also contribute to a decrease of the bottom height of the ionosphere over oceans.

Since the electromagnetic source for the excitation of the cavity is lightning, our results must contain information about the global lightning patterns as well. In Gemelos et al. [121], the spectral electric field intensity in the range of 5 - 10 kHz (measured by DEMETER) is related to energetic electron precipitation due to lightning. Their results are in good agreement with our maps for the different seasons. By observing their seasonal maps it can be noticed that an increase on electric field intensity on the mentioned range corresponds to a decrease of the cut-off frequency and vice versa.

As described in Section 3.2.2, it is possible to calculate the electron density as well as the conductivity at the effective reflection height obtained from the first cut-off frequency value. These results have been plotted in Figure 3.10, for the corresponding effective heights of Figure 3.9. The necessary value of neutral density was obtained from MSIS model.

Monitoring the cut-off frequency in order to extract the mentioned parameters can provide valuable information about the waveguide properties since it is a tool

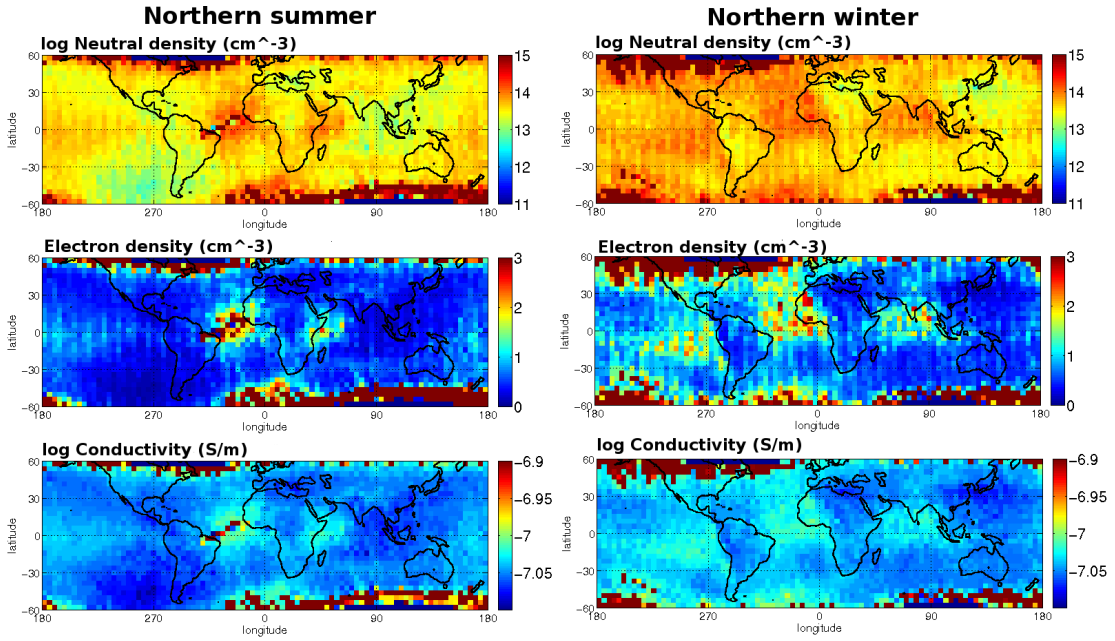

FIGURE 3.10: Map of neutral density, electron density, and conductivity at effective height. The values correspond to the seasonal average (May - September for northern summer and November - March for northern winter) of years 2006 - 2009. The density of neutrals was obtained from MSIS model for the corresponding effective height shown in Figure 3.9. Then, the electron density and conductivity are calculated.

to effectively remote sensing the lower D-region of the ionosphere [122, 123]. Direct relation between the cut-off frequency and the electron density is shown by Shvets and Hayakawa [124] and Ohya et al. [125]. This region of the ionosphere is one of the less observed regions, due to the fact that in-situ measurements could not be done because this region is too high to be reached by balloons and too low for satellite orbits. Therefore, information from this region must be obtained by remote sensing, which is done with satellites as well as with ground-based radars, natural or man-made VLF waves, and optical measurements (e.g., [123]).

By looking at Figure 3.8, it can be noticed that there is a general decrease of the cut-off frequency over the four years. It can be observed at northern cold season plots, for ocean areas near the geomagnetic equator. Winter plots at these areas show decreasing average values for the cut-off frequency (i.e. increasing reflection heights) from 2006 to 2009. We explain this behavior due to the decreasing solar activity, measured by means of F10.7 index, along these years, extensively reported by Solomon et al. [126].

The F10.7 index is a measure of the solar radio flux per unit frequency (i.e.

noise produced by the Sun) at a wavelength of 10.7 cm at the Earth, often expressed in solar flux units. At this wavelength, the radiation arriving the Sun ionizes the ionosphere. It is an excellent indicator of overall solar activity levels, and there exist records of it since 1947. It is a basic parameter for space weather models.

Lower solar activity implies lower electron density at the ionosphere, thus increasing the effective height of the ionosphere and lowering the cut-off frequency. In order to confirm that, we calculated the global average value (all valid points between ±60° latitude) of the effective height for each month of 2006 - 2009. Then a 13-month running average was computed in order to minimize the seasonal effects described above. In Figure 3.11, this result is compared with the 13-month Zurich average [127] of the F10.7 cm solar flux parameter, extracted from *http://http://sail.msfc.nasa.gov/*. It can be observed that during the major part of the time span both parameters decrease, except for the last six months where the solar flux parameter starts increasing. The ripple of the average cut-off frequency curve is caused by the seasonal patterns described above. Although a time span larger than 4 years is required to confirm that, the Figure 3.11 suggests that it may be possible to use the global cut-off frequency of the Earth-ionosphere waveguide as a proxy for the solar activity.

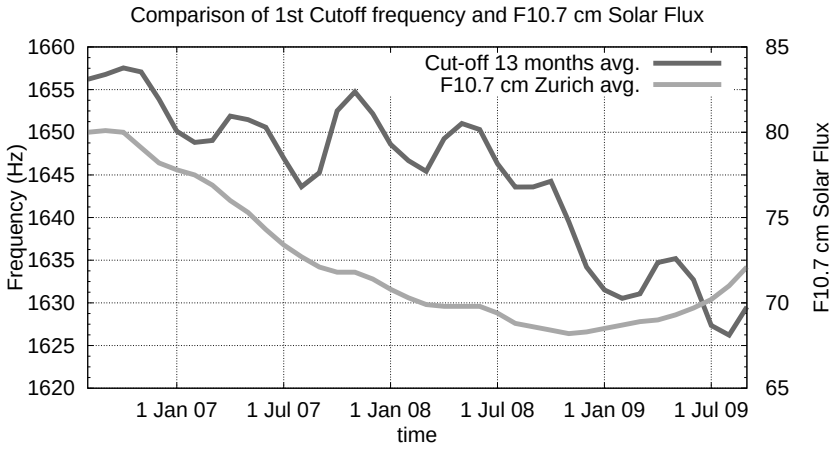

FIGURE 3.11: Comparison of F10.7 cm solar flux and global cut-off frequency detected by DEMETER. The global cut-off is calculated each month for the entire globe (latitude ±60°) and then a 13-month running average is plotted, in order to minimize seasonal effects. F10.7 cm solar flux index is also a 13-month running average, documented in [127].

3.2.4 Comparison with IRI and MSIS models

IRI stands for International Reference Ionosphere [128–130], and it is an empirical model which is the international standard for values of electron density, electron temperature, ion temperature, total electron content, and ion composition in the non-auroral ionosphere for magnetically quiet conditions. It comprises values for the mentioned variables in the range between 50 and 2,000 km of altitude. It does not rely on theoretical assumptions but, instead, its data is inferred exclusively from empirical measurements. The major data sources are the worldwide network of ionosondes [131], the powerful incoherent scatter radars (Jicamarca, Arecibo, Millstone Hill, Malvern, St. Santin) [132], the ISIS and Alouette topside sounders [133], and in situ instruments on several satellites and rockets. It is maintained by a workgroup sponsored from both URSI (International Union of Radio Science) and COSPAR (Committee On Space Research).

The Mass-Spectrometer-Incoherent-Scatter (MSIS) model [102, 134] describes the neutral temperature and densities in the upper atmosphere. Data sources include measurements from several rockets, satellites (OGO 6, San Marco 3, AEROS-A, AE-C, AE-D, AE-E, ESRO 4, and DE 2), and incoherent scatter radars (Millstone Hill, St. Santin, Arecibo, Jicamarca, and Malvern) [132]. The model expects as input year, day of year, Universal Time, altitude, geodetic latitude and longitude, local apparent solar time, solar F10.7 flux, and magnetic Activity (Ap) index. For these conditions the following output parameters are calculated: number density of He, O, N_2, O_2, Ar, H, and N, total mass density; neutral temperature and exospheric temperature.

It is the first time that the first cut-off frequency, and its corresponding effective reflection height of the Earth-ionosphere waveguide is extensively inferred over the whole Earth, including ocean areas, and therefore there are not experimental data to compare with. The International Reference Ionosphere model, which is of empirical nature, do not contain much information about D and E regions of the ionosphere, owing to this lack of measurements, as stated in Bilitza and Reinisch [128]. The measurements employed to build the model correspond mainly to incoherent scatter radar systems and data from rockets. Therefore, the information is reduced to a very small dataset over land areas, and no data from above the oceans are available.

The results of computing the boundary layer between D and E regions, for the two seasons of 2007, from the IRI model is depicted in Figure 3.12. It was computed with the Fortran code available at *http://nssdcftp.gsfc.nasa.gov/models/ionospheric/iri/*. the boundary has been calculated at 22.30 LT, the time at which DEMETER collects data, owing to its Sun-synchronous orbit. It can be seen that the only changes that can be observed depend basically on the latitude and they are caused by the angle between the Earth's equator and the position of the Sun.

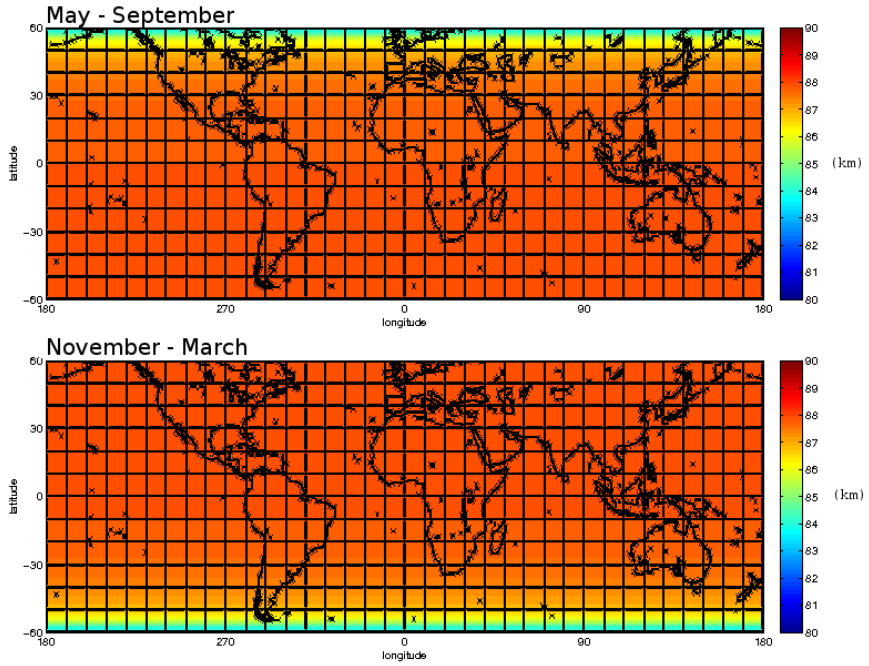

FIGURE 3.12: Map of the height of the boundary between D and E region calculated with IRI 2007 model.

We calculated the effective reflection height maps for each month (2006 - 2009) based on models IRI, to obtain the electron density profile, and MSIS, to obtain the neutral density profile. From them, we obtained the altitude at which the condition from Equation 3.4 is satisfied. In Figure 3.13 the results for the year 2006 are depicted. Other years yield similar maps. All the calculations are made at 22.30 LT, the time at which DEMETER gathers data. It can be observed that the models do not contain information about the seasonal shifts detected in our measurements and described in Section 3.2.3. It is also interesting to note that the model predicts total shifts of no more than 3 - 4 km, while the maps from Figure 3.7 contain shifts greater than 10 km.

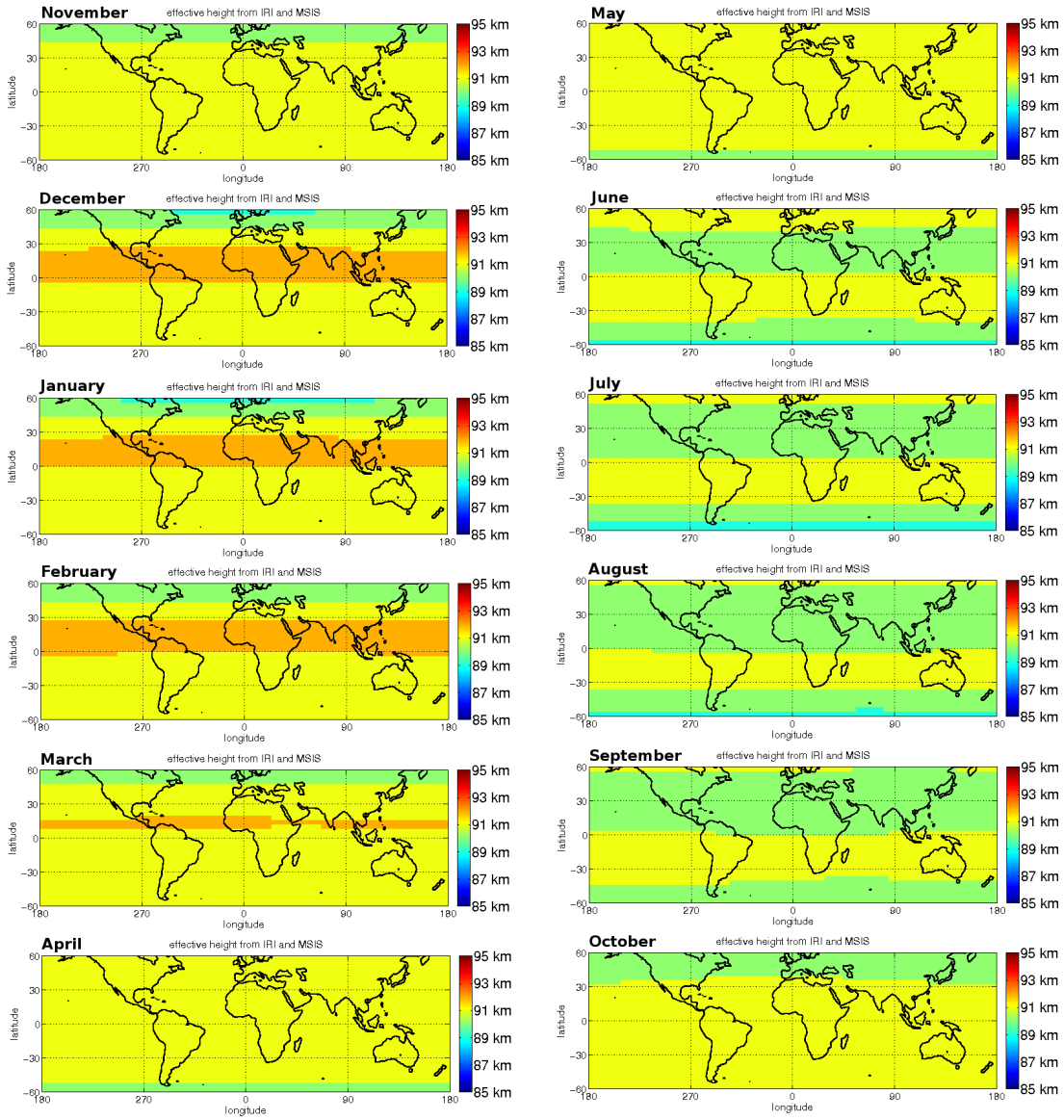

FIGURE 3.13: Map of the effective reflection height at 22.30 LT, calculated with IRI+MSIS models.

3.3 Conclusion

A large data set of electric field measurements from DEMETER has been employed to draw average maps of the effective reflection height with dependence of geolocation. There exist previous works which use the cut-off frequency to calculate the effective height of the Earth-ionosphere cavity from ground observations, e.g., [135–137], but it was never done before, to the knowledge of the authors, by using data taken from spacecraft. This technique has the clear advantage of monitoring most of the surface of Earth. Ground based studies of the cut-off frequency can only obtain averaged values along the path that the atmospheric

wave followed (from source to point of observation), while measurements at the satellite are directly related to the ionosphere conditions in the vicinity of the measurement point. Thus, we present detailed maps (up to 2° resolution) over the whole Earth (±60° latitude) for the effective reflection height of the ionosphere or the D-region altitude, which is inversely proportional to the cut-off frequency. From these measurements, it is possible to infer the electron density as well as the conductivity at the effective height, although it is necessary to extract the neutral density parameter from a model, MSIS in this case.

The main result of this study is that we observe, during nighttime, certain seasonal patterns (mainly over the oceans), which repeat over the four years of the study, for the effective reflection height of the ionosphere. In addition, we suggest that the global cut-off frequency could be used as a proxy of the solar activity.

Chapter 4

The Transmission-Line Matrix method (TLM)

In this chapter, the TLM method is described and analyzed, together with its advantages and drawbacks with respect to other time domain methods. The method is introduced and an historical review of its advances follows. This review permits to get introduced to the method in a gradual way, starting with the simplest 2D nodes, and finishing with the formulation for the 3D symmetrical condensed node, which enables the study of heterogeneous anisotropic media. Other aspects, such as the source modeling or the boundary conditions implementation are also discussed. Finally, we justify the election of this method in order to model Earth-ionosphere cavity in the following chapters.

4.1 Introduction

The use of electrical networks for solving differential equations is a well-known technique for scientists and engineers. For instance, the oscillating movement of a mass connected to a string is often studied by means of an equivalent RLC circuit in which a simple analogy can be established between the mechanic and the electric quantities. In this manner, the knowledge of one of the solutions allows a direct knowledge of the solution for the other problem.

Harmonic oscillation is essentially a non-propagating local phenomenon which can be solved by an analogous electric circuit. The study of propagating phenomena through equivalent networks is conceptually equivalent but now the circuits must be defined in terms of transmission lines. The reason for this choice is that transmission lines are able to take into account all the phenomena underlying in propagation phenomena: delays, transmission, reflection, etc. Effectively, ideal transmission lines are defined in terms of two parameters, capacitance and inductance per unit length, C and L, respectively, or, alternatively, transmission line speed, $v_l{=}1/\sqrt{CL}$, and characteristic impedance $Z{=}\sqrt{L/C}$ (or characteristic admittance $Y{=}1/Z$). The transmission line speed allows defining wave propagation delays, while the characteristic impedance or admittance allows defining the transmission and reflection coefficients required to describe wave propagation at interfaces.

The solution of Maxwell equations using electric networks was already proposed in the 1940s by Kron [138], Whinnery et al. [139]. The concepts in this work seem to be the basis for Johns and Beurle to develop a conceptually new numerical algorithm in 1971 [140]; the Transmission Line Matrix Method or TLM method. This method is a numerical approach, devised in the time domain, which has been extensively used since then for the computer simulation of wave propagation problems, mainly of an electromagnetic nature, but also for problems in acoustics or particle diffusion [141–143]. The method is not only a numerical model for solving certain phenomena, but most of all, it is a conceptual algorithm that does not solve approximately the analytical equations governing the phenomenon, but deals directly with the original phenomenon by means of an equivalent transmission line circuit, instead. This conceptual nature of TLM makes this method a powerful tool which allows considering challenging problems from a hybrid numerical-conceptual point of view in an elegant and suitable way.

The TLM method sets up a spatial and time discretization associating to each elementary volume of the original medium to model, an equivalent cell unit or TLM node. The electromagnetic properties of the TLM node, namely: capacitance, conductance, electric or magnetic resistance, must be equivalent to the elementary volume of actual medium for each spatial direction. Thus, the TLM nodes constitute a transmission line network where voltages and currents behave similarly to the electromagnetic fields in the original system. Defined the node, the difficult task, the TLM algorithm is quite simple. The delay at the transmission

lines comprising the node and its size define a time delay or time step, Δt, which, together with the node size, controls the valid frequency band for the time domain solution. Space and time are discretized according to the node size and this time step. For the n-th time calculation, $t{=}n\Delta t$ and a set of voltage pulses represented by a column matrix V_i^n are incident at each node in the TLM mesh, which after scattering at the node center, produce a set of reflected pulses represented by a column matrix V_n^r. The two pulse sets are related by the scattering matrix of the node, S, by equation

$$V_n^r = SV_n^i. \tag{4.1}$$

It is important to note that the details of the node geometry and, thus, of the analogy with the actual medium to model is fully contained in the scattering matrix, S. The rest of the algorithm is basically identical for other nodes or, even, other types of propagation (acoustic, diffusion, etc.).

Reflected pulses propagate through all the lines in the nodes and become incident pulses at neighbor nodes for the next time step. Time synchronism must be imposed for the nodes so that all the voltage pulses in the mesh are simultaneously incident at all node centers at each discrete time $n\Delta t$. As a result, the algorithm provides voltage pulses at all positions and time, which, by means of the analogy can be converted to the desired electromagnetic quantities.

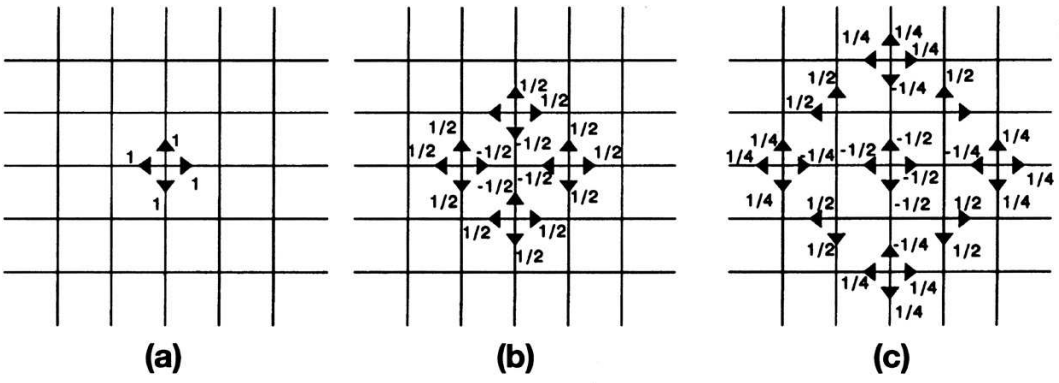

FIGURE 4.1: Dynamics of the TLM algorithm at three consecutive time steps for a mesh formed with 2D parallel nodes.

The dynamics of the TLM method is sketched in Figure 4.1 for a typical two-dimensional (2D) mesh consisting of interconnected parallel nodes that will be described later. Four voltage pulses are launched at a single given node. After propagating during a time step, they reach neighbor nodes, becoming the new

incident voltage pulses, and reflect again at node centers and next time calculation. The process is repeated for each time step.

4.2 Historical review of TLM nodes

4.2.1 Two-dimensional parallel nodes

Since its origin, this method has been developed in different geometries and using different node structures [140, 141, 144]. Initial geometries were devised for dealing with two-dimensional modes at waveguides. Figure 4.2a shows the parallel or shunt node. Four lines of unitary capacitance and inductance C and L, respectively, characteristic admittance Y_0 are connected as shown, in order to model TE_{n0} modes at rectangular waveguides. The 2D geometry of the node, with actual connections between the lines at the node center, allowed considering the lumped element equivalent circuit shown in Figure 4.2b.

The differential equations describing the circuit in Figure 4.2b are:

$$-\frac{\partial}{\partial x}\left(I_{x1}-I_{x3}\right)-\frac{\partial}{\partial z}\left(I_{z2}-I_{z4}\right)=2C\frac{\partial V_y}{\partial t}, \tag{4.2}$$

$$-\frac{\partial V_y}{\partial x}=L\frac{\partial}{\partial t}\left(I_{x1}-I_{x3}\right)=L\frac{\partial I_x}{\partial t} \tag{4.3}$$

and

$$-\frac{\partial V_y}{\partial z}=L\frac{\partial}{\partial t}\left(I_{z2}-I_{z4}\right)=L\frac{\partial I_z}{\partial t}. \tag{4.4}$$

On the other hand, let us consider a TE_{n0} 2D mode for a rectangular waveguide with quantities E_y, H_x, and H_z propagating in y-constant planes. The term defining the mode is not unique in the literature, in our choice, it defines an electric field transversal to the propagation constant-y plane. The partial differential equations defining these modes are:

$$\frac{\partial H_x}{\partial z}-\frac{\partial H_z}{\partial x}=\varepsilon\frac{\partial E_y}{\partial t}, \tag{4.5}$$

$$\frac{\partial E_y}{\partial x}=\mu\frac{\partial H_z}{\partial t} \tag{4.6}$$

and

$$\frac{\partial E_y}{\partial z}=\mu\frac{\partial H_x}{\partial t}. \tag{4.7}$$

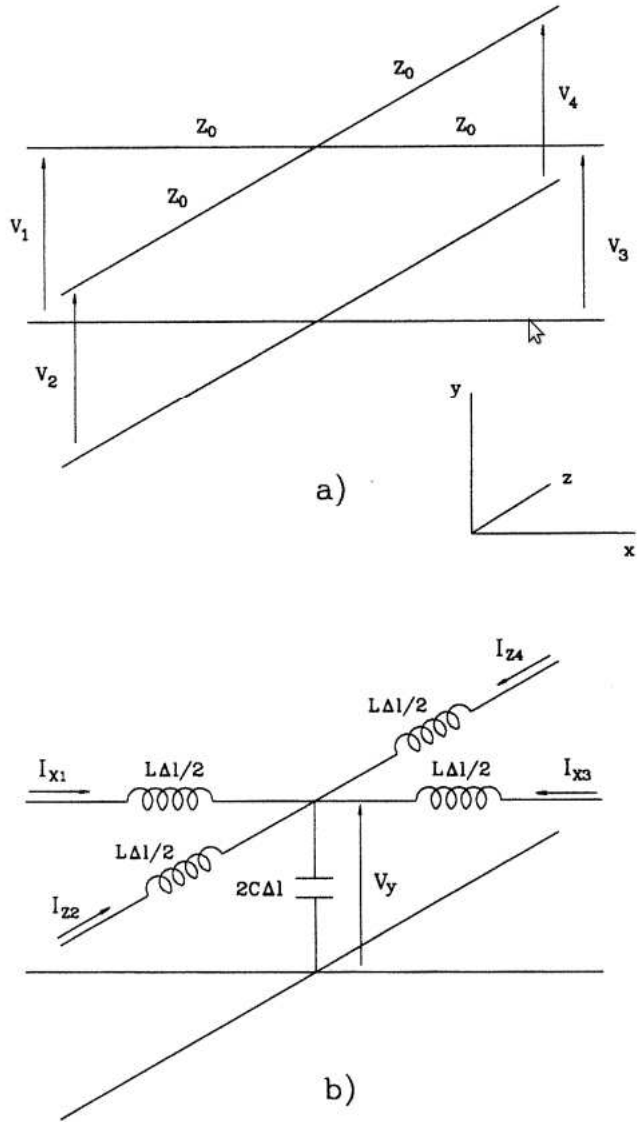

FIGURE 4.2: (a) Topology of the 2D parallel node without stubs, and (b) equivalent lumped-element circuit.

It is direct to notice that both systems of equations are analogous if we identify:

$$E_z \equiv V_z, \qquad H_x \equiv I_y, \qquad H_y \equiv -I_x, \qquad \varepsilon \equiv 2C, \qquad \mu \equiv 2L. \tag{4.8}$$

In other words, the study of the original electromagnetic propagation problem can be carried out by considering how individual voltage pulses propagate through a mesh of connected parallel nodes. This problem is quite simpler if one bears in mind that in its journey through individual lines, only a time delay must be taken into account and that at the node centers, pulses scatter to the different lines.

The existence of an actual circuit for the node in Figure 4.2a allows obtaining

the scattering matrix relating incident and reflected pulses by simply taking into account reflection and transmission coefficients at transmission line discontinuities. For instance, a unitary voltage pulse entering the node through port 1, with a characteristic admittance of Y_0, reaches the center, with a load admittance of $3Y_0$, which means that it will be scattered to all the lines in the node according to the reflection and transmission coefficients, Γ and T, given by:

$$\Gamma = \frac{Y_0 - Y_L}{Y_0 + Y_L} = -\frac{1}{2}, \qquad T = \frac{2Y_0}{Y_0 - Y_L} = \frac{1}{2}. \tag{4.9}$$

Considering incidence from all the lines in the node, the particular geometry of the parallel node without stubs is summarized by expression 4.1 with the scattering matrix being defined by

$$S = \frac{1}{2}\begin{pmatrix} -1 & 1 & 1 & 1 \\ 1 & -1 & 1 & 1 \\ 1 & 1 & -1 & 1 \\ 1 & 1 & 1 & -1 \end{pmatrix}. \tag{4.10}$$

The speed at individual lines, v_l, and at the modeled medium , v_m, will be related through analogy by

$$v_m = \frac{1}{\sqrt{\mu\varepsilon}} = \frac{1}{\sqrt{L2C}} = \frac{v_l}{\sqrt{2}}. \tag{4.11}$$

And, if the node has equal dimensions, Δl, the time step is given by expression $v_l = \Delta l/\Delta t$.

The pulses at four lines connect the node to adjacent node, allowing propagation. These lines are termed main or link lines.

A posterior modification of the node considered the inclusion of a capacitive stub, i.e., an additional open ended line o admittance YY_0 [145]. This line is not connected to adjacent nodes but to the node center. Its aim is not propagation but controlling the capacity of the node and, thus, the permittivity of the modeled medium. The equivalent lumped element circuit is shown in Figure 4.3b but with an extra capacitance, $CY\Delta l/2$ at the center, which makes the modeled permittivity to be:

$$\varepsilon = 2C(1 + Y/4). \tag{4.12}$$

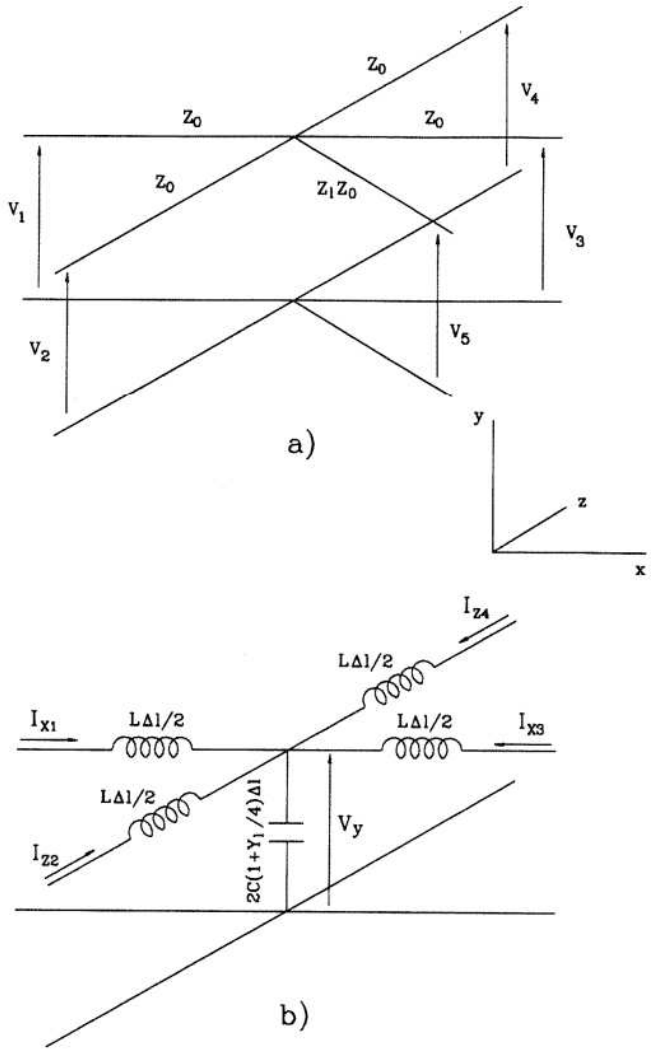

FIGURE 4.3: (a) Topology of the 2D parallel node with stubs, and (b) equivalent lumped-element circuit.

The scattering matrix can be recalculated considering the four main lines and the new extra capacitive stub, to obtain

$$S = \frac{1}{4+Y}\begin{pmatrix} -2-Y & 2 & 2 & 2 & 2Y \\ 2 & -2-Y & 2 & 2 & 2Y \\ 2 & 2 & -2-Y & 2 & 2Y \\ 2 & 2 & 2 & -2-Y & 2Y \\ 2 & 2 & 2 & 2 & Y-4 \end{pmatrix}. \tag{4.13}$$

But, as mentioned above, the important point to be noticed is that the only difference between one and other node relies on the scattering matrix. Once this matrix has been obtained, the algorithm is again summarized by expression 4.1.

4.2.2 2D series nodes

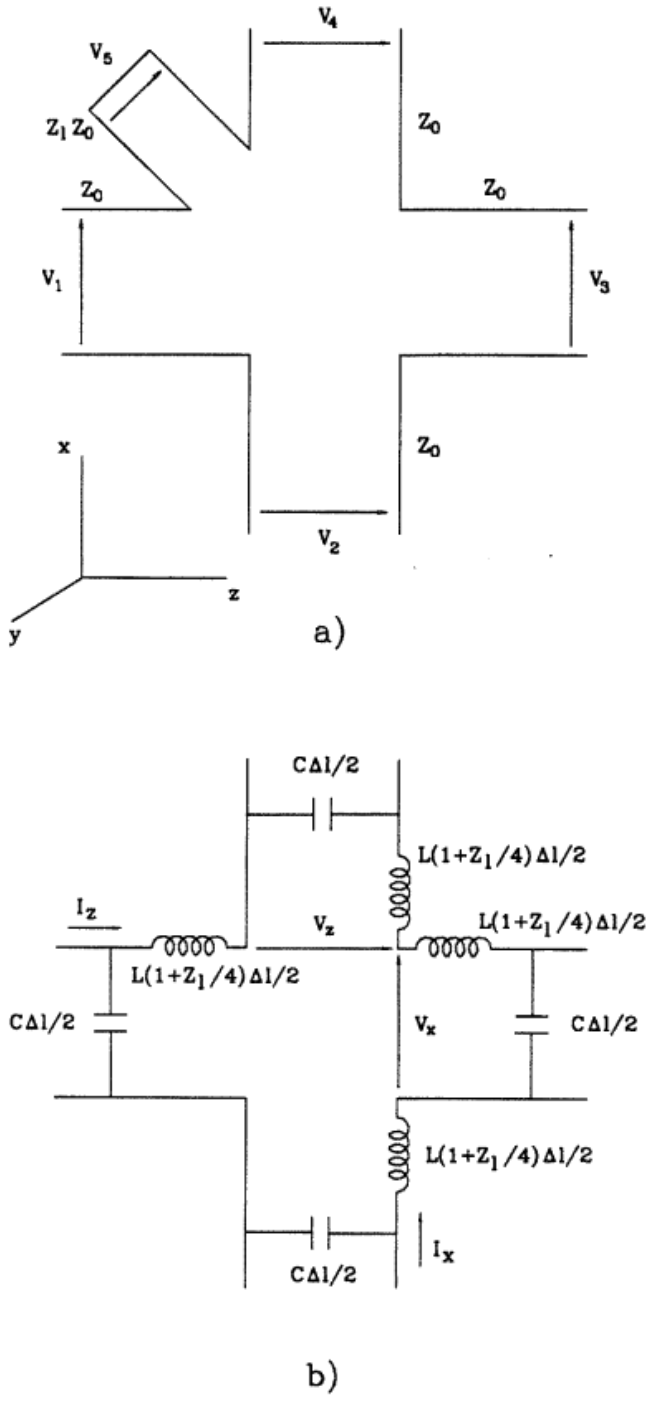

FIGURE 4.4: (a) The 2D series node with stubs, and (b) lumped element equivalence.

After the parallel nodes, Johns [145] developed dual 2D nodes, the series nodes, to deal with TM_{n0} modes in rectangular waveguides. Figure 4.4 shows the 2D series node with stubs and its equivalent lumped element circuit. Lines 1 to 4

are the link lines, mainly responsible of propagation, while line 5 is an inductive extra stub, of impedance Z relative to the characteristic impedance of the main lines, Z_0. This stub allows controlling the conductance of the node circuit and therefore the permeability of the medium to be modeled. The analogy relates now the quantities in the following manner:

$$\frac{\partial I}{\partial x} = -C\frac{\partial V_x}{\partial t}, \tag{4.14}$$

$$-\frac{\partial I}{\partial z} = -C\frac{\partial V_z}{\partial t} \tag{4.15}$$

and

$$\frac{\partial V_x}{\partial z} - \frac{\partial V_z}{\partial x} = -2L\left(1 + Z_l/4\right)\frac{\partial I}{\partial t}. \tag{4.16}$$

The existence of actual connections between lines allows defining a lumped element circuit from which the analogy, scattering matrix and other quantities may be derived, resulting

$$S = \frac{1}{4+Z_l}\begin{pmatrix} 2+Z_l & 2 & 2 & -2 & -2 \\ 2 & 2+Z_l & -2 & 2 & 2 \\ 2 & -2 & 2+Z_l & 2 & 2 \\ -2 & 2 & 2 & 2+Z_l & -2 \\ -2Z_l & 2Z_l & 2Z_l & -2Z_l & 4-Z_l \end{pmatrix}. \tag{4.17}$$

4.2.3 The first 3D node: the asymmetric expanded node

A significant difficulty arose when dealing with fully three-dimensional (3D) media. Initial efforts concentrated on obtaining nodes consisting of 3 parallel and 3 series 2D nodes connected, as shown in Figure 4.5 [146–148]. The common voltage at each parallel node defined each component of the electric field, while the common current at each series node defined each component of the magnetic field. The node was termed asymmetrical expanded node, since it was asymmetric and defined each field component at a different point and even at different time in an scheme that resembled the Yee's FDTD scheme [149].

The expanded character of the node made boundary conditions and excitation difficult to implement and its asymmetry, even in the case that symmetric media were to be modeled, was indeed undesirable. Several attempts were made to

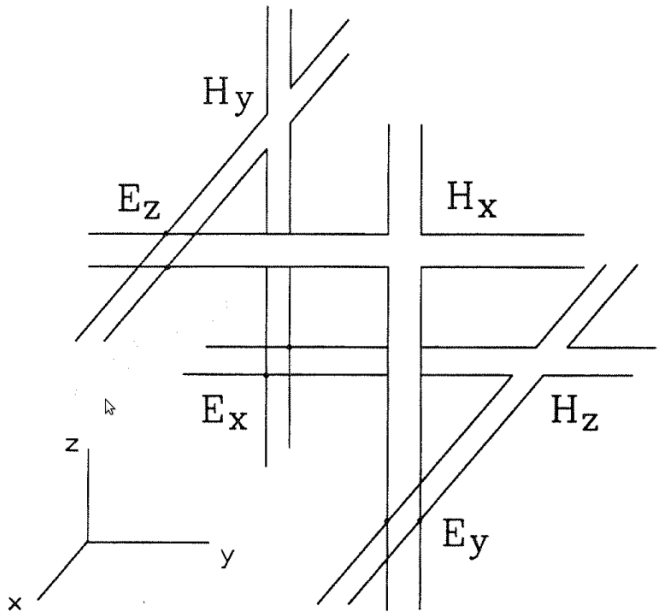

FIGURE 4.5: The 3D asymmetrical expanded node.

obtain symmetrical and condensed nodes but symmetry was incompatible with actual connections to define equivalent lumped element circuits, at least in an easy and conceptually clear form [150–153].

4.2.4 A new conceptual approach: the 3D symmetrical condensed node

A significant improvement was achieved when, in 1986, P.B. Johns changed the way in what the TLM nodes have to be considered [154, 155]. He realized that the constraint of actual connections made it impossible to get condensed and symmetric nodes, so he considered thinking of the nodes in a new and conceptual way. He proposed the 3D node shown in Figure 4.6, in which 12 link lines of characteristic impedance Z_0=$1/Y_0$, formally connected at its center, these connections being directly governed or defined by Maxwell equations.

Each line is now thought of as a means of propagating a certain component of the electric and the magnetic field along a specific direction, together with a means of injecting capacitance, conductance or resistance to the medium. For a Cartesian node of dimensions (Δx, Δy, Δz), line 1, for example, defines E_x=$V_1/\Delta x$ and H_z=-$V_1/(Z_0\Delta x)$ propagating along the y direction. It is worth noting that electric fields are oriented from points of higher electric potential to points of lower

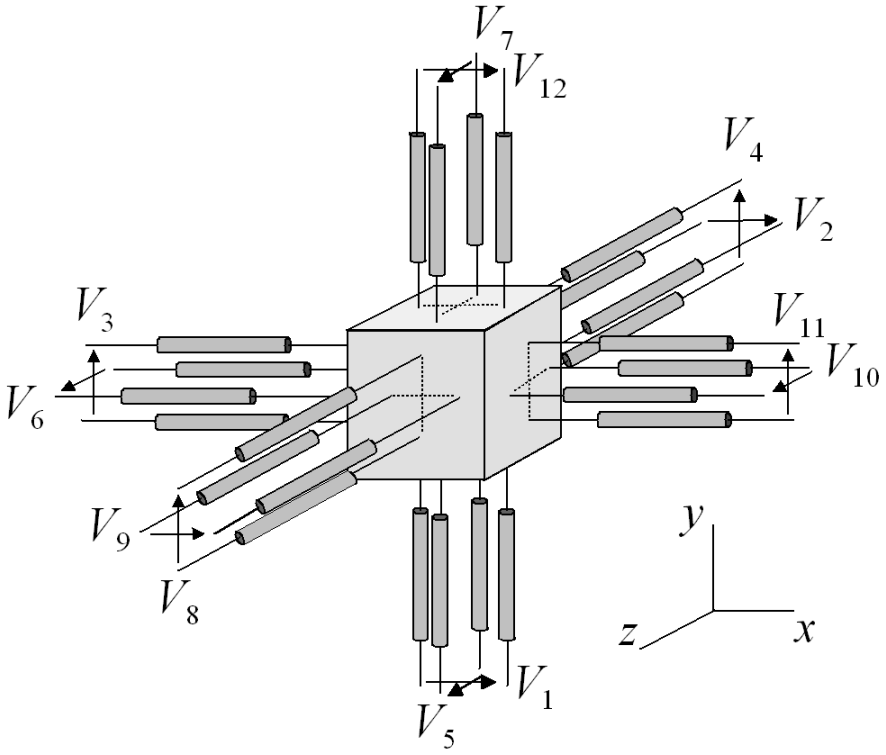

FIGURE 4.6: The 3D symmetrical condensed node.

electric potential, so the polarity between voltage and electric field in the analogy is inversed. This explains the need of also inverting the polarity of magnetic fields and currents. However, for historical reasons, most of the authors working with TLM still maintain this oppositely defined analogy and so we will do.

Other important effect of the existence of a given line is the total capacitance and inductance, C_{line} and L_{line}, that each line introduces to the node describing the medium. In terms of the capacitance and inductance per unit length, C and L, and node length, Δl, these quantities are dependent on the line length $\Delta l/2$.

$$C_{line} = \frac{1}{2} C \Delta l, \qquad L_{line} = \frac{1}{2} L \Delta l. \tag{4.18}$$

It is more interesting to define them in terms of characteristic admittances and impedances, since now the parameters are not length-dependent. Effectively, the total capacitance and inductance introduced by this and the rest of link lines is given by

$$C_{line} = \frac{1}{2} Y_0 \Delta t, \qquad L_{line} = \frac{1}{2} Z_0 \Delta t. \tag{4.19}$$

Extra lines, not represented in the figure, are also considered to provide independent control of electromagnetic parameters. Three capacitive lines (13 to 15, with

relative admittance Y_x, Y_y and Y_z, respectively add capacitance to each Cartesian direction. Line 13, for instance, defines E_x=V_{13}/Δx and adds a capacitance

$$C_{line13} = \frac{1}{2} Y_x Y_0 \Delta t \tag{4.20}$$

to the node.

Short circuit or inductive stubs 16 to 18, of relative impedances Z_x, Z_y and Z_z, respectively, define magnetic field and add inductance to the node. Line 16, for instance, defines H_x=$I_{13}/\Delta x$ and introduces an inductance

$$L_{line16} = \frac{1}{2} Z_z Z_0 \Delta t \tag{4.21}$$

to the node.

Optionally, infinitely long or resistive stubs, 19 to 21, of relative electric conductance G_x, G_y, and G_z, respectively, and 22 to 24, of relative magnetic resistance, R_x, R_y, and R_z, respectively, are responsible of modeling electric and magnetic losses by means of pulses entering these lines which never reflect back to the node center due to its infinite length.

Table 4.1 summarizes the field components defined, the direction of propagation, capacitance, and inductance defined by each line.

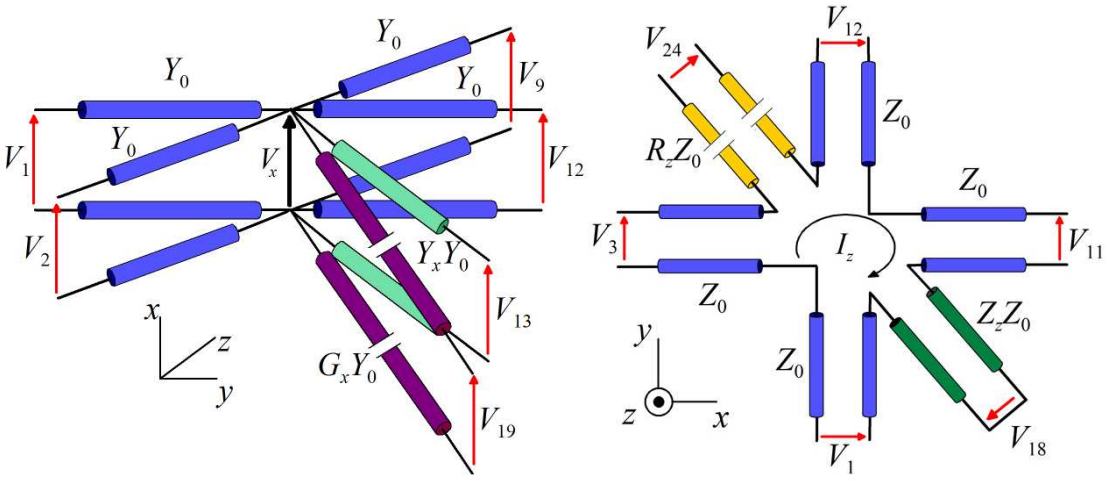

FIGURE 4.7: Parallel and series sub-circuits to define E_x and H_z in the 3D symmetrical condensed node.

Although conceptually intuitive, the global 3D node is difficult to deal with because there is no actual circuit containing all the lines in the node. Stub lines

TABLE 4.1: Magnitudes related to the link and stub transmission lines.

Line	$\overline{E}$	$\overline{H}$	$\overline{k}$	Capacitance	Inductance
1	$E_x \equiv V_1/\Delta x$	$H_z \equiv -I_1/\Delta z$	y	$Y_0\Delta t/2$	$Z_0\Delta t/2$
2	$E_x \equiv V_2/\Delta x$	$H_y \equiv +I_2/\Delta y$	z	$Y_0\Delta t/2$	$Z_0\Delta t/2$
3	$E_y \equiv V_3/\Delta y$	$H_z \equiv +I_3/\Delta z$	x	$Y_0\Delta t/2$	$Z_0\Delta t/2$
4	$E_y \equiv V_4/\Delta y$	$H_x \equiv -I_4/\Delta x$	z	$Y_0\Delta t/2$	$Z_0\Delta t/2$
5	$E_z \equiv V_5/\Delta z$	$H_x \equiv +I_5/\Delta x$	y	$Y_0\Delta t/2$	$Z_0\Delta t/2$
6	$E_z \equiv V_6/\Delta z$	$H_y \equiv -I_6/\Delta y$	x	$Y_0\Delta t/2$	$Z_0\Delta t/2$
7	$E_z \equiv V_7/\Delta z$	$H_x \equiv -I_7/\Delta x$	y	$Y_0\Delta t/2$	$Z_0\Delta t/2$
8	$E_y \equiv V_8/\Delta y$	$H_x \equiv +I_8/\Delta x$	z	$Y_0\Delta t/2$	$Z_0\Delta t/2$
9	$E_x \equiv V_9/\Delta x$	$H_y \equiv -I_9/\Delta y$	z	$Y_0\Delta t/2$	$Z_0\Delta t/2$
10	$E_z \equiv V_{10}/\Delta z$	$H_y \equiv +I_{10}/\Delta y$	x	$Y_0\Delta t/2$	$Z_0\Delta t/2$
11	$E_y \equiv V_{11}/\Delta y$	$H_z \equiv -I_{11}/\Delta z$	x	$Y_0\Delta t/2$	$Z_0\Delta t/2$
12	$E_x \equiv V_{12}/\Delta x$	$H_z \equiv +I_{12}/\Delta z$	y	$Y_0\Delta t/2$	$Z_0\Delta t/2$
13	$E_x \equiv V_{13}/\Delta y$			$Y_xY_0\Delta t/2$	
14	$E_y \equiv V_{14}/\Delta y$			$Y_yY_0\Delta t/2$	
15	$E_z \equiv V_{15}/\Delta y$			$Y_zY_0\Delta t/2$	
16		$H_x \equiv +I_{16}/\Delta x$			$Z_xZ_0\Delta t/2$
17		$H_y \equiv +I_{17}/\Delta y$			$Z_yZ_0\Delta t/2$
18		$H_z \equiv +I_{18}/\Delta z$			$Z_zZ_0\Delta t/2$
19	$E_x \equiv V_{19}/\Delta y$			$G_xY_0\Delta t/2$	
20	$E_y \equiv V_{20}/\Delta y$			$G_yY_0\Delta t/2$	
21	$E_z \equiv V_{21}/\Delta y$			$G_zY_0\Delta t/2$	
22		$H_x \equiv +I_{22}/\Delta x$			$R_xZ_0\Delta t/2$
23		$H_y \equiv +I_{23}/\Delta y$			$R_yZ_0\Delta t/2$
24		$H_z \equiv +I_{24}/\Delta z$			$R_zZ_0\Delta t/2$

cannot even be represented. The node must be understood as a conceptual circuit in which connections between lines are not real but are formal connections describing Ampère's and Faraday's laws, instead. For simplicity's sake and from a mathematical point of view, Maxwell equations are vector differential equations which are usually split into six coupled scalar equations. In a similar manner and to simplify the situation, the node can be regarded as six coupled 2D transmission line circuits or 2D nodes. Figure 6 shows the sub-circuits corresponding to E_x and H_z. Three of them are termed parallel or shunt nodes, which, by means of its common voltage, capacity and electric conductance are able to describe a component of Ampère's law, including Joule losses. The other three sub-circuits are series nodes, defining a common current, conductance and magnetic resistance, thus describing the three components of Faraday's law and the associated quantities [156].

This separation of components allows a better understanding and control of

the analogy required to model a certain isotropic medium with permittivity ε, permeability μ, electric conductivity σ_e, and magnetic conductivity σ_m. Although not considered in this text, anisotropies may be derived by choosing different values of the parameters, as long as the parameters are defined in terms of principal directions. Regarding the parallel node for E_x, Figure 4.7a, the common voltage defines E_x by $E_x \equiv V_x/m$. The total capacitance and electric conductance of this circuit and the medium capacitance and conductance along the x direction must coincide, respectively. This yields the following expressions relating the node and the medium to model

$$4Y_0\frac{\Delta t}{2} + Y_0 Y_x \frac{\Delta t}{2} = \varepsilon \frac{\Delta y \Delta z}{\Delta x} \tag{4.22}$$

$$G_x Y_0 = \sigma_e \frac{\Delta y \Delta z}{\Delta x}. \tag{4.23}$$

Similarly, considering the series node for H_z shown in figure 4.7b, and identifying the total inductance of the medium and inductance of the circuit, it results that the line parameters must be chosen to meet

$$4Z_0\frac{\Delta t}{2} + Z_0 Z_x \frac{\Delta t}{2} = \mu \frac{\Delta x \Delta y}{\Delta z}. \tag{4.24}$$

Regarding the magnetic resistance of the medium, the magnetic resistive line must fulfill

$$R_z Z_0 = \sigma_m \frac{\Delta x \Delta y}{\Delta z}, \tag{4.25}$$

and similar equations can be obtained for the rest of lines.

The above equations provide information for defining the parameters of the stubs, since simple manipulation results in the following expressions for the parameters defining the lines:

$$Y_x = \frac{2\varepsilon}{Y_0 \Delta t}\frac{\Delta y \Delta z}{\Delta x} - 4, \tag{4.26a}$$

$$Y_y = \frac{2\varepsilon}{Y_0 \Delta t}\frac{\Delta x \Delta z}{\Delta y} - 4, \tag{4.26b}$$

$$Y_z = \frac{2\varepsilon}{Y_0 \Delta t}\frac{\Delta x \Delta y}{\Delta z} - 4, \tag{4.26c}$$

$$Z_x = \frac{2\mu}{Z_0 \Delta t}\frac{\Delta y \Delta z}{\Delta x} - 4, \tag{4.26d}$$

$$Z_y = \frac{2\mu}{Z_0 \Delta t}\frac{\Delta x \Delta z}{\Delta y} - 4, \tag{4.26e}$$

$$Z_z = \frac{2\mu}{Z_0 \Delta t}\frac{\Delta x \Delta y}{\Delta z} - 4 \tag{4.26f}$$

$$G_x = \frac{\sigma_x^e}{Y_0}\frac{\Delta y \Delta z}{\Delta x}, \tag{4.26g}$$

$$G_y = \frac{\sigma_y^e}{Y_0}\frac{\Delta x \Delta z}{\Delta y}, \tag{4.26h}$$

$$G_z = \frac{\sigma_z^e}{Y_0}\frac{\Delta x \Delta y}{\Delta z}, \tag{4.26i}$$

$$R_x = \frac{\sigma_x^m}{Y_0}\frac{\Delta y \Delta z}{\Delta x}, \tag{4.26j}$$

$$R_y = \frac{\sigma_y^m}{Y_0}\frac{\Delta x \Delta z}{\Delta y}, \tag{4.26k}$$

$$R_z = \frac{\sigma_z^m}{Y_0}\frac{\Delta x \Delta y}{\Delta z}. \tag{4.26l}$$

There is some degree of freedom in choosing the stub characteristic impedances and admittances appearing in the previous equation, the only condition being that, for stability's sake, that all these quantities must be positive. This condition fixes an upper allowable value for the time step, Δt, with the interesting fact that choosing this maximum allowable time step causes that at least one of the stubs vanishes and minimal dispersion error.

Regarding the derivation of the scattering matrix for this node, transmission and reflection coefficients are no longer valid, since there are no actual connections for the node. In his initial works, Johns derived the scattering matrix, S, by imposing Maxwell equations to the node, together with energy and charge conservation laws and conditions of electric potential continuity [154]. This is an elegant but complicated task to do because of the great number of equations to be dealt with, most of them nonlinear equations.

Fortunately, this process can be greatly simplified by applying the concept of common and uncommon lines introduced to the series and parallel nodes described above [156]. The process considers a unitary pulse entering the node through a link line. This line and the opposite appear in a series circuit and in a shunt circuit, the common lines. For example, for a pulse incident through port 1, this line and line 12 simultaneously appear in the 2D circuits of figure 4.7a and 4.7b. Lines 1, 12 are the common lines. It is not clear how they are connected, since they must connect in both 2D circuits. On the other side, the rest of lines in these two circuits only appear in one or the other sub-circuit, the uncommon lines. In

our example, lines 2, 9, 13 and 19 are the uncommon lines for the parallel node and lines 3, 11, 18 and 24, are the uncommon lines of the 2D series circuit.

The difference with respect to common lines is that the connections of uncommon lines are perfectly clear and, therefore, the circuit coefficients define how the pulse from line 1 scatters to the uncommon lines in an easy way. As regards the pair of common lines, they simultaneously appear in the parallel and the series sub-circuit so the coupling between them impedes the use of the circuits to obtain the pulses reflected to the common lines. Alternatively, the use of the original components of Ampere's and Faraday's laws allows defining the coupling by simple imposing charge conservation at the shunt node and continuity of electrical potential at the series node. These consist of a pair of linear equations from which simple manipulation provides the pulses reflected at both common lines.

To fix ideas, let us obtain pulses reflected at the node when a unitary voltage pulse enters through line 1 by using the scheme described above.

1. **Reflection at uncommon lines in the parallel sub-circuit:**

   The pulse V_1^i=1 reaches the node center through a line with characteristic admittance Y_0. According to the parallel sub-circuit, it connects to a load admittance Y_l given by

   $$Y_L = Y_2 + Y_9 + Y_{12} + Y_{13} + Y_{19} = 3Y_0 + Y_x Y_0 + G_x Y_0. \tag{4.27}$$

   The corresponding transmission coefficient, τ, is given by

   $$\tau = \frac{2Y_0}{Y_0 + Y_L}. \tag{4.28}$$

   So, reflected pulses at the uncommon lines are

   $$c_x = V_2^r = V_9^r = V_{13}^r = V_{19}^r = \tau = \frac{2}{4 + Y_x + G_x}. \tag{4.29}$$

2. **Reflected pulses at uncommon lines of the series sub-circuit:**

   Now considering the circuit in figure 4.2b, port 1, of impedance Z_0, meets a load impedance Z_L, given by

   $$Z_L = Z_3 + Z_{11} + Z_{12} + Z_{18} + Z_{24} = 3Z_0 + Z_z Z_0 + R_z Z_0. \tag{4.30}$$

The transmission coefficient is now:

$$\tau = \frac{2Z_L}{Z_0 + Z_L}. \tag{4.31}$$

The uncommon lines are series connected, so, reflected pulses at these lines are obtained with the new transmission coefficient together with a voltage division, resulting

$$d_z = V_3^r = -V_{11}^r = \tau\frac{Z_0}{Z_L} = \frac{2}{4 + Z_z + R_z}, \tag{4.32a}$$

$$e_z = V_{18}^r = \tau\frac{Z_z Z_0}{Z_L} = \frac{2Z_z}{4 + Z_z + R_z}, \tag{4.32b}$$

$$V_{24}^r = \tau\frac{R_z Z_0}{Z_L} = \frac{2R_z}{4 + Z_z + R_z}. \tag{4.32c}$$

3. Pulses reflected at common lines:

To determine pulses reflected at lines 1 and 12, let us consider the charge conservation condition at the parallel sub-circuit of Figure 4.7a,

$$\begin{aligned} I_1^i &= I_1^r + I_2^r + I_9^r + I_{12}^r + I_{13}^r + I_{19}^r \\ \Rightarrow Y_0 &= a_{xz}Y_0 + 2c_xY_0 + b_{xz}Y_0 + c_xY_xY_0 + V_{19}^r G_x Y_0, \end{aligned} \tag{4.33}$$

and the continuity of electric potential at the series sub-circuit of Figure 4.7b

$$\begin{aligned} -V_1 + V_3 - V_{11} + V_{12} + V_{18} + V_{24} &= 0 \\ \Rightarrow -(1 + a_{xz}) + 2d_z + b_{xz} + e_z + V_{24}^r &= 0. \end{aligned} \tag{4.34}$$

Simple calculations allow obtaining the desired reflected pulses

$$a_{xz} = -\frac{Y_x + G_x}{2(4 + Y_x + G_x)} + \frac{Z_z + R_z}{2(4 + Z_z + R_z)}, \tag{4.35a}$$

$$b_{xz} = -\frac{Y_x + G_x}{2(4 + Y_x + G_x)} - \frac{Z_z + R_z}{2(4 + Z_z + R_z)}. \tag{4.35b}$$

For pulses entering through capacitive or inductive stubs, the problem is simpler since they only appear in a parallel circuit or in a series circuit. This means that they are uncommon lines and the circuit itself describes the situation through the reflection and transmission coefficient.

Finally, ports 19 to 24 are resistive ones, so no incident pulses are ever expected and do no require elements at the scattering matrix.

The final result for the scattering matrix of standard lossy Cartesian node is:

$$\begin{bmatrix}
a_{xz} & c_x & d_z & 0 & 0 & 0 & 0 & 0 & c_x & 0 & -d_z & b_{xz} & g_x & 0 & 0 & 0 & 0 & i_z \\
c_x & a_{xy} & 0 & 0 & 0 & d_y & 0 & 0 & b_{xy} & -d_y & 0 & c_x & g_x & 0 & 0 & 0 & -i_y & 0 \\
d_z & 0 & a_{yz} & c_y & 0 & 0 & 0 & c_y & 0 & 0 & b_{yz} & -d_z & 0 & g_y & 0 & 0 & 0 & -i_z \\
0 & 0 & c_y & a_{yx} & d_x & 0 & -d_x & b_{yx} & 0 & 0 & c_y & 0 & 0 & g_y & 0 & i_x & 0 & 0 \\
0 & 0 & 0 & d_x & a_{zx} & c_z & b_{zx} & -d_x & 0 & c_z & 0 & 0 & 0 & 0 & g_z & -i_x & 0 & 0 \\
0 & d_y & 0 & 0 & c_z & a_{zy} & c_z & 0 & -d_y & b_{zy} & 0 & 0 & 0 & 0 & g_z & 0 & i_y & 0 \\
0 & 0 & 0 & -d_x & b_{zx} & c_z & a_{zx} & d_x & 0 & c_z & 0 & 0 & 0 & 0 & g_z & i_x & 0 & 0 \\
0 & 0 & c_y & b_{yx} & -d_x & 0 & d_x & a_{yx} & 0 & 0 & c_y & 0 & 0 & g_y & 0 & -i_x & 0 & 0 \\
c_x & b_{xy} & 0 & 0 & 0 & -d_y & 0 & 0 & a_{xy} & d_y & 0 & c_x & g_x & 0 & 0 & 0 & i_y & 0 \\
0 & -d_y & 0 & 0 & c_z & b_{zy} & c_z & 0 & d_y & a_{zy} & 0 & 0 & 0 & 0 & g_z & 0 & -i_y & 0 \\
-d_z & 0 & b_{yz} & c_y & 0 & 0 & 0 & c_y & 0 & 0 & a_{yz} & d_z & 0 & g_y & 0 & 0 & 0 & i_z \\
b_{xz} & c_x & -d_z & 0 & 0 & 0 & 0 & 0 & c_x & 0 & d_z & a_{xz} & g_x & 0 & 0 & 0 & 0 & -i_z \\
c_x & c_x & 0 & 0 & 0 & 0 & 0 & 0 & c_x & 0 & 0 & c_x & f_x & 0 & 0 & 0 & 0 & 0 \\
0 & 0 & c_y & c_y & 0 & 0 & 0 & c_y & 0 & 0 & c_y & 0 & 0 & f_y & 0 & 0 & 0 & 0 \\
0 & 0 & 0 & 0 & c_z & c_z & c_z & 0 & 0 & c_z & 0 & 0 & 0 & 0 & f_z & 0 & 0 & 0 \\
0 & 0 & 0 & e_x & -e_x & 0 & e_x & -e_x & 0 & 0 & 0 & 0 & 0 & 0 & 0 & h_x & 0 & 0 \\
0 & -e_y & 0 & 0 & 0 & e_y & 0 & 0 & e_y & -e_y & 0 & 0 & 0 & 0 & 0 & 0 & h_y & 0 \\
e_z & 0 & -e_z & 0 & 0 & 0 & 0 & 0 & 0 & 0 & e_z & -e_z & 0 & 0 & 0 & 0 & 0 & h_z
\end{bmatrix}, \tag{4.36}$$

where the elements of S matrix are given by

$$\begin{aligned}
a_{pq} &= -\tfrac{Y_p+G_p}{2(4+Y_p+G_p)} + \tfrac{Z_q+R_q}{2(4+Z_q+R_q)}, & d_q &= \tfrac{2}{4+Z_q+R_q}, & g_p &= \tfrac{2Y_p}{4+Y_p+G_p}, \\
b_{pq} &= -\tfrac{Y_p+G_p}{2(4+Y_p+G_p)} - \tfrac{Z_q+R_q}{2(4+Z_q+R_q)}, & e_q &= \tfrac{2Z_q}{4+Z_q+R_q}, & h_q &= \tfrac{4-Z_q+R_q}{4+Z_q+R_q}, \\
c_p &= \tfrac{2}{4+Y_p+G_p}, & f_p &= \tfrac{-4+Y_p-G_p}{4+Y_p+G_p}, & i_q &= \tfrac{2}{4+Z_q+R_q},
\end{aligned} \tag{4.37}$$

with {p,q}={x,y}.

As regards field definition through node incident pulses, Johns proposed a calculation of charge and magnetic flux storage at the node to define electric and magnetic field components [154]. This procedure is rather difficult because it requires a relatively deep theoretical knowledge. Nevertheless, one additional advantage in considering separated sub-circuits is that individual information provided by the parallel and series circuits allows a more direct the determination of expressions for the electromagnetic field in terms of the incident pulses. To do so, Thevenin's theorem is applied to each parallel node leading to a simple parallel circuit in which each line in the node is substituted by a series connection of a voltage source of value twice the incident voltage and an impedance equal to the characteristic impedance of the transmission line [141]. The common voltage at the node center can be then derived by simple Circuit Theory calculations. As regards E_x, Figure 4.8 shows the circuit after applying Thevenin's theorem. The voltage for this circuit, V_x, is analogous to $E_x\Delta\mathrm{x}$, which simply yields

$$E_x = \frac{2}{\Delta x(4+Y_x+G_x)}\left(V_1^i + V_2^i + V_9^i + V_{12}^i + Y_x V_{13}^i\right). \tag{4.38}$$

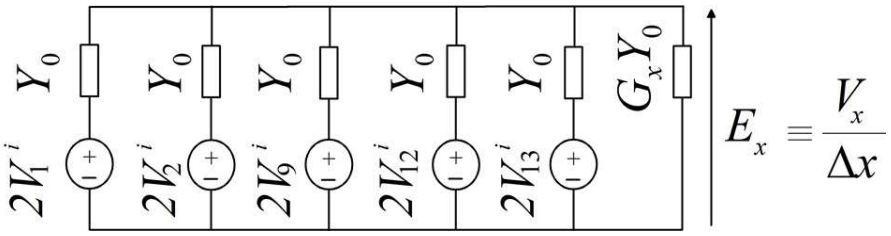

FIGURE 4.8: Thevenin's equivalent circuit for the E_x parallel circuit.

In a similar manner, the y and z components of the electric field are given by

$$E_y = \frac{2}{\Delta y(4 + Y_y + G_y)} \left(V_3^i + V_4^i + V_8^i + V_{11}^i + Y_y V_{14}^i\right). \tag{4.39}$$

$$E_z = \frac{2}{\Delta z(4 + Y_z + G_z)} \left(V_5^i + V_6^i + V_7^i + V_{10}^i + Y_z V_{15}^i\right). \tag{4.40}$$

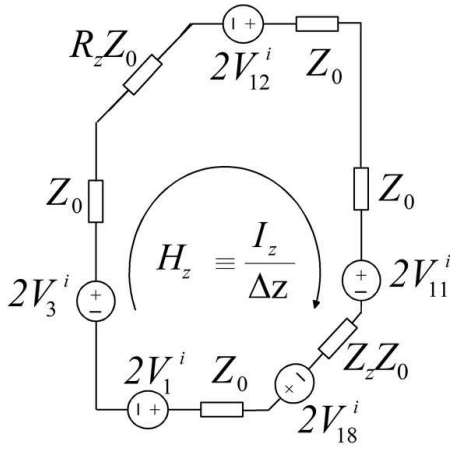

FIGURE 4.9: Thevenin's equivalent circuit for the H_z series circuit.

Similarly, applying Thevenin's theorem to the series nodes and by identifying current at the node with magnetic field components, leads to the following expression for H_z:

$$H_z = \frac{2}{\Delta z Z_0(4 + Z_z + R_z)} \left(-V_1^i + V_3^i - V_{11}^i + V_{12}^i + Y_z V_{18}^i\right). \tag{4.41}$$

The other series nodes provide expressions for H_x and H_y,

$$H_x = \frac{2}{\Delta x Z_0(4 + Z_x + R_x)} \left(-V_4^i + V_5^i - V_7^i + V_8^i + Y_z V_{16}^i\right) \tag{4.42}$$

and

$$H_y = \frac{2}{\Delta y Z_0(4 + Z_y + R_y)} \left(V_2^i - V_6^i - V_9^i + V_{10}^i + Y_z V_{17}^i\right). \tag{4.43}$$

4.3 Excitation

Sources can be excited by adding extra voltage sources to existing pulses in the TLM mesh. To do so, the expressions from above must be considered in the following manner. Let us consider that a value E_{0x} is to be excited as the x component of the source electric field. In order to avoid that excitation of E_{0x} also excites other field components, identical pulses at lines 1 and 12, and at lines 2 and 9 are set. Choosing identical incident excitation pulses of amplitude a_x incident from each line at the node for E_x, except for the resistive one, meets this condition. The only component of the electromagnetic field generated by this excitation pulses would be

$$E_{0x} = \frac{2a_x}{\Delta x(4 + Y_x + G_x)}(4 + Y_x) \tag{4.44}$$

which provides the value a_x for the incident pulse through lines 1, 2, 9, 12, and 13. Similar expressions can be obtained to only excite y or z electric field components.

Similarly, to only excite a given component of the magnetic field, opposite current pulses must be launched to opposite lines at the corresponding series node. Let us consider the lines in the series circuit for H_z shown in figure 4.7b. Choosing $-V_1^i = V_{12}^i = V_3^i = -V_{11}^i = V_{18}^i/Z_z = b_z Z_0$ to excite a source field H_{0z}, the only non-zero component of the electromagnetic field excited is

$$H_{0x} = \frac{2Z_0 b_z}{\Delta z Z_0(4 + Z_z + R_z)}(4 + Z_z) \tag{4.45}$$

which allows easily obtaining b_z.

Summarizing, the incident pulses needed to excite a field $\vec{E} = (E_{0x}, E_{0y}, E_{0z}$, $\vec{H} = (H_{0x}, H_{0y}, H_{0z}$ are given by:

$$V_1^i = \frac{1}{2}\left(\Delta x E_{0x}\frac{4 + Y_x + G_x}{4 + Y_x} - \Delta z Z_0 H_{0z}\frac{4 + Z_z + R_z}{4 + Z_z}\right), \tag{4.46a}$$

$$V_2^i = \frac{1}{2}\left(\Delta x E_{0x}\frac{4 + Y_x + G_x}{4 + Y_x} + \Delta y Z_0 H_{0y}\frac{4 + Z_y + R_y}{4 + Z_y}\right), \tag{4.46b}$$

$$V_3^i = \frac{1}{2}\left(\Delta y E_{0y}\frac{4 + Y_y + G_y}{4 + Y_y} + \Delta z Z_0 H_{0z}\frac{4 + Z_z + R_z}{4 + Z_z}\right), \tag{4.46c}$$

$$V_4^i = \frac{1}{2}\left(\Delta y E_{0y}\frac{4 + Y_y + G_y}{4 + Y_y} - \Delta x Z_0 H_{0x}\frac{4 + Z_x + R_x}{4 + Z_x}\right), \tag{4.46d}$$

$$V_5^i = \frac{1}{2}\left(\Delta z E_{0z}\frac{4+Y_z+G_z}{4+Y_z} + \Delta x Z_0 H_{0x}\frac{4+Z_x+R_x}{4+Z_x}\right), \tag{4.46e}$$

$$V_6^i = \frac{1}{2}\left(\Delta z E_{0z}\frac{4+Y_z+G_z}{4+Y_z} - \Delta y Z_0 H_{0y}\frac{4+Z_y+R_y}{4+Z_y}\right), \tag{4.46f}$$

$$V_7^i = \frac{1}{2}\left(\Delta z E_{0z}\frac{4+Y_z+G_z}{4+Y_z} - \Delta x Z_0 H_{0x}\frac{4+Z_x+R_x}{4+Z_x}\right), \tag{4.46g}$$

$$V_8^i = \frac{1}{2}\left(\Delta y E_{0y}\frac{4+Y_y+G_y}{4+Y_y} + \Delta x Z_0 H_{0x}\frac{4+Z_x+R_x}{4+Z_x}\right), \tag{4.46h}$$

$$V_9^i = \frac{1}{2}\left(\Delta x E_{0x}\frac{4+Y_x+G_x}{4+Y_x} - \Delta y Z_0 H_{0y}\frac{4+Z_y+R_y}{4+Z_y}\right), \tag{4.46i}$$

$$V_{10}^i = \frac{1}{2}\left(\Delta z E_{0z}\frac{4+Y_z+G_z}{4+Y_z} + \Delta y Z_0 H_{0y}\frac{4+Z_y+R_y}{4+Z_y}\right), \tag{4.46j}$$

$$V_{11}^i = \frac{1}{2}\left(\Delta y E_{0y}\frac{4+Y_y+G_y}{4+Y_y} - \Delta z Z_0 H_{0z}\frac{4+Z_z+R_z}{4+Z_z}\right), \tag{4.46k}$$

$$V_{12}^i = \frac{1}{2}\left(\Delta x E_{0x}\frac{4+Y_x+G_x}{4+Y_x} + \Delta z Z_0 H_{0z}\frac{4+Z_z+R_z}{4+Z_z}\right), \tag{4.46l}$$

$$V_{13}^i = \frac{1}{2}\Delta x E_{0x}\frac{4+Y_x+G_x}{4+Y_x}, \tag{4.46m}$$

$$V_{14}^i = \frac{1}{2}\Delta y E_{0y}\frac{4+Y_y+G_y}{4+Y_y}, \tag{4.46n}$$

$$V_{15}^i = \frac{1}{2}\Delta z E_{0z}\frac{4+Y_z+G_z}{4+Y_z}, \tag{4.46o}$$

$$V_{16}^i = \frac{1}{2}Z_x Z_0 \Delta x H_{0x}\frac{4+Z_x+R_x}{4+Z_x}, \tag{4.46p}$$

$$V_{17}^i = \frac{1}{2}Z_y Z_0 \Delta y H_{0y}\frac{4+Z_y+R_y}{4+Z_y}, \tag{4.46q}$$

$$V_{18}^i = \frac{1}{2}Z_z Z_0 \Delta z H_{0z}\frac{4+Z_z+R_z}{4+Z_z}. \tag{4.46r}$$

4.4 Boundary conditions

The problem of imposing boundary conditions to allow the use of finite size even when an infinite free space is required is an important and difficult problem. Several works are available in the literature in this sense [157–159]. Fortunately, the problems to be modeled in this work are confined problems concerned with nodes reaching conducting regions. In this particular case, it is enough to consider the node lines reaching the conducting zone to be connected to a load impedance, Z_L. This load impedance causes that pulses be reflected back to the node center

according to simple reflection coefficient at the boundary, τ_b,

$$\tau_b = \frac{Z_L - Z_0}{Z_L + Z_0} \tag{4.47}$$

4.5 Particular case: isotropic media modeled with SCN

A particular but usual case is that in which an isotropic medium with parameters ε, μ, σ_e and σ_m is to be modeled by a symmetrical condensed node. Let $\eta{=}\sqrt{\mu/\varepsilon}$ stand for the medium impedance and $v_m{=}1/\sqrt{\varepsilon\mu}$ for the medium velocity. Let us also suppose that we want to model the medium with nodes with identical length Δl along the tree Cartesian directions. We can arbitrarily choose the characteristic impedance of the link lines, so let us choose $Z_0{=}\eta$.

The time step value which makes each stub parameter to vanish can be obtained by imposing the relative admittances or impedances in equation 4.26. It results that choosing

$$dt = \frac{\Delta l}{v_l} = \frac{\Delta l}{2v_m} = \frac{\Delta l\sqrt{\varepsilon\mu}}{2} \tag{4.48}$$

i.e., speed of pulses at the line twice the wave speed of the medium, and all the extra stubs vanishes, which turns into an important saving in memory and time requirements for computation purposes. Besides, in this particular but usual case, the scattering matrix becomes very simple,

$$S = \begin{bmatrix}
0 & 1/2 & 1/2 & 0 & 0 & 0 & 0 & 0 & 1/2 & 0 & -1/2 & 0 \\
1/2 & 0 & 0 & 0 & 0 & 1/2 & 0 & 0 & 0 & -1/2 & 0 & 1/2 \\
1/2 & 0 & 0 & 1/2 & 0 & 0 & 0 & 1/2 & 0 & 0 & 0 & -1/2 \\
0 & 0 & 1/2 & 0 & 1/2 & 0 & -1/2 & 0 & 1/2 & 0 & 1/2 & 0 \\
0 & 0 & 0 & 1/2 & 0 & 1/2 & 0 & -1/2 & 0 & 1/2 & 0 & 0 \\
0 & 1/2 & 0 & 0 & 1/2 & 0 & 1/2 & 0 & -1/2 & 0 & 0 & 0 \\
0 & 0 & 0 & -1/2 & 0 & 1/2 & 0 & 1/2 & 0 & 1/2 & 0 & 0 \\
0 & 0 & 1/2 & 0 & -1/2 & 0 & 1/2 & 0 & 0 & 0 & 1/2 & 0 \\
1/2 & 0 & 0 & 0 & 0 & -1/2 & 0 & 0 & 0 & 1/2 & 0 & 1/2 \\
0 & -1/2 & 0 & 0 & 1/2 & 0 & 1/2 & 0 & 1/2 & 0 & 0 & 0 \\
-1/2 & 0 & 0 & 1/2 & 0 & 0 & 0 & 1/2 & 0 & 0 & 0 & 1/2 \\
0 & 1/2 & -1/2 & 0 & 0 & 0 & 0 & 0 & 1/2 & 0 & 1/2 & 0
\end{bmatrix} \tag{4.49}$$

In addition, numerical dispersion behavior is better. Similar simplifications can be found if expressions for field definition and excitation are considered.

4.6 Frequency response considerations

The study of the frequency response of Cartesian 3D symmetrical nodes is described by Morente et al. [160, 161]. Basically, the numerical discretization causes frequency dependence in the results even if the actual medium may be non-dispersive. This undesirable effect is usual in low frequency numerical methods. The result common to all these methods is that spatial division must sample at least ten times the shortest valid wavelength, thus controlling the maximum valid frequency in the results. Of course, time sampling must also be taken into account to define the maximum valid frequency, but Shannon theorem is less restrictive than the spatial condition sampling mentioned above.

In this sense, results provided by nodes with stubs are valid for lower frequencies than those results obtained by nodes without stubs. The use of stubs is always related to the need of storing part of the energy at the node center by producing energy to flow to the stubs instead of going to the main lines. This is so because the node length is too long and a direct propagation of all the energy to the main lines would produce a group speed faster than it should. In a certain sense, it can be thought of as a reminder that a node longer than needed is being used and the stub lowers the group velocity to adjust node size and speed at individual ports. In fact, these conceptual reasons provided to understand the Physics underlying the process, are confirmed by the dispersion characteristics analysis which goes to the simple and well-known result on the wavelength sampling result, the node size must be at least one tenth of the node size, which, on the other hand, is common to other low frequency numerical methods such as Moments method or FDTD.

This condition is the basis for the choice of the parameters. First, a maximum valid frequency for the results is chosen. From this frequency, the minimum valid wavelength is determined. The node size, Δl, must be at least about one tenth of the wavelength. For the simplest case of an homogeneous mesh of nodes without stubs, Δl and the medium velocity determines the time step. A design frequency resolution, Δf, is also necessary, and it determines the number of time calculations, N_t, to be carried out for reaching that resolution by means of $\Delta f{=}1/(N_t \Delta t)$.

4.7 Cylindrical and spherical nodes

Some problems show cylindrical geometry, which seems to advise that the use of cylindrical nodes should be better than Cartesian ones. The situation is quite similar to that described in the Cartesian case. The basic difference is the substitution of coordinates and elementary lengths. Thus directly making the following substitutions in the Cartesian node expressions yield a suitable cylindrical condensed node [162]:

$$\begin{cases} x \leftrightarrow r, \\ y \leftrightarrow \varphi, \\ z \leftrightarrow z, \end{cases} \quad \Rightarrow \quad \begin{cases} \Delta x \leftrightarrow \Delta r, \\ \Delta y \leftrightarrow r\Delta\varphi, \\ \Delta z \leftrightarrow \Delta z, \end{cases} \tag{4.50}$$

Similarly, for obtaining a spherical node, the following substitutions have to be made:

$$\begin{cases} x \leftrightarrow \varphi, \\ y \leftrightarrow r, \\ z \leftrightarrow \theta, \end{cases} \quad \Rightarrow \quad \begin{cases} \Delta x \leftrightarrow r\sin\theta\Delta\varphi, \\ \Delta y \leftrightarrow \Delta r, \\ \Delta z \leftrightarrow r\Delta\theta, \end{cases} \tag{4.51}$$

These curved nodes avoid the staircase approximation required by the use of Cartesian nodes. Nevertheless, they present some drawbacks.

- For the cylindrical case, the z-axis is a singular region which requires approximation. In any case, lines from all the nodes at the z-axis connect at this axis and a special node is required for this region.
- The same holds for spherical nodes at polar points ($\theta = 0$).
- The nodes do not have identical length for the three directions and the node size grows as the distance to the axis (cylindrical) or center (spherical) increments.
- This means that stubs are always required, especially high for external nodes, which turn into more memory and time calculation requirements, together with inherent dispersion problems.

For the reasons mentioned above, our TLM simulations will be carried out using Cartesian homogeneous nodes. The problem of staircase approximation is only apparent, since this curved detail is not relevant at low frequencies where the method is valid.

4.8 Final considerations about the choice of the TLM method

An interesting question arises concerning the reason why TLM method has been chosen for calculations in the following Chapter. Why choosing TLM method instead of more popular methods, such as FDTD?

The response is difficult and most likely has a great degree of subjectivity. TLM method and FDTD present multiple similarities but TLM requires more memory resources for each elementary volume to be modeled. While FDTD needs 6 components of the electromagnetic field, the TLM method uses 12 voltages in its best formulation. Despite this drawback, TLM presents some advantages which justify our choice. It is true that TLM uses more variables but it also provides more and better information than FDTD. Namely, all the field quantities are provided at the node center at the same time. All the transversal fields are also known at interface between nodes and intermediate time steps. These two facts simplify source excitation, boundary conditions and even hybridization with other methods, numerical or analytical. The formulation of the scattering matrix is essentially stable, since energy and charge conservation are imposed, as well as continuity of potential. This makes TLM a stable method, with simple operations.

Finally, the conceptual basis of TLM method always keeps in mind the Physics of the problem since it is not involved with equations that substitute the original phenomenon, but it is directly concerned with the phenomenon itself. This conceptual approach is difficult to deal with at first, but after some experience allows considering new elements as new concepts, or circuits, to be added to the basic TLM node.

Maybe one of the most outstanding examples in this sense is that of single wire modeling with TLM [163–165]. In this sense, for example, a thin wire can be considered as an inductive and capacitive element which couples to a given component of the electric field. So, a simple circuit describing the node is adapted to the 3D symmetrical condensed node. A new scattering matrix is obtained and, since then, the same basic algorithm as in a basic case is launched. Figure 4.10 is a plot of the transmission line circuit to add to the node geometry for the case of a thin conducting wire with a resistive nonlinear load. Nonlinearity is simply modeled by changing the line parameters according to the field obtained at the

previous time calculation. Figure 4.11 is a comparison of the results for a linear antenna loaded with a non-linear resistive load. The interesting point in this example is that the node length is 47.6mm, while the antenna radius is only 5mm [165].

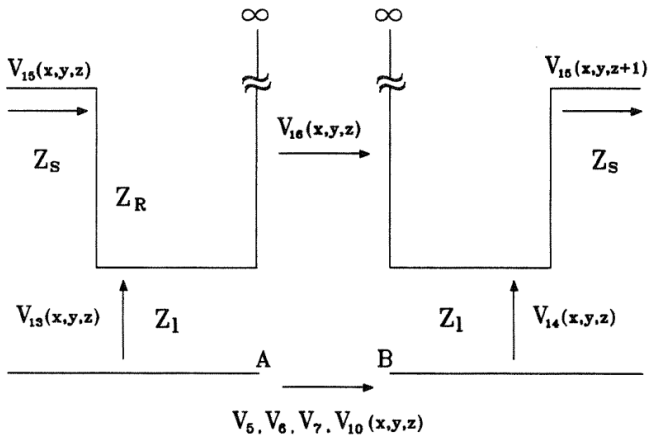

FIGURE 4.10: Transmission lines structure for modeling a thin-wire antenna with SCN node. Extracted from [166]

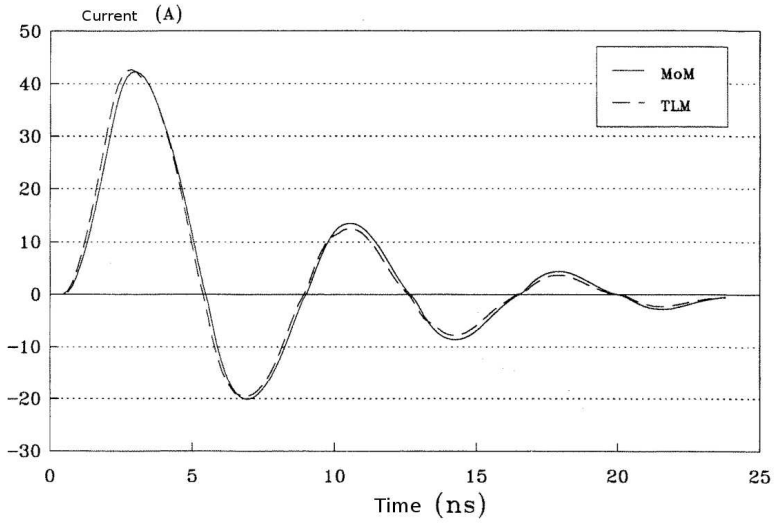

FIGURE 4.11: Current in a thin-wire antenna charged with nonlinear load. Extracted from [166]

Finally, another interesting application directly resulting from the versatility of the TLM method is concerned with metamaterial modeling. Materials with Double Negative Properties (DNG) at certain frequencies are usual in recent years. These artificial materials have interesting applications such as perfect lens focusing or electromagnetic invisibility (cloaking). Some of these materials are built by means of transmission lines with capacitors and inductors connected in a dual way as that shown in lumped element circuits of transmission lines. TLM is able of modeling

this in an almost direct way: we have only to interchange inductive stubs with capacitive stubs. No recalculation of scattering matrix is needed. Field, source or boundary expressions are also maintained. It becomes clear then that the effort carried out to study wave propagating in vacuum is the same as that required for metamaterial modeling. Figure 4.12 is the TLM result of wave propagation around a conducting cylinder coated with a DNG material which shows the TLM capability for modeling remarkably difficult situations without significant added burden [167].

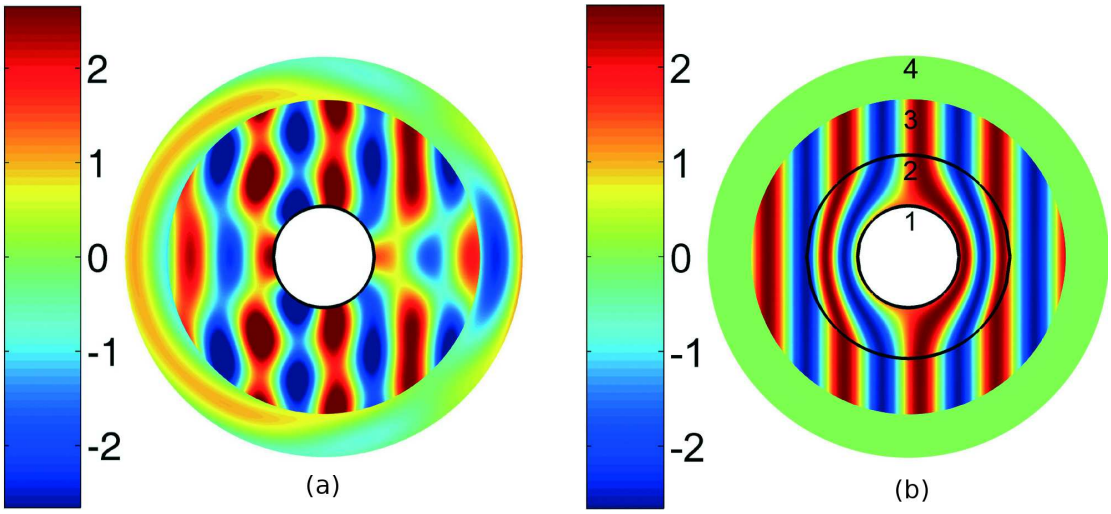

FIGURE 4.12: (a) Magnetic field mapping in the vicinity of a PEC cylinder. (b) Magnetic field mapping in the vicinity of a cloaked PEC cylinder once stability has been reached. Extracted from [167]

Chapter 5

Parallelization of the TLM [3]

This chapter is devoted to the design of a parallel algorithm capable of modeling the Earth-ionosphere cavity with Transmission-Line Matrix method (TLM). We briefly review the different approaches available when using parallel techniques, which depend basically on the hardware underneath. The final decision was to start parallelization under shared memory environments, by using OpenMP directives. This election seems natural for a group with no previous experience on parallelization of algorithms, and who needs reliable results in a short period of time. The main difficulty when simulating the Earth-ionosphere cavity with TLM is that it is huge but very thin. We describe the inherent difficulties of using a spherical topology, which may seem the logical way to approach the problem. Finally, we decided to use cubic Cartesian topology. This decision implies the need of using at least $5{\cdot}10^7$ nodes to accomplish the required spatial resolution. In addition, due to the spatial arrangement of the cavity, some preprocess is necessary, as we will see. The preprocess converts the problem to one-dimensional (1D), and therefore any arbitrary geometry conveniently preprocessed can be solved by our parallel algorithm. This fact converts our code in a very promising tool for facing new problems. Then, the designed algorithm is described, as well as the optimizations applied to it, and how it was implemented with OpenMP directives. Finally, we show two independent benchmarks of the algorithm, for slightly different versions of it. The results show that, for small problems, superlinear speedup can be achieved, due to the re-use of the caches. For large problems, like the Earth-ionosphere waveguide one, speedups up to 16 have been measured with a 32 cores computer.

5.1 Parallelization techniques

For some years, CPUs have been evolving into a new paradigm. The maximum speed for processors seems to have reached its peak, due to issues relating to the dissipation of power, as well as problems with cross-talking between nearby lines. Manufacturers are no longer trying to increase the speed of CPUs, reducing it instead, in order to obtain better consumption ratios [168]. Despite the use of Graphic Processing Units (GPUs), which is growing as an emergent technology for large scientific calculations [169, 170], the new approach of CPU manufacturers is to ship computers which include multiple CPUs [171]. Not long ago, if you wanted to speed up your algorithm, according to Moore's law, you had only to wait for a new CPU to appear on the market. With the new paradigm, the algorithms must be revised, adapted and rewritten to take advantage of multi-CPU computers, and to keep them competitive, in order to solve problems of increasing complexity.

Numerical simulations are an important tool for the study of electromagnetic phenomena and for designing electromagnetic devices [172, 173]. Depending on the problem, analytical solutions are often impossible and experimental approaches are frequently too expensive for essay-error iteration; or they may not even be feasible when studying natural effects, like the electromagnetic cavities of planets and moons in the solar system. When simulating Maxwell equations, the transmission-line modeling method (TLM) presents some interesting advantages over other methods; it has inherent stability [141], and has E and H fields calculated at the same spatial point and time. These two facts are the main differences with Finite Difference Time Domain (FDTD), which defines each component of the electromagnetic field at a different position and even at a different time [174]. Another advantage of TLM is that unlike random-walk algorithms [175], it calculates solutions for every point of the lattice, which provides versatility for defining boundaries or sources, and simplifies connectivity with other numerical or analytical algorithms.

The parallelization techniques can be categorized attending to the hardware underneath. Different hardware approaches have been designed in the last years in order to boost the power of scientific calculations. We will briefly introduce the most common ones and explain their advantages and drawbacks. The principal idea behind all the approaches is to have several circuits (CPUs or cores) available for performing the computations. The differences arise in the way that

they communicate between each other and the nature of the circuit itself (case of GPUs).

5.1.1 Shared memory

The Shared Memory (SM) environments are computers with several sockets for microprocessors inside a single machine. In addition, each socket may accommodate a processor with multiple cores. The principal difference with other hardware solutions is that all the cores/CPUs of the system have access to the same memory addresses. Therefore, the exchange of information between threads is straightforward, and no special manual operations must be performed in the code to exchange information. Therefore, porting serial codes to SM paradigm is less critical than porting to other parallel architectures. However, there are still many new situations inherent to parallel programming, such as race conditions, synchronization, deadlocks or memory allocation policies which have to be accounted for, especially if we expect optimal performance. The communication between CPUs and the memory is internal and sustained by dedicated buses, so SM is the hardware solution which presents less global latency when accessing to memory.

Another concept which must be taken into account is the internal disposal of memory. The SM platforms can be either UMA (Uniform Memory Access) or NUMA (Non Uniform Memory Access), being the second much more common when the system holds a large number of circuits. UMA stands for systems where there are not preferred areas of memory for the individual cores, and the time access to an arbitrary portion of memory is the same regardless of the CPU accessing to it. On the other hand, NUMA architectures present different latency depending on which processor acceses which portion of memory. By doing this, the global latency can be reduced. In the practice, the most powerful SM machines are of NUMA nature, because this implementation permits a larger number of CPUs. The concurrent memory accesses by multiple CPUs become the bottleneck for large simulations which need a lot of memory (up to tens of GBytes in our case), and they are the main limitation for scalability. In this sense, it is worth noting that the more the number of processors in a computer, the less the available bandwidth for each core to access memory. In addition, the total amount of memory is not highly scalable. For instance, the most powerful machine that we use in this work comprises 32 cores (4 CPUs of 8 cores each), with 96 GB of RAM in

a NUMA deployment. There are not efficient SM computers with more than few hundred cores. The programmer must take into account the NUMA architecture and take some countermeasures (see below) to exploit efficiently the slow (when compared to CPU calculations) memory accesses. The most common Application Package Interface (API) used to exploit the parallel capabilities of SM computers is OpenMP.

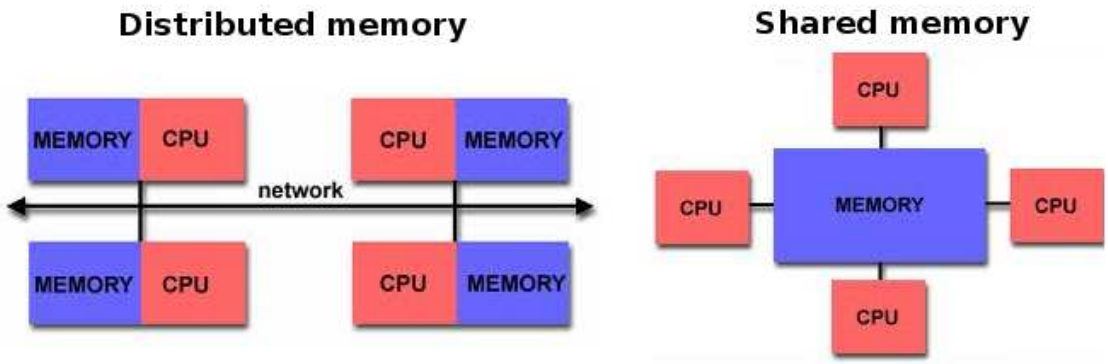

FIGURE 5.1: Hardware schemes for (left) Distributed Memory and (right) Shared Memory environments.

5.1.2 Distributed memory

The paradigm of Distributed Memory (DM) is more often known as cluster solutions. Several networked computers are all used for the same scientific calculation, and therefore we have all CPUs available from all the nodes. The bottleneck of this approach is the network communication between processes of different machines. Special network technologies, like for instance InfinyBand, have been developed to minimize this fact, but the passing of data between machines is much slower than for a single machine with multiple processors. On the other hand, this approach is much more scalable, in the sense that clusters with even thousands of independent cores are common. The total memory of the system does also scale very well, since each machine added to the cluster adds its memory to the global system. The principal drawback of this solution, in addition to the cost of acquiring and maintaining a cluster, is that the programmer must manually take care of the communication between processes, and therefore the port of serial codes becomes much more complicated. The typical API employed to work in these environments is Message Passing Interface (MPI).

It is very common in large clusters to use a hybrid solution between SM and DM. Nowadays clusters are usually comprised by several SM platforms, which execute SM code implemented with openMP directives, and they interact with other platforms in the cluster through MPI.

5.1.3 Graphics Processing Units (GPUs)

The use of GPUs for scientific calculations is growing fast, e.g., [169, 170]. GPUs were special kind of CPUs intended to deal with specific vector operations related to the display of 2D and 3D graphics. One GPU module can be composed of several thousands of GPUs. The principal problem of these systems is that the amount of memory available for each GPU is very limited, and their access to RAM is very slow. Usually these special processors are used to carry out low-level logical operations. Therefore, programming them efficiently becomes even trickier, and the approach is quite different to when programming in SM or DM platforms. Again the different approaches can co-exist on a single system, and a SM computer can include a GPU module. One interesting application of GPUs is to use them as a virtual memory space [176]. The idea behind is that the GPU module can re-calculate data each time we need it, with the purpose of not having to store all the results in memory but, instead, computing it on the fly as we need them.

There exist other dedicated parallel architectures, such as Vectorial Processing Units, Application-Specific Integrated Circuits (ASICs), Asynchronous arrays of simple processors (AsAPs), which will not be covered here, since a complete review of all the hardware available for parallelizing is out of the scope of this text.

5.2 Modeling of the Earth-ionosphere cavity

The main difficulty when modeling the Earth-ionosphere cavity arises from the asymmetry of its dimensions. The radius of Earth is approximately 6,370 km, while the height of the lower-ionosphere is only about 100 km. This makes a huge but thin spherically shaped cavity. Different works [18, 58, 177] have simulated the Earth-Ionosphere cavity of Earth, providing valuable information about it. They use the inherent symmetries of the cavity in order to extract the resonances with minimum computation. The works of [178, 179] report the first full-3D-FDTD

models of the cavity. In this work we go one step further by providing a full-3D parallelized TLM solution. This model enables the possibility of studying complex problems, like the interaction of multiple storms in arbitrary positions, the day-night asymmetry, the influence of solar proton events or the influence of local events like earthquake precursors, for instance.

In the Earth's atmosphere, lightning discharges from the thunderstorms are believed to be the strongest source of natural electromagnetic noise existing in the spherical shell cavity. Most of the energy produced by these natural events is propagated both at extremely low frequency, ELF: 3 Hz - 3 kHz, and very low frequency, VLF: 3 kHz - 30 kHz electromagnetic bands. Atmospherics or sferics is the term generally used to denote the natural electromagnetic radio noise in the VLF band. For the ELF band, Schumann resonance is the term employed. Any electromagnetic perturbation in a spherical shell can be described as a superposition of TE^r (transverse electric to r) and TM^r (transverse magnetic to r) modes, except for the TEM ones, which represent the static solution, taking the form of a plane wave without cut-off or resonance frequencies [45]. The TM^r modes can be divided into two different kinds. One consists of modes with wavelengths related to the Earth's diameter; these are known as Schumann resonances [4, 180]. The other kind of TM^r and all the TE^r modes have half-wavelengths proportional to the distance between the ground and the ionosphere; these are known as sferics [44, 97]. As commented before, Schumann resonances are modes globally coupled with the Earth-ionosphere cavity, which should be detected anywhere on Earth and their resonant frequencies are in the ELF band. Transverse modes, on the other hand, are included practically in the VLF band and are local phenomena because their energy remains concentrated around the excitation source [14, 181].

The electromagnetic wave propagation of atmospheric signals in the ELF range associated with the Schumann resonances can be modeled by considering the system as an inhomogeneous lossy cavity formed by two conducting spherical surfaces. This is justified by the relatively high conductivity values on the ground surface, around 4 S/m for seawater and from 10^{-3} to 10^{-5} S/m for land surface, and on the strong increase in atmospheric conductivity, which changes from 10^{-14} S/m near ground level to 10^{-3} S/m at a height just below 100 km, with an appreciable increment on the slope at an altitude of around 60 km [182], as is shown in Figure 5.2. With these values, at 25 Hz, a frequency in the middle of the range of interest, the ratio between the displacement and conductivity current, $\omega\epsilon_0/\sigma$,

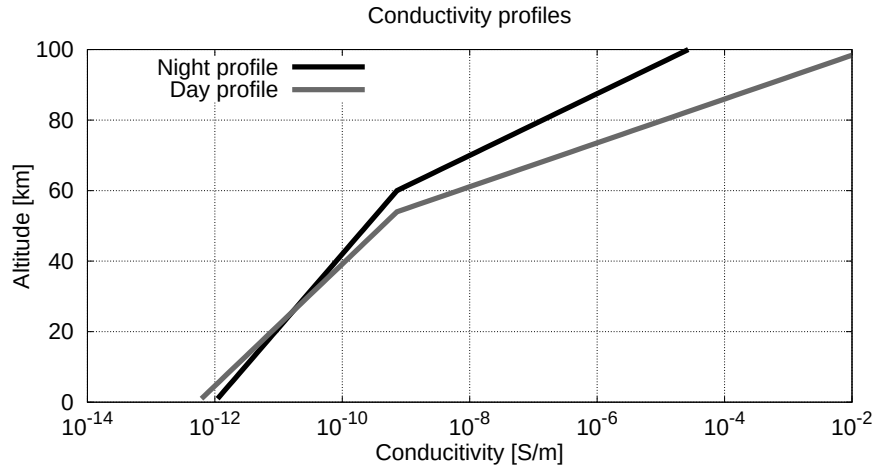

FIGURE 5.2: Conductivity profiles for Earth's lower atmosphere. Extracted from Pechony and Price [182]

is $1.4 \cdot 10^5$ at ground level and $1.4 \cdot 10^{-6}$ at a height of 100 km; consequently, the atmosphere behaves like a dielectric with low losses at ground level, becoming a good conductor for higher regions.

5.3 Parallelization

A first approach to the problem will suggest using spherical nodes, due to the spherical nature of the problem. However, using spherical TLM nodes adds two issues which have to be addressed:

1. The nodes have different size in each of its directions and, moreover, the size of the node is variable and depends of its position (see Figure 5.3). This different sizing implies the use of capacitive and inductive stubs at the node, which turns into dispersion errors at high frequencies [161], which have to be accounted for. This requirement of using very high inductive or capacitive stubs for these directions implies the use of a time step much lower than the allowed for the shortest direction. This high decompensation between lengths for a single node is on the basis of the serious dispersion problems mentioned.

2. Secondly, the spherical geometry has an indetermination at θ=0 (see Figure 5.3). When translated to TLM and the spherical shell problem, we find that for this location there is a special interface where several nodes must be

attached all together to a punctual area, and therefore the standard TLM node is no longer valid, requiring the use of a specific node for this singular point. This same problem has also been reported for cylindrical systems with the z-axis [183] (see Figure 5.3).

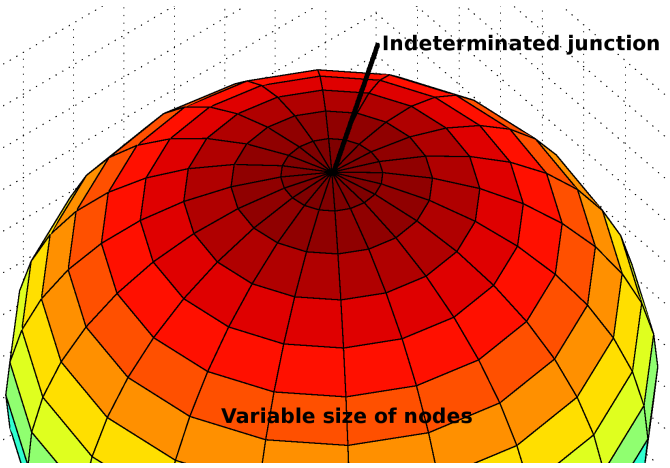

FIGURE 5.3: Problems associated to a spherical grid approach.

We had previous experience in working with spherical nodes [14, 58], and we finally decided to employ the cubic Cartesian node to avoid the problems of dispersion and indetermination at certain points and interfaces. However, there also exist two drawbacks for this selection which we discuss below:

1. The first is only apparent and related to the modeling of a spherical shape by cubes. The justification to this decision is that the size of the cubes is much smaller (5 or 10 km) than the radius of the sphere to model (6,370 km), and therefore, the model adjusts quite well the initial shape. In other words, although a Cartesian model of a sphere seems imperfect, the differences observed are concerned with high frequency details outside the band of interest.

2. Secondly, since the smallest size of the cavity is 100 km in the r direction, the maximum size of the TLM node will be 10 km, in order to have at least 10 nodes in the r direction. However, 10 km of size is very small node for the ϕ and θ directions (the Earth's perimeter is about 40,000 km), where no such a huge resolution is required. This means that the use of ten nodes along the r direction implies the use of about 4000 nodes for both angular directions which turns into memory and time calculation problems. The solution to

that is indeed parallelization, to reduce the amount of time required for the computations.

Due to the singular shape of the Earth-ionosphere cavity (spherical and very thin compared to its radius), if we try to fit the cavity on a Cartesian grid, most of the cells obtained will not belong to the concentric cavity, since they are located below the ground level or outside the ionosphere where the high conductivity avoids propagation. Taking the cell size as 10 km, and bearing in mind that the external radius of the cavity is approximately 6470 km, there are over $2 \cdot 10^9$ cells in a box that fits the geometry. Only around $5 \cdot 10^7$ (2.5%) of the cells belong to the concentric cavity itself. One 3D-SCN node needs, in its most simple form, 100 Bytes for a parallelizable solution. Fitting the problem in a Cartesian grid would require 200 GBytes of RAM memory. If we find a topology which only accounts for the relevant nodes, we will reduce the amount of RAM to 5 GBytes.

To program 3D-SCN nodes, each node would need at least 12 floats (no variable permittivity or permeability), or 18 for variable permittivity and permeability, for storing the line voltages, plus one integer at least to denote the kind of material simulated. We will neglect the amount of space required to store the matrices, since each matrix is used by several amount of nodes (all nodes which belong to the same medium). This yields 52 - 76 Bytes per node.

In addition, parallelizing the independent matrix multiplications of Equation 4.1 requires doubling the memory size required to hold the problem. Since the input voltage for one node is the output voltage for another node, V_n^i and V_n^r must be stored in different variables. Doubling the required memory size is a non-avoidable penalty of engaging parallelization, since we do not know the order in which the matrix multiplications will be performed. Therefore, we need a minimum of 100 Bytes (148 Bytes for the heterogeneous case) to hold a node, as mentioned above.

5.3.1 Preprocess

Our approach is to create an algorithm that attempts to work efficiently regardless of the geometry of the problem. Therefore, there is no general topology we can take advantage of. The problem is split into two parts: the preprocess and the TLM calculation itself. The purpose of the preprocess is to assign a unique identification

number to each node, independent of its spatial position. Each node must know the type of media it is simulating and the unique numbers of its adjacent nodes (see Figure 5.4). This adds a penalty of 6 integers (24 Bytes) to the memory requirements of each node.

In our algorithm, the geometry presented above needs less than 9 GBytes to be stored, because only the relevant nodes are taken into account. Thus, the second part no longer knows about the initial location of the nodes; instead, it has a one-dimensional vector of cells and data about the neighboring nodes in between. Any geometry of the problem is simplified to this concept, where the variable of interest is the total amount of nodes.

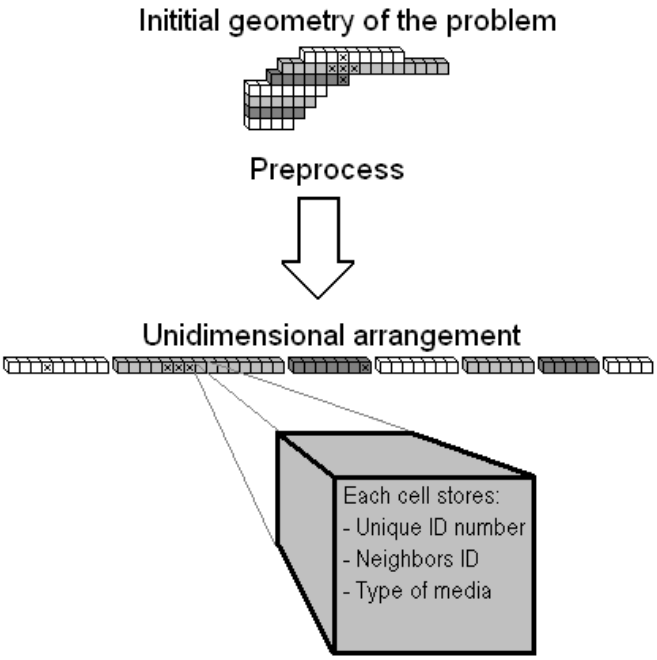

FIGURE 5.4: Role of the preprocess.

The preprocess is a fast operation compared to the TLM computation, and any method of implementing it (parallel or otherwise) will satisfy our needs. Basically, it consists in evaluating all the cells in the initial Cartesian grid in order to discover whether they belong or not to the geometry of interest. If the cell belongs, a unique identifier is assigned to it. The unique identifiers of its neighbors are also stored, together with and identifier of the cell medium. With this approach, if we want to face different problems than the spherical shell cavity, we will have only to write the preprocess code which translates the initial problem to this one-dimensional arrangement. The core computations can be efficiently coded and be used for any geometry.

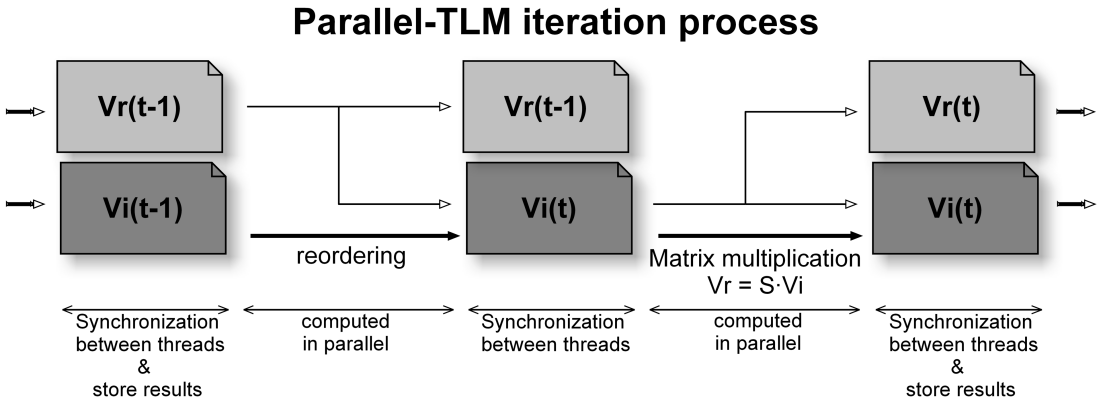

FIGURE 5.5: Diagram of the parallel-TLM iteration process. At each time-step there are two parallel zones; thread synchronization between them must be ensured. The gray boxes represent the portions of memory involved during the iteration.

5.3.2 The TLM core computation

The TLM algorithm presented in Chapter 4 is suitable for spatial parallelization, since calculations of new V_n^r and reordering of V_n^r into V_n^i for a given time step are independent. The main block of our algorithm is the iteration over time steps, calculating for each cell the new reflected pulses $V_n^r(t+1)$ from the reflected pulses $V_n^r(t)$ of adjacent cells.

Initially, this step in our algorithm consisted of two different parallel parts (See Figure 5.5). The first part transformed reflected pulses from nearby cells into incident pulses of the connected cells. This step was of a purely reordering nature and no specific calculations had to be made but, instead, large portions of memory had to be swapped. The V_n^r vectors were permuted and translated into V_n^i vectors, by using the information stored in the neighboring variables. The second part calculated V_n^r at each node by multiplying V_n^i by the scattering matrix (S).

However, it is possible to optimize the above algorithm. The idea is to avoid the large swapping of memory for reordering the pulses after reflection. Instead, we just swap the pointers of the two data structures. Of course, by doing this, we are not performing the reordering (or neighboring) process. The neighboring is implemented implicitly in the matrix multiplication, adding considerable complexity to this portion of code, but reducing the overall time of execution. We avoid one of the three memory reads required for each pulse, and in addition we avoid all the memory writing related to reorder the elements (again one per pulse). The initial algorithm reads each reflected pulse (operation which requires two memory

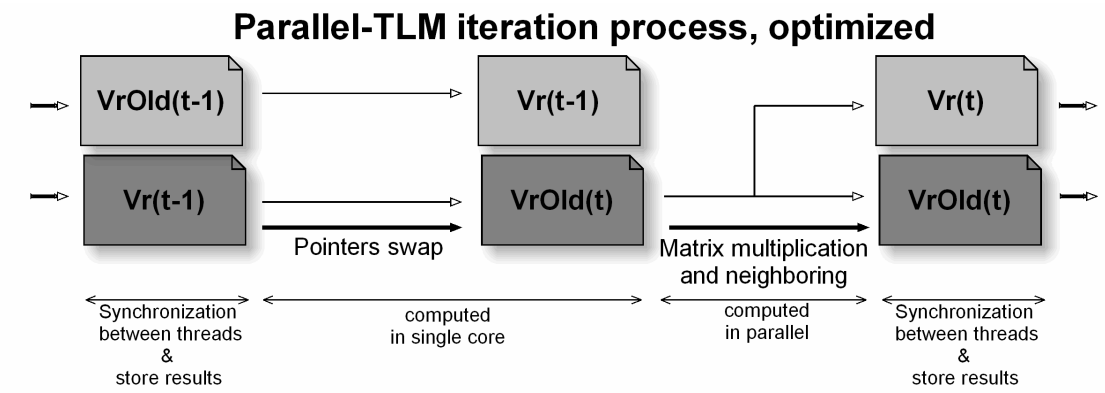

FIGURE 5.6: Diagram of the parallel-TLM iteration process optimized

accesses, one for determining the neighbor and one for obtaining the value of the pulse itself) and writes it into a new incident pulses structure (V_n^i), and afterwards reads it again, computes the matrix multiplication and stores the results into V_n^r. The second approach directly reads the pulse and the neighbor, computes the multiplication and stores the new V_n^r, at the cost of more binary operations (`if` decisions), which are much faster than memory accesses and writings. The nomenclature of V_n^r and V_n^i is not correct under this new paradigm, because we are not storing V_n^i anymore. A more appropriate calling for the variables is V_n^r and V_n^{rOld}.

The main complexity added for merging the two parallelizable sections into only one (see Figure 5.6) is that the new unified code is different for nodes which have at least one side at the edge of the problem. These nodes use their own reflected pulses as input voltage, instead of the neighbor ones. Different code for matrix multiplication must be written for each case of having one side at the border of the geometry. Finally, nodes with more than one side on the border require extra computations, but they are a small portion of the total (9% for the Earth-ionosphere waveguide). Therefore, we define an extra variable for each node which stores information about the borders of the node. This leads to a final memory size of 128 Bytes per node (12 floats for V_n^r, 12 floats for V_n^{rOld}, one integer for the kind of medium, 6 integers for the six neighbors, plus one integer to store information about its borders).

5.4 Implementation

The parallelization architecture chosen is Shared Memory (SM), using openMP directives and writing the code in C. Under this architecture, all the CPUs have access to the same memory space, except for the cache, where each CPU has its own. This architecture makes the exchange of data extremely simple compared to Distributed Memory (DM) environments [184]. Concurrent write access to memory becomes the bottleneck operation on SM environments, since the multiple core CPUs share the same memory access bus, this fact affecting scalability. However, each CPU has its own cache, thus giving a larger total cache memory with more CPUs in use. The machines employed in this study all have NUMA architecture memory disposal, as described in [185, 186].

The TLM computation loop employed is shown in high-level pseudo-code below, where the OpenMP directives have been included:

```
#pragma omp parallel private(private variables)
{   for(t=0..TotalTime)
    {   #pragma omp single
         {   //Swap the pointers to the voltage data structures
                    &Vr   ⇔  &VrOld;
               //system feeding
                    for(i=0..NumberOfFeeds)   V[i]= feeding;
               //store the relevant output
                    for(i=0..NumberOfOutputs) output=V[i];
         }
          //matrix multiplication and neighboring together
          #pragma omp for schedule (static)
               for(i=0..Nodes) Vr[i]=S*(Neighboring(VrOld[i]));
     }end for(t)
}end pragma parallel
```

The main loop of the code is inside a `#pragma omp`. In this way, the overhead of creating (and destroying) new threads needs to be computed only once for all the execution. It mainly consists of iteration over time steps, which is not parallelizable, and which needs synchronization of the threads which work inside each

iteration. Each time step iteration is divided into two blocks; a sequential block and a parallel block. The sequential block performs three different operations:

- Swap V_n^r by V_n^{rOld}. As we mentioned before, V_n^r and V_n^{rOld} must be stored in separate memory addresses in order to enable parallelization. At the beginning of a time step, the reflected pulses from the previous iteration become the incident pulses on the neighbor nodes. In our implementation we limit here to swap the pointers of the vectors V_n^r and V_n^{rOld}, and the complexity of neighboring swapping is done implicitly in the matrix calculations, avoiding extra reading and writing to memory, although adding a penalty of more processing and larger code, as commented before.

- System feeding. Our initial electromagnetic problem may have sources on its initial definition. These sources bring external voltage pulses to the system, which are added in this portion of code.

- Output storage. Some key nodes are marked as output and therefore the temporal evolution of their voltages is necessary to reconstruct the fields' evolution afterwards. All the line voltages at each time step from these output nodes are stored in memory, and dumped to disk at the end of the computation.

The parallel block is in charge for the matrix multiplication of each node. It is composed of a parallel `for`. Since the V_n^r calculation can be performed independently for each node, the OpenMP directive (`#pragma omp for`) is in charge to distribute the computations between the available number of threads. Therefore, each thread will compute a portion of the total range of `i`. Since the clause `schedule (static)` is present, all the available threads will iterate an equal amount of the `i` range. If this clause would not be present, the default behavior is to balance the amount of load dynamically, with an extra computation cost for monitoring and redistributing the work to different threads. This approach is useful when different iterations may require considerable different amount of CPU time.

In order to reduce the total time of computation, several optimizations have been included here, which make the real code complex and hard to interpret. The most complex one, deals with the implicit neighboring of the nodes in the matrix multiplication. It is implemented in such a way that the nodes on the edges of the initial geometry are treated in a different manner than the internal nodes.

The code is different but the amount of computation remains similar for internal and external nodes, except for the nodes which are edge in more than one of its sides. In this case the computations are a bit larger (six extra `if else` sentences). The number of nodes being edge in more than one side is usually small on most geometries. For the case of the Earth-ionosphere cavity, roughly 9% of the nodes are multi-edge. It is worth noting that for our problems scheduling the `parallel for` as `static` improves the performance of the algorithm, although 9% nodes require a bit more computation than the rest.

As we have seen in Equation 4.36, S is a disperse matrix with many zeros, so direct implementation of the matrix multiplication is preferable to using optimized libraries, such as AMD Core Math Library (ACML). For the general case of variable permittivity and permeability, 126 multiplications and 108 additions have to be carried out for each cell in order to obtain V_r from the matrix multiplication. All these computations are independent between cells and comprise the most parallelizable part of the TLM algorithm. Synchronization between threads is of vital importance in the algorithms presented above. All the threads must finish the one time step before any of them starts computing the next time iteration.

Many simulations of the Earth-ionosphere cavity do not need to account for variable permittivity or permeability, and the electric conductivity of the nodes is the same regardless of the direction. Under this situation, we can avoid the use six stubs on the SCN node (see Section 4.5). Then, the matrix S is considerably simplified and therefore the number of multiplications and additions can be substantially reduced. In fact, the resulting matrix can be defined by only three coefficients:

$$S = \begin{bmatrix} a & c & d & 0 & 0 & 0 & 0 & 0 & c & 0 & -d & a \\ c & a & 0 & 0 & 0 & d & 0 & 0 & a & -d & 0 & c \\ d & 0 & a & c & 0 & 0 & 0 & c & 0 & 0 & a & -d \\ 0 & 0 & c & a & d & 0 & -d & a & c & 0 & c & 0 \\ 0 & 0 & 0 & d & a & c & a & -d & 0 & c & 0 & 0 \\ 0 & d & 0 & 0 & c & a & c & 0 & -d & a & 0 & 0 \\ 0 & 0 & 0 & -d & a & c & a & d & 0 & c & 0 & 0 \\ 0 & 0 & c & a & -d & 0 & d & a & 0 & 0 & c & 0 \\ c & a & 0 & 0 & 0 & -d & 0 & 0 & a & d & 0 & c \\ 0 & -d & 0 & 0 & c & a & c & 0 & d & a & 0 & 0 \\ -d & 0 & a & c & 0 & 0 & 0 & c & 0 & 0 & a & d \\ a & c & -d & 0 & 0 & 0 & 0 & 0 & c & 0 & d & a \end{bmatrix}$$

where d=1/2, and the other two depend on the conductivity G:

$$a = -\frac{G}{2(4+G)} \qquad\qquad c = \frac{2}{4+G}$$

If we define the intermediate variables

$$\begin{aligned} A &= a(V_1^i + V_{12}^i) + c(V_2^i + V_9^i); & Z &= d(V_3^i - V_{11}^i); \\ B &= c(V_1^i + V_{11}^i) + a(V_2^i + V_9^i); & Y &= d(V_6^i - V_{10}^i); \\ C &= a(V_3^i + V_{11}^i) + c(V_4^i + V_8^i); & X &= d(V_1^i - V_{12}^i); \\ D &= c(V_3^i + V_7^i) + a(V_4^i + V_8^i); & W &= d(V_5^i - V_7^i); \\ E &= a(V_5^i + V_7^i) + c(V_6^i + V_{10}^i); & V &= d(V_4^i - V_8^i); \\ F &= c(V_5^i + V_7^i) + a(V_6^i + V_{10}^i); & U &= d(V_2^i - V_9^i); \end{aligned}$$

then, the reflected pulses can be obtained as

$$\begin{aligned} V_1^r &= A + Z; & V_5^r &= E + V; & V_9^r &= B - Y; \\ V_2^r &= B + Y; & V_6^r &= F + U; & V_{10}^r &= F - U; \\ V_3^r &= C + X; & V_7^r &= E - V; & V_{11}^r &= C - X; \\ V_4^r &= D + W; & V_8^r &= D - W; & V_{12}^r &= A - Z; \end{aligned}$$

reducing the computation to 18 multiplications and 36 additions per node.

5.5 Algorithm benchmarking

5.5.1 Rectangular cavity

In order to see the relevance of the parallelization of the code, we have benchmarked a canonical problem of a 3D rectangular cavity run on different platforms. In addition, the results obtained served to validate the code, since it is a problem with known analytical solution. The problem consists of a 3D rectangular cavity with perfect conducting walls and an homogeneous dielectric medium inside. We introduce an initial pulse and let it propagate. In order to study the scalability of the algorithm, we have performed four different simulations of the problem, in which we change the size of the cavity as well as the number of time iterations. The general node which accounts for variable permittivity, permeability and conductivity has been employed, together with the implementation which does not perform the reordering implicitly. The dimensions of each simulation can be seen in Table 5.1.

TABLE 5.1: Description of the four simulations performed for benchmarking.

Legend	No. of nodes	Memory size	Time iterations	step-node computations
P1	10^4	1.72 MB	10^5	10^9
P2	$4 \cdot 10^4$	6.88 MB	$2.5 \cdot 10^4$	10^9
P3	10^6	172 MB	10^3	10^9
P4	$5 \cdot 10^7$	8.6 GB	$2 \cdot 10^1$	10^9

P4 simulates the largest cavity, with a number of nodes of the same order as the Earth-ionosphere cavity. P3 has still more nodes than P1 and P2 by two orders of magnitude. The time iterations were compensated in each simulation in order to have the same total number of step-node computations in all the simulations. An step-node is a unit of computation which comprises the process of computing one matrix multiplication to obtain V_r plus the reordering required for that node. The number of step-nodes in a simulation is calculated by multiplying the time iterations by the number of nodes.

The calculations of P1 and P2 were repeated, decreasing the time steps by a factor of ten. The results showed a total decrease in the execution time by a factor of ten regardless of the number of CPUs employed for the calculations. This

trial illustrates the sequential nature of the iteration over time, i.e., doubling the time iterations will always double the required computation time, regardless of the RAM required by the problem, the number of nodes or the amount of CPUs employed.

We have measured the total execution time over different computers and using a different number of CPUs, in order to determine the scalability of our algorithm. Three different computers have been used in the benchmarking process:

- SuperMicro8 (SM8). Server with 2 AMD opteron quad-core processors 2.0 GHz and 32 GB RAM, in Not Uniform Memory Access (NUMA) configuration. The OS is OpenSUSE 11.4 and the compiler employed is opencc 4.2.4 (level 2 of optimization).
- SunFire16 (SF16). Server with 8 AMD opteron dual core processors 2.2 GHz and 64 GB RAM, in Not Uniform Memory Access (NUMA) configuration. The OS is SUSE Linux Enterprise 10 and the compiler employed is Opencc 4.2.4 (level 2 of optimization).
- SuperMicro32 (SM32). Server with 4 AMD opteron eight-core processors 2.0 GHz and 96 GB RAM, in Not Uniform Memory Access (NUMA) configuration. The OS is OpenSUSE 11.4 and the compiler employed is opencc 4.2.4 (level 2 of optimization).

The use of level 2 of optimization (-O2) leads to a decrease of 5 times the execution time of a single CPU execution, when compared to level 0 of optimization, but at a cost of worse scaling. Nevertheless, the best absolute times are obtained with this level of optimization (-O2). The code has been written in C and is exactly the same on every machine and in every simulation.

In Figure 5.7, we show a summary of the results obtained with the different computers presented above. On the left side, the total execution time is presented as a function of the number of CPUs employed in the calculation. On the right side, the speedup (execution time with 1 CPU / execution time with n CPUs) is presented, again as a function of the number of CPUs. In an ideal case, doubling the number of CPUs would double the speedup.

Regarding the total time execution pictures, we can observe the speed of servers when execution is carried out over one CPU, SunFire16 being the slowest and

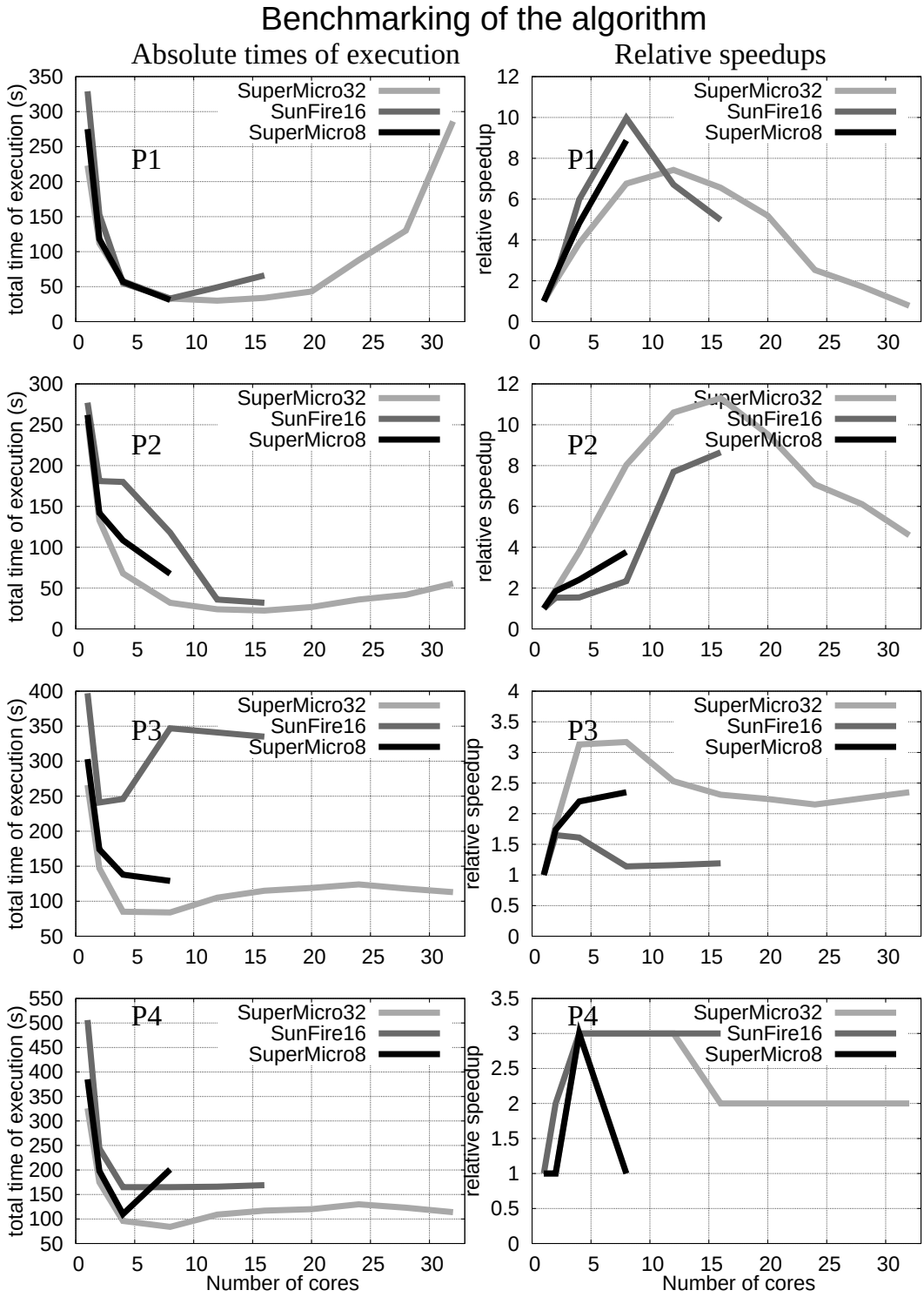

FIGURE 5.7: Speedups for the four canonical problems with a first touch policy memory allocation.

SuperMicro32 the fastest for all the simulations. It can also be seen that as the size of the problem increases (from P1 to P4) the computation of step-nodes becomes more costly.

Regarding the results shown in Figure 5.7, one can see that there is not a simple relation between the scalability of the algorithm and its size. It depends on multiple variables, such as multi-core configuration, disposal of RAM memory or the total size of cache.

The worst results are obtained by SunFire16, and this is probably due to its internal arrangement of CPUs. It is composed of 8 dual-core circuits, in contrast to SuperMicro8 (2 quad-cores) and SuperMicro32 (4 eight-cores). It seems that larger multi-core circuits give better results than many smaller (dual-core) circuits for our algorithm.

Maximum speedups are obtained for smaller problems (P1 and P2), and we believe this is due to the cache effect, as stated by Ciamulski and Sypniewski [186]. The cache sizes (L2) for the different machines are 8· 512 KB = 4 MB for SuperMicro8, 16· 512 KB = 8 MB for SunFire16, and 32 · 512 KB= 16 MB for SuperMicro32. By looking at Table 5.1, we can see that cache size and memory usage in P1 and P2 simulations are in the same order of magnitude, thus access to RAM is drastically reduced for these simulations. For P3 and P4, the memory usage required exceeds the cache capacity by two or three orders of magnitude, and therefore the speedup does not reach its maximum values.

Under specific circumstances, superlinear speedup is achieved by our algorithm. It occurs for the smallest memory size problem (P1), with platforms SuperMicro8 and SunFire16. The superlinear speedups achievements are summarized in Table 5.2. The values which correspond to superlinear speedup are shown in bold font. This behavior is due to a better re-use of the cache memory, which is much faster than RAM memory. We can see that this behavior is architecture-dependent, since the superlinear speedup is not achieved for the same problem under SuperMicro32 platform.

The maximum speedup obtained is 11.3, for P2, using SuperMicro32 with 16 CPUs. This is a good result if we compare it with other TLM parallelization attempts. In [187], speedups of up to 8.72 are obtained with 12 CPUs in a distributed memory environment, while in [188] a speedup of 7.1 is obtained with the use of GPUs.

TABLE 5.2: Speedups obtained in P1 simulation.

	2 cores	4 cores	8 cores	12 cores	16 cores
SuperMicro8	**2.33**	**4.82**	**8.87**		
SunFire 16	**2.15**	**5.98**	**9.97**	6.71	4.98
SuperMicro32	1.99	3.84	6.76	7.43	6.56

5.5.1.1 Memory allocation policy

The mentioned computers are constructed under NUMA architecture. That means that the access time (for both reading and writing) may vary depending on which CPU wants to access which portion of memory. As programmers developing code for a SM environment, we cannot decide in which physical address we want to store each variable or vector, this is done internally by the OS. The default policy is to reserve memory on the nearest memory space. Since the reservation is made at the beginning of the code by a single thread, some memory areas hold all or most of the variables, i.e., all their available space. However, there is a tool called `numactl` which allows the programmer to specify some rules to the OS on how to reserve memory. We can ask for using only certain portions of the memory, for instance. An interesting policy is the round-robin memory allocation, which has been used in this study to boost the performance of the algorithm. The idea behind round-robin planification is very simple; it consists in filling the resources (the RAM memory in this case) in a circular way, taking into account all the different physical areas. In this way, all the different portions of memory will hold part of the data. Since each CPU has its preferred areas of memory, showing less latency when accessing to them, if we do not specify any `numactl` policy, the data will be likely be stored contiguously, meaning that few CPUs will show low latency when accessing to them while the rest will need long times to retrieve data. In addition, there will be competition between the nodes when trying to write through the same bus. This situation is avoided by making use of the round-robin memory allocation policy, which establishes that the data will be distributed equally among the different physical areas of the memory. With this situation, the global execution time of P3 and P4 is considerably decreased when using several CPUs, as it is shown in Figure 5.8. This optimization does not affect P1 and P2, since most of the variables fit in the local caches, and the results are practically the same regardless of the memory policy set. On the other hand, speedups up

to 12 for P3 and 15 for P4 have been achieved, with the use of 32 cores in SM32 computer.

5.5.2 Modeling atmospherics

The algorithm described in Section 5.3 has been employed to simulate a local portion of the Earth-ionosphere waveguide, on a very first approximation. The purpose of this simulation is again to benchmark the algorithm. The surface of Earth behaves like a good conductor in the Very Low Frequency range (VLF, i.e., in the order of kHz), with conductivity $\sim 10^{-2}$ S/m for ground and ~ 3.2 S/m for sea water [189]. Above the ground there is air, which is of dielectric nature. As the altitude increases the number of free electrons increases too, the density of neutral decreases, and the air starts behaving like a conductor. A typical conductivity profile with altitude is shown in Figure 5.2. Since the atmospherics are attenuated by the conductivity of the system, they are of local nature and exist only in an area of few thousand km. Therefore, for the benchmarking purpose of this section, we will consider as a first approximation to the waveguide two conducting parallel plates separated by a dielectric of varying conductivity, and we will neglect the sphericity of the waveguide.

The main excitation sources of the waveguide are lightning, they generate a broadband signal which differs in orientation, strength and duration depending of its nature (cloud to ground, cloud to cloud, Q-bursts, etc.). A typical stroke in positive cloud to ground lightning generates a current which has been depicted in Figure 5.9 [190]. This current has been employed as excitation source in our problem.

The signal originated by the stroke travels a certain distance guided between the two parallel plates before vanishing due to losses. On a first approximation, the system can be regarded as a parallel infinite plates waveguide. According to [191], for a lossless waveguide of this geometry the cut-off frequencies are located at $f_n = nc/2h$, where c is the speed of light in vacuum, h is the distance between the parallel plates, n is the mode number, and f_n the associated cut-off frequency of the mode (see Chapter 1).

The problem has been simulated with our algorithm, both for a lossless and for a lossy waveguide. For the lossless waveguide, the conductivity is supposed

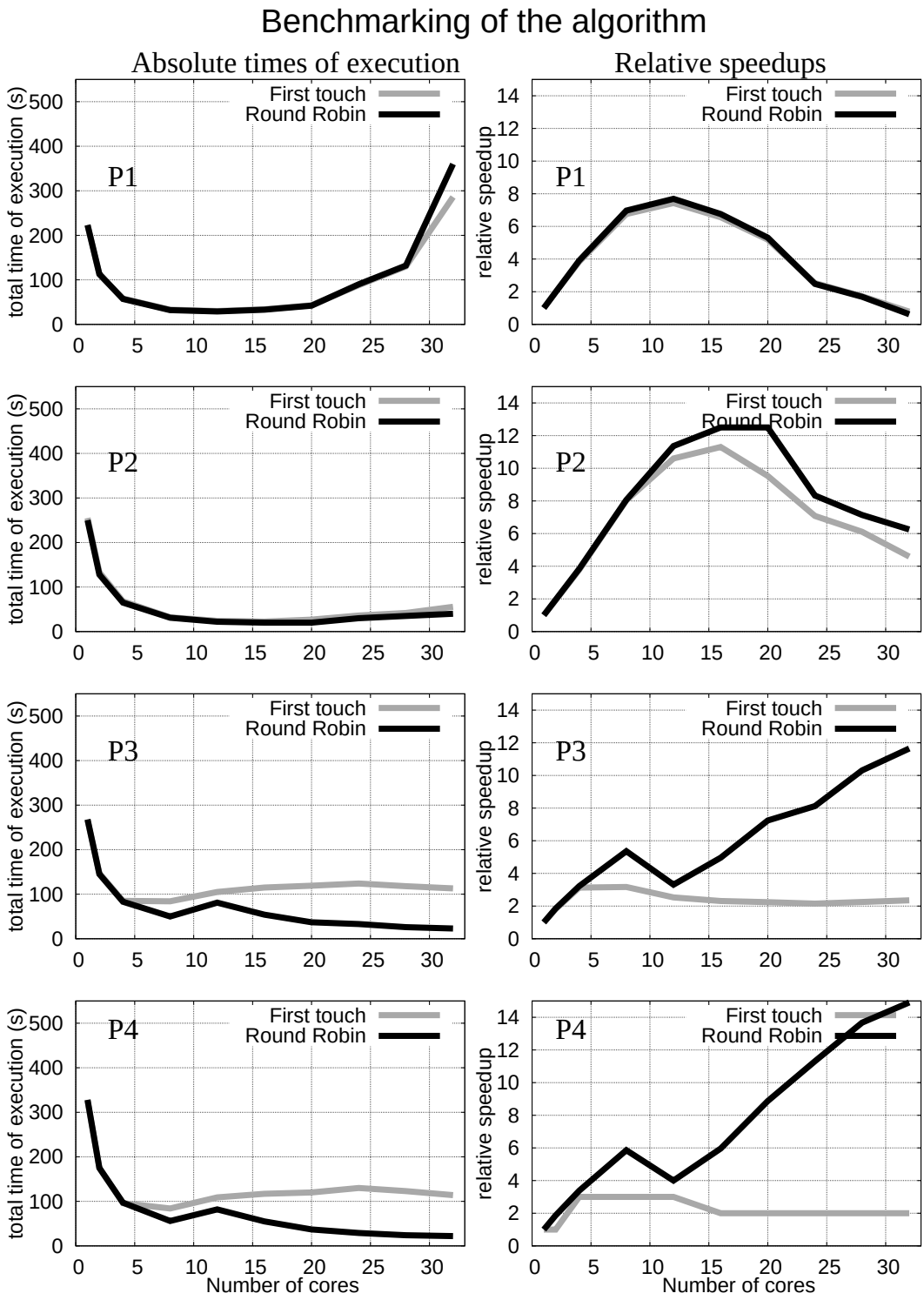

FIGURE 5.8: Speedups for the four canonical problems with a Round-robin policy memory allocation.

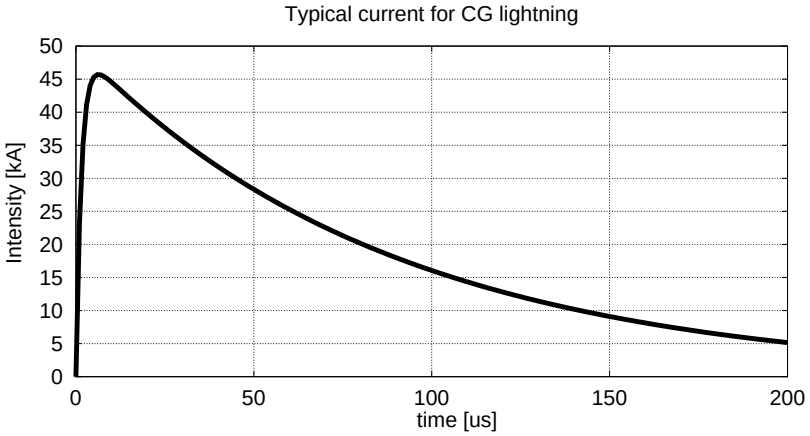

FIGURE 5.9: Typical current for cloud to ground lightning.

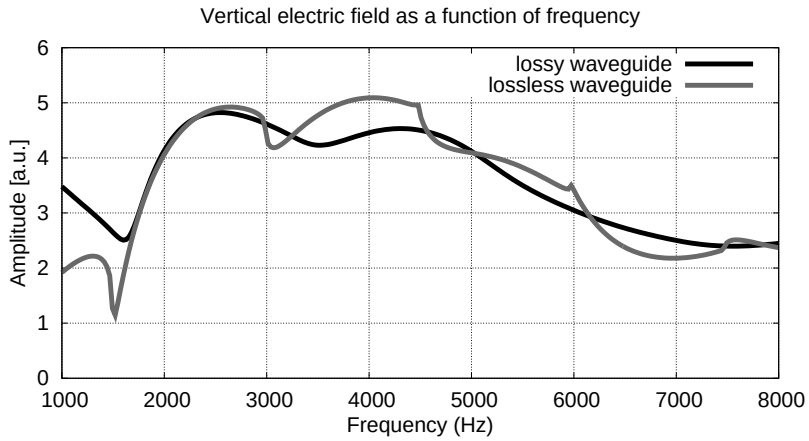

FIGURE 5.10: Detail of the first cut-off frequency for the lossless and the lossy Earth-ionosphere waveguide.

to be zero in the dielectric. For the lossy waveguide, the conductivity profile from Figure 5.2 is applied. In both cases the parallel plates are taken as perfect conductors. A detail of the first and second cut-off frequencies are depicted in Figure 5.10, which corresponds to electric field in the z direction, at a distance of 45 km in the y direction from the source (see Figure 5.11 for definition of the directions). It is interesting to see the effect of the conductivity, which increases the value of the cut-off frequencies, being equivalent to have a narrower waveguide. The quantitative results of this simulation are in agreement with the experimental results from Chapter 3.

We have measured the total execution time over different computers and using a different number of CPUs, in order to determine the scalability of our algorithm. Two different computers have been used in the benchmarking process:

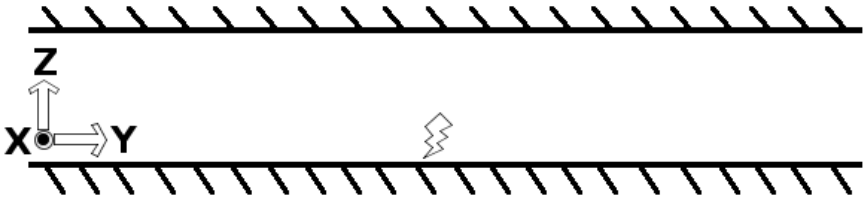

FIGURE 5.11: Spatial arrangement of the problem

- SuperMicro8 (SM8). Server with 2 AMD opteron quad-core processors 2.0 GHz and 32 GB RAM, in Not Uniform Memory Access (NUMA) configuration. The OS is OpenSUSE 11.4 and the compiler employed is opencc 4.2.4 (level 2 of optimization).
- SuperMicro32 (SM32). Server with 4 AMD opteron eight-core processors 2.0 GHz and 96 GB RAM, in Not Uniform Memory Access (NUMA) configuration. The OS is OpenSUSE 11.4 and the compiler employed is opencc 4.2.4 (level 2 of optimization).

The problem benchmarked makes use of symmetry and the initial grid is two-dimensional. According to Figure 5.11, the symmetry is applied in the x direction. The conductivity profile is extended along z direction, and the output measured at a certain distance on the y direction. The node size is 1.5 km, the time step is 2.5 μs, the number of time steps is 7,500, and the total number of nodes is $\sim 10^6$ (67 nodes in z, 15,000 nodes in y). For this simulation, the optimized algorithm from Section 5.3 has been employed, together with the simplified node which permits to substantially reduce the computations. The excitation is placed next to the ground, in the center of the waveguide.

With this configuration, a total of $7.5 \cdot 10^9$ step-node computations must be performed to solve the problem. The total execution time and relative speedups are shown in Figure 5.12, for the two platforms. A maximum speedup of 6 is arisen with SM8, when making use of its 8 CPUs. On SM32, we obtain a maximum speedup of 16 when using 30 CPUs.

Due to the size of the problem (roughly 128 MBytes), again we obtain better results when the round-robin memory allocation policy is employed. The comparison is plotted in Figure 5.12.

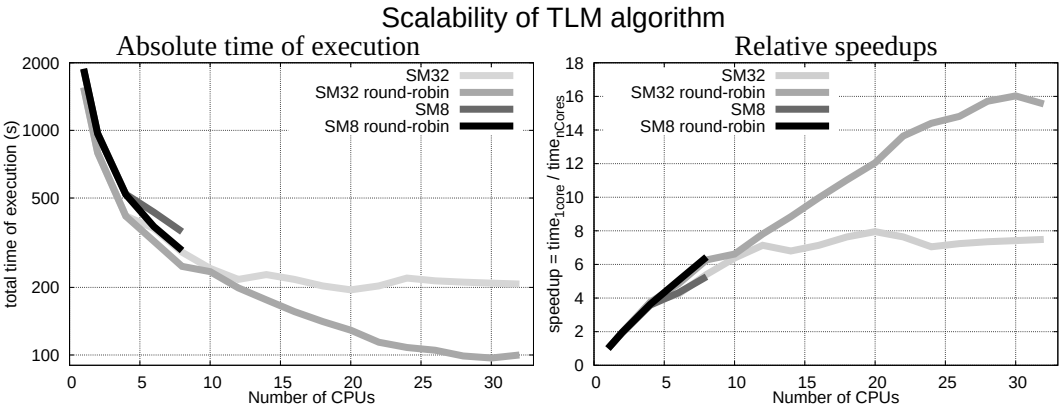

FIGURE 5.12: Total time of execution and relative speedups for the different platforms

5.6 Conclusion

We have described the different hardware solutions for computing parallel-intensive code. Then we have focused on modeling the Earth-ionosphere cavity by means of an efficient parallel algorithm based on TLM. The inherent parallel areas of the method have been pointed out, and a translation from arbitrary topology to 1D has been defined (preprocess). We have parallelized it for shared memory architectures, by using OpenMP directives. Several optimizations have been made recursively to the initial code, and the most important ones are briefly explained. The solution obtained is benchmarked by two independent studies, which yield similar results over different computers. In order to obtain the maxima speedups, it is necessary to set a policy of round-robin memory allocation, in order to minimize the effects of the NUMA architecture. Speedups of up to 16 have been measured by using 32 CPUs, for models of the size of the Earth-ionosphere cavity. Under certain circumstances (small memory requirements which allow the model to fit in the caches), superlinear speedup has been achieved.

Chapter 6

Modeling the Earth-ionosphere cavity

In this chapter, we present the first results for our 3D parallel algorithm, when applied to the study of the Earth-ionosphere cavity and the Schumann resonances. First, the employed model for lightning, i.e., the source or excitation for the simulations, is introduced. Then, a simulation of the cavity without accounting for losses is performed. The results are in excellent agreement with the analytical solution for the problem, including the spatial distribution of the modes. After that, a conductivity profile which varies with height is added to the model, and the resulting SR frequencies are lower than for the lossless cavity, as expected. Finally, three simulations which make use of the 3D nature of our model are presented, with the aim of showing the future potential of the tool. However, processing the large and complex amount of output data that the models give will require specific techniques, like for instance the one shown by Morente et al. [192], which will not covered here, since the data analysis from the models deserves a deep study which is beyond the scope of this thesis.

6.1 Model employed for lightning discharges

The excitation of all the simulations presented in this chapter was based on a vertical current of 5/10 km length, i.e., the length of one node. The time evolution of the current is generated by a double exponential, as it was introduced in Section

5.5.2, see Figure 5.9, following the equation

$$I = I_0 \left(e^{-\alpha t} - e^{\beta t} \right) \tag{6.1}$$

with the typical values for a positive cloud to ground lightning of $1/\alpha$=88 μs, $1/\beta$=1.55 μs. A typical value for I_0, for a severe stroke, can be up to 50 kA or even more. However, in the simulations, we employed arbitrary units, and I_0 usually equals to 1.

In Figure 6.1, DFT modulus of the current employed for lightning can be observed. The response is constant in the ELF band, so the spectra that we will show in the following simulations correspond to the impulse response of the system.

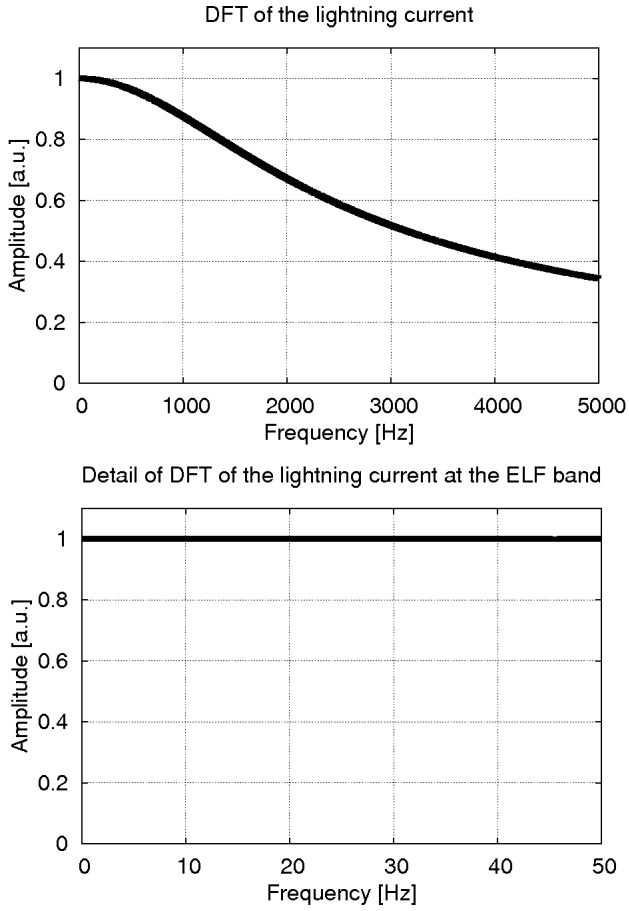

FIGURE 6.1: DFT modulus of the current employed to model the lightning sources for the model.

6.2 Earth-ionosphere cavity without losses, SR dependence with distance to the source

The first simulation we want to present in this chapter is the simplest one, and it is interesting in order to validate the algorithm presented in the previous chapter, when applied to the whole Earth-ionosphere cavity. The cavity has been considered as the space between two concentric spheres of 6,370 and 6,470 km, with perfect conducting walls at the borders and no conductivity in the interior. The spherical shell has been modeled by cubic nodes, in this case of Δl=5 km of size. The total number of nodes is $\sim 4.14 \cdot 10^8$, and the amount of RAM required is ~61.5 GBytes. Around 1.1 GBytes is employed for storing the outputs. For a spatial grid with 5 km resolution, the time step required is 8.34 μs. The number of time iterations calculated was $2.4 \cdot 10^5$, and therefore the simulated time length is ~2 s. With these parameters, when the FFT is computed, a frequency resolution of 0.5 Hz is achieved. The total time of computation required when using 32 cores on SM32 (see Section 5.5.1) is roughly $6.0 \cdot 10^5$ s, i.e., around seven days.

The excitation source of the cavity has been located at θ=0 and r=6,372 km, i.e., the North Pole. The excitation corresponds to a vertical positive Cloud to Ground (+CG) lightning, and its current is shown in Figure 5.9. This stroke starts at t=0, and lasts for 500 μs.

With this spatial arrangement, the problem has symmetry over the ϕ coordinate, and the therefore the outputs had been located all ϕ=0. A total of 101 nodes are marked as output, and they are equally spaced along the coordinate θ, from 0 to π, for r=6,370 km, i.e., at the surface, because it is the common location for SR measurements.

As expected from Section 1.3, the two relevant components of the electromagnetic field are E_r and H_ϕ. In Figure 6.2, we have plotted the six components of the output corresponding to θ=$\pi/4$, in order to show this fact. The other output nodes show similar results, where the two components mentioned are much greater than the rest.

In order to corroborate the results from the simulations, we have plotted the relationship between the modal amplitude of the six first SR and the angular distance to the source for the 101 nodes marked as output (θ=0, θ=$\pi/100$,..., θ=π), in Figure 6.3. This result is in agreement with Figure 2.10.

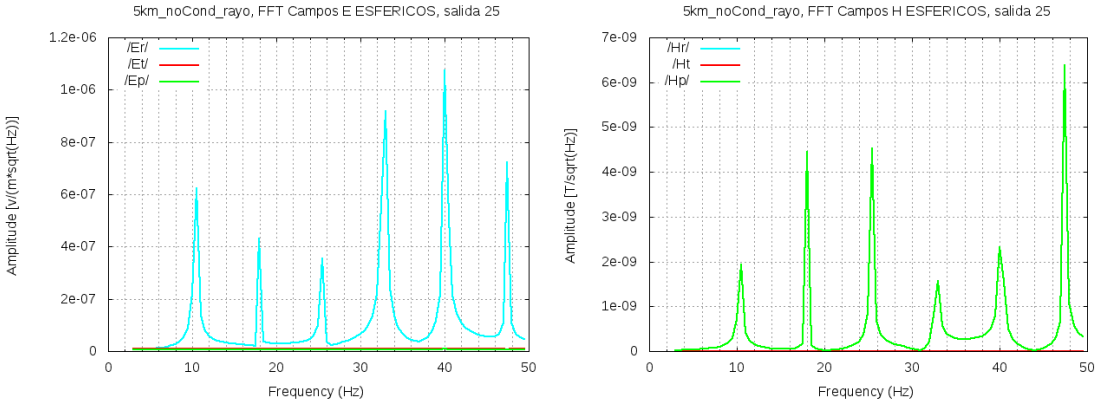

FIGURE 6.2: Spectra of the six electromagnetic components. The relevance of E_r and H_ϕ can be observed.

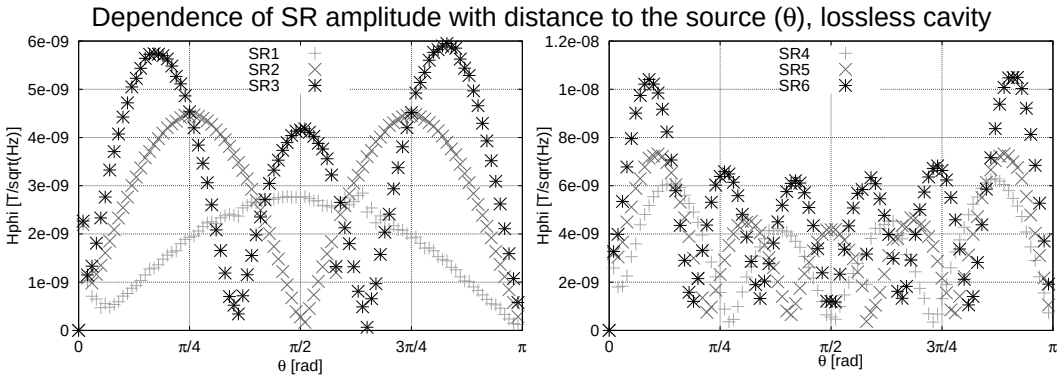

FIGURE 6.3: Dependence of SR modal amplitude with θ, for the lossless cavity.

The simulation has been repeated changing only the size of the spatial grid to Δl=10 km. Doubling the size of the nodes reduces by a factor of eight the number of nodes, at the cost of a poorer fitting of the spherical geometry and worse spatial resolution. The maximum valid frequency is also reduced by a factor of two, but this is not important for the study of SR, because the top frequency is still 3 kHz (the condition is $\lambda \geq 10\Delta l$). The amount of memory required is reduced to 9.1 GBytes (with 1.1 GBytes for storing the results). The time of computation, again with 32 cores in SM32, is reduced to $7.6{\cdot}10^4$ s, i.e., roughly 21 hours. The magnetic fields in ϕ direction at an angular distance of $\pi/4$ of the two simulations are compared in Figure 6.4.

The six maxima from each spectra of H_ϕ have been extracted and averaged, with the aim of using them as a proxy of the resonance position. The results are shown in Table 6.1, for both simulations.

It can be observed that the results for the central frequencies of the six SR are

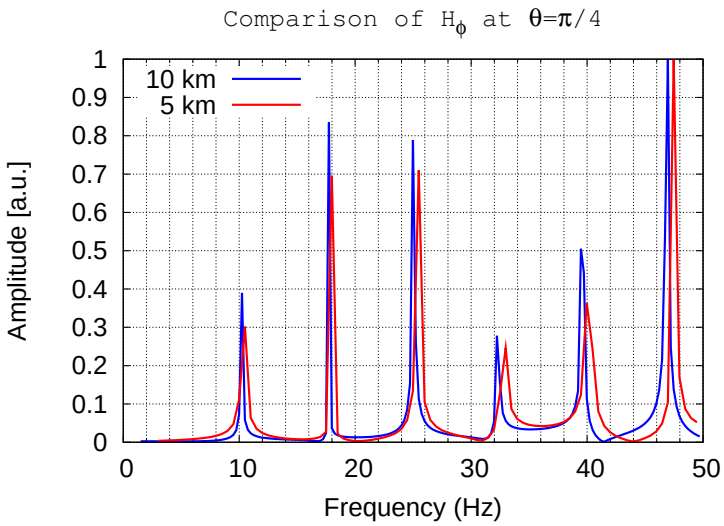

FIGURE 6.4: Comparison of H_ϕ at $\theta=\pi/4$, for the two simulations (5 km and 10 km).

TABLE 6.1: Central values in Hertz for the six first SR, lossless cavity. The last file shows the values obtained with the analytical solution for the same cavity.

	1st SR	2nd SR	3rd SR	4th SR	5th SR	6th SR
10 km	10.24	17.74	24.98	32.35	39.63	46.93
5 km	10.47	17.99	25.48	32.96	39.98	47.47
Analytical	10.51	18.20	25.75	33.24	40.71	48.17

similar in the two simulations and with the results from the analytical solution. For the case of the 10 km size simulation, the errors for the central frequencies are always under 3%. This error is reduced to less than 1.5% for the 5 km simulation.

6.3 Earth-ionosphere cavity with losses

The next simulation that we will present shares all the configuration with the previous one, with the exception that the conductivity profile from Figure 6.5 has been added to the cavity, and that the number of time iterations has been increased to 480,000 (for the 10 km model) in order to obtain better frequency resolution. The frequency resolution achieved is 0.125 Hz. The computation time required is therefore roughly 42 hours, for the 32 cores computer.

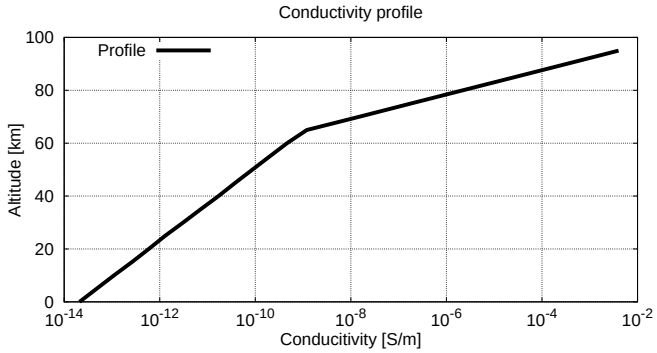

FIGURE 6.5: Conductivity profile for the lossy cavity which does not take into account the day-night asymmetry. Extracted from [58].

In Figure 6.6, we have plotted the output spectra for the magnetic field for three different values of the distance to the source (θ=$\pi/4$, $\pi/2$, $3\pi/4$). It is interesting to note that the resonances are not sharp and well defined for the lossy cavity, as a main difference with the lossless cavity, its quality factor, Q, being a new parameter to take into account.

In addition, the frequencies are sensibly lower than in the previous model. The central values of the frequencies, obtained as an average from all the outputs, are summarized in Table 6.2. Since the frequency of the resonance varies depending on the distance to the source at which is measured, the standard deviation of the distribution for each frequency has been also calculated.

TABLE 6.2: Central values (f_c) in Hz and standard deviation for the four first SR, lossy cavity. The central values differ depending on the distance to the source.

	1st SR	2nd SR	3rd SR	4th SR
f_c 10 km	8.11	14.57	20.96	24.42
Std. dev. 10 km	0.260	0.384	0.502	0.601
f_c 5 km	8.23	14.76	21.26	27.78
Std. dev. 5 km	0.343	0.451	0.538	0.551
Experimental [12]	7.8	13.9	20.0	26.0

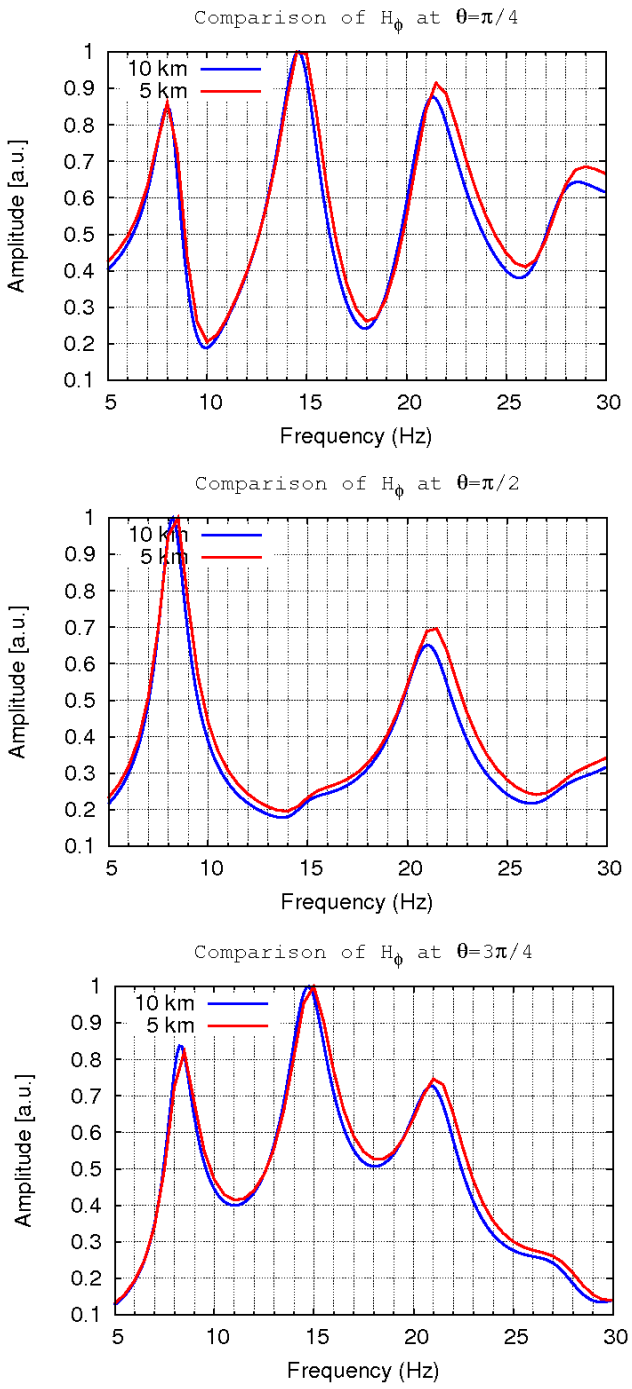

FIGURE 6.6: Different H_ϕ spectra ($\theta=\pi/4,\ \pi/2,\ 3\pi/4$) comparison between simulations of 5 and 10 km, for the lossy cavity.

6.4 Chi-Chi earthquake simulation

The team from the University of Electro-Communications, Department of Electronic Engineering in Chofu, Tokio, Japan, continuously monitors the three orthogonal components of the ELF magnetic field at the Nakatsugawa observatory (35.4° N, 137.5° E), since the beginning of 1999. The 21 of September of the same year, a severe earthquake occurred in Taiwan (the so-called Chi-Chi earthquake), with its epicenter located at (23.77° N, 121° E). Several papers have appeared relating this earthquake with anomalies in the electromagnetic spectrum, e.g., [193–196].

This study is motivated by the paper by Hayakawa et al. [196], in which they report an anomalous behavior in the 4th mode of the SR during several days prior and after the earthquake. SR frequencies are known to be stable along time [12], but the measurements from the Japanese team found, for these days, shifts on the magnetic field 4th SR of 0.6 - 0.8 Hz. In addition, its amplitude is extremely enhanced (see Figure 6.7).

The authors suggest that the reason for this anomaly in the 4th SR is an ionospheric perturbation which may occur prior to an earthquake, like the ones reported by Hayakawa et al. [197] or Molchanov and Hayakawa [95], for instance. These perturbations occur at the lower part of the ionosphere, centered over the epicenter of the earthquake. They consist on an increase of the conductivity in the area of the disturbance, lowering the effective height of reflection of the cavity.

According to their calculus, in order to produce such effect on the 4th SR, the principal excitation source must be located in the South American center of storms (see Section 2.1.4). Under this situation, the Source, the disturbance and the point of observation are roughly aligned (see Figure 6.8).

We have employed our model to simulate this situation. A single lighting located at (0° N, 50° W), i.e., in South America, serves as a source, which occurs at $t = 0$. The outputs chosen are in Japan (35.4° N, 137.5° E). A matrix of 5x5 points centered on the mentioned coordinate has been chosen as output. The distance between points of the matrix is 500 km. The output points have been called J0 - J24 (see Figure 6.9).

Since there is almost no information regarding the disturbance, we have run the model with different parameters for the disturbance. Each of them is modeled

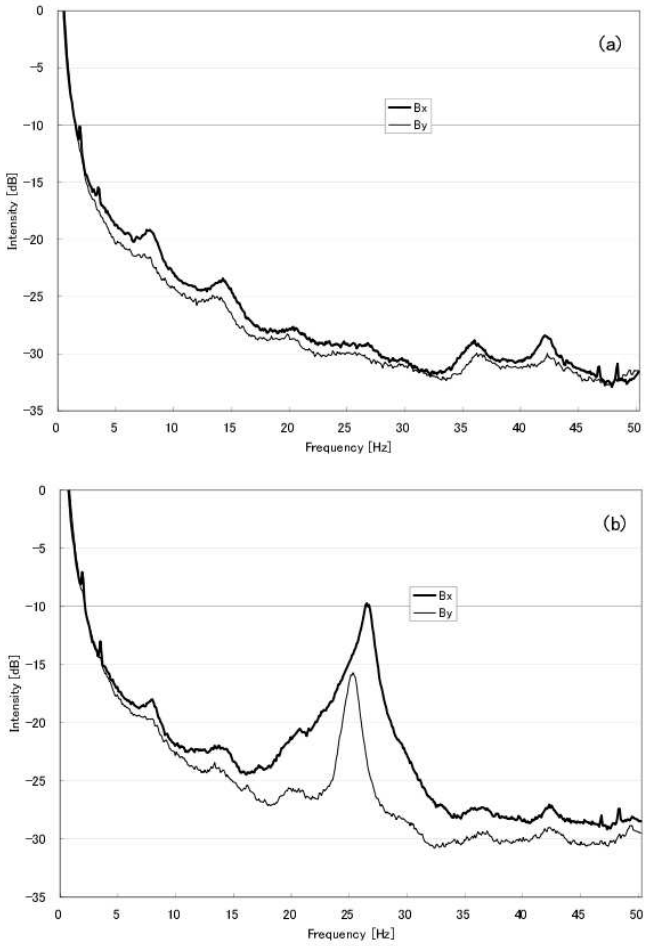

FIGURE 6.7: Comparison of SR spectra on 10 September (normal condition) (a), and on 16 September (abnormal condition) (b), for the magnetic field. Extracted from Hayakawa et al. [196].

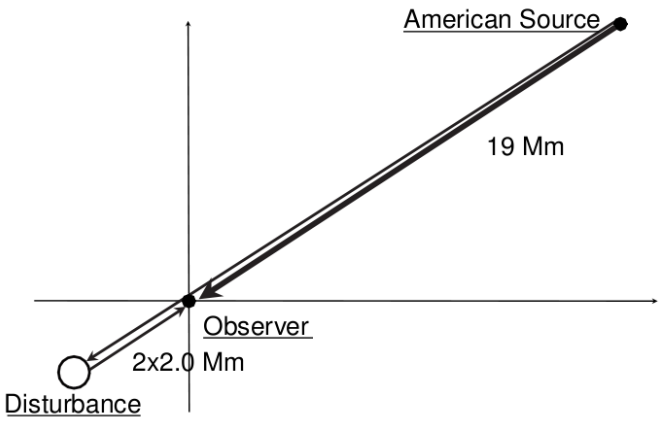

FIGURE 6.8: Configuration of the direct and scattered path for an American Source. Extracted from Hayakawa et al. [196].

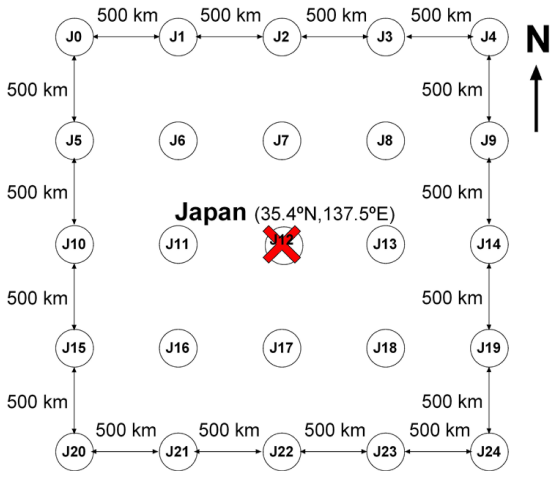

FIGURE 6.9: Definition of the output points for the simulation.

by a 3D-cone like the one in Figure 6.10, with its center C is placed at the spherical coordinates (r=6,470 km, θ=1.1559 rad, ϕ=2.1118 rad), i.e., above the earthquake epicenter, and oriented towards the center of Earth. Therefore, each disturbance is completely defined by h, r, R, and its conductivity value σ_d. In table 6.3 the parameters of each of the disturbances employed are summarized.

TABLE 6.3: Parameters for the different disturbances employed.

	R [km]	r [km]	h [km]	σ_d [$\Omega \cdot m$]
D_a	1000	10	75	10
D_b	100	100	100	50,000
D_c	10	10	100	50,000

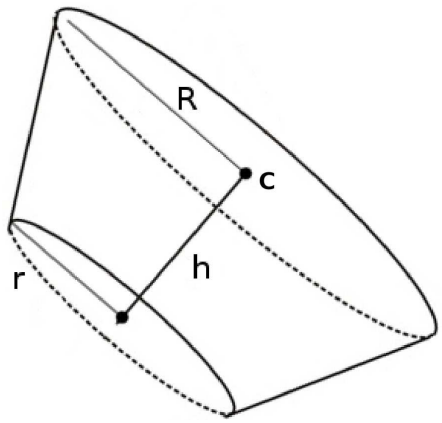

FIGURE 6.10: Definition of the disturbance parameters.

This model was run for Δl = 10 km, during 120,000 time steps, which corresponds to 2 s (Δt=1.66 μs) of total time simulated. It took roughly 10 hours of

computation on a 32 cores computer for each model, leading to a total time of 40 hours (3 disturbances plus one model without any disturbance, for comparison). A frequency resolution of 0.5 Hz was achieved.

Below, two outputs of our model are presented, Figures 6.11 and 6.12), where both H_θ and H_ϕ components for the 4 models are depicted together, for comparison. These plots put into manifest some remarkable points:

1. Disturbance D_a seems not to substantially vary the SR frequencies, while D_b and D_c do. The reasons may be the lower conductivity of D_a and/or the length of the disturbance ($h_a = 75$ km, $h_b = h_c = 100$ km).

2. In J4 output, there is an enhancement of the 4th resonance for models D_b and D_c, together with an increase on its central frequency, for H_θ. This is in agreement with the experimental results by Hayakawa et al. [196]. However, this change in the 4th resonance only appears for one of the components and it cannot be observed in the output J12.

3. There are variations in other SR, as for example the H_θ component of the 1st SR in output J4, or the H_θ component of the 2nd SR in output J12

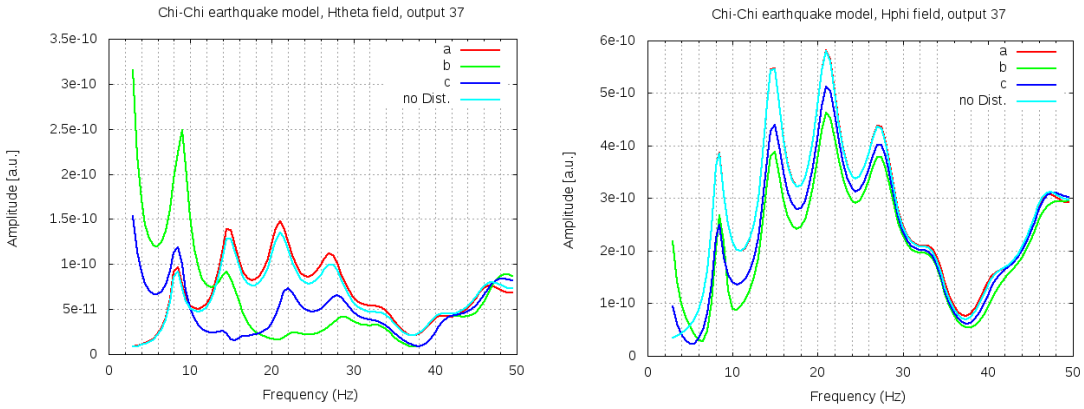

FIGURE 6.11: (left) E_r and (right) H_ϕ components measured in Japan (J12), for the 4 models.

This model proves the effect on SR of a local variation of the atmospheric conductivity. However, little is known about these changes and their connection with earthquakes. In addition, the source employed in the model is an extreme simplification of the real source of the cavity, where many thunderstorms are active at the same time, generating a global rate of several tens of strokes per second. That being said, we will show another interesting result from our model; the effects

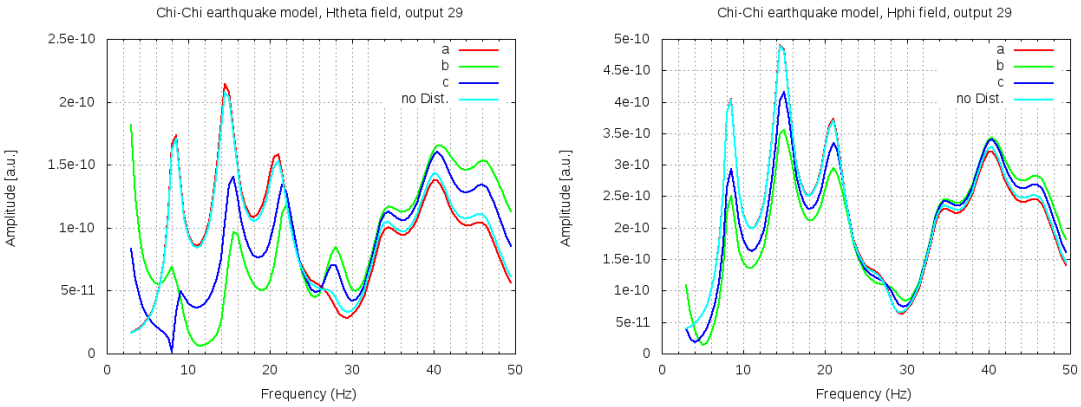

FIGURE 6.12: (left) E_r and (right) H_ϕ components measured in Japan (J4), for the 4 models.

of a disturbance can be detected far away from it. As an example, we show the magnetic recorded field by our model in the North Pole (Figure 6.13). Due to the angular distance ($\pi/2$) between the source (over the equator) and the Pole, the even resonances cannot be measured in the magnetic field components (see the results without disturbance). However, the reflection of the signal generated by the stroke over the disturbance causes the 2nd SR to appear in models D_b and D_c.

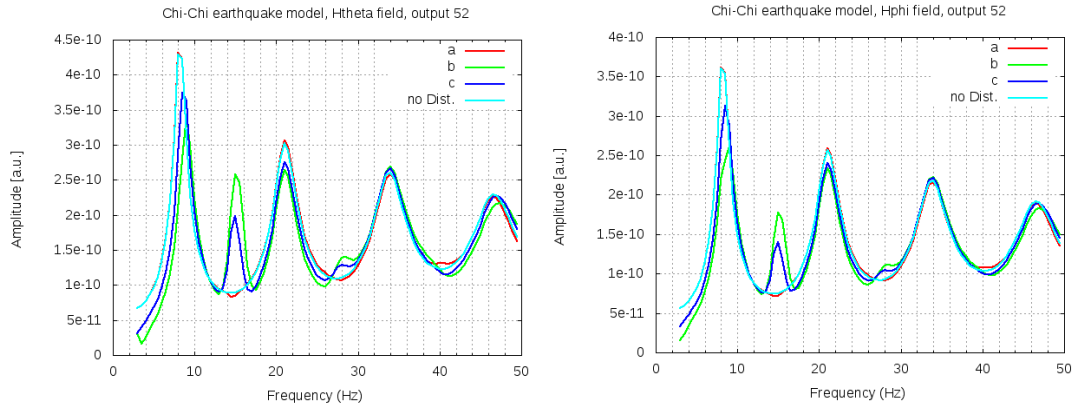

FIGURE 6.13: (left) E_r and (right) H_ϕ components measured in the North Pole, for the 4 models.

6.5 Modeling different storms

This simulation is intended to study if different storms would produce different SR components. Three different parameters of the storm (spatial size, rate of lightning, and variation of intensity of each individual stroke) have been taken into account for generating eight different storms. This is the first simulation where

more than one individual stroke excites the cavity. Under this new situation, we do not get anymore clean spectra but, instead, a very noisy one where Bartlett's method must be applied in order to see the SR (see Section 2.1.1). This implies having to simulate a much longer time, in order to have enough data to average and still keep a reasonable frequency resolution. The cavity of 10 km size per cell has been employed for the eight storms. For each kind of storm, 10 independent simulations of 8 s length (480,000 time steps) each have been carried out, leading to 80 s of data for each storm. Each simulation has been split into two segments (4 s each), and then averaged together with the other segments pertaining to simulations with the same storm parameters. The frequency resolution achieved is 0.25 Hz. It is worth noting that each simulation required roughly $7.2{\cdot}10^3$ s, i.e., 20 hours, so the total amount of computation time for the 32 cores computer (see Section 5.5.1) was $5.76{\cdot}10^6$ s, i.e., almost 67 days. This points out the cost of adding several sources spatiated at random times. In addition, the storm with a single lightning as a source (canonical source, or St_c) has been modeled for comparison purposes.

In Table 6.4, the characteristics which define each of the eight storms are summarized. Two radius for the storms (10 and 2,000 km) have been employed, together with two lightning rates (5 and 100 lightning/s) and two kinds of individual intensity for the strokes (fixed or uniform density of probability).

TABLE 6.4: Different storms simulated. U[a,b] stands for the Uniform distribution of probability in the interval [a,b].

	radius [km]	rate [s^{-1}]	Intensity factor
St_1	10	5	20
St_2	10	5	U[0,40]
St_3	10	100	1
St_4	10	100	U[0,2]
St_5	2,000	5	20
St_6	2,000	5	U[0,40]
St_7	2,000	100	1
St_8	2,000	100	U[0,2]
St_c	1	X	800

Each kind of storm resulted in a final single spectrum for each output node, after applying Bartlett as mentioned above. The storm was located centered at

$\theta = 0$, and the 101 nodes were marked as output along this coordinate ($\theta = 0...\pi$). The spectra were cut at 30 Hz and then, we applied a Lorentzian fit of four peaks for the outputs located at $\pi/4$, $\pi/2$, and $4\pi/5$. The Lorentzian fit scheme employed responds to the following equation

$$S_{fit}(f) = y_0 + \sum_{i=1}^{4} \frac{2A_i}{\pi w_i} \frac{1}{\left(\frac{f-f_c^i}{w_i/2}\right)^2 + 1} \tag{6.2}$$

where A_i accounts for the amplitude of the peak, f_c^i represents the central frequency of the resonance, and w_i gives a measure of its quality factor.

As an example, three of these spectra form storm 1 (St_1) are plotted in Figure 6.14, together with the results of a Lorentzian fit to extract the main parameters of the SR.

In Figure 6.15, the three first SR frequencies and their corresponding Δf_{3dB} have been plotted. However, it is difficult to relate these results with the characteristics of the storms. It may be necessary to perform even longer simulations, in order to stabilize the random nature of the storms (location, time, and intensity of each stroke) and obtain statistically significant results.

6.6 Study of the effects of Day-night asymmetry on SR

The last simulation which will be presented in this thesis models the day-night asymmetry of the cavity, which is produced by the solar wind. The solar radiation is the main responsible for the ionization of the ionosphere, and the side of the Earth which receives direct radiation presents a much more conductive ionosphere, lowering the effective reflection height. The two conductivity profiles employed in this model are defined in Figure 5.2. The cavity is modeled for an equinox day, i.e., the Sun is located in the equatorial plane of Earth. The terminator, i.e., the interface between the two conductivity profiles, is located at $\phi = 0, \pi$. Midnight time is located at $\phi = \pi/2$, and noon at $\phi = 3\pi/2$.

For this asymmetrical cavity which accounts for the two conductivity profiles, 24 simulations were run; the source (single lightning) was placed at the equator

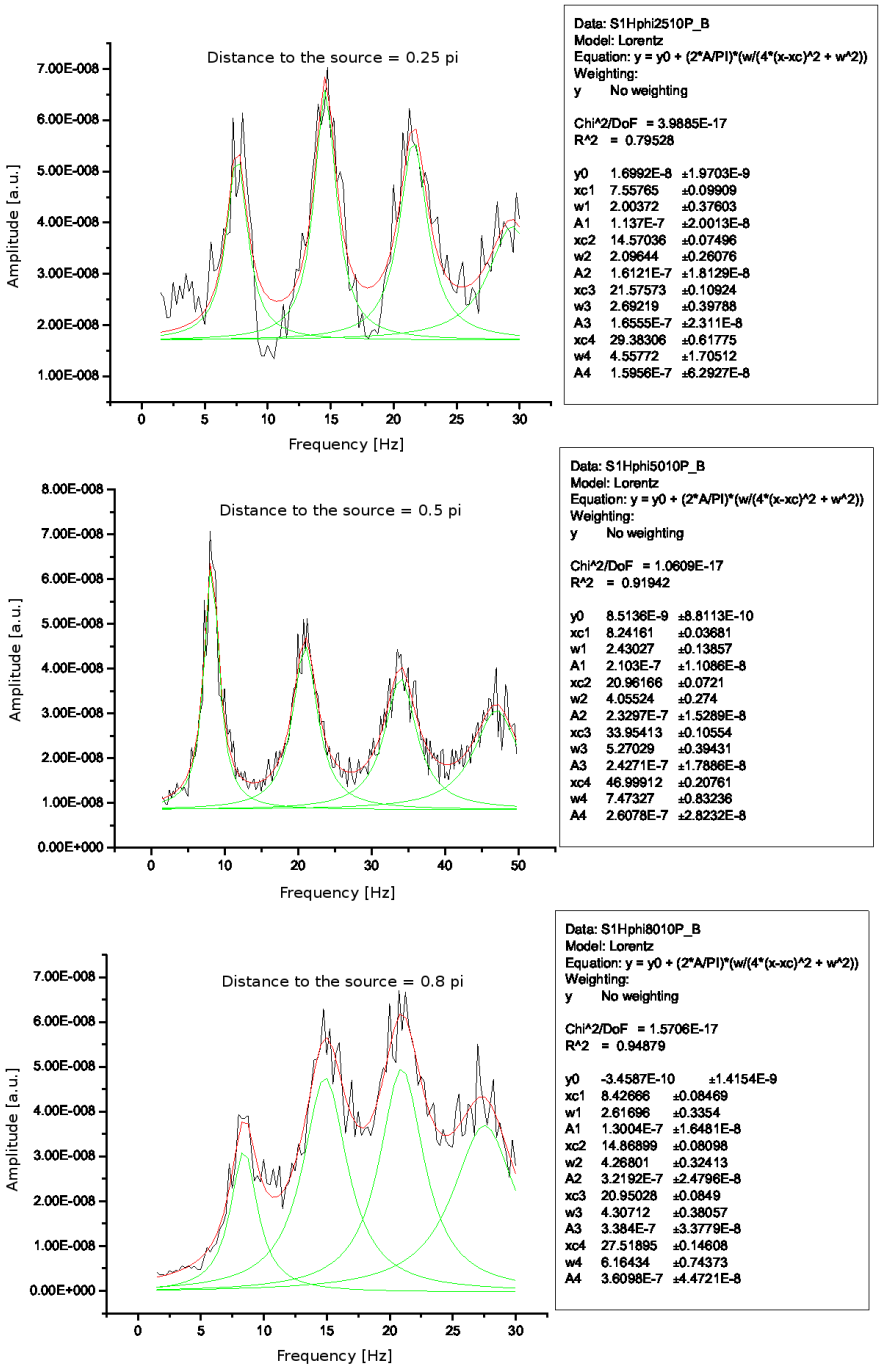

FIGURE 6.14: Resulting spectrum of St_1 at three different distances from the source.

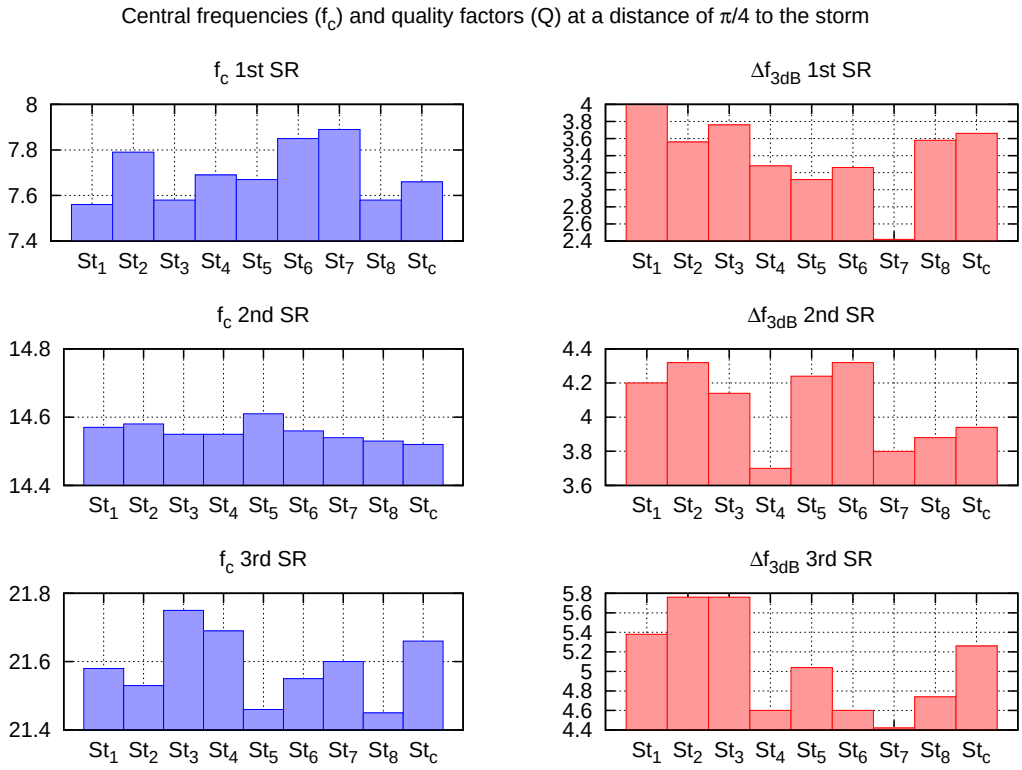

FIGURE 6.15: (blue) Central frequency and (red) Δf_{3dB} for the different storms, at a distance of $\pi/4$ to the source.

(θ=$\pi/2$), and each run simulated a storm located at a different local time, i.e., ϕ=0, $\pi/12$...$23\pi/12$. In addition, for comparison purposes, a model with the source located at (θ=$\pi/2$, ϕ=0) was computed for the symmetrical cavity. The time iterations employed at each simulation was 240,000, leading to a frequency resolution of 0.25 Hz (nodes of 10 km length). Therefore the total amount of computer time for the 32 cores computer was roughly 500 hours, i.e., almost 21 days.

In Figure 6.16, the H_ϕ component is plotted for both models (day-night and symmetrical), with the source located at 00 LT (midnight). The output was taken at the coordinate ($\theta = \pi/6$, $\phi = \pi/2$), which is located at a distance of $\pi/3$ from the lightning. It is interesting to see that SR frequencies have lower value in the day-night cavity. The third resonance is almost inexistent, due to the distance between the source and the point of measurement.

Another output is shown in Figure 6.17. It corresponds to the coordinate ($\theta = \pi/3$, $\phi = \pi/6$), where the first four SR can be observed. The values of their central frequencies are shown in Table 8.5.

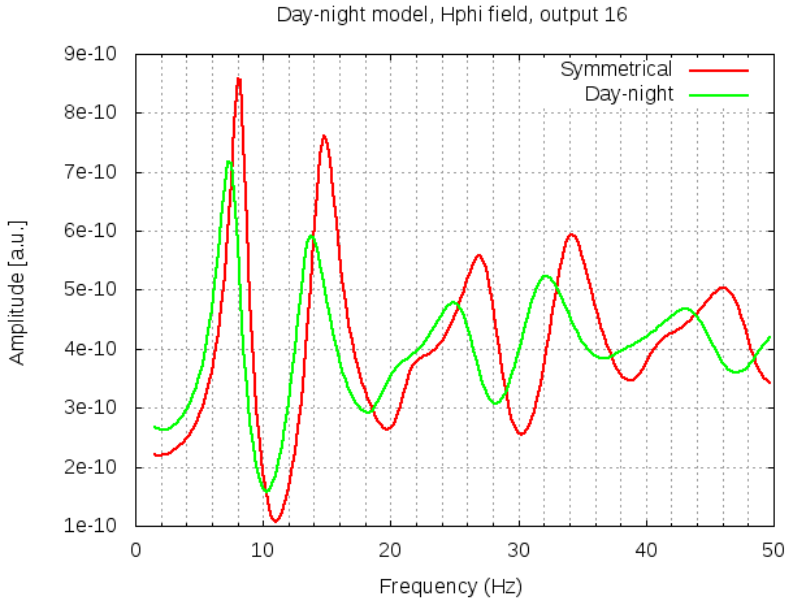

FIGURE 6.16: Comparison of H_ϕ component at a distance of $\pi/3$ towards North for the symmetrical and the day-night cavities.

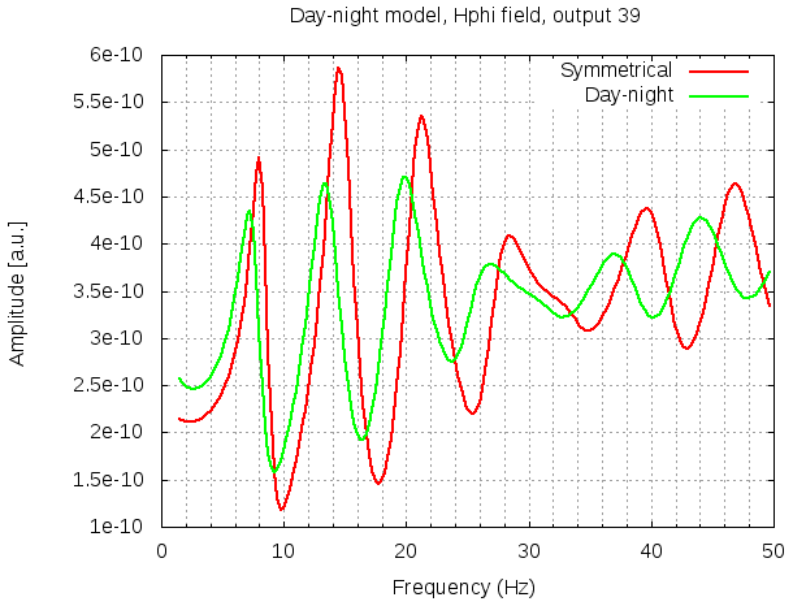

FIGURE 6.17: Comparison of H_ϕ component at the output coordinate ($\theta = \pi/3$, $\phi = \pi/6$) for the symmetrical and the day-night cavities.

TABLE 6.5: Central values (f_c) in Hz for the four first SR, at the output coordinate ($\theta = \pi/3$, $\phi = \pi/6$), for the symmetrical and the day-night cavity.

	1st SR	2nd SR	3rd SR	4th SR
Symmetrical	8.00	14.49	21.23	28.48
Day-night	7.25	13.49	19.98	26.98
Experimental [12]	7.8	13.9	20.0	26.0

Finally, we will show the magnetic field components for different location of the source. We have chosen 4 different sources, those located at 00:00 LT, 06:00 LT, 12:00 LT, and 18:00 LT. In Figure 6.18, the output for each source was located at a relative distance of $\pi/3$ towards North. With this position for the source and for the observer, in a symmetrical lossless cavity there will be only H_ϕ component. However, for this problem we find a small component in H_θ, although it is 2 orders of magnitude lower than H_ϕ. It is interesting to see that for the sources located over the terminator, i.e., interface between day and night, this component is enhanced with respect to the sources located at 00:00 LT and 12:00 LT. The changes in H_ϕ are very small and correspond mainly to the amplitude of the modes.

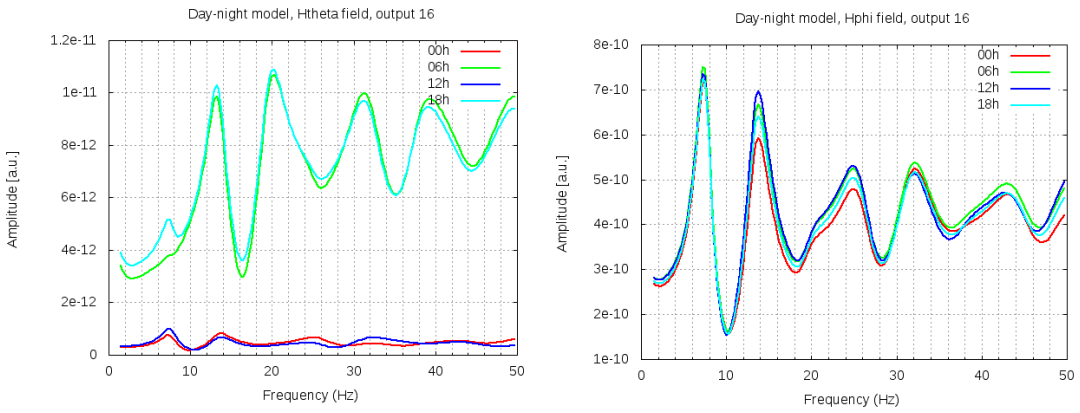

FIGURE 6.18: Comparison of H components for four different times of the storm, with an output relative displacement from the source of $\theta = -\pi/3$.

Finally, in Figure 6.19, we repeated the previous simulation but changing the relative position of the observation point with respect to the source (the lightning) to $\theta = -\pi/6$, $\phi = -\pi/6$. Now the two components are almost equal (for a symmetrical lossless cavity they should be equal), and the largest changes between the location of the source with respect to the asymmetrical cavity are found in the higher modes.

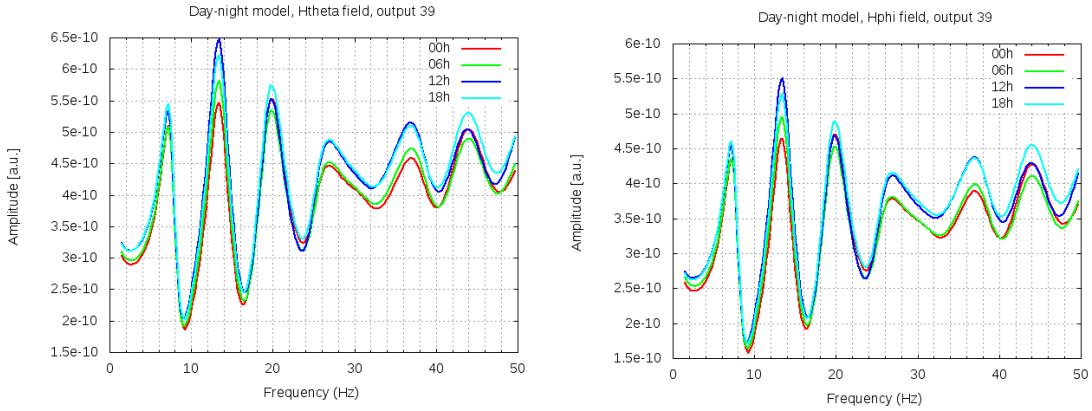

FIGURE 6.19: Comparison of H components for four different times of the storm, with an output relative displacement of $\theta = -\pi/6$, $\phi = -\pi/6$.

6.7 Conclusion

Several models of the Earth-ionosphere cavity have been presented in this Chapter. The main purpose is to validate the model, by showing that it yields results which are consistent with analytical calculations, as well as with other models, e.g., [58], and finally with experimental results. We show few of the multiple possibilities that our model enables, like the choice of parameters of the cavity, addition of singularities such as earthquake precursors, modeling the storms, etc. However, obtaining conclusions about these phenomena and their relation with SR is not an straightforward task. In some cases, a huge number of runs may be necessary, especially if we add random parameters to the simulation, e.g., real storms, in order to get statistics of them. In other cases, it may be necessary to develop new techniques of data processing, like improving the extraction of SR parameters by Lorentzian fit or even defining new parameters for the study of SR.

Chapter 7

Conclusions and future outlook

7.1 Conclusions

This thesis is devoted to the study of the electromagnetic noise in the Earth-ionosphere cavity. The various contributions to the study of these phenomena may be separated into two main categories: the results from experimental measurements and a study based in modeling the problem with the TLM method.

In this sense, Chapter 2 analyzes signals measured at ground level, and relates its main results with the analytical model of the cavity, presented in Chapter 1. The daily and seasonal variations of the ELF signals are discussed, and linked to the global storm activity. In Chapter 3, the measurements are taken from DEMETER spacecraft, which orbits in the upper region of the ionosphere ($\sim$700 km). A method for monitoring the effective reflection height of VLF signals is presented, and it is employed to study its variations in monthly, seasonal, and annual time scales.

The second part, the simulation of the problem, starts by reviewing the main characteristics of the TLM method, in Chapter 4. We justify the chosen configuration of the method for the study of the Earth-ionosphere cavity. Chapter 5 deals with the principal problem for the model, the huge amount of resources required for modeling the whole cavity in 3D, which is solved by parallelization and an abstraction of the initial geometry. In Chapter 6, the model is validated and some simulations are presented.

Below, we present the main conclusions from each of the Chapters of this thesis.

Chapter 2 proves the presence of Schumann resonances in magnetotelluric records. All the measured components (NS and EW for the electric field, NS, EW and vertical for the magnetic field) contain SR except the vertical magnetic field (even though 5% of these also showed the resonances).

From the spectral analysis, the following conclusions can be formed:

1. Evidence of three main storm centers located in Asia, Africa, and America with their main activity in the local afternoon. The field amplitudes observed for each component are in agreement with the predictions for the TM^r modes. Therefore, the campaigns registered in January and February show less modal amplitude, while those taken during the northern hemisphere spring and summer are the most energetic. Moreover, decay in amplitude with the modal order is observed in the magnetic components, while this is not present for the electric components. The magnetic field measurements have been shown to be robust regarding local effects, and small shifts of km of the observation point do not affect the measurement, while electric field measurements can vary their amplitude up to one order of magnitude within a few km of distance. However, the frequency contents do not vary with the shift of the point of observation, either in magnetic or in electric field measurements.

2. Measurements have shown that a minimum of amplitude appears in the second mode of the magnetic NS (and electric EW) component in the Antarctic campaign, when the main center of storms is located in Africa (around 16:00 UT). This behavior is explained according to the analytical model predictions.

3. The central frequencies for the first three SR modes averaged in the different campaigns are 7.8, 14, and 20.5 Hz. The measurements around these central values are subject to shifts, which may contain information about different geophysical processes, such as the properties of the storms, the solar wind, or seismic events, for instance. These variations are stronger in the second and third modes than in the first.

4. In all the time series, the spectral correlation between magnetic NS and electric EW components has been proved. The same occurs between magnetic EW and electric NS. The modes show close frequency shifts and relative amplitudes between them.

The rescaled range analysis has been applied to series taken in Antarctica, where the anthropogenic noise is almost inexistent, and the persistent nature of the SR has been proved. By following the analysis by Nickolaenko et al. [81], this analysis permits to estimate the average rate of discharges from which the signal originated. According to this, the signals analyzed show an average rate of around 16 - 32 discharges per second. In order to corroborate this statement, a numerical simulation was performed.

In Chapter 3, a large data set of electric field measurements from DEMETER has been employed to draw average maps of the effective reflection height with dependence of geolocation. There exist previous works which use the cut-off frequency to calculate the effective height of the Earth-ionosphere cavity from ground observations, e.g., [135–137], but it was never done before, to the knowledge of the authors, by using data taken from spacecraft. This technique has the clear advantage of monitoring most of the surface of Earth. Ground based studies of the cut-off frequency can only obtain averaged values along the path that the atmospheric wave followed (from source to point of observation), while measurements from satellite are directly related to the ionosphere conditions in the vicinity of the measurement point. Thus, we present detailed maps (up to 2° resolution) over the whole Earth (±60° latitude) for the effective reflection height of the ionosphere or D-region altitude, which is inversely proportional to the cut-off frequency. From these measurements, it is possible to infer the electron density as well as the conductivity at the effective height, although it is necessary to extract the neutral density parameter from a model, MSIS in this case.

The main result of this study is that we observe, during night time, certain seasonal patterns (mainly over the oceans), which repeat over the four years of the study, for the effective reflection height of the ionosphere. In addition, we suggest that the global cut-off frequency could be used as a proxy of the solar activity.

After that, the TLM method is introduced and we review its most relevant configurations. The final decision for our models is to employ the cubic Cartesian SCN. This decision is made in order avoid problems of dispersion and indetermination at certain areas which are inherent to the spherical SCN.

In Chapter 5, we describe the different hardware solutions for computing parallel-intensive code. Then, we focuse on modeling the Earth-ionosphere cavity

by means of an efficient parallel algorithm based on TLM. A translation from arbitrary topology to 1D (preprocess) is required to efficiently simulate the problem. The solution obtained is benchmarked by two independent studies, which yield similar results over different computers. To obtain the maxima speedups, it is necessary to set a policy of round-robin memory allocation, in order to minimize the effects of the NUMA architecture. Speedups of up to 16 have been measured by using 32 CPUs, for models of the size of the Earth-ionosphere cavity. Under certain circumstances (small memory requirements which allow the model to fit in the caches), superlinear speedup is achieved.

Finally, in Chapter 6, several models of the Earth-ionosphere cavity have been presented. The main purpose is to validate the model, by showing that it yields results which are consistent with analytical calculations, as well as with other models, e.g., [58], and finally with experimental results. We show few of the multiple possibilities that our model enables, like selection of cavity parameters, addition of singularities such as the ones which are generated as earthquake precursors, modeling storms, etc. However, obtaining conclusions about these phenomena and their relation with SR is not a straightforward task. In some cases, a huge number of runs may be necessary, especially if we add random parameters to the simulation (e.g., real storms), in order to get statistics of them. In other cases, it may be necessary to develop new techniques of data processing, like improving the extraction of SR parameters by Lorentzian fit or even defining new parameters for the study of SR.

7.2 Future outlook

The work presented in this thesis is far from finished. In fact, it is just starting. Our team, under the project *"Study of Natural Electromagnetic Phenomena for Monitoring the Environment"*, is engaged in the design, construction, and deployment of a fixed SR measurement station. Currently we are in the deployment phase, and it is scheduled to be operative by the end of summer 2012. The chosen location for the station is Sierra Nevada, Granada, Spain. Continuous measurements with high sensitivity will be recorded for both horizontal components of the magnetic field. Together with classical Fourier analysis, we want to work in applying deeper fractal analysis than the one presented in Section 2.2. We are

also very interested in sharing the SR records with other research groups in order to get feedback and compare our results with other SR stations.

And, as it can be observed from Chapter 6, the results from the models are far from complete. The presented 3D-parallel TLM algorithm is a powerful tool to study the electromagnetic signals propagating in the Earth-ionosphere cavity. Further optimizations must be performed to the algorithm, together with porting the code to distributed memory environments (clusters), for instance. We believe in the possibility of bridging the gap, or at least reducing the distance, which exists nowadays between models and experimental results in SR studies.

Chapter 8

Resumen y conclusiones

8.1 Introducción

Hasta ahora las Ciencias del Medio Ambiente y Geofísicas no han considerado a los fenómenos electromagnéticos naturales como método de diagnóstico del estado de la Tierra debido a que: (1) aún no se conocen en profundidad muchos de estos fenómenos, es decir, hay medidas experimentales pero no modelos que generen resultados coherentes con dichas medidas; y (2) las variaciones producidas por anomalías o cambios en el Medio Ambiente son pequeñas y, por tanto, son difíciles de medir y modelar.

¿Es posible la predicción fiable y a corto plazo de un terremoto? ¿Existe un termómetro que nos mida el calentamiento global del planeta? La respuesta afirmativa a estas preguntas sería un avance muy importante para las ciencias medioambientales y la prevención de desastres.

Para la primera cuestión, las predicciones actuales son vagas hasta el punto de que, usando estudios históricos junto a determinaciones vía satélite de movimientos de la corteza terrestre y medidas de tensiones en su interior, los científicos pueden determinar con gran probabilidad la ocurrencia de un terremoto en un plazo de tiempo de 30 años [8]. La predicción a corto plazo no vendrá del estudio de movimientos de la corteza terrestre sino de fenómenos electromagnéticos, y no solo procedentes de la superficie terrestre sino incluso de la ionosfera.

Respecto a la segunda cuestión, en 1992 apareció en la revista Science un artículo en el que se propone un mecanismo de detección de la temperatura global del trópico [5] basado en el estudio de otro fenómeno electromagnético de origen natural: las frecuencias de resonancia de Schumann [10], que ocurren en la cavidad natural formada por la superficie de la Tierra y la baja ionosfera, las cuales forman dos enormes superficies esféricas concéntricas conductoras, separadas por un dieléctrico con pérdidas, la baja atmósfera. Las dimensiones de dicha cavidad son peculiares: frente a un perímetro de unos 40,000 km, la altura de la ionosfera es de tan solo 50 - 60 km durante el día y 80 - 90 km durante la noche. Las resonancias de Schumann consisten en oscilaciones ELF (del inglés, *Extremely Low Frequency*) producidas por los rayos y que se propagan a través de toda la cavidad en forma de modos TM (del inglés, *Transverse Magnetic*), proporcionando una herramienta para estudiar los parámetros de la baja ionosfera y la intensidad de la actividad tormentosa. Los estudios llevados a cabo por Williams durante seis años demostraron la correlación entre las variaciones anuales de las amplitudes de las primeras resonancias de Schumann y la temperatura del trópico, evaluada a través del promedio temporal del número de rayos en la Tierra. Las constantes descargas que se producen de forma simultánea en la Tierra son fuentes de campos electromagnéticos que se propagan a través de la atmósfera, reflejándose sucesivamente en la ionosfera y en la superficie terrestre. En la banda ELF y debido a la conductividad de la atmósfera, las ondas pueden dar varias vueltas a todo el perímetro terrestre dando lugar a la aparición de resonancias.

8.1.1 Resonancias en la cavidad Tierra-ionosfera

La Historia de la radio ingeniería comenzó hace unos cien años. En esta época la radiación electromagnética que se conocía provenía de los rayos o de las descargas generadas en el laboratorio. Posteriormente, las ondas de radio con variación armónica se usaron para la transmisión de señales. Descubierta la ionosfera, se produjo una gran expansión de la radio en onda corta (banda HF, entre 3 y 30 MHz). Durante y después de la II Guerra Mundial, se desarrolló el radar en el ámbito militar, posteriormente usado para investigación de medios electromagnéticos naturales. En 1952 se predijo, por parte W. O. Schumann [10], la existencia de resonancias en toda la cavidad Tierra-Ionosfera. La evidencia experimental se realizó en 1960 por parte de Balser y Wagner [13]. Durante la segunda mitad del siglo de la radio se produjo una fuerte investigación en la banda VLF y ELF con

objetivos, cómo no, militares, en comunicaciones de radio globales y comunicación con submarinos. Con la finalización de la guerra fría la investigación en la banda ELF decayó fuertemente. Sin embargo, en los 90, el interés en las resonancias de Schumann volvió como una herramienta para estudiar el calentamiento global a través de la monitorización de la actividad global de rayos en las tormentas generadas por la convección atmosférica, que depende de la temperatura de la superficie terrestre. También ha contribuido en aumentar el interés en esta banda la posibilidad de localización de rayos con gran intensidad que generan señales transitorias ELF (*Q-bursts*), causando modificaciones en la mesosfera (*red sprites, elves*, etc.).

Se puede ver el sistema Tierra-ionosfera como una guía de ondas, una cavidad o un condensador, dependiendo de la longitud de onda que estemos considerando. Hablaremos de guía de ondas si el radio de la Tierra $a >> \lambda$ es mucho mayor que la longitud de onda λ (caso de resonancias transversales). Las oscilaciones naturales se vuelven cuasi-electrostáticas en el caso contrario $a << \lambda$ y la descripción de campo se puede reducir al proceso de carga y descarga de un condensador esférico. El término resonador es apropiado cuando la longitud de onda es comparable con la circunferencia de la tierra $\lambda \simeq 2\pi a$.

Las frecuencias de resonancia se pueden deducir de forma muy aproximada tanto para las resonancias de Schumann como para las transversales. En el primer caso, la condición es que el desfase debido a la circunvalación de la onda a todo el perímetro terrestre ($2\pi a \simeq 40$Mm) sea múltiplo entero de la longitud de onda:

$$f_n = \frac{c}{2\pi a} n = 7.5n$$

Para las resonancias transversales, la condición es que la altura efectiva de la cavidad sea múltiplo entero de media longitud de onda :

$$F_p = \frac{c}{2h} p = 2\ 10^3 p \text{ Hz}$$

A frecuencias de decenas de Hz, la atenuación de la atmósfera es de solo unas pocas décimas de dB por 1,000 km, lo que permite a la señal dar varias vueltas a la Tierra antes de atenuarse. Sin embargo, las resonancias transversales son un fenómeno local debido al alto factor de atenuación de la atmósfera a estas frecuencias, entorno a 20 dB/1,000 km, lo que hace que la onda no se propague

lejos de las fuentes (los rayos), por lo que la resonancia tiene un carácter mucho más local. La resonancia transversal se observa mejor durante la noche debido a que la ionosfera es mucho más estable y predecible y el ruido proveniente del plasma ionosférico es mucho menor.

8.1.2 Fenómenos electromagnéticos asociados con terremotos (y/o erupciones volcánicas)

Podemos llamar Seísmo-Electromagnetismo a la disciplina surgida recientemente para estudiar los fenómenos electromagnéticos originados en los movimientos sísmicos. Actualmente hay acumuladas multitud de observaciones experimentales, pero faltan modelos teóricos que generen datos concordantes con dichas observaciones [6]. El rango de frecuencias de estos fenómenos va desde DC (del inglés, *Direct Current*) hasta VHF (del inglés, *Very High Frequency*), pero nos centraremos en describir aquellos más relevantes (o que parecen serlo según las investigaciones recientes) para la predicción a corto plazo de terremotos. Este interés en observaciones no-sísmicas surge en paralelo con las dudas de si observaciones puramente sísmicas puedan predecirlos [8].

Podemos destacar los siguientes fenómenos:

1. Señales sísmicas eléctricas procedentes de la torsión elevada que sufren las rocas ígneas.

2. Emisiones sísmicas de ondas electromagnéticas en el rango de décimas de hercio debidas a un proceso de separación de carga en micro fracturas de rocas. También se producen alteraciones en la ionosfera que generan, a su vez, perturbación en las resonancias de Schumann.

3. Acoplamiento litosfera-atmósfera-ionosfera que afecta a la propagación en las bandas VLF, LF y VHF y cuya causa primaria estaría en la perturbación de la ionosfera por parte de fenómenos previos a terremotos superficiales (principalmente en Tierra) y con intensidad superior a 6.

8.1.3 Resonancias en una corona esférica

Para encontrar las frecuencias de resonancia de una cavidad esférica constituida por la Tierra y la ionosfera debemos resolver las ecuaciones de Maxwell junto con las ecuaciones constitutivas para el campo eléctrico y para el campo magnético. Debido al carácter dispersivo del medio es usual trabajar en el dominio de la frecuencia. Dentro de la banda ELF (considerada desde 3 Hz hasta 3 kHz) se puede despreciar el efecto del campo magnético terrestre y considerar la permitividad del medio como un escalar función de la posición y de la frecuencia $\epsilon\left[\vec{r},\omega\right]$. En este rango de frecuencias también podemos considerar a la Tierra como un conductor perfecto.

El modelo considerado por Schumann en su primer estudio [10] considera un perfil de la atmósfera definido por:

$$\epsilon\left[\vec{r},\omega\right] = \begin{cases} 1 & a \leq r < b \\ \epsilon & r \geq b \end{cases}$$

y para considerar la ionosfera como conductor perfecto se efectúa el límite $\epsilon \to \infty$.

La solución de las ecuaciones de Maxwell sin fuentes en el dominio de la frecuencia se obtiene de forma más simple usando los potenciales de Debye [15, 16] (U y V asociados a la parte eléctrica y magnética respectivamente del campo electromagnético). En el caso de no considerar la ionosfera como conductor perfecto, pero sí homogénea, debemos añadir una condición adicional a los potenciales de Debye conocida como condición de radiación de Sommerfeld [42].

El análisis modal se obtiene haciendo cero alternativamente cada uno de los potenciales de Debye. Los modos TM (u onda eléctrica) se obtienen haciendo $V = 0, U \neq 0$ y los modos TE (u onda magnética) haciendo $U = 0, V \neq 0$.

Para los modos TM, la condición de contorno se obtiene a partir de la derivada de U con respecto a r. El valor de las frecuencias de resonancia se obtiene a partir de la relación de dispersión, pero para obtener una expresión analítica hay que efectuar un desarrollo en serie basándose en la diferencia entre el radio de la Tierra ($a = 6,370\text{km}$) y la altura de la ionosfera (entre 60 y 100 km para el día y la noche). Con esto, se obtiene para las frecuencias de resonancia:

$$f_n = \frac{c}{2\pi a}\sqrt{n(n+1)},$$

expresión publicada por Schumann en 1952 y referenciada como resonancias o resonancia (ambas expresiones figuran en la bibliografía) de Schumann. Las primeras resonancias dan unos valores de 10.6, 18.3, 25.9 y 33.5 Hz. Los campos para este modo de propagación tienen componente eléctrica en la dirección radial y componente magnética en la dirección acimutal. Son modos TM, a los que en la bibliografía se les suele llamar TEM debido al carácter ortogonal de los campos y la dirección de propagación. Este hecho explica la débil dependencia de los campos con la altura [12]. En este modo de propagación podemos hablar de frecuencia cero cuando n=0. Este caso corresponde a la solución estática generada por el condensador Tierra-ionosfera cargado con una diferencia de potencial de algunos cientos de kilovoltios, con campo magnético cero y campo eléctrico orientado desde la ionosfera hacia la Tierra, con valores de 120 V/m en puntos próximos a la superficie (fair weather field) [12].

Bliokh et al. [43] obtiene una fórmula más aproximada en la forma:

$$\beta_n a = \sqrt{n(n+1)\left(1 - \frac{b-a}{a}\right)}$$

siendo $\beta = 2\pi/\lambda$, y b el radio de la ionosfera (no la altura).

Las resonancias de Schumann corresponden a ondas que pueden dar varias vueltas a la Tierra y por tanto pueden ser observadas en cualquier punto del planeta, llevando información global de las propiedades de la ionosfera. Este hecho es el que ha despertado un gran interés en el estudio de las resonancias de Schumann como una herramienta para el estudio de las características y estado de la ionosfera y de la distribución global de las fuentes de la radiación ELF (los rayos) [12].

De forma análoga, para los modos TE, la condición de contorno se obtiene directamente del potencial V, y la relación de dispersión a la que se llega considerando las aproximaciones $ka, kb >> 1$:

$$\beta_{pn} \approx \sqrt{\frac{n(n+1)}{a^2} + \left(\frac{p\pi}{b-a}\right)^2},$$

donde aparecen dos índices relacionados con la propagación transversal y longitudinal. El primero indica el número de medias longitudes de onda que caben en la altura de la cavidad y el segundo indica el número de longitudes de onda que caben en la circunferencia terrestre. La resonancia transversal básica ($p = 1$), que

se conoce como frecuencia de corte, está entorno a 1-2 kHz, y como estas resonancias se detectan mejor por la noche [44] la altura de la ionosfera está próxima a los 100 km y $f_{1,0} = 1.5$kHz.

Las frecuencias de resonancia se pueden obtener numéricamente como los pasos por cero de la función obtenida a partir de la aplicación de las condiciones de contorno a los campos. En la Figura 8.1 las hemos representado, para los modos TE^r (línea sólida) y TM^r (línea discontinua). Podemos ver como para ambos modos y para los diferentes valores de n, los pasos por cero que definen las frecuencias de resonancia se producen para el mismo valor del número de ondas β, excepto para la parte próxima a frecuencia cero en los modos TM^r, donde podemos comprobar que los modos se separan.

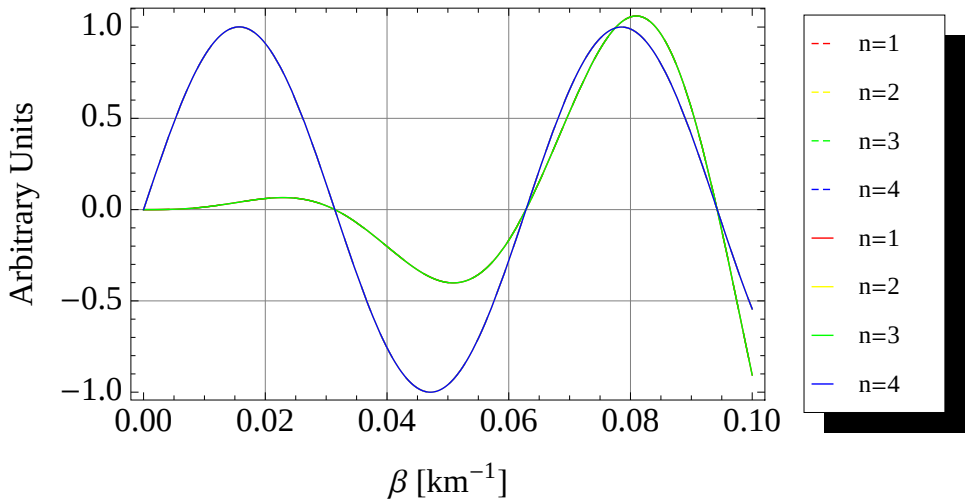

FIGURE 8.1: Relación de dispersión para los modos TM^r y TE^r en la cavidad Tierra-ionosfera.

En la Figura 8.2 se representa la función de dispersión para valores pequeños de β y para los cuatro primeros modos TM^r, de donde se puede obtener los valores de las cuatro primeras frecuencias de Schumann.

8.1.4 Electricidad en la atmósfera

En un día despejado se puede medir un campo eléctrico en el aire de 100 V/m, orientado hacia la tierra. Es lo que se conoce como *fair weather field,* el cual genera, debido a la pequeña conductividad de la atmósfera, una corriente global de unos 1,800 A. Esta corriente es la corriente de descarga de un inmenso condensador formado por la ionosfera y la Tierra cargado a una diferencia de potencial

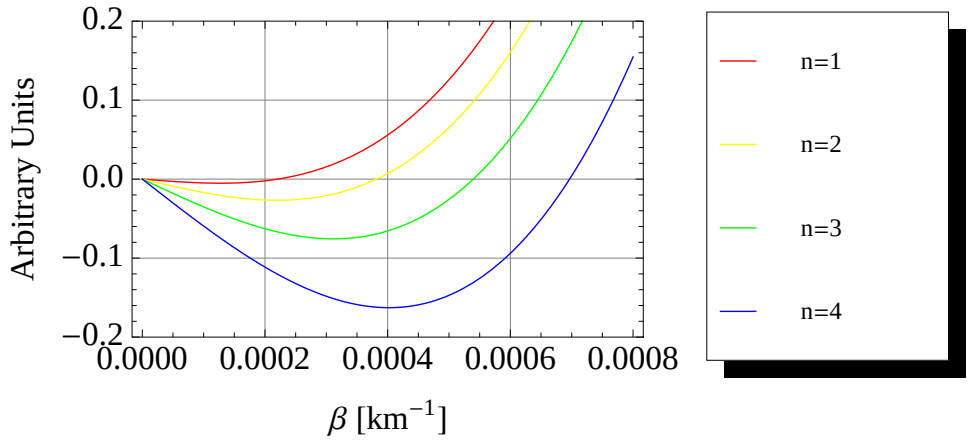

FIGURE 8.2: Detalle de la Figura 8.1, donde se ven los cortes por cero que representan las SR.

de varios cientos de miles de voltios. El mecanismo de carga de este condensador natural es la actividad tormentosa, con los rayos como batería suministradora de la diferencia de potencial.

Unas 2,000 tormentas están activas de forma permanente en la globalidad de la Tierra. Su distribución no es uniforme, sino que tienden a concentrarse en tres núcleos importantes: África Central, América del Sur y Central y el Sudeste Asiático (ver Figura 8.3).

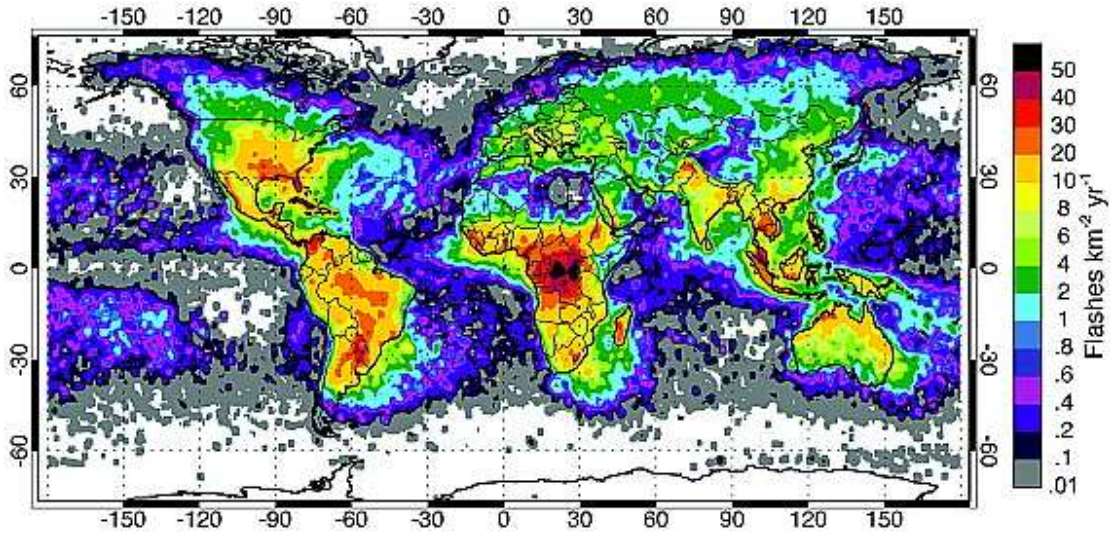

FIGURE 8.3: Distribución anual de la actividad tormentosa global (rayos). Unidades de rayos km^{-2} año^{-1}. Extraído de [25].

La actividad tormentosa es también función de la hora local. El máximo se da pasado el mediodía, alrededor de las 15:00 LT.

8.1.5 Medidas de las resonancias de Schumann

A lo largo de los 60 años de historia de las resonancias de Schumann se han llevado a cabo numerosos estudios experimentales. En Nickolaenko and Hayakawa [12] se describen todos los resultados experimentales de dichos estudios. El interés actual se centra en observatorios que de forma continua miden la señal temporal en diferentes rangos de frecuencia, lo que permite hacer estudios a largo plazo y simultáneos de los diferentes parámetros de las resonancias de Schumann (amplitud, frecuencia de pico, factor de calidad) para establecer modelos sobre la electrodinámica de la atmósfera. Actualmente hay observatorios ubicados en Europa Central, Japón o Estados Unidos principalmente. Para finales de verano de 2012, esperamos también contar con la primera estación de medida en España, diseñada, construída e instalada por nuestro grupo de investigación bajo el proyecto *Estudio de fenómenos electromagnéticos naturales para el diagnóstico del medio ambiente*. Se ubicará en el Parque Nacional de Sierra Nevada, a 2,500 metros de altitud. En la Figura 8.4 se muestra un espectro del campo magnético medido por uno de los magnetómetros que han sido diseñados y construidos por nuestro grupo de investigación para dicha estación. Los datos están sin calibrar por lo que la cuarta resonancia aparece amplificada por la resonancia del magnetómetro.

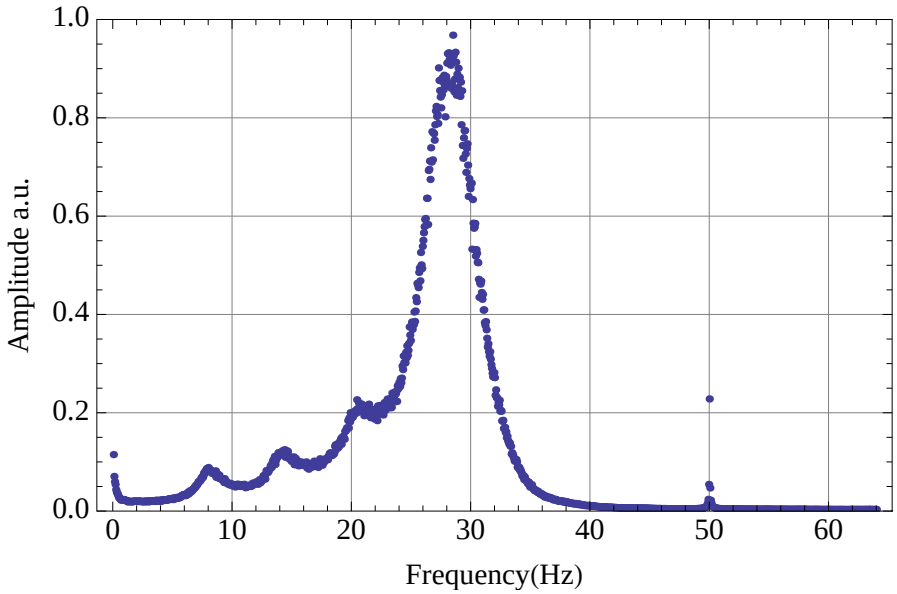

FIGURE 8.4: Resonancias de Schumann medidas en Granada, España, junio de 2011. Espectro no calibrado.

8.1.6 Historial del grupo de investigación en atmósferas planetarias

La investigación sobre los campos electromagnéticos naturales en las atmósferas planetarias llevada a cabo por el grupo de investigación en el que se ha realizado esta tesis comenzó cuando, en diciembre del 2000, el Dr. Konrad Schwingenschuh, del Instituto de Investigación Espacial (IWF) de la Academia de ciencias de Austria (OEAB), coordinador científico del instrumento HASI, solicitó al Dr. Juan Antonio Morente un estudio de las resonancias Schumann en la atmósfera de Titán para indicar a los técnicos de la misión Cassini/Huygens la banda de frecuencias más apropiada a la que sintonizar el sensor de impedancia mutua del experimento PWA, con el fin de detectar estas resonancias en Titán. Este estudio se realizó y fue publicado en la revista Icarus de la Sociedad Americana de Astrofísica [55]. El interés científico por el tema lo pone de manifiesto el hecho de que poco tiempo después se publicó un número especial de la revista Radio Science con el título: *Recent Advances in Studies of Schumann Resonances on Earth and Other Planets of the Solar System* [56], en cuya introducción V. P. Pasko cita otro de los trabajos realizados por Gregorio Molina-Cuberos con su grupo de investigación sobre las Resonancias de Schumann en Marte [57]. Estudios análogos fueron llevados a cabo en la Tierra [14, 58–60]. Debido a las limitaciones de memoria y tiempo de cálculo, el modelo efectuado de la cavidad considera el espacio entre dos meridianos y la alimentación solo se produce en el eje Z de un sistema centrado en la esfera.

Un análisis de las medidas efectuadas por la sonda Huygens fue realizado por J.A. Morente, usando un algoritmo de filtrado a partir de la reconstrucción de la señal en el Dominio del Tiempo lo que permitió identificar las frecuencias de resonancia en la banda ELF [61] y VLF [62].

8.2 Análisis de las series temporales de registros magnetotelúricos

El método Magnetotelúrico (MT) intenta determinar la estructura y composición del subsuelo a través del tensor impedancia obtenido a partir de las medidas de campo eléctrico (en sus componentes N-S, E-O y vertical) y de campo magnético

(en sus componentes N-S, E-O) en función del tiempo [69, 70]. Las medidas se repiten en diferentes localizaciones para cubrir una determinada área de terreno. El rango en frecuencias de las medidas varía desde 1 mHz hasta 20 kHz para suministrar información a diferentes profundidades.

El Departamento de Geodinámica de la Universidad de Granada trabaja con el método magnetotelúrico desde hace algunos años [72, 73], lo que ha permitido generar una base de datos de señales temporales con diferentes duraciones y efectuadas en distintos puntos geográficos. En la Tabla 2.2 se muestran los datos geográficos de las medidas, donde se puede ver que éstas se ubican en Andalucía, Marruecos y en la Antártida. Con estas series se ha efectuado un doble estudio: Análisis Espectral de Fourier, que permite determinar las características de las resonancias de Schumann, y Análisis R/S desarrollado por E. Hurst [63], que permite determinar componentes estadísticas de las series.

8.2.1 Análisis Espectral

Las señales magnetotelúricas son unos valores discretos de voltaje que corresponden a valores de campo eléctrico y campo magnético medidos por las antenas del sistema. La transformada discreta de Fourier de esta serie no aporta mucha información debido a que contiene mucho ruido asociado tanto a los sensores, como a la propia señal (de hecho se habla de en la literatura de ruido electromagnético natural). En la parte del campo magnético la señal tiene una intensidad del orden de pT, mientras que el campo magnético terrestre oscila alrededor de 30 μT, es decir, más de un millón de veces superior en intensidad. Por eso es necesario aplicar el Método de Bartlett [66] a la señal: se trocea en intervalos cuyo número de muestras nos defina suficiente resolución en frecuencias; se le aplica a cada intervalo una ventana de Hanning para minimizar el efecto de truncado de la señal; se evalúa la Transformada Discreta de Fourier también en cada intervalo y, finalmente, se hace la media (en módulo, que es la parte que nos interesa) a todos los intervalos en que hemos dividido la señal completa.

Los parámetros que nos interesan calcular del espectro en módulo de la señal (obtenido a partir del procedimiento de Bartlett) son: los valores de pico de las resonancias, las amplitudes de estos picos y el factor de calidad, definido como el cociente entre el valor de pico y el ancho de banda en que este valor de pico cae 3

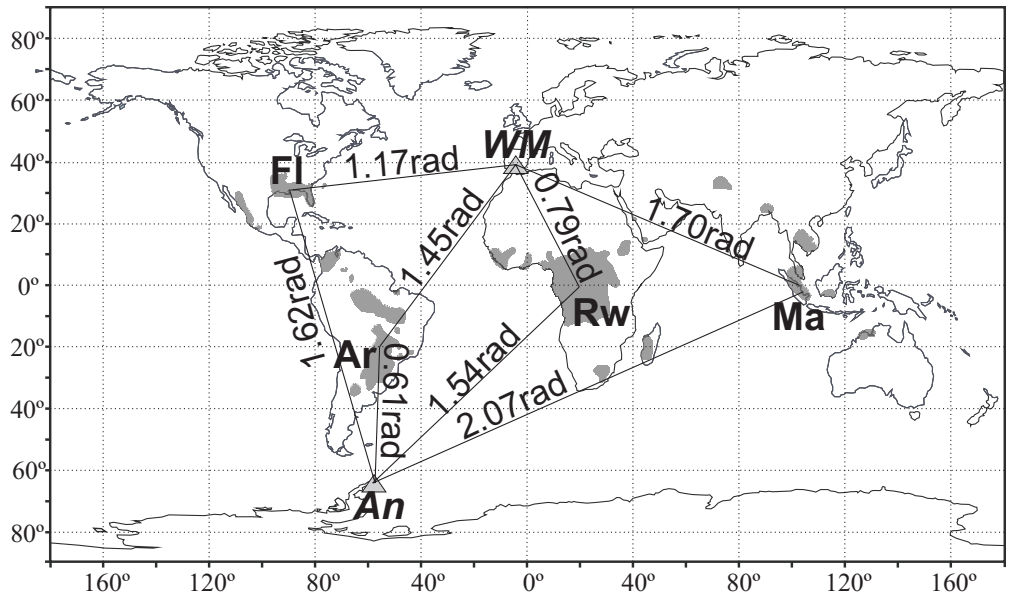

FIGURE 8.5: Mapa con las distancias angulares entre las campañas del estudio y las principales zonas tormentosas.

dB:

$$Q_n = \frac{f_{max,n}}{\Delta f_n}.$$

Estos parámetros se pueden obtener haciendo un ajuste mediante Lorentzianas [68]:

$$F_{Lfit}(f) = \sum_{n=0}^{N} \frac{B_n}{\left(\frac{f-f_{max,n}}{\Delta f_n}\right)^2 + 1}.$$

donde cada resonancia B_n es la amplitud de la resonancia n con frecuencia central $f_{\max,n}$ y ancho de banda Δf_n.

8.2.1.1 Descripción de las medidas Magnetotelúricas

Para el análisis de las medidas es fundamental determinar la distancia angular entre los principales centros tormentosos que dominan la generación de rayos y los puntos geográficos donde se efectuaron las medidas. Estas distancias, junto con las áreas con densidad de rayos mayor que 20 rayos $/\mathrm{km}^2/$ año se muestran en la Figura 8.5. Estas distancias nos determinan la amplitud de cada modo según se ha visto en el Capítulo 1. Es importante señalar que la amplitud del modo correspondiente a $n = 2$ es cercano a cero para las medidas en Antártica con fuentes localizadas en África Central.

Además de la distancia angular hay que tener en cuenta la proyección de la componente ϕ del campo magnético (componente principal) de cada una de las fuentes en cada uno de los puntos donde se han efectuado las medidas.

Como hemos señalado anteriormente, las medidas magnetotelúricas se efectúan en diferentes localizaciones de una zona amplia lo que añade una variable más, de carácter local. El campo eléctrico se ha mostrado más sensible a los cambios de localización, mientras que el campo magnético no se ve afectado por las variaciones locales.

De todas las series temporales suministradas por el departamento de Geodinámica, hay dos que tienen una duración que permite hacer un seguimiento de la evolución diaria de las resonancias de Schumann. Estas series han sido tomadas en Marruecos y en la Antártida y tienen una duración de 15 y 14 horas respectivamente, lo que ha permitido hacer sendos espectrogramas que se muestran en las Figuras 8.6 y 8.7.

En el espectrograma correspondiente a Marruecos se pueden identificar las cuatro primeras resonancias (entorno a 8, 14, 20 y 26 Hz) y un incremento en la amplitud de la señal en el intervalo de 06:00 - 08:00 UT, que corresponde a la hora de activación del centro tormentoso de Malasia (Asia). El espectrograma de la Antártida es mucho más limpio debido a la poca actividad humana en la zona y se pueden distinguir hasta 7 resonancias. Este punto de medida tiene la mayor parte de la energía en la componente EO del campo magnético, que corresponde a los centros tormentosos de América y Malasia, y también tiene una activación a las 06:00 - 08:00 UT, que de nuevo corresponde al centro tormentoso de Malasia.

8.2.1.2 Variaciones diarias de las resonancias de Schumann

Debido a la discontinuidad con que se efectuaron las medidas, no se ha podido efectuar un estudio sistemático de la variación diaria de las resonancias de Schumann. Sin embargo, la ubicación de la Antártida respecto a los principales centros tormentosos permite identificar importantes comportamientos diurnos de la segunda resonancia que se muestran en la Figura 8.8, donde se muestra el espectro de los campos magnético y eléctrico, en intervalos temporales donde se activan los centros tormentosos en África (14:30 - 17:30 UT) y en América (17:30 - 22:30 UT) y para las dos componentes horizontales. Se puede observar que, efectivamente, el

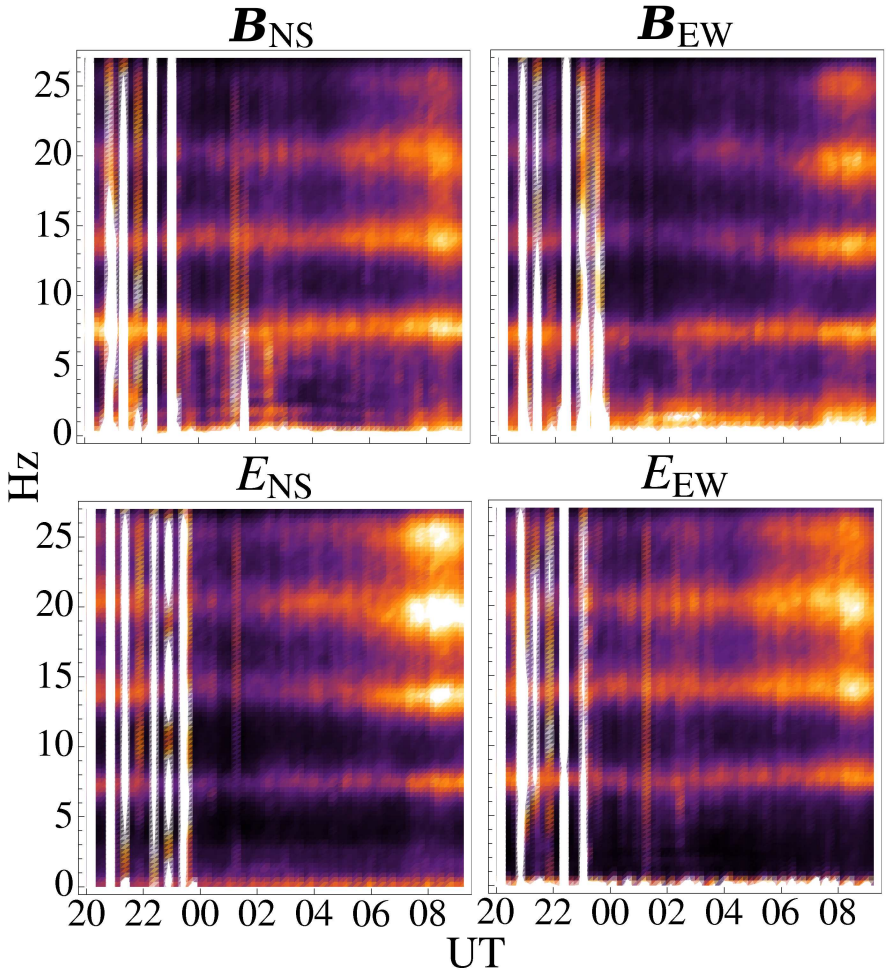

FIGURE 8.6: Espectrograma de las componentes eléctrica y magnética de la noche del 5 al 6 de febrero de 2006, tomada en la campaña de Marruecos.

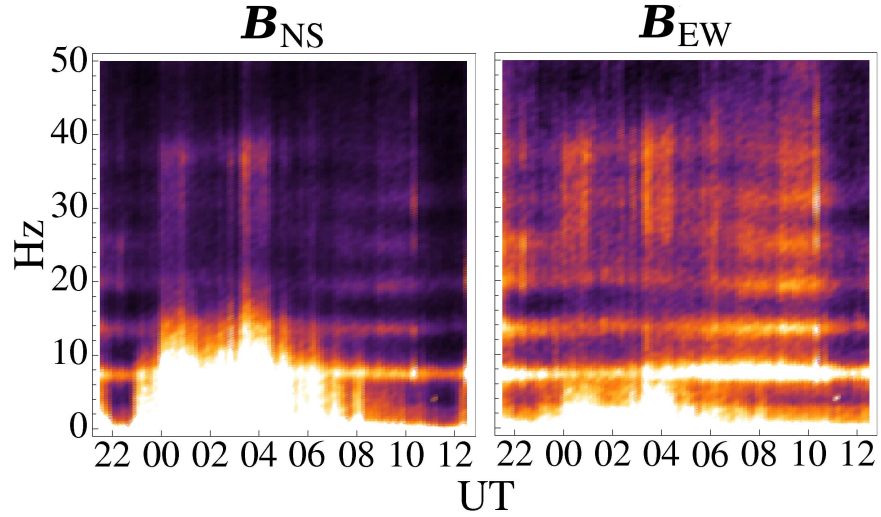

FIGURE 8.7: Espectrograma de las componentes magnéticas del 29 - 30 de enero de 2008, tomada en la campaña Antártica.

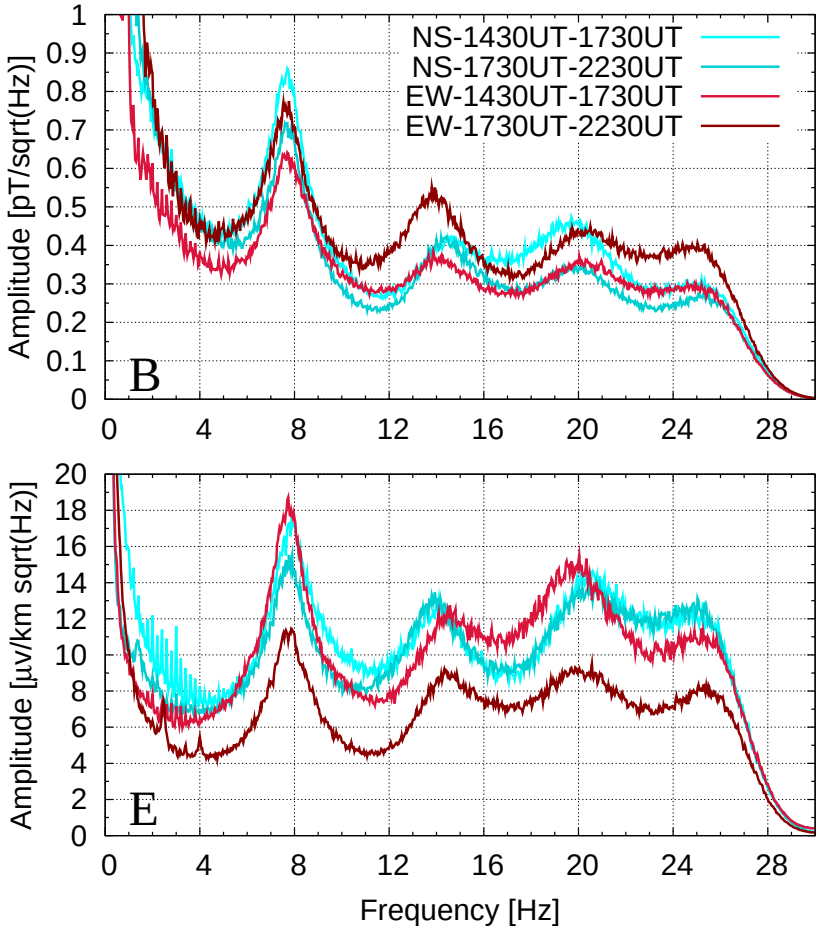

FIGURE 8.8: Variación del segundo modo de las RS para las señales medidas en la Antártida.

segundo modo para el campo magnético generado por las tormentas de África en la componente N-S tiene menor amplitud que el tercer modo. Esto es debido a la distancia angular que hace que para el segundo modo se tenga un mínimo. Por el contrario, en la componente E-O, los dos modos se igualan en amplitud debido a que en esta componente intervienen otros centros tormentosos que, aunque de mucha menor intensidad, también contribuyen al campo global. El centro tormentoso de América no cumple la condición de mínimo asociado a la distancia angular y, como ocurre en el resto de espectros estudiado, el segundo modo tiene mayor amplitud que el tercero. Para este centro tormentoso y como predice el modelo analítico, la componente E-O es la mayor en el campo magnético.

En el análisis de estas medidas también se puede comprobar que hay una pequeña variación en la frecuencia central entre ambas componentes de los campos (en la Tabla 8.1 se muestran para el campo magnético) y la tendencia de esta variación depende del modo, de acuerdo con otros estudios experimentales [74].

TABLE 8.1: Frecuencia central de las componentes N-S y E-O del campo magnético de los espectros de la Figura 8.8.

Hora (UT)	Componente	Frecuencia (Hz)		
		1er modo	2do modo	3er modo
1430-1730 UT	NS	7.69	14.56	19.86
1430-1730 UT	EO	7.80	14.05	20.50
1730-2230 UT	NS	7.73	14.45	20.07
1730-2230 UT	EO	7.61	13.83	20.53

8.2.1.3 Variaciones estacionales de las resonancias de Schumann

En el estudio de las variaciones anuales también hay que señalar que la muestra de medidas no es estadísticamente significativa pero puede servir para corroborar resultados obtenidos en otros trabajos como los de Ondrášková et al. [74] o Roldugin et al. [76]. Se han utilizado señales de al menos 90 minutos de duración, divididas en bloques de 30 segundos, para aplicarles el método de Bartlett.

En amplitud, la componente E-O del campo magnético medido en Andalucía y Marruecos muestra cierta estabilidad anual mientras que la componente N-S presenta máximos coincidentes con las estaciones más cálidas en el hemisferio Norte. Los meses de menor amplitud corresponden a enero (medida efectuada en 2008) y febrero (medida efectuada en 2006), corroborando los resultados de otros autores [77, 78], ver Figura 8.9. El campo eléctrico presenta una variación local muy grande (hasta un orden de magnitud), por lo que no se puede extraer ninguna conclusión sobre la variación estacional. Sin embargo, las amplitudes para los tres primeros modos estudiados del campo eléctrico presentan similar amplitud en cada campaña, por lo que este campo se presta más al estudio experimental de modos altos de las resonancias de Schumann.

Las frecuencias centrales de los tres primeros modos oscilan entorno a 7.8, 14 y 20.5 Hz, existiendo correlación entre las componentes B_{NS} y E_{EO} y viceversa. Los cambios más significativos coinciden, como en la sección anterior, en las medidas efectuadas en la Antártida en el segundo y tercer modos. Según [74], estos desplazamientos en frecuencia de las resonancias de Schumann están relacionados con el tamaño efectivo del núcleo tormentoso.

Por último, el factor de calidad Q no muestra variación en las diferentes campañas y tiene tendencia a ser mayor para los modos más altos.

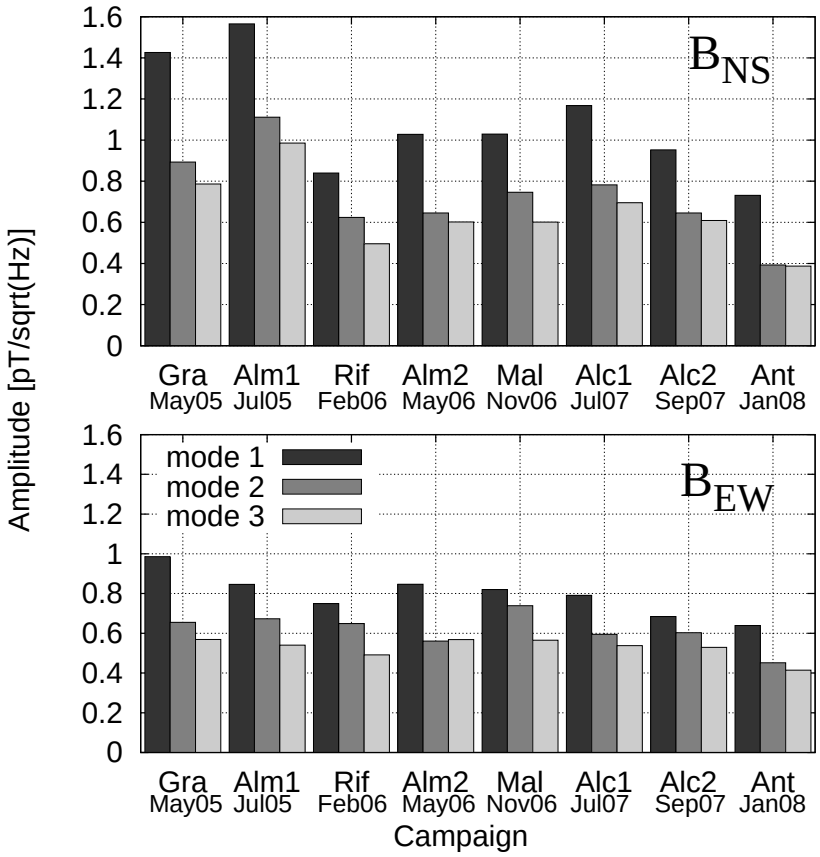

FIGURE 8.9: Amplitud del campo magnético para las tres primeras resonancias de Schumann.

8.2.2 Análisis *Rescaled Range* (R/S)

Las series temporales pueden ser descompuestas en: (1) una componente de tendencia que recoja el comportamiento macroscópico del sistema generador de la serie y su tendencia a largo plazo, (2) otra componente que recoja las discontinuidades, (3) otra con la componente periódica que suele ser frecuente en procesos naturales (mareas, rotación de planetas, etc.) y, finalmente, (4) una componente estocástica que recoja las fluctuaciones y que podríamos denominar genéricamente como ruido. El análisis R/S estudia la persistencia de la componente estocástica en las series temporales [63, 79] a través del exponente de Hurst (Hu). Para el ruido blanco gaussiano, Hu=0.5, las señales con Hu entre 0.5 y 1 se califican como persistentes, y antipersistentes si Hu es inferior a 0.5. Las señales naturales suelen ser persistentes [80]. Este coeficiente se relaciona con el coeficiente Z obtenido a partir del cociente entre el rango R y la desviación estándar S de la señal (de ahí

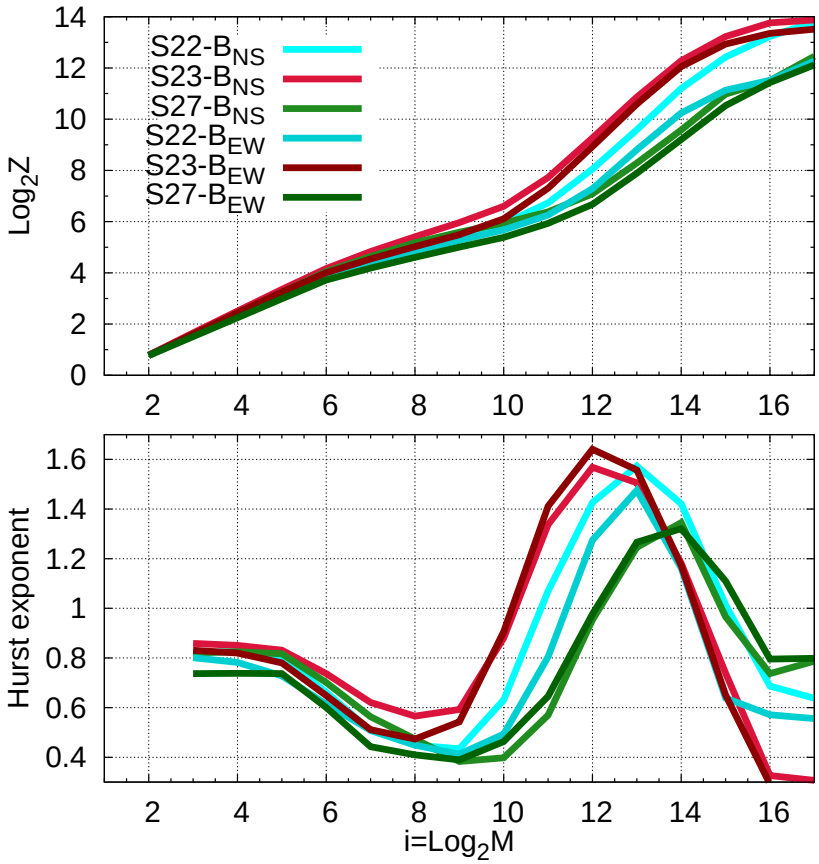

FIGURE 8.10: Resultados del análisis R/S aplicado a señales medidas en la Antártida.

el nombre R/S del método) mediante una ley de potencia:

$$Z = \left(\frac{M}{2}\right)^2$$

donde M representa diferentes escalas en la serie temporal.

Este análisis ha sido aplicado a las señales magnetotelúricas medidas en la Antártida, donde el ruido antropogénico es prácticamente inexistente. Los resultados se muestran en la Figura 8.10, donde se observan tres zonas diferentes. Una primera para I=[2,5] que corresponde a una escala temporal de hasta 1/16 s, donde Hu oscila entre 0.75 y 0.85, dependiendo de la serie analizada. La segunda zona corresponde al intervalo de escalas entre 1/8 y 2 segundos (I entre 6 y 10), donde el valor de Hu tiende a 0.5, indicando un comportamiento aleatorio. La tercera parte corresponde a valores del exponente de Hurst que no siguen una ley de potencias y por tanto éstos no tienen un sentido claro.

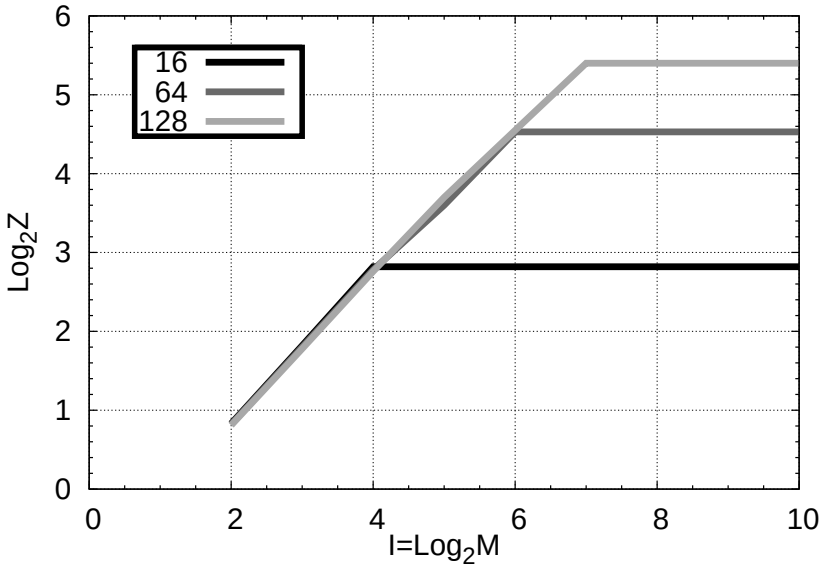

FIGURE 8.11: Curva $\mathrm{Log}_2 Z$-I de una simulación emulando el contenido ELF de una serie temporal.

Otro aspecto muy importante del análisis R/S es que permite definir valores de magnitudes con claro carácter estocástico. El número de rayos que en promedio se producen cada segundo en la Tierra es una de esas magnitudes porque su valor influye en el rango y la desviación estándar de la señal. Nickolaenko et al. [81] propone que dicha magnitud se puede evaluar a partir de la escala donde el exponente de Hurst cambia su tendencia de un valor constante. Con el objetivo de comprobar esta hipótesis, se ha efectuado una simulación numérica consistente en generar una sucesión de señales electromagnéticas similares a la que generan los rayos, controlando su secuencia y aplicando el método R/S a las diferentes series. En la Figura 8.11 se muestra la representación de Z en función de la escala para las tres series obtenidas variando la secuencia de señales a través del número de muestras entre cada descarga (en la figura se muestran las curvas para 16, 64 y 128 muestras). Se puede ver como se confirma la hipótesis pudiéndose identificar claramente a partir del cambio en la pendiente del logaritmo de Z (proporcional al exponente de Hurst) la razón de señales por segundo. A partir de la Figura 8.10 se puede inferir una razón de entre 16 y 32 rayos por segundo, que está de acuerdo con los valores experimentales de esta variable [12].

8.3 Determinación de la altura efectiva de la ionosfera a partir de la 1ª frecuencia de corte de la guía de ondas.

El satélite francés DEMETER fue diseñado y lanzado con el propósito de estudiar las perturbaciones causadas en la ionosfera por fenómenos naturales. Uno de sus principales objetivos es establecer la conexión entre desastres naturales (principalmente terremotos y erupciones volcánicas) y perturbaciones ionosféricas para futuros sistemas de predicción [9, 84–87]. A través del sensor de campo eléctrico (ICE) es posible medir las tres componentes de campo a través de la ionosfera en una órbita circular síncrona con el Sol a unos 700 km de altura. De todas las bandas en que puede efectuar medidas, nos interesa la banda VLF, en la que el satélite efectúa mediciones a 40 kHz y envía el espectro de potencia promediado y normalizado, porque es en ella donde está la primera frecuencia de corte de la guía de ondas, formada por la superficie de la Tierra y la ionosfera. Debido a que la distancia a la que se propagan las ondas electromagnéticas hasta atenuarse en esta banda es de pocos miles de kilómetros podemos aproximar la geometría a una guía plano-paralela donde la primera frecuencia de corte, f_c, corresponde a una longitud de onda igual al doble de la altura de la guía, h:

$$f_c = \frac{c}{2h}$$

donde c es la velocidad de la luz.

En el espectro medido por el satélite en la banda VLF esta frecuencia de corte corresponde a un mínimo situado entre 1.4 y 2.0 kHz, tras un acondicionamiento de la señal [2]. A partir de la altura efectiva podemos determinar parámetros muy importantes en la zona correspondiente a la altura efectiva, inaccesible para medidas in-situ tanto para satélites como para globos sonda, como son la densidad de electrones o la conductividad efectiva.

Con el fin de poder hacer un mapa global de la altura efectiva se ha seleccionado un paso espacial de entre 1° y 5° y un intervalo temporal, que dependerá del estudio que estemos efectuando. A continuación, se toman todas las medidas nocturnas efectuadas por DEMETER en el intervalo espacio-temporal y se efectúa un promedio que suministre un espectro único. A partir de este espectro un algoritmo

detecta el mínimo correspondiente a la frecuencia de corte de la guía. La razón de seleccionar las medidas nocturnas es que la estabilidad del plasma de la ionosfera hace que las señales tengan mucho menos ruido. Las medidas consideradas se han efectuado desde enero de 2006 hasta febrero de 2010.

En la Figura 8.12, se muestra un mapa global con el valor de la altura promedio en los 4 años para los doce meses. La órbita del satélite se sitúa entre $\pm 65°$ de latitud, por lo que solo esta franja aparece en el mapa. Se puede observar que la altura efectiva es menor en el hemisferio norte en las estaciones frías, básicamente entre noviembre y marzo, siendo más notable este descenso en las zonas de océano. Hay una gran excepción en el Este Asiático y en el Pacífico Oeste. La variación observada es de 5 a 10 km.

En cuanto a variaciones estacionales, la más destacable se produce en el Océano Pacifico Sur donde la altura efectiva es superior a 100 km entre mayo y septiembre, para luego decrecer a 90 km desde noviembre a marzo (Figura 8.13). Debido al carácter estacional, la causa de esta variación debe venir (directa o indirectamente) de cambios en la irradiación solar recibida y/o cambios en la climatología local.

Otra variación que puede observarse ocurre en latitudes ecuatoriales, tanto en el Océano Atlántico como en el Océano Índico, que aunque separados por el continente africano, experimentan idénticos cambios en la altura efectiva dos veces por año. En general se observa que los mayores cambios se producen sobre el océano. Se plantean como posibles causas:

1. Efecto de los aerosoles en el circuito eléctrico global [107, 108].
2. Efecto de la menor actividad tormentosa en el océano frente a la de los continentes.
3. Efecto de eventos transitorios luminosos (*elves, sprites, jets*, etc.) cuya ocurrencia es mucho mayor sobre los océanos que sobre los continentes [120].

A partir de la altura efectiva se puede calcular la densidad de electrones considerando que a esa altura se produce una reflexión total de una onda electromagnética que incida normalmente en la ionosfera, debiéndose cumplir la relación [103]:

$$\omega_p^2 = \omega\nu$$

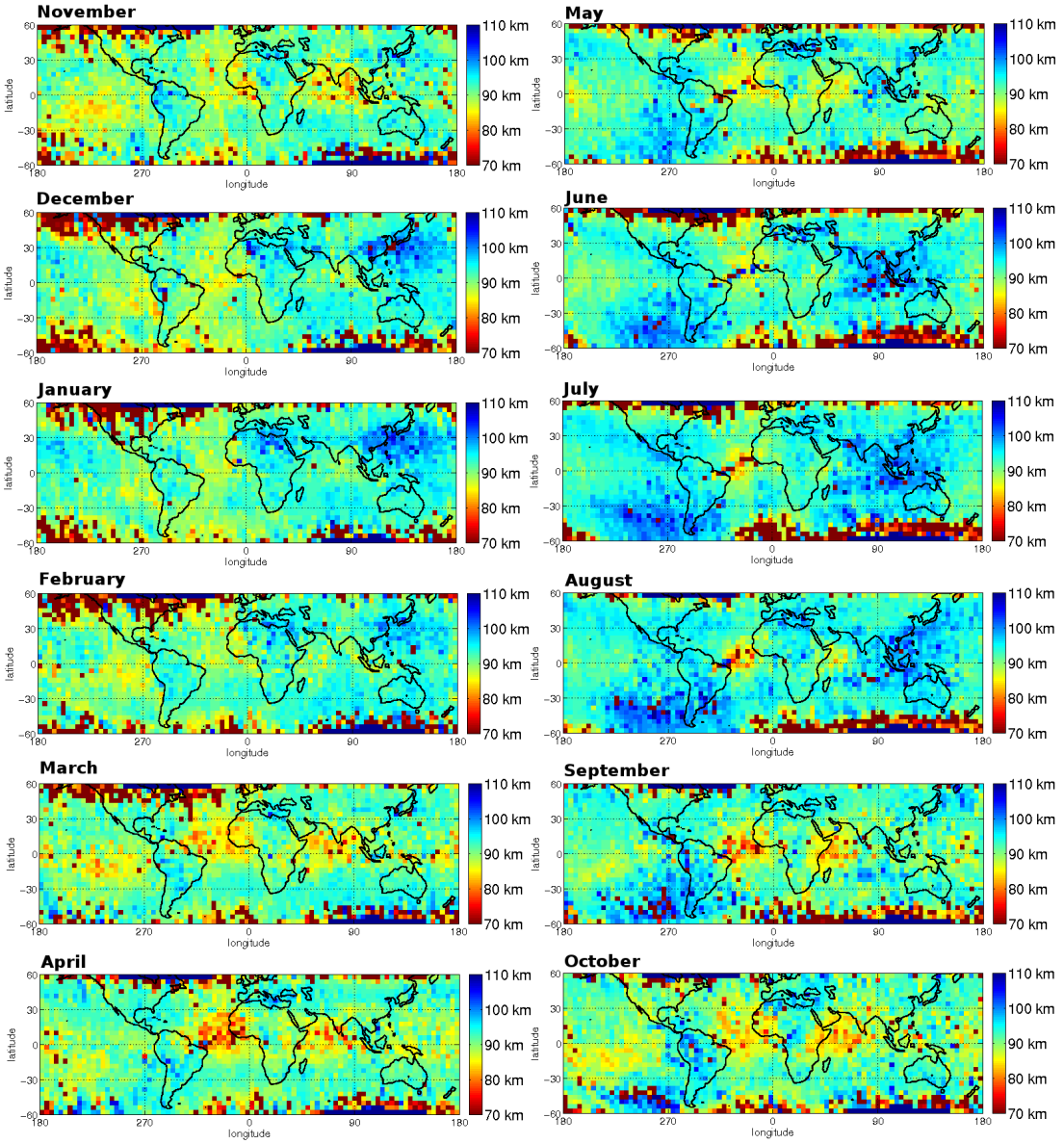

FIGURE 8.12: Mapa de la altura efectiva de la ionosfera para los 12 meses, promediados entre 2006 y 2009.

donde ω_p es la frecuencia angular del plasma a esa altura, ω la frecuencia angular de la señal y ν la frecuencia de colisión. A partir de la densidad de electrones y tomando como dato la densidad de neutros del modelo MSIS [101, 102], es posible calcular también la conductividad de la ionosfera a la altura efectiva. En la Figura 8.14 se muestra el mapa global de la densidad de electrones y conductividad efectiva a la altura efectiva promediados por estaciones.

La medida de la actividad solar es muy importante para el estudio del Medio Ambiente. A través del índice F10.7 [126] es posible establecer una correlación

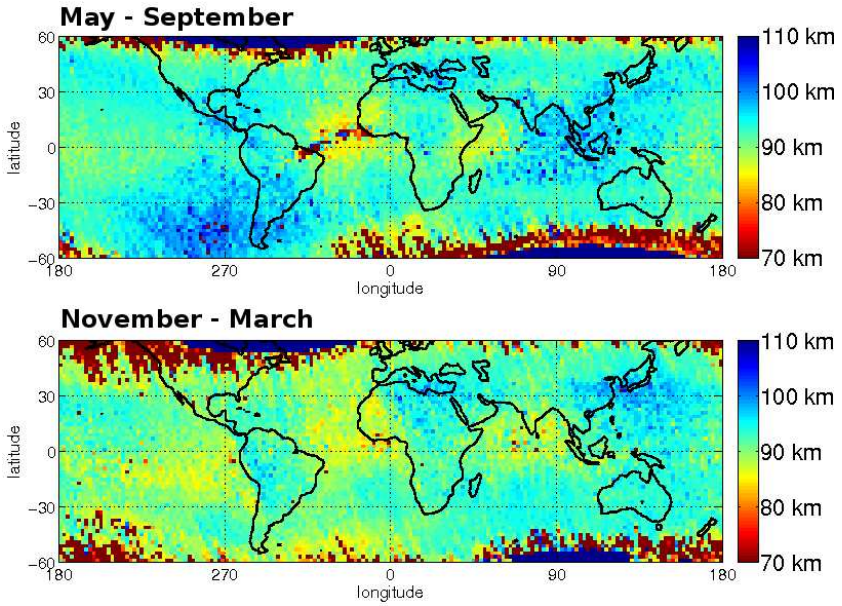

FIGURE 8.13: Mapa de la altura efectiva de la ionosfera para dos épocas del año, promediadas entre 2006 y 2009.

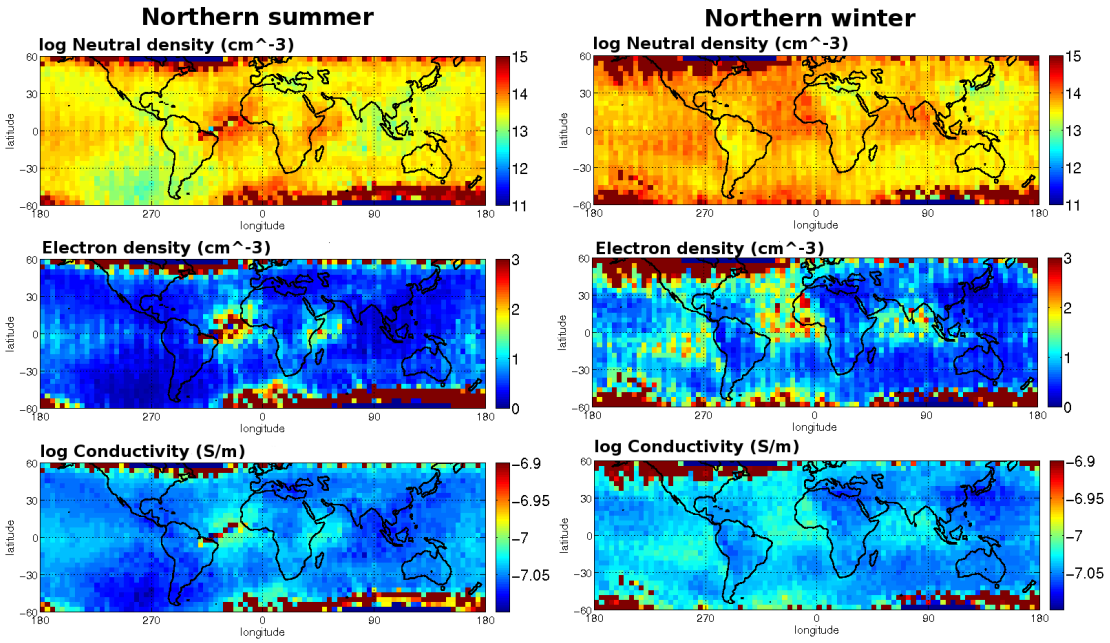

FIGURE 8.14: Mapa de la densidad de neutros, densidad de electrones y conductividad a la altura efectiva de la ionosfera.

entre la actividad solar y la frecuencia de corte medida durante el periodo 2006-2009 por el satélite DEMETER. En la Figura 8.15 se puede ver como durante este periodo se ha detectado un decrecimiento global de la frecuencia de corte que se puede explicar por una menor actividad solar, medida a través del parámetro solar F10.7. El rizado que se observa en la curva de la frecuencia de corte está causado por las variaciones estacionales descritas anteriormente. Sería conveniente en estudios futuros establecer esta correlación en un periodo de tiempo mucho más largo.

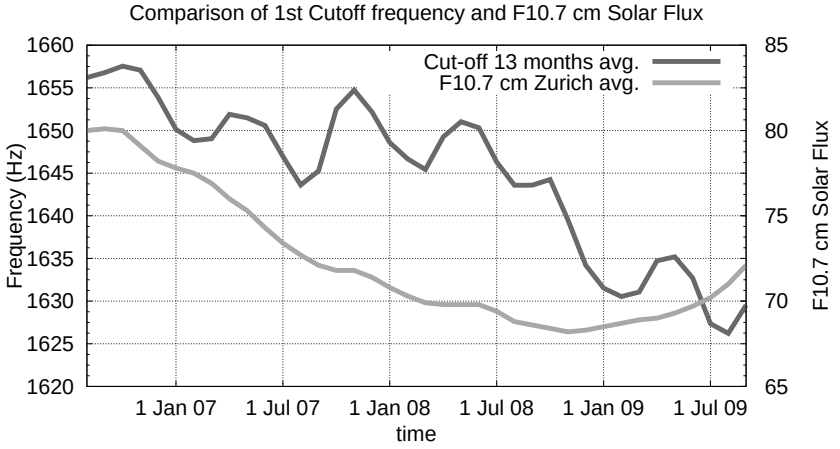

FIGURE 8.15: Comparativa del parámetro F10.7 y la frecuencia de corte inferida a partir de los datos de DEMETER.

Los datos presentados en este estudio revelan por primera vez la frecuencia de corte y su correspondiente altura efectiva de reflexión en la totalidad de la Tierra, incluyendo las áreas sobre los océanos. Hay una gran falta de medidas en las regiones D y E de la ionosfera [128] y las que hay (utilizadas en los modelos empíricos IRI y MSIS) no revelan todos los detalles mostrados en las figuras anteriores, como las variaciones estacionales y las variaciones tan acusadas en la altura efectiva de la ionosfera.

8.4 El método TLM

El método de la Matriz de Líneas de Transmisión o método TLM es una aproximación numérica en el dominio del tiempo a las ecuaciones de Maxwell desarrollada por Johns y Beurle en 1971 [140], estableciendo un modelo equivalente del problema basado en circuitos de líneas de transmisión. Esta naturaleza conceptual, en contraposición a una simple aproximación numérica, hace que el método sea una

poderosa herramienta capaz de resolver no solo problemas de propagación de ondas electromagnéticas sino también problemas de acústica o difusión de partículas, por ejemplo [141–143].

El método TLM establece una discretización del espacio y del tiempo en celdas elementales o nudos TLM. Las variables voltaje e intensidad sustituyen a los campos electromagnéticos, mientras que los parámetros característicos de las líneas de transmisión modelan el medio por el que se propaga el campo. En cada instante temporal $t = n\Delta\mathrm{t}$, una secuencia de pulsos incidentes, V_n^i, son dispersados en cada nudo TLM, transformándose en voltajes reflejados, V_n^r, a través de la ecuación:

$$V_n^r = SV_n^i$$

donde S es la matriz de dispersión que modela el medio. Estos voltajes reflejados se convierten en incidentes en el instante temporal siguiente y en los nudos vecinos. El procedimiento básico en la resolución numérica de un problema físico mediante el método TLM consiste en establecer un nudo que genere ecuaciones diferenciales equivalentes a las del problema y calcular su matriz de dispersión.

Inicialmente, el método TLM fue propuesto para problemas bidimensionales usando diferentes nudos con distribución de líneas de transmisión en paralelo y en serie [140, 141, 144]. Después, se resolvieron problemas tridimensionales usando el nudo asimétrico expandido [146, 147, 147]. Pero no fue hasta 1986 cuando P. B. Johns cambió la manera de entender el nudo TLM a través del nudo simétrico condensado [154, 155], consistente en 12 líneas unidas formalmente en su centro a través de las ecuaciones de Maxwell (líneas principales) y que dan cuenta de la propagación, junto con otras 6 líneas, representadas por stubs inductivos y capacitivos, que representan las inhomogeneidades del medio en permeabilidad magnética y permitividad eléctrica. Si el medio tiene pérdidas, tanto eléctricas como magnéticas, a estas 18 líneas hay que añadirles otros 6 stubs de pérdidas, uno por cada dirección del campo eléctrico y de campo magnético. La matriz de dispersión resultante tiene dimensión 18x24 y los coeficientes vienen definidos por las características electromagnéticas del medio.

La excitación en el método TLM no es inmediata. En principio el campo incidente aparece como un voltaje incidente por la línea principal correspondiente. El problema es que pueden aparecer otros campos asociados al voltaje incidente añadido que no tienen equivalente en el problema original. Sin embargo añadiendo

otros pulsos de voltaje incidente por otras líneas se puede compensar este efecto [166].

La discretización espacio-temporal genera un medio numérico dispersivo [160, 161], por lo que como norma general de los métodos numéricos de baja frecuencia como es el TLM, el muestreo espacial debe ser como máximo 1/10 la longitud de onda mínima de la señal de excitación. Naturalmente, el muestreo temporal debe ser controlado también, pero el teorema de Shannon impone una restricción casi siempre menor a la comentada.

El uso del método TLM para otras geometrías, como cilíndricas o esféricas, es similar al cartesiano. Sin embargo, aparecen los siguientes inconvenientes: i) aparecen singularidades en el eje Z tanto en cilíndricas como en esféricas; ii) el tamaño de los nudos se va incrementando con las coordenadas radiales tanto en cilíndricas como en esféricas, por lo que el método se vuelve muy dispersivo.

Como ventaja de estos métodos es que evita el mallado en escalera cuando la geometría del problema tiene superficies cilíndricas o esféricas.

La pregunta clave que surge cuando se resuelve numéricamente un problema es ¿Por qué se elige un método y no otro? En nuestro caso, ¿Por qué se elige TLM y no el más popular basado en diferencias finitas en el dominio del tiempo, FDTD? En principio TLM requiere más memoria que FDTD y como nuestro problema es computacionalmente grande, esto es un inconveniente. Sin embargo TLM es incondicionalmente estable y todas las componentes de los campos están ubicadas en el mismo punto e instante. Además, el método TLM supone un modelo del problema físico, lo que hace que inicialmente el método tenga más dificultad, pero hace que aporte más y mejor información de la solución que otros métodos numéricos. Así el método TLM puede usarse para resolver problemas tan diferentes como la radiación de una antena de hilo [163–165], donde el sistema tiene dimensiones físicas dispares, o el modelado de metamateriales con propiedades electromagnéticas singulares que permiten diseñar capas de invisibilidad electromagnética [167].

8.5 Paralelización del método TLM

En los métodos numéricos, disponer de una herramienta de cálculo con suficiente potencia es una necesidad continua. La potencia de las CPU (del inglés, *Central Processing Unit*) parece haber alcanzado su máximo y la opción más efectiva para incrementar la potencia de cálculo es la paralelización usando múltiples CPU y/o con múltiples núcleos. La paralelización se puede realizar, con los medios disponibles en nuestro entorno de investigación, mediante tres vías: sistemas con memoria compartida, sistemas con memoria distribuida y unidades de procesamiento gráfico (GPU, del inglés *Graphics Processing Unit*).

Los sistemas de memoria compartida consisten en una unidad o placa con varios procesadores que a su vez suelen estar compuestos de varios núcleos. Esta unidad dispone de memoria RAM (del inglés, *Random Access Memory*) accesible a todos los núcleos a través de un sistema de comunicación interno que opera a una velocidad de acceso alta. Es precisamente este acceso a memoria por parte de los diferentes núcleos el cuello de botella de esta tecnología, en especial cuando el número de núcleos accediendo a la misma memoria es alto. Para mitigar este problema, en máquinas con muchos procesadores se suele utilizar la arquitectura NUMA (del inglés, *Non Uniform Access Memory*) que permite un acceso más rápido por parte de cada núcleo a una parte de la memoria, con lo que la paralelización es más eficiente. La paralelización con sistema de memoria compartida deja de ser eficiente a partir de la centena de núcleos, aproximadamente. El protocolo o API (del inglés *Application Package Interface*) más usado en estos sistemas es OpenMP.

Los sistemas de memoria distribuida consisten en un número de sistemas de memoria compartida unidos mediante un sistema de comunicación que permite el tránsito de información de unos núcleos con otros. De nuevo es este sistema de comunicación el cuello de botella del proceso de paralelización. El protocolo o API más usado en este tipo de sistemas es MPI (del inglés *Message Passing Interface*).

Las GPUs están diseñadas específicamente para operaciones vectoriales por lo que su potencia de cálculo es mucho mayor que la de las CPUs, pero la memoria disponible es muy limitada. La programación con ellas es muy específica y completamente diferente a los sistemas de memoria compartida o distribuida.

La simulación numérica de la cavidad Tierra-ionosfera tiene como dificultad principal la desproporción de sus dimensiones (100 km de espesor frente a un radio esférico de 6,370 km). Los rayos son la principal fuente de campo electromagnético y su espectro se concentra fundamentalmente en las bandas ELF y VLF. Puesto que las ondas electromagnéticas en la banda ELF pueden dar varias vueltas a la tierra es necesario un modelo tridimensional de la misma. Para esta banda de frecuencias podemos considerar que la corteza terrestre es un conductor perfecto, las capas bajas de la ionosfera como dieléctrico perfecto y a medida que subimos en altura ir incrementando la conductividad, véase Figura 8.16, hasta poder considerar de nuevo la condición de conductor perfecto a 100 km.

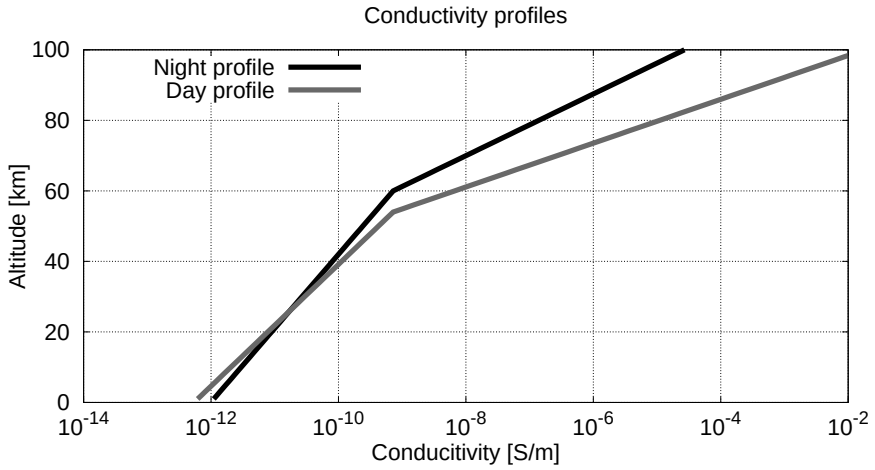

FIGURE 8.16: Perfiles de conductividad de la atmósfera. Extraído de Pechony and Price [182].

8.5.1 Paralelización

Dada la geometría de la cavidad, un modelo esférico permitiría un modelado geométrico más óptimo. Sin embargo la singularidad en el eje Z hace que la unión de nodos sea complicada y que las dimensiones de los mismos sean variables, lo que genera una gran dispersión numérica en la malla. El modelado en nudos cartesianos evita este problema pero genera un modelado en escalera, en el sentido de que las formas esféricas deben ser aproximadas por cubos. Para evitar problemas de dispersión hemos preferido usar el modelo cartesiano aunque evidentemente el esférico queda como un objetivo futuro.

Las propiedades electromagnéticas de las celdas comprendidas entre un radio de 6,370 km y otro de 6,470 km tienen una permitividad eléctrica y permeabilidad

magnética igual a la del vacío pero presentan una conductividad en función de la altura. En una primera versión hemos considerado a la ionosfera como un plasma isótropo. La introducción de la anisotropía se ha dejado como un objetivo futuro. Con el fin de reducir el tiempo de cálculo se han incrementado los requerimientos de memoria, por lo que cada nodo necesita un mínimo de 100 Bytes de memoria. Para un tamaño de celda de 10 km^3 son necesarias del orden de 5 10^7 celdas para rellenar toda la corona esférica por lo que se requieren unos 5 GBytes de memoria.

La paralelización requiere un esfuerzo de programación muy grande por lo que hacer un programa paralelizado óptimamente para cada problema es inviable, para una herramienta tan versátil como el método TLM. Por ello se ha elaborado un preproceso que transforma cualquier problema (tridimensional, bidimensional o unidimensional) en unidimensional y que sirve de entrada para el programa central de cálculo que ha sido paralelizado y que es común a cualquier geometría.

El preproceso consiste en asociar a cada nudo (identificado mediante un número único) con los identificadores de sus nudos vecinos. Así cualquier geometría se transforma en una agrupación unidimensional de nodos donde cada uno tiene información sobre las características electromagnéticas de la celda que define y los números identificadores de sus vecinos, incluyendo las condiciones de contorno si el nudo cae en la frontera.

En proceso de cálculo principal y que se ha paralelizado consiste en que en cada instante temporal los voltajes incidentes en cada nudo se transforman en reflejados a través de los coeficientes de la matriz de dispersión. Si usamos un sistema de punteros asociados a los nudos vecinos, estos voltajes reflejados se pueden escribir en las direcciones de memoria en las que luego se lee el voltaje incidente. Por tanto cada núcleo puede encargarse de unos nudos concretos en cada instante temporal con la condición de que todos los núcleos se sincronicen al final de cada iteración temporal.

8.5.2 Implementación y pruebas de rendimiento

El programa desarrollado utiliza la arquitectura de memoria compartida usando las directivas openMP y ha sido escrito en lenguaje C. Durante el proceso de paralelización ha sido necesario desarrollar estrategias locales como la multiplicación de los voltajes incidente por la matriz de dispersión para reducir al mínimo el

número de operaciones, así como la propia redefinición de la matriz en base a tres coeficientes.

Para comprobar el funcionamiento del programa en diferentes arquitecturas se ha elegido una cavidad rectangular con diferentes dimensiones según se muestra en la Tabla 8.2. Las arquitecturas probadas han sido tres:

1. SuperMicro8 (SM8) con 2 procesadores AMD opteron de cuatro núcleos a 2.0 GHz y 32 GB de RAM.
2. SunFire (SF16) con 8 procesadores AMD opteron de doble núcleo a 2.2 GHz y 64 GB de RAM.
3. SuperMicro32 (SM32) con 4 procesadores de 8 núcleos a 2.0 GHz y 96 GB de RAM.

TABLE 8.2: Descripción de las cuatro simulaciones empleadas para las pruebas de rendimiento.

Leyenda	Nº de nudos	Memoria	iter. temporales	nodos·iteraciones
P1	10^4	1.72 MB	10^5	10^9
P2	$4 \cdot 10^4$	6.88 MB	$2.5 \cdot 10^4$	10^9
P3	10^6	172 MB	10^3	10^9
P4	$5 \cdot 10^7$	8.6 GB	$2 \cdot 10^1$	10^9

Los resultados obtenidos demuestran que el tiempo de ejecución crece linealmente con el número de iteraciones temporales, independientemente del número de núcleos utilizados. Este hecho pone de manifiesto la secuencialidad de éstas. En la Figura 8.17 se muestra una serie de gráficas con el tiempo total de ejecución y la aceleración (cociente entre el tiempo empleado con 1 núcleo y el empleado con n núcleos). Se puede observar que no hay una relación simple entre escalabilidad del algoritmo y su tamaño sino que intervienen múltiples variables como la configuración de la CPU en núcleos, disposición de la memoria RAM o el tamaño de la caché. La influencia de la caché se pone de manifiesto en que la máxima aceleración se consigue en los problemas P1 y P2 llegándose incluso a alcanzar aceleraciones superlineales (aceleración superior al número de núcleos utilizados). La máxima aceleración conseguida ha sido 11.3 con 16 núcleos en el ordenador

SuperMicro32 en el problema P2, que es un buen resultado de paralelización si se compara con otros trabajos [187, 188].

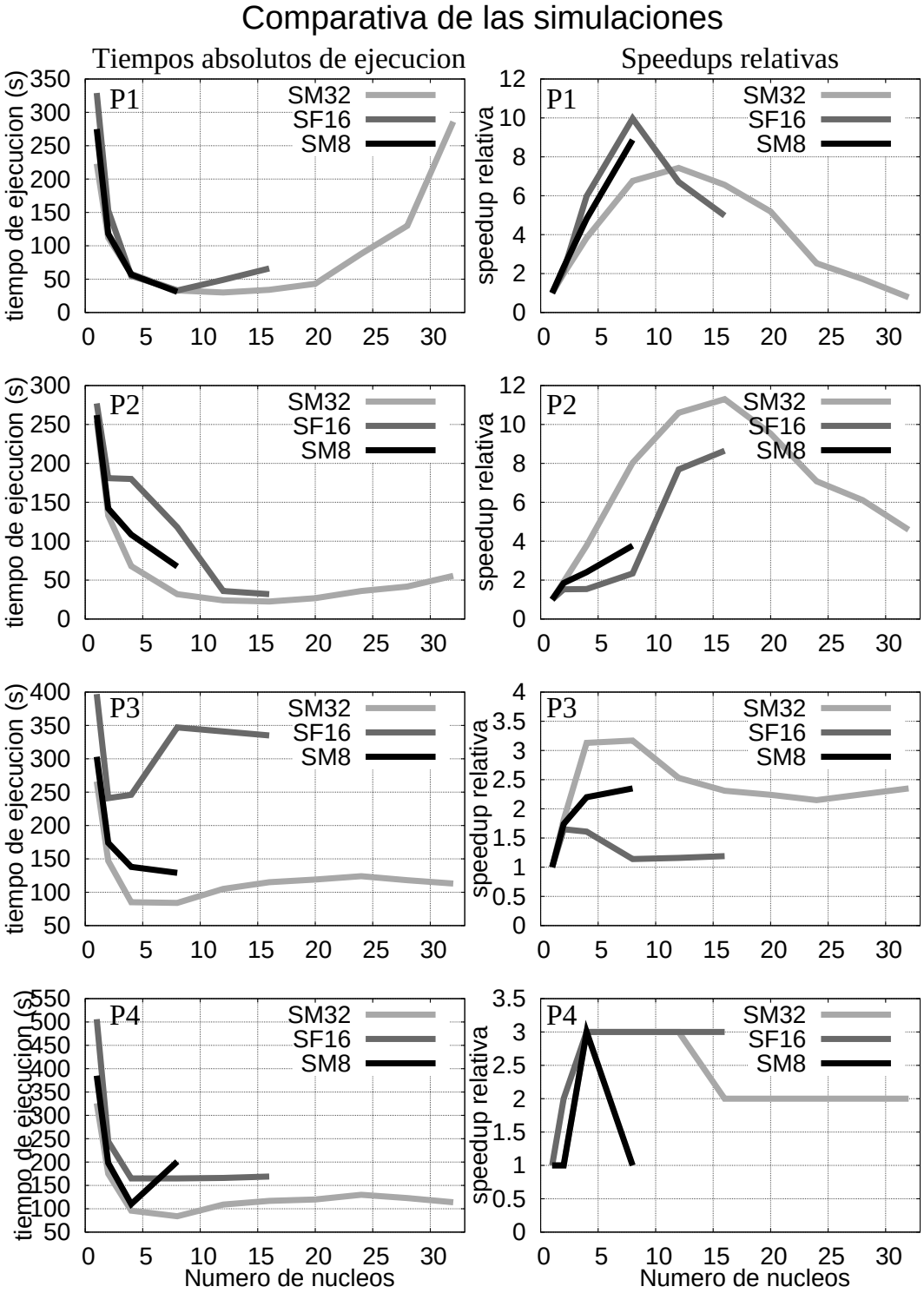

FIGURE 8.17: Aceleraciones obtenidas para la cavidad rectangular.

En la optimización de la paralelización para problemas grandes (P3 y P4) ha sido fundamental el uso de la herramienta `numactl` que permite modificar la

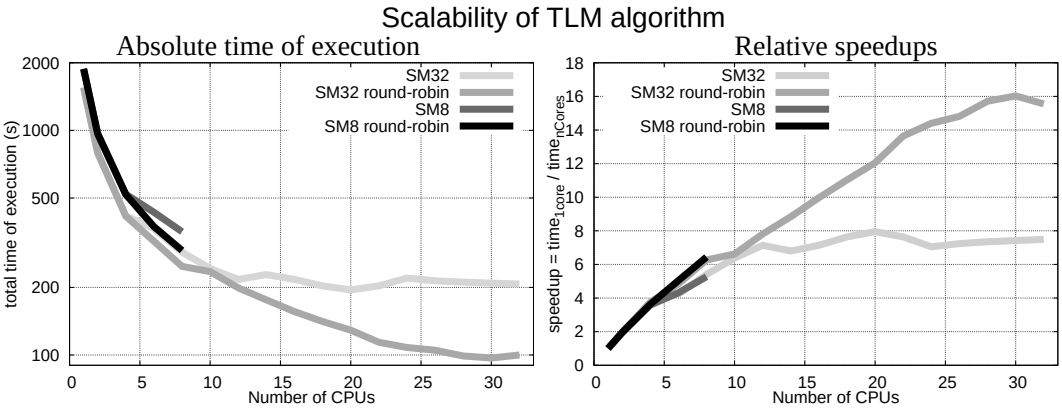

FIGURE 8.18: Comparación de la aceleración obtenida al utilizar el esquema *round-robin*.

política de asignación de memoria a un esquema de tipo *round-robin*, de manera que la memoria sea asignada uniformemente entre los diferentes segmentos de la arquitectura NUMA.

Como ejemplo de la versatilidad del programa en el tratamiento de diferentes geometrías también se ha simulado la propagación de una señal electromagnética en la banda VLF, para lo cual se ha modelado aquella parte de la cavidad a la que llega la señal (la atenuación de la atmósfera es muy grande a estas frecuencias) por lo que la geometría se convierte en una guía de placas plano-paralelas infinita. Se ha estudiado el caso con pérdidas y sin pérdidas. El tamaño de la celda usado en esta simulación es de 1.5 km y se han simulado 7,500 instantes temporales de 2.5 μs con un total de 10^6 celdas. Las simulaciones se han efectuado en dos ordenadores, SM32 y SM8. Se ha logrado una aceleración máxima de 6 en SM8 usando los 8 núcleos disponibles y de 16 usando 30 núcleos en SM32. Debido al tamaño del problema, la gestión de la memoria usando *round-robin* ha sido determinante. En la Figura 8.18 se pone de manifiesto la aceleración conseguida al emplear esta técnica.

8.6 Simulación de la cavidad Tierra-ionosfera

El estudio numérico de la cavidad electromagnética Tierra-ionosfera lo hemos efectuado simulando cinco problemas: la cavidad sin pérdidas, con pérdidas, ionosfera deformada por un efecto provocado por seísmo, simulación de tormentas con diferentes extensiones y número de rayos, y por último la cavidad asimétrica con las

zonas día-noche.

El modelo de rayo tiene una transformada de Fourier cuyo módulo es constante en la banda ELF por lo que la respuesta del sistema en frecuencia será equivalente a la respuesta impulso.

8.6.1 Cavidad sin pérdidas

La cavidad consiste en dos esferas concéntricas conductoras perfectas con radios 6,370 y 6,470 km. Se han usado dos tamaños de celda con lados de 5 y 10 km. Para el primero ha sido necesario un total de 4.14 10^8 celdas y 61.5 GBytes de memoria de RAM. La simulación ha requerido 7 días de cálculo. Para la segunda simulación el número de celdas se ha reducido en un factor 8, la memoria RAM utilizada por la simulación ha sido de 9.2 GBytes y el tiempo de cálculo ha sido de 21 horas. En la Tabla 8.3 se muestran las resonancias de Schumann obtenidas con ambas simulaciones y se comparan con las analíticas.

TABLE 8.3: Frecuencias de las SR en Hz para las seis primeras resonancias en la cavidad sin pérdidas.

	1era SR	2da SR	3era SR	4ta SR	5ta SR	6ta SR
10 km	10.24	17.74	24.98	32.35	39.63	46.93
5 km	10.47	17.99	25.48	32.96	39.98	47.47
Analíticas	10.51	18.20	25.75	33.24	40.71	48.17

8.6.2 Cavidad con pérdidas

Con igual configuración que en el caso anterior se ha incluido un perfil de conductividad obtenido de [182]. Ahora las frecuencias de resonancia se hacen menores y se aproximan a las experimentales, según se muestra en la Tabla 8.4.

El efecto de la conductividad en la cavidad también hace que las resonancias no sean tan acusadas y aparece el factor de calidad como otro parámetro a tener en cuenta.

TABLE 8.4: Frecuencias de las SR en Hz para las cuatro primeras resonancias en la cavidad con pérdidas, junto con la desviación estándar de la medida.

	1era SR	2da SR	3era SR	4ta SR
f_c 10 km	8.11	14.57	20.96	24.42
Desv. std. 10 km	0.260	0.384	0.502	0.601
f_c 5 km	8.23	14.76	21.26	27.78
Desv. std 5 km	0.343	0.451	0.538	0.551
Experimentales [12]	7.8	13.9	20.0	26.0

8.6.3 Simulación del terremoto de Chi-Chi

Medidas efectuadas en el observatorio situado en Chofu, Japón, registraron anomalías en las resonancias de Schumann asociadas al terremoto ocurrido el 21 de Septiembre de 1999 en Taiwan, [13, 188-190]. Estas anomalías se han justificado mediante una deformación de la ionosfera provocada, de una forma que no se conoce, por fenómenos previos al terremoto en sí. La deformación de la ionosfera se ha simulado numéricamente mediante un cono truncado con dimensiones variables con conductividad alta. Se han situado varios puntos de observación. El total de simulaciones efectuadas ha requerido 40 horas de cómputo. En la Figura 8.19 se muestran diferentes componentes de los campos en diferentes puntos de observación, y con diferentes perturbaciones de la ionosfera, incluyendo el caso sin perturbar. Se observa cómo efectivamente se detectan anomalías pero están son de una intensidad menor que las detectadas en el observatorio. Además, en la simulación se han detectado anomalías lejos de la deformación, y a modo de ejemplo se muestra la aparición de la segunda resonancia en el Polo Norte, que no debería medirse cuando la tormenta se encuentra en el ecuador.

8.6.4 Modelado de tormentas

Un total de 8 tipos de tormentas se han simulado variando el radio de alcance, la razón de rayos y la intensidad de los mismos. La simulación ha requerido 67 días de cálculo. La señal medida en diferentes puntos de observación tiene ahora una componente estocástica por lo que ha sido necesario usar el método de Bartlett para obtener las resonancias de Schumann. En la Figura 8.20 se muestra el espectro

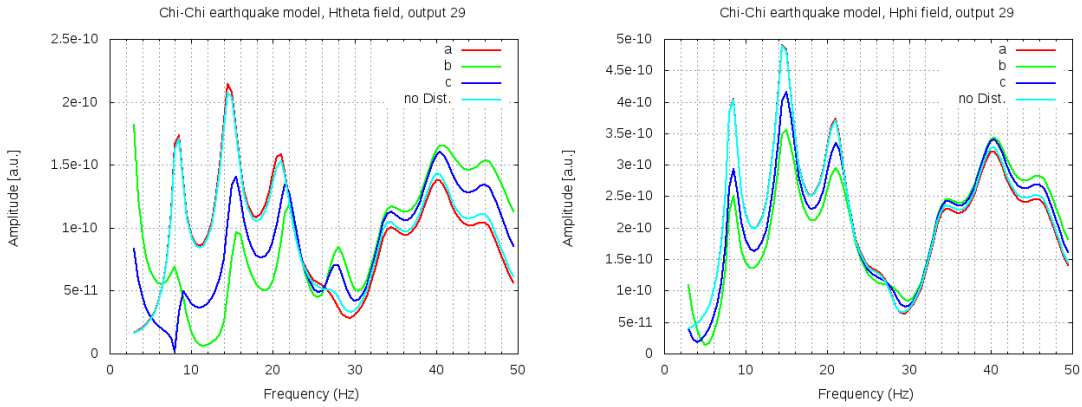

FIGURE 8.19: Componentes (izq.) E_r y (der.) H_ϕ medidas en Japón, para los 4 modelos de deformación.

de diferentes señales y su ajuste mediante Lorentzianas. Sería necesario hacer simulaciones mucho más largas para poder obtener resultados estadísticamente significativos.

8.6.5 Estudio del efecto de la asimetría día-noche

Por último se ha efectuado una simulación más real del estado de la cavidad Tierra-ionosfera, con una zona de día donde la altura efectiva de la ionosfera se reduce, mientras que por la noche se hace mayor. Se han introducido por tanto dos perfiles de conductividad. Las fuentes se han situado en el ecuador, para diferentes horas locales. La simulación ha requerido 21 días de cálculo. En la Tabla 6.5 se muestran las resonancias de Schumann en un punto de observación y se comparan con la cavidad simétrica y el valor experimental.

TABLE 8.5: Frecuencias de las 4 primeras SR, para la cavidad simétrica y la cavidad día-noche, medidas en la coordenada ($\theta = \pi/3$, $\phi = \pi/6$).

	1era SR	2da SR	3era SR	4ta SR
Simétrica	8.00	14.49	21.23	28.48
Día-noche	7.25	13.49	19.98	26.98
Experimental [12]	7.8	13.9	20.0	26.0

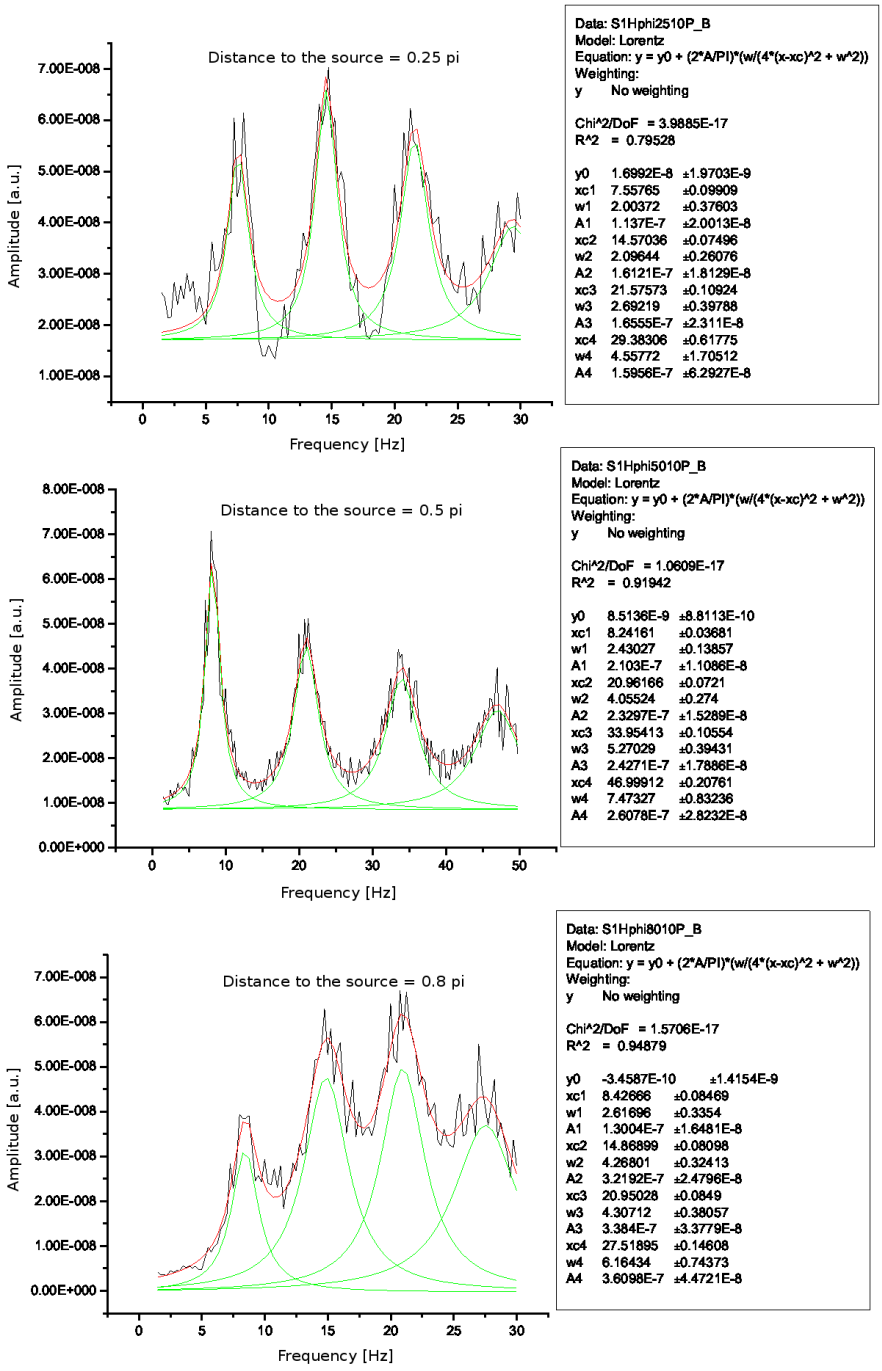

FIGURE 8.20: Espectros resultantes de la tormenta Sr_2 tres puntos de observación.

8.6.6 Conclusiones

Las simulaciones efectuadas confirman que el método numérico y el programa desarrollado pueden simular muchos aspectos y situaciones de la cavidad electromagnética Tierra-ionosfera, generando resultados muy concordantes con las predicciones teóricas y con las medidas experimentales. Sin embargo la información generada por el método es tan amplia y al mismo tiempo las simulaciones son tan costosas computacionalmente que será necesario un gran esfuerzo investigador para sacarle todo el partido a esta herramienta. Queda pues como un objetivo futuro.

8.7 Conclusiones

Esta tesis esta dedicada al estudio del ruido electromagnético natural en la cavidad Tierra-ionosfera. Las contribuciones efectuadas se pueden agrupar en dos clases: análisis de medidas experimentales y estudio numérico con el método TLM.

En el Capítulo 2 se analiza la señal electromagnética medida en la superficie terrestre y se relaciona con los principales resultados analíticos revisados en el Capítulo 1. Variaciones diurnas y estacionales del campo electromagnético natural en la banda ELF son discutidas y relacionadas con la actividad tormentosa global de la Tierra. En el Capítulo 3 se analizan las medidas efectuadas por el satélite DEMETER, con orbita situada a 700 km de altura, del campo eléctrico en la banda VLF y se desarrolla un método de obtención de la altura efectiva de reflexión, se presenta un mapa global de la misma y se hace un estudio de sus variaciones mensuales, estacionales y anuales.

La segunda parte de la tesis estudia la aplicación del método TLM al estudio de la cavidad electromagnética Tierra-ionosfera. En el Capítulo 4 se hace una revisión del método y se justifica su elección. El Capítulo 5 está dedicado a resolver el principal problema que plantea el estudio numérico: la gran necesidad de recursos computacionales debido a las dimensiones tan dispares que presenta la geometría. La paralelización del algoritmo numérico después de una linealización de la geometría es la solución planteada. En el Capítulo 6 el modelo numérico se valida y se aplica a diferentes problemas.

Presentadas por capítulos, las principales conclusiones obtenidas en esta tesis se enumeran a continuación.

En el Capítulo 2 se muestra la presencia de las resonancias de Schumann en las medidas magnetotelúricas. Estas resonancias están presentes de forma clara en las componentes horizontales de los campos eléctrico y magnético. En la componente vertical del campo magnético solo se han evidenciado en un 5% de las medidas. A partir del análisis espectral se han obtenido las siguientes conclusiones:

1. Evidencia de los tres principales centros tormentosos en Asia, África y América, siendo su periodo de mayor actividad pasado el mediodía local. Las amplitudes observadas están de acuerdo con las predicciones analíticas para los modos TM^r. Las campañas de medidas efectuadas en enero y febrero muestran menos amplitud en las resonancias mientras que las efectuadas en verano y otoño (en el hemisferio Norte) son más energéticas. El decaimiento en amplitud con el orden de cada modo se ha observado para el campo magnético, pero no para el eléctrico. Este último también se ha mostrado más sensible a variaciones locales en el punto de medida, llegando a variar hasta un orden de magnitud en su amplitud, mientras que el campo magnético se muestra robusto y con variaciones mínimas en su amplitud. Sin embargo las frecuencias centrales de las amplitudes no muestran variación ni para el campo eléctrico ni para el magnético.

2. Las medidas efectuadas en la Antártida muestran un mínimo de amplitud en el segundo modo de la componente N-S del campo magnético (equivalente a E-O del campo eléctrico) cuando el centro tormentoso se sitúa en África (entorno a las 16 UT) según predice el modelo analítico.

3. La frecuencia central de las tres primeras resonancias de Schumann promediadas en las diferentes campañas de medidas son 7.8, 14 y 20.5 Hz. Las variaciones de estas frecuencias pueden contener información sobre diferentes procesos geofísicos como pueden ser tormentas, viento solar o terremotos. Estas variaciones son mayores en la segunda y tercera resonancia.

4. En todas las series temporales se ha encontrado correlación entre la componente N-S del campo magnético y la E-O del eléctrico y viceversa. Esta correlación aparece tanto en variaciones de la frecuencia central como en las amplitudes.

También en el Capítulo 2 se ha efectuado un análisis de algunas series temporales obtenidas en la Antártida mediante el método *Rescaled Range* (R/S), y se ha demostrado la naturaleza persistente de la señal. Según Nickolaenko et al. [82], este análisis permite hacer una estimación de la razón de rayos promedio en toda la Tierra, encontrándose un valor de 16-32 rayos/s en la señal analizada. También se ha efectuado un estudio numérico que confirma la validez de esta hipótesis.

En el Capítulo 3 se ha elaborado un mapa global de la Tierra (excluyendo zonas aurales) de la altura efectiva de reflexión, con los datos del campo eléctrico medido por el satélite DEMETER. Aunque hay trabajos previos de evaluación de la altura efectiva de la ionosfera a partir de la frecuencia de corte determinada desde dispositivos terrestres, p.e. [133-135], nunca había sido evaluado con medidas efectuadas desde un satélite. Este método presenta la ventaja de muestrear la región D de la Ionosfera de una manera mucho más uniforme. A partir de esta altura efectiva también es posible determinar la densidad de electrones y la conductividad efectiva a esa altura, aunque para ello es necesario disponer de la densidad de neutros (se ha usado el modelo MSIS en esta tesis).

Como resultado principal de este estudio, se ha observado, al menos durante la noche, cierto diagrama estacional que se ha repetido durante los cuatro años de estudio de la altura efectiva de la ionosfera, especialmente sobre los océanos.

A continuación, se introduce el método TLM efectuando una revisión de los aspectos, así como sus ventajas e inconvenientes, más importantes. Esto ha justificado nuestra elección de usar un sistema cartesiano para modelar la corona esférica: evitar los problemas de dispersión e indefinición inherentes al nudo esférico.

En el Capítulo 5 se describe la solución adoptada frente a las necesidades de paralelización que los altos requerimientos computacionales del problema han exigido. El código paralelizado desarrollado para modelar la cavidad electromagnética Tierra-ionosfera ha requerido además una linealización del problema que haga que el esfuerzo de paralelización sea independiente del problema. El programa ha sido chequeado con dos problemas diferentes, presentando un rendimiento computacional similar en diferentes ordenadores. La aceleración necesaria se ha logrado incorporando además una optimización del uso de la memoria compartida por las diferentes CPUs en arquitectura NUMA a través de las directivas *round-robin*. Se han conseguido aceleraciones numéricas de hasta 16 usando 32 núcleos.

Bajo determinados tamaños del problema se han conseguido aceleraciones superlineales gracias al papel de la memoria caché de cada CPU.

Finalmente, en el Capítulo 6 se presentan las simulaciones numéricas de diferentes condiciones de la cavidad Tierra-ionosfera, lo que ha permitido comprobar el funcionamiento del programa y del método numérico en diferentes problemas. Primeramente se ha modelado la cavidad sin pérdidas, lo que ha permitido reproducir las resonancias teóricas. La introducción de un perfil de conductividad en el programa permite obtener las frecuencias de resonancia experimentales. Problemas que requieren un modelo tridimensional también han sido simulados. La transición día-noche con alimentación en el ecuador, perturbaciones de la ionosfera por fenómenos previos a un terremoto, así como su repercusión en las resonancias de Schumann, y la simulación de una zona tormentosa con generación aleatoria de rayos de diferente intensidad han sido problemas resueltos, y la solución obtenida está de acuerdo con las evidencias experimentales, aunque es necesario un proceso mucho más elaborado de toda la información generada con cada simulación numérica, lo que queda como un objetivo futuro de investigación.

List of Figures

List of Tables

Bibliography

[1] S. Toledo-Redondo, A. Salinas, J. Portí, J. A. Morente, J. Fornieles, A. Méndez, J. Galindo-Zaldívar, A. Pedrera, A. Ruiz-Constán, and F. Anahnah. Study of Schumann resonances based on magnetotelluric records from the western Mediterranean and Antarctica. *J. Geophys. Res.*, 115:D22114, 2010.

[2] S. Toledo-Redondo, M. Parrot, and A. Salinas. Variation of the first cut-off frequency of the Earth-ionosphere waveguide observed by DEMETER. *J. Geophys. Res.*, Status:In Press, 2012.

[3] S. Toledo-Redondo, A. Salinas, J. A. Morente-Molinera, A. Méndez, and J. Fornieles. Parallel 3D-TLM algorithm for simulation of the Earth-ionosphere cavity. *J. Comp. Phys.*, Status:Under Review, 2012.

[4] B. P. Besser. Synopsis of the historical development of Schumann resonances. *Radio Sci.*, 42:RS2S02, 2007.

[5] E. R. Williams. The Schumann resonance: A global tropical thermometer. *Science*, 256 no. 5060:1184–1187, May 1992.

[6] M. Hayakawa, S. Pulinets, M. Parrot, and O. A. Molchanov. Recent progress in seismo electromagnetics and related phenomena. *Phys. Chem. Earth*, 31: 129–131, 2006.

[7] I. Main. Is the reliable prediction of individual earthquakes a realistic scientific goal? In *Nature debates, 25 February*, 1999.

[8] T. Bleier and F. Freund. Earthquake, earthquake warning systems. *IEEE Spectrum*, 42:22–27, 2005.

[9] M. Parrot. Special issue of planetary and space science "DEMETER". *Planetary and Space Science*, 54:411–412, 2006.

[10] W. O. Schumann. Über die strahlungslosen eigenschwingungen einer leitenden kugel, die von einer luftschicht und einer ionosphärenhülle umgeben ist. *Zeitschrift fur Naturforschung, Section A-A Journal of Physical Sciences*, 7(2):149–154, 1952.

[11] L. J. Lanzerotti and D. J. Southwood. *Solar system plasma physics III*, chapter Hidromagnetic waves. North-Holland, 1979.

[12] A. P. Nickolaenko and M. Hayakawa. *Resonances in the Earth-ionosphere cavity*. Kluwer Academic Publishers, Dordrecht, The Netherlands, 2002.

[13] M. Balser and C. A. Wagner. Observations of Earth-ionosphere cavity resonances. *Nature*, 168:638–641, 1960.

[14] J. A. Morente, J. A. Portí, B. P. Besser, A. Salinas, H. I. M. Lichtenegger, E. A. Navarro, and G. J. Molina-Cuberos. A numerical study of atmospheric signals in the Earth-ionosphere electromagnetic cavity with the Transmission Line Matrix method. *J. Geophys. Res.*, 111(A1):0305, 2006.

[15] J. R. Wait. *Electromagnetic waves in stratified media*. Pergamon Press, 1962.

[16] J. Galejs. *Terrestrial propagation on long electromagnetic waves*. Pergamon, 1972.

[17] A. I. Sukhorukov, S. Shimakura, and M. Hayakawa. Approximate solution for the VLF eigenvalues near cut-off frequencies in the nocturnal inhomogeneous Earth-ionosphere waveguide. *Planet. Space Sci.*, 40(10):1363–1369, 1992.

[18] S. A. Cummer. Modeling electromagnetic propagation in the Earth-ionosphere waveguide. *IEEE Trans. Ant. Propagation*, 48(9):1420–30, 2000.

[19] Y. N. Taranenko, U. S. Inan, and T. F. Bell. Interaction with the lower ionosphere of electromagnetic pulses from lightning: heating, attachment, and ionization. *Geophys. Res. Lett.*, 20:1539–1542, 1993.

[20] K. G. Budden. *Radio Waves in the Ionosphere*. Cambridge Univ. Press, 1961.

[21] J. K. Hargreaves. *The solar-terrestrial environment*. Cambridge Univ. Press, 1992.

[22] C. Greifinger and P. Greifinger. Approximate method for determining ELF eigenvalues in the Earth-ionosphere waveguide. *Radio Sci.*, 13:831–837, 1978.

[23] C. Greifinger and P. Greifinger. On the ionospheric parameters which govern high-latitude ELF propagation in the Earth-ionosphere waveguide. *Radio Sci.*, 14:889–895, 1979.

[24] J. R. Wait. On ELF transmission in the Earth-ionosphere waveguide. *J. Atm. Terr. Phys.*, 54:109–111, 1992.

[25] H. J. Christian, R. J. Blakeslee, D. J. Boccippio, W. L. Boeck, , D. E. Buechler, K. T. Driscoll, S. J. Goodman, J. M. Hall, W. J. Koshak, D. M. Mach, and M. F. Stewart. Global frequency and distribution of lightning as observed from space by the Optical Transient Detector. *J. Geophys. Res.*, 108(D1):4005, 2003.

[26] V. A. Rakov and M. A. Uman. *Lightning: Physics and effects.* Cambridge Univ. Press, 2003.

[27] F. F. Chen. *Introduction to plasma physics and controlled fusion, plasma physics.* Plenum Press, 1984.

[28] O. A. Molchanov adn M. Hayakawa. Subionospheric VLF signal perturbations, possibly related to earthquakes. *J. Geophys. Res.*, 103:17489–17504, 1998.

[29] P. Varotsos, N. Sarlis, M. Lazaridou, and P. Kapiris. Transmission of stress induced electric signals in dielectric media. *J. App. phys.*, 83:60–70, 1998.

[30] A. C. Fraser-Smith, A. Bernardi, P. R. McGuill, M. E. Ladd, R. A. Helliwel, and O. G. Vollard Jr. Low frequency magnetic field measurements near the epicenter of the Ms7.1 Loma Prieta earthquake. *Geophys. Res. Lett.*, 17: 1465–1468, 1990.

[31] M. Hayakawa, R. Kawate, O. A. Molchanov, and K. Yumoto. Results of ultra-low-frequency magnetic field measurements during the Guan earthquake of 8 August 1993. *Geophys. Res. Lett.*, 23:241–244, 1996.

[32] M. Parrot, J. J. Berthelier, J. P. Lebreton, J. A. Sauvaud, Ol Santolik, and J. Blecki. Examples of unusual ionospheric observations made by the DEMETER satellite over seismic regions. *Phys. Chem. Earth*, 31(4-9):486–495, 2006.

[33] O. A. Molchanov, M. Hayakawa, and V. A. Rafalsky. Penetration characteristics of electromagnetic emissions from an underground seismic source into the atmosphere, ionosphere, and magnetosphere. *J. Geophys. Res.*, 100: 1691–1712, 1995.

[34] N. A. Smirnova and M. Hayakawa. Fractal characteristics of the ground-observed ULF emissions in relation to geomagnetic and seismic activities. *J. Atm. Solar-Terr. Phys.*, 69:1833–1841, 2007.

[35] M. Seto, K. Murayama, Y. Kitamura, and T. Watanabe. *Lithosphere-atmosphere-ionosphere coupling*, chapter Observation of seismo-genic ELF magnetic field variations and seismo-electric currents in a power transmission system, pages 69–75. Terrapub, Tokio, 2002.

[36] H. C. Koons and J. L. Roeder. *Atmospheric and ionospheric electromagnetic phenomena associated with earthquakes*, chapter A comparison of ULF/ELF measurements associated with earthquakes. Terrapub, Tokio, 1999.

[37] V. A. Tsarev and H. Sasaki. *Atmospheric and Ionospheric electromagnetic phenomena associated with earthquakes.*, chapter Low frequency seismogenic electromagnetic radiation: How does it propagate in the Earth's crust and where can it be detected? Terrapub, Tokio, 1999.

[38] E. A. Rauscher and W. L. V. Bise. *Atmospheric and ionospheric electromagnetic phenomena associated with earthquakes*, chapter The relationship of extremely low frequency electromagnetic and magnetic fields associated with seismic and volcanic natural activity and artificial ionosphere disturbances, pages 459–487. Terrapub, Tokio, 1999.

[39] M. Hayakawa, K. Ohta, and N. Watanabe. *Electromagnetic phenomenon related to earthquakes and volcanoes*, chapter Anomalous Schumann resonance phenomena observed in Japan, in possible association with earthquakes in Taiwan. Narosa Publishing House, New Delhi, 2008.

[40] M. Hayakawa, K. Ohta, V. M. Sorokin, A. K. Yaschenko, J. Izutsu, Y. Hobara, and A. P. Nickolaenko. Interpretation in terms of gyrotropic waves of Schumann-resonance-like line emissions observed at Nakatsugawa in possible association with nearby Japanese earthquakes. *J. Atm. Sol.-Terr. Phys.*, 72: 1292–1298, 2010.

[41] M. Hayakawa, V. V. Surkov, Y. Fukumoto, and N. Yonaiguchi. Characteristics of VHF over-horizon signals possibly related to impending earthquakes and a mechanism of seismo-atmospheric perturbations. *J. Atm. Sol.-Terr. Phys.*, 69:1057–1062, 2007.

[42] J. A. Stratton. *Electromagnetic theory.* John Wiley & sons, 1941.

[43] P. V. Bliokh, A. P. Nickolaenko, and I. F. Filipov. *Schumann resonances in the Earth-ionosphere cavity.* Peter Peregrinus, 1980.

[44] M. Hayakawa, K. Ohta, and K. Baba. Wave characteristics of tweek atmospherics deduced from the direction-finding measurement and theoretical interpretation. *J. Geophys. Res.*, 99(D5):10733–43, 1994.

[45] C. A. Balanis. *Advanced engineering electromagnetics.* John Wiley & sons, 1989.

[46] S. A. Schelkunoff. *Electromagnetic waves.* D. Van Nostran Company, 1943.

[47] G. B. Arfken. *Mathematical methods for physicists*, page 668. Academic Press, 1970.

[48] J. R. Reitz, F. J. Milford, and R. W. Christy. *Foundations of electromagnetic theory.* Addison-Wesley, 2008 (4th edition).

[49] R. Feynman, R. Leighton, and M. Sands. *Vol II: Electromagnetismo y materia.* Fondo educativo Iberoamericano, 1972.

[50] World Meteorological Organization (WMO). *World distribution of thunderstorm days.* Publ. 21, TP 6 and Suppl. (1956), 1953.

[51] K. L. Cummins, E. P. Krider, and M. D. Mallone. The US national lightning detection network and applications of cloud-to-ground lightning data by electric power utilities. *IEEE Trans. Electromagn. Compatibility*, 40:465–480, 1998.

[52] V. Idone, D. Davis, P. Moore, Y. Wang, R. Henderson, M. Ries, and P. Jamason. Performance evaluation of the US national lightning detection network in Eastern New York. *J. Geophys. Res.*, 103:9045–9069, 1998.

[53] Z.-I. Kawasaki, K. Yamamoto, K. Matsura, P. Richard, T. Matsui, Y. Sonoi, and N. Shimakura. SAFIR operation and evaluation of its performance. *J. Geophys. Res.*, 21:1133–1136, 1994.

[54] M. Füllekrug, S. Constable, G. Heinson, M. Sato, Y. Takahashi, C. Price, and E. Williams. Global lightning acquisition system installed. *EOS Transactions*, 81(30):333, 2000.

[55] J. A. Morente, G. J. Molina-Cuberos, J. A. Portí, K. Schwingenschuh, and B. P. Besser. A study of the propagation of electromagnetic waves in Titan's atmosphere with the TLM numerical method. *Icarus*, 162:374–384, 2003.

[56] V. P. Pasko. Introduction to special section: Recent advances in studies of Schumann resonances on Earth and other planets of the solar system. *Radio Sci.*, 41:RS2S01, 2006.

[57] G. J. Molina-Cuberos, J. A. Morente, B. P. Besser, J. Portí, H. Lichtenegger, K. Schwingenschuch, A. Salinas, and J. Margineda. Schumann resonances as a tool to study the lower ionospheric structure of Mars. *Radio Sci.*, 41: RS1003, 2006.

[58] J. A. Morente, G. J. Molina-Cuberos, J. A. Portí, B. P. Besser, A. Salinas, K. Schwingenschuh, and H. Lichtenegger. A numerical simulation of Earth's electromagnetic cavity with the Transmission Line Matrix method: Schumann resonances. *J. Geophys. Res.*, 108(A5):1195, 2003.

[59] J. A. Morente, J. A. Portí, A. Salinas, G. J. Molina-Cuberos, H. Lichtenegger, B. P. Besser, and K. Schwingenschuh. Do Schumann resonance frequencies depend on altitude? *J. Geophys. Res.*, 109:A05306, 2004.

[60] J. A. Morente, J. A. Portí, C. Blanchard, B. P. Besser, H. I. M. Lichtenegger, A. Salinas, E. A. Navarro, and G. J. Molina-Cuberos. Transmission line meshes for computational simulation of electromagnetic modes in the Earth's atmosphere. *COMPEL*, 26:650–660, 2007.

[61] J. A. Morente, J. A. Portí, A. Salinas, and E. A. Navarro. Evidence of electrical activity on Titan drawn from the Schumann resonances sent by Huygens probe. *Icarus*, 195:802–811, 2008.

[62] J. A. Morente, J. A. Portí, C. Blanchard, E. A. Navarro, and A. Salinas. An analysis of VLF electric field spectra measured in Titan's atmosphere by the Huygens probe. *J. Geophys. Res.*, 114:E06002, 2009.

[63] H. E. Hurst, R. P. Black, and Y. M. Simaika. *Long-Term storage: an experimental study.* Constable, 1965.

[64] J. B. Fourier. *Théorie Analytique de la Chaleur*. Libraires pour les mathématiques, l´architecture Hydraulique et la marine, 1822.

[65] Peter Bloomfield. *Fourier analysis of time series, an introduction*. Wiley series in probability and statistics, 2000.

[66] M. S. Bartlett. Smoothing periodograms from time series with continuous spectra. *Nature*, 161:686–7, 1948.

[67] M. S. Bartlett and J. Medhi. On the efficiency procedures for smoothing periodograms from Time Series with continuous spectra. *Biometrika*, 42(1/2): 143–150, 1955.

[68] D. Sentman. Magnetic elliptical polarization of Schumann resonances. *Radio Sci.*, 22(4):595–606, 1987.

[69] L. Cagniard. Basic theory of the magnetotelluric method of geophysical prospecting. *Geophysics*, 18(3):605–635, 1953.

[70] K. Vozoff. The magnetotelluric method in the exploration of sedimentary basins. *Geophysics*, 37(1):98–141, 1972.

[71] V. Pronenko and V. Korepanov. Induction coil magnetometers - a review. In *EGU General Assembly 2009, held 19-24 April, 2009 in Vienna, Austria*, 2009.

[72] A. Pedrera, J. Galindo-Zaldívar, A. Ruiz-Constán, C. Duque, C. Marín-Lechado, and I. Serrano. Recent large fold nucleation in the upper crust: Insight from gravity, magnetic, magnetotelluric and seismicity data (Sierra de los Filabres - Sierra de las Estancias, internal zones, Betic cordillera). *Tectonophysics*, 463:145–160, 2009.

[73] A. Ruiz-Constán, J. Galindo-Zaldívar, A. Pedrera, J. A. Arzate, J. Pous, F. Anahnah, W. Heise, F. Monteiro Santos, and C. Marín-Lechado. Deep deformation pattern from electrical anisotropy in an arched orogen (Betic cordillera, Western Mediterranean). *Geology*, 38(8):731–734, 2010.

[74] A. Ondrášková, P. Kostecký, S. Ševčík, and L. Rosenberg. Long-term observation of Schumann resonances at Modra observatory. *Radio Sci.*, 42: RS2S09, 2007.

[75] C. Price and A. Melkinov. Diurnal, seasonal and interannual variations in the Schumann resonance parameters. *J. Atmos. Sol. Terr. Phys.*, 66(13-14): 1179–85, 2004.

[76] V. C. Roldugin, A. N. Vasiljev, and A. A. Ostapenko. Comparison of the Schumann resonance parameters in horizontal magnetic and electric fields according to observations on the Kola peninsula. *Radio Sci.*, 41:RS2S07, 2006.

[77] G. Sátori and B. Zieger. Spectral characteristics of Schumann resonances observed in central Europe. *J. Geophys. Res.*, 101(D23):29663–9, 1996.

[78] A. P. Nickolaenko, M. Hayakawa, and Y. Hobara. Long-term periodical variations in global lightning activity deduced from the Schumann resonance monitoring. *J. Geophys. Res.*, 104(D22):27585–91, 1999.

[79] J. Feder. *Fractals.* Plenum Press, 1988.

[80] D. L. Turcotte. *Fractals and Chaos in Geology and Geophysics.* Cambridge Univ. Press, 1997.

[81] A. P. Nickolaenko, C. Price, and D. D. Iudin. Hurst exponent derived for natural terrestrial radio noise in Schumann resonance band. *J. Geophys. Res. Lett.*, 27(19):3185–8, 2000.

[82] B. B. Mandelbrot and J. R. Wallis. Robustness of the rescaled range R/S in the measurement of noncyclic long run statistical dependence. *Water Resour. Res.*, 5:967–968, 1969.

[83] J. D. Jackson. *Classical Electrodynamics.* John Wiley, 1998.

[84] T. Cussac, M.-A. Clair, P. Ultré-Guerard, F. Buisson, G. Lassalle-Balier, M. Ledu, C. Elisabelar, X. Passot, and N. Rey. The DEMETER microsatellite and ground segment. *Planetary and Space Science*, 54(5):413 – 427, 2006. ISSN 0032-0633. doi: 10.1016/j.pss.2005.10.013.

[85] X. Zhang, X. Shen, M. Parrot, Z. Zeren, X. Ouyang, J. Liu, J. Qian, S. Zhao, and Y. Miao. Phenomena of electrostatic perturbations before strong earthquakes (2005-2010) observed on DEMETER. *Natural Hazards and Earth System Sci.*, 12(1):75–83, 2012.

[86] D. Pisa, M. Parrot, and O. Santolik. Ionospheric density variations recorded before de 2010 M(w) 8.8 earthquake in Chile. *J. Geophys. Res.*, 116:A08309, 2011.

[87] J. Zlotnicki, F. Li, and M. Parrot. Signals recorded by DEMETER satellite over active volcanoes during the period 2004 August - 2007 December. *Geophysical Journal International*, 183(3):1332–1347, 2010.

[88] M. Parrot, D. Benoist, J. J. Berthelier, J. Błęcki, Y. Chapuis, F. Colin, F. Elie, P. Fergeau, D. Lagoutte, F. Lefeuvre, , C. Legendre, M. Lévêque, , J. L. Pinçon, B. Poirier, H.-C. Seran, and P. Zamora. The magnetic field experiment IMSC and its data processing onboard DEMETER: Scientific objectives, description and first results. *Planetary and Space Science*, 54: 441–455, 2006.

[89] J.-P. Lebreton, S. Stverak, P. Travnicek, M. Maksimovic, D. Klinge, S. Merikallio, D. Lagoutte, B. Poirier, P.-L. Blelly, Z. Kozaceck, and M. Salaquarda. The ISL Langmuir probe experimient processing onboard DEMETER: Scientific objectives, description and first results. *Planetary and Space Science*, 54:472–486, 2006.

[90] L. H. Brace. *Measurement techniques in space plasmas*, chapter Langmuir probe masurements in the ionosphere. American Geophysical Union, 1996.

[91] J. J. Berthelier, M. Godefroy, F. Leblanc, E. Seran, D. Peschard, P. Gilbert, and J. Artru. IAP, the thermal plasma analyzer on DEMETER. *Planetary and Space Science*, 54:487–501, 2006.

[92] J. A. Sauvaud, T. Moreau, R. Maggiolo, J.-P. Treilhou, C. Jacquey, A. Cros, J. Coutelier, J. Rouzaud, E. Penou, and M. Gangloff. High-energy electron detection on board DEMETER: The IDP spectrometer, description and first results on the inner belt. *Planetary and Space Science*, 54:502–511, 2006.

[93] D. Lagoutte, J.Y. Brochot, D. de Carvalho, F. Elie, F. Harivelo, Y. Hobara, L. Madrias, M. Parrot, J.L. Pinçon, J.J. Berthelier, D. Peschard, E. Seran, M. Gangloff, J.A. Sauvaud, J.P. Lebreton, S. Stverak, P. Travnicek, J. Grygorczuk, J. Slominski, R. Wronowski, S. Barbier, P. Bernard, A. Gaboriaud, and J.M. Wallut. The DEMETER science mission centre. *Planetary and Space Science*, 54(5):428 – 440, 2006. ISSN 0032-0633. doi: 10.1016/j.pss.2005.10.014.

[94] O. A. Molchanov and M. Hayakawa. On the generation mechanism of ULF seismogenic electromagnetic emissions. *Phys. Earth. Planet. Int.*, 105:201–220, 1998.

[95] O. A. Molchanov and M. Hayakawa. Subionospheric VLF signal perturbations possibly related to earthquakes. *J. Geophys. Res.*, 103:489–504, 1998.

[96] J.J. Berthelier, M. Godefroy, F. Leblanc, M. Malingre, M. Menvielle, D. Lagoutte, J.Y. Brochot, F. Colin, F. Elie, C. Legendre, P. Zamora, D. Benoist, Y. Chapuis, J. Artru, and R. Pfaff. ICE, the electric field experiment on DEMETER. *Planetary and Space Science*, 54(5):456 – 471, 2006. ISSN 0032-0633. doi: 10.1016/j.pss.2005.10.016.

[97] R. Barr, D. LL. Jones, and C. J. Rodger. ELF and VLF radio waves. *J. Atm. Sol. Terr. Phys.*, 62:1689–1718, 2000.

[98] S. Ramo, J. R. Whinnery, and T. V. Duzer. *Fields and waves in communication electronics, 3rd edition.* John Wiley and Sons, 1994.

[99] A. Taflove and S. C. Hagness. *Computational electrodynamics, the Finite-Difference Time Domain method, 3rd edition.* Artech House, 2005.

[100] T. Onishi and J. J. Berthelier. Synthetic characterization of VLF electric field spectra from the ICE experiment on DEMETER. automatic recognition and characterization of natural and man made emissions. Technical report, Institut Pierre Simon Laplace, 2010.

[101] K. Labitzke, J. J. Barnett, and B. Edwards. *Handbook MAP 16.* SCOSTEP, 1985.

[102] A. E. Hedin. Extension of the MSIS thermospheric model into the middle and lower atmosphere. *J. Geophys. Res.*, 96:1159–11991, 1991.

[103] J. A. Ratcliffe. *The magneto-ionic theory and its applications to the ionosphere.* Cambridge University Press, 1959.

[104] V. P. Pasko, U. S. Inan, T. F. Bell, and Y. N. Taranenko. Sprites produced by quasi-electrostatic heating and ionization in the lower ionosphere. *J. Geophys. Res.*, 102(A3):4529–4561, 1997.

[105] H. Kil and R. A. Heelis. Global distribution of density irregularities in the equatorial ionosphere. *J. Geophys. Res.*, 103(A1):407–417, 1998.

[106] S. Y. Su, C. H. Liu, H. H. Ho, and C. K. Chao. Distribution characteristics of topside ionospheric density irregularities: Equatorial versus midlatitude regions. *J. Geophys. Res.*, 111:A06305, 2006.

[107] M. J. Rycroft, S. Israelson, and C. Price. The global atmospheric electric circuit, solar activity and climate change. *J. Atmos. Sol. Terr. Phys.*, 62: 1563–1576, 2000.

[108] E. R. Williams. The global electrical circuit: a review. *Atmospheric Research*, 91:140–152, 2009.

[109] R. G. Harrison. The global atmospheric electrical circuit and climate. *Surv. Geophys.*, 25:441–484, 2004.

[110] H. Israel. *Atmospheric Electricity, vol. I, Fundamentals, conductivity, ions.* Published for the National Science Foundation by the Israel program for scientific translations, 1973.

[111] H. Israel. *Atmospheric Electricity, vol. II, fields, charges and currents.* Published for the National Science Foundation by the Israel program for scientific translations, 1973.

[112] S. K. Satheesh and K. K. Moorthy. Radiative effects of natural aerosols: A review. *Atmospheric Environment*, 39(11):2089–2110, 2005.

[113] R. B. Husar, J. D. Husar, and L. Martin. Distribution of continental surface aerosol extinction based on visual range data. *Atmospheric Environment*, 34:5067–78, 2000.

[114] V. P. Pasko, U. S. Inan, and T. F. Bell. Ionospheric effects due to electrostatic thundercloud fields. *J. Atmos. Sol. Terr. Phys.*, 60:863–870, 1998.

[115] M. Füllekrug. The contribution of intense lightning discharges to the global atmospheric electric circuit during April 1998. *J. Atmos. Sol.-Terr. Phys.*, 66:1115–19, 2004.

[116] U. S. Inan, S. A. Cummer, and R. A. Marshall. A survey of ELF and VLF research on lightning-ionosphere interactions and causative discharges. *J. Geophys. Res.*, 115:A00E36, 2010.

[117] M. J. Rycroft, A. Odzimek, N. F. Arnold, M. Füllekrug, A. Kulak, and T. Neubert. New model simulations of the global atmospheric electric circuit

driven by thunderstorms and electrified shower clouds. *J. Atmos. Sol. Terr. Phys.*, 69:2485–2509, 2007.

[118] C. J. Rodger, M. Cho, M. A. Clilverd, and M. J. Rycroft. Lower ionospheric modification by lightning EMP: simulation of the night ionosphere over the United States. *Geophys. Res. Lett.*, 28(2):199–202, 2001.

[119] S. B. Mende, H. U. Frey, R. R. Hsu, H. T. Su, A. B. Chen, L. C. Lee, D. D. Sentman, Y. Takahashi, and H. Fukunishi. D region ionization by lightning-induced electromagnetic pulses. *J. Geophys. Res.*, 110:A11312, 2005.

[120] A. B. Chen, C.-L. Kuo, Y.-J. Lee, H.-T. Su, R.-R. Hsu, J.-L. Chem, H. U. Frey, S. B. Mende, Y. Takahashi, H. Fukunishi, Y.-S. Chang, T.-Y. Liu, and L.-C. Lee. Global distributions and occurrence rates of transient luminous events. *J. Geophys. Res.*, 113:A08306, 2008.

[121] E. S. Gemelos, U. S. Inan, M. Walt, M. Parrot, , and J. A. Sauvaud. Seasonal dependence of energetic electron precipitation: Evidence for a global role of lightning. *Geophys. Res. Lett.*, 36:L21107, 2009. doi: 10.1029/2009GL040396.

[122] B. S. Ryabov. Tweek propagation peculiarities in the Earth-ionosphere waveguide and low ionosphere parameters. *Adv. Space Res.*, 12(6):255–258, 1992.

[123] S. A. Cummer, U. S. Inan, and T. F. Bell. Ionospheric D region remote sensing using VLF radio atmopherics. *Radio Science*, 33(6):1781–92, 1998.

[124] A. V. Shvets and M. Hayakawa. Polarisation effects for tweek propagation. *J. Atmos. Sol. Terr. Phys.*, 60(44):461–469, 1997.

[125] H. Ohya, M. Nishino, Y. Murayama, and K. Igarashi. Equivalent electron densities at reflection heights of tweek atmospherics in the low-middle latitude D-region ionosphere. *Earth Planets and Space*, 55(10):627–635, 2003. ISSN 1343-8832.

[126] S. C. Solomon, L. Qian, L. V. Didkovsky, R. A. Viereck, and T. N. Woods. Causes of low thermospheric density during the 2007-2009 solar minimum. *J. Geophys. Res.-Space Phys.*, 116(A00H07):A00H07, Jul 11 2011. doi: 10.1029/2011JA016508.

[127] M. Waldmeier. *The sunspot activity in the years 1610 - 1960.* Zurich Schulthess and Company, 1961.

[128] D. Bilitza and B. W. Reinisch. International Reference Ionosphere 2007: Improvements and new parameters. *Advances in Space Research*, 42:599–609, 2007.

[129] D. Bilitza. International Reference Ionosphere 2000. *Radio Sci.*, 36(2):261–275, 2001.

[130] K. Rawer, D. Bilitza, and S. Ramakrishnan. Goals and status of the International Reference Ionosphere. *Rev. Geophys.*, 16:177–81, 1978.

[131] R. W. Schunk, L. Scherliess, J. J. Sojka, D. C. Thompson, D. N. Anderson, M. Codrescu, C. Minter, T. J. Fuller-Rowell, R. A. Heelis, M. Hairston, and B. M. Howe. Global assimilation of ionospheric measurements. *Radio Science*, 39(1):RS1S02, 2004.

[132] W. E. Gordon. Incoherent scattering of radio waves by free electrons with applications to space exploration by radar. *Proceedings of the IRE*, 46(11): 1824–1829, 1958.

[133] D. Bilitza and R. Williamson. Towards a better representation of the IRI topside based on ISIS and Alouette data. *Lower ionosphere: measurements and models, Advances in Space Research*, 25(1):149–152, 1999.

[134] S. Batten, T. J. Fuller-Rowell, and D. Rees. A numerical data base for VAX and personal computers for storage, reconstruction, and display of global thermospheric and ionospheric models. *Planet. Space Sci.*, 35:1167, 1987.

[135] H. Ohya, M. Nishino, Y. Murayama, K. Igarashi, and A. Saito. Using tweek atmospherics to measure the response of the low-middle latitude D-region ionosphere to a magnetic storm. *J. Atm. Sol. Terr. Phys.*, 68:697–709, 2006.

[136] S. Kumar, A. Deo, and V. Ramachandran. Nighttime D-region equivalent electron density determined from tweeks sferics observed in the south pacific region. *Earth Planets and Space*, 61:905–911, 2009.

[137] A. A. Ostapenko, E. E. Titova, A. P. Nickolaenko, J. Manninen T. Turunen and, and T. Raita. Characteristics of VLF atmospherics near the resonance frequency of the Earth-ionosphere waveguide 1.6-2.3 kHz by observations in the auroral region. *Annales Geophysicae*, 28:193–202, 2010.

[138] G. Kron. Equivalent circuit of the field equations of Maxwell-Part I. *Proc. IRE*, 32:289–299, 1944.

[139] J. R. Whinnery, C. Concordia, W. Ridgway, and G. Kron. Network analyzer studies of electromagnetic cavity resonators. *Proc. IRE*, 32:360–367, 1944.

[140] P. B. Johns and R. L. Beurle. Numerical solution of 2-dimensional scattering problems using a transmission-line matrix. *Proc. Inst. Elec. Eng.*, 118(9): 1203–1208, 1971.

[141] C. Christopoulos. *The transmission-line modeling method: TLM.* The Institute of Electrical and Electronic Engineers, 1995.

[142] D. de Cogan. *Transmission Line Matrix TLM techniques for diffusion applications.* Gordon and Breach, 1998.

[143] J. A. Portí and J. A. Morente. A three-dimensional symmetrical condensed TLM node for acoustics. *Journal of Sound and Vibration*, 241(2):207–222, 2001.

[144] P. B. Johns. Application of the transmission-line matrix method to homogeneous waveguides of arbitrary cross-section. *Proc. Inst. Elec.*, 119(8): 1086–1091, 1972.

[145] P. B. Johns. The solution of inhomogeneous waveguide problems using a transmission-line matrix. *IEEE Trans. Microwave Theory Tech.*, MTT-22: 209–215, 1974.

[146] S. Akhtarzad and P. B. Johns. Solutions of 6-component electromagnetic fields in three space dimensions and time by the TLM method. *Electron. Letters*, 10(25):535–537, 1974.

[147] S. Akhtarzad and P. B. Johns. Three-dimensional transmission-line matrix computer analysis of microstrip resonators. *Electron. Letters*, MTT-23:990–997, 1975.

[148] S. Akhtarzad and P. B. Johns. Solution of Maxwell's equations in three space dimensions and time by the TLM method of analysis. *Proc. Inst. Elec. Eng.*, 122(12):1344–1348, 1975.

[149] K. Yee. Numerical solution of initial boundary value problems involving Maxwell's equations in isotropic media. *IEEE Trans. on Antennas and Propagation*, 14(3):302–307, 1966.

[150] N. Yoshida, I. Fukai, and J. Fukuoka. Transient analysis of two-dimensional Maxwell's equations by Bergeron's method. *Trans. IECE Japan*, J62B:511–518, 1979.

[151] N. Yoshida, I. Fukai, and J. Fukuoka. Transient analysis of three-dimensional electromagnetic fields by nodal equations. *Trans. IECE Japan*, J63B:876–883, 1979.

[152] N. Yoshida, I. Fukai, and J. Fukuoka. Application of Bergeron's method to anisotropic media. *Trans. IECE Japan*, J64B:1242–1249, 1981.

[153] N. Yoshida and I. Fukai. Transient analysis of a stripline having a corner in three-dimensional space. *IEEE Trans. Microwave Theory Tech.*, MTT-32: 491–498, 1984.

[154] P. B. Johns. New symmetrical condensed node for three-dimensional solution of electromagnetic wave problems by TLM. *Electron. Lett.*, 22(3):162–164, 1986.

[155] P. B. Johns. Use of condensed and symmetrical TLM nodes in computer-aided electromagnetic design. *Proc. Inst. Elec. Eng.*, 133(H5):368–374, 1986.

[156] J. A. Portí, J. A. Morente, and M. C. Carrión. Simple derivation of scattering matrix for TLM nodes. *Electron. Letters*, 34(18):1763–1764, 1998.

[157] J. A. Morente, J. Portí, and M. Khalladi. Absorbing boundary conditions for the TLM method. *IEEE Trans. Microwave Theory Tech.*, MTT-40:2095–2099, 1984.

[158] J. P. Berenger. A perfectly matched layer for the absorption of electromagnetic waves. *J. Comput. Physics*, 114:185–200, 1994.

[159] N. Pena. Absorbing-boundary conditions using perfectly matched-layer (PML) technique for three-dimensional TLM simulations. *IEEE Trans. Microw. Theory Tech.*, 45(10):1749–1755, 1997.

[160] J. A. Morente, G. Giménez, J. Portí, and M. Khalladi. Group and phase velocities in the TLM-symmetrical-condensed node mesh. *IEEE Trans. Microw. Theory Tech.*, 42(3):514–517, 1994.

[161] J. A. Morente, G. Giménez, J. A. Portí, and M. Khalladi. Dispersion analysis for a TLM mesh of symmetrical condensed nodes with stubs. *IEEE Trans. Microwave and techniques*, 43:453–456, 1995.

[162] Cédric Blanchard. *Simulation of Electromagnetic waves propagating in complex media with the TLM method.* PhD thesis, University of Granada, 2009.

[163] P. Naylor, C. Christopoulos, and P. B. Johns. Coupling between electromagnetic fields and wires using transmission-line modeling. *Proc. Inst. Elec. Eng.*, 134(A8):679–686, 1987.

[164] J. A. Portí, J. A. Morente, M. Khalladi, and A. Gallego. Comparison of thin-wire models for TLM method. *Electron. Lett.*, 28(20):1910–1911, 1992.

[165] J. A. Morente, J. A. Portí, G. Giménez, and A. Gallego. Loaded-wire node for TLM method. *Electron. Lett.*, 29(2):182–184, 1993.

[166] Jorge Portí. *Contribución al estudio del nudo simétrico condensado en el método numérico TLM.* PhD thesis, Universidad de Granada, 1993.

[167] C. Blanchard, J. A. Portí, B. I. Wu, J. A. Morente, A. Salinas, and J. A. Kong. Time domain simulation of electromagnetic cloaking structures with TLM method. *Optics Express*, 16(9):6461–6470, 2008.

[168] L. J. Flynn. *Intel halts development of 2 new microprocessors.* The New York times, May 8 2004.

[169] B. Huang, J. Mielikainen, H. Oh, and H. L. A. Huang. Development of a GPU-based high-performance radiative transfer model for the Infrared Atmospheric Sounding Interferometer (IASI). *J. Comp. Physics*, 230(6): 2207–2221, 2011.

[170] D. Komatitsch, G. Elrlebacher, D. Goddeke, and D. Michea. High-order finite-element seismic wave propagation modeling with MPI on a large GPU cluster. *J. Comp. Physics*, 229(20):7692–7714, 2010.

[171] W. Yu, X. Yang, Y. Liu, L.-C. Ma, T. Su, N.-T. Huang, R. Mittra, R. Maaskant, Y. Lu, Q. Che, R. Lu, and Z. Su. A new direction in computational electromagnetics: solving large problems using the parallel FDTD on the BlueGene/L supercomputer providing teraflop performance. *IEEE antennas and Propag. Mag.*, 50(2):26–44, 2008.

[172] P. P. M. So, C. Eswarappa, and W. J. R. Hoefer. Parallel and distributed TLM compuation with signal processing for electromagnetic field modelling. *Int. J. Modelling: Electronic Networks, devices and fields*, 8:169–185, 1995.

[173] J. Tian, Z. Q. Lv, X. W. Shi, L. Xu, and F. Wei. An efficient approach for multifrontal algorithm to solve non-positive-definite finite element equations in electromagnetic problems. *Prog. Electromagn. Res.*, 95:121–133, 2009.

[174] A. Taflove. *Computational Electrodynamics: The Finite-Difference Time-Domain Method*. Artech House, 1995.

[175] K. Chatterjee and J. Poggie. A parallelized 3D floating random-walk algorithm for the solution of the nonlinear Poisson-Boltzmann equation. *Prog. Electromagn. Res.*, 57:237–252, 2006.

[176] L. C. G. G. Persoon, M. Podesta, W. J. C. van Elmpt, S. M. J. J. G. Nijsten, and F. Verhaegen. A fast three-dimensional gamma evaluation using a GPU utilizing texture memory for on-the-fly interpolations. *Medical Physics*, 38(7):4032–4035, 2011.

[177] A. Soriano, E. A. Navarro, D. L. Paul, J. A. Portí, J. A. Morente, and I. J. Craddock. Finite difference time domain simulation of the Earth-ionosphere resonant cavity: Schumann resonances. *IEEE Trans. Antennas Propag.*, 53(4):1535–1541, 2005.

[178] J. J. Simpson and A. Taflove. Three-dimensional FDTD modeling of impulsive ELF propagation about the Earth-sphere. *IEEE Trans. Antennas Propag.*, 52(2):443–451, 2004.

[179] H. Yang and V. Pasko. Three-dimensional finite difference time domain modeling of the Earth-ionosphere cavity resonances. *Geophys. Res. Lett.*, 32:L03114, 2005.

[180] D. D. Sentman. *Schumann resonances, in Handbook of Atmospheric Electrodynamics*. CRC Press, 1995.

[181] D. D. Sentman. Schumann resonance spectra in a two-scale-height Earth-ionosphere cavity. *J. Geophys. Res.*, 101(D5):9479–9487, 1996.

[182] O. Pechony and C. Price. Schumann resonance parameters calculated with a partially uniform model on Earth, Venus, Mars, and Titan. *Radio Sci.*, 39:RS5007, 2004.

[183] J. A. Morente, J. A. Portí, O. Torres, and A. Carvajal. Un nudo TLM tridimensional y no ortogonal para el eje z de coordenadas cilíndricas. In *XVI Symposium Nacional de la Unión Científica Internacional de Radio (URSI). Actas del congreso, pp. 215-216, Villaviciosa de Ocón (Madrid), 19-21 Septiembre*, 2001.

[184] M. J. Quinn. *Parallel programming in C with MPI and openMP.* Mc Graw Hill, 2004.

[185] P. T. Lin and J. N. Shadid. Towards large-scale multi-socket, multicore parallel simulations: Performance of an MPI-only semiconductor device simulator. *J. Comput. Phys. Chem. Earth*, 229:6804–6818, 2010.

[186] T. Ciamulski and M. Sypniewski. Linear and superlinear speedup in parallel FDTD processing. *IEEE Antennas and propagation society international symposium*, 1(12):4448–4451, 2007.

[187] P. J. Parsons, S. R. Jaques, S. H. Pulko, and F. A. Rabhi. TLM modelling using distributed computing. *Microwave and guided wave letters*, 6(3):141–142, 1996.

[188] F. Rossi and P. So. Parallelized computational electromagnetics TLM algorithms on NVIDIA graphics processing units. *IEEE Pacific rim conference on communications*, 1(2):814–819, 2009.

[189] M. J. Rycroft, R. G. Harrison, K. A. Nicoll, and E. A. Mareev. An overview of Earth's global electric circuit and atmospheric conductivity. *Space Sci. Rev.*, 137:83–105, 2008.

[190] Y. Baba and V. A. Rakov. *Present understanding of the lightning return stroke, in Lightning: Principles, instruments and applications.* Springer, 2009.

[191] David K. Cheng. *Field and wave electromagnetics.* Addison-Wesley, 1989.

[192] J. A. Morente, E. A. Navarro, J. A. Portí, A. Salinas, J. A. Morente-Molinera, S. Toledo-Redondo, W. J. O'Connor, B. P. Besser, H. I. M. Lichtenegger, J. Fornieles, and A. Méndez. A late-time analysis procedure for extracting weak resonances. Application to the Schumann resonances obtained with the TLM method. *Prog. Electromagn. Res.*, 117:1–18, 2011.

[193] K. Ohta, K. Umeda, N. Watanabe, and M. Hayakawa. ULF/ELF emissions observed in Japan, possibly associated with the Chi-Chi earthquake in Taiwan. *Natural Hazards and Earth System Sci.*, 1:37–42, 2001.

[194] Y. Akinaga, M. Hayakawa, J. Y. Liu, K. Yumoto, and K. Hattori. A precursory ULF signature for the Chi-Chi earthquake in Taiwan. *Natural Hazards and Earth System Sci.*, 1:33–36, 2001.

[195] Y. J. Chuo, J. Y. Liu, S. A. Pulinets, and Y. I. Chen. The ionospheric perturbations prior to the Chi-Chi and Chia-Yi earthquakes. *Journal of Geodynamics*, 33:509–517, 2002.

[196] M. Hayakawa, K. Ohta, A. P. Nickolaenko, and Y. Ando. Anomalous effect in Schumann resonance phenomena observed in Japan, possibly associated with the Chi-chi earthquake in Taiwan. *Annales Geophysicae*, 23:1335–1346, 2005.

[197] M. Hayakawa, O. A. Molchanov, T. Ondoh, and E. Kawai. The precursory signature effect of the Kobe earthquake on VLF subionospheric signals. *J. Comm. Res. Lab., Tokio*, 169-180:1996, 43.